Measurement of Equation of State of Compressed Hydrogen and Deuterium

Katerina Falk
Merton College
University of Oxford

A thesis submitted for the degree of
Doctor of Philosophy
Michaelmas term, 2011

For my grandmother
and Matthew (Smithers) Smith

may they rest in peace ...

Measurement of Equation of State of Compressed Hydrogen and Deuterium

Katerina Falk

Merton College, University of Oxford

Thesis Submitted for the Degree of Doctor of Philosophy

Michaelmas term, 2011

Abstract

Detailed understanding of the equation of state of light elements such as the hydrogen isotopes in the warm dense matter (WDM) regime is essential for the modeling of the inner structure of many astrophysical objects, in particular Jovian planets as well as inertial confinement fusion (ICF) research. In these systems quantum degeneracy and strong inter-particle forces play an important role making its theoretical description extremely challenging.

The Omega laser was used to drive a planar shock wave in cryogenically cooled deuterium creating WDM conditions [1]. We used a set of independent diagnostics to measure the thermodynamic conditions of WDM including velocity interferometry (VISAR), streaked optical pyrometry (SOP) and x-ray Thomson scattering (XRTS). With a narrow-band x-ray backlighter probe at backscattering geometry the spectrally resolved XRTS accessed the boundary of collective and non-collective regimes making our measurement sensitive to both electron temperature and density.

This work presents a full set of measurements of the thermodynamic properties for different laser intensity drives creating warm dense deuterium at various degrees of degeneracy and coupling. The measured electron densities and temperatures ranged between 0.2 and 2.15×10^{23} cm^{-3} and $0.6 - 20$ eV respectively. The scattering measurement confirmed the findings from the VISAR and SOP data and together density-functional molecular dynamics (DFT-MD) simulations provides a novel self-consistent approach for an accurate characterization of the microscopic structure of WDM [2].

Complementary to the laser compression work, findings from project employing static compression hydrogen with the use of diamond anvil cells is also be presented. The first direct measurement of the local field correction to the Coulomb interactions in degenerate plasma was obtained from inelastic scattering (20 keV probe) at the Diamond Light Source synchrotron facility [3].

Acknowledgements

First of all, I would like to thank my DPhil supervisors Gianluca Gregori, Andrew Jephcoat and Justin Wark for the opportunity to work on this project, their advice and support for the past three years. A special thanks also goes to Dave Riley, who acted like a true mentor on many experiments, and Sean Regan, who was the key leader of the Omega project. Thanks to Chris Murphy for his selfless help in all scientific and other matters.

This work is the result of a large collaborative effort that relied on many people, to all of whom I am grateful. Thanks to Tom Boehly, Dayne Frantanduono, Maria Barrios, Suxing Hu, Radha Bahukutumbi, Mark Bonino, Jack Armstrong, Wolf Seka, Ray Bahr, Fred Marshall, Greg Pien, and the rest of the LLE staff, without whose tremendous effort this project would have never been possible. To Steve Rothman for his consultations about VISAR. Thanks also go to Dirk Gericke and Jan Vorberger from the University of Warwick for their theory work, which formed the backbone of this work. To Fida Khattak, Roland Fäustlin, Sven Toleikis, Annette Kleppe, Heribert Wilhelm and the rest of the DLS sfaff involved in the DAC experiment.

Thanks to Isabel, Lionel, Tim, Marta, Jack, Jablanka, Lema, Amrita, Carly, Chris, Mike, Mark, James, Ian, Rachel, Maria, Maruška, Jian, Will, Anne, Tom, Miloš, Kubo, Petr, Vašek and all my Oxford friends for making these years truly special. To Lan, who made all Rochester visits a lot of fun. A very special thanks goes to my parents, brother and the rest of my family back in the Czech Republic for believing in me and supporting me for all those years I have spent away from home, I always think of you. Last but far from least goes my deepest thanks to Bose for making me tea always at the most perfect moment!

Contents

Chapter 1

Hydrogen isotopes under extreme conditions

1.1 Introduction

Knowledge of the equation of state of hydrogen and its electronic properties at high densities, pressures and temperatures are crucial to development in the study of warm dense matter (WDM). This is an intermediate state of matter on the transition from a solid to an ideal plasma with characteristic medium-to-high temperatures ($1-100$ eV) and solid densities (~ 1 g/cm^3) and pressures $>$ Mbar. Such extreme conditions result in a very peculiar state of matter that stands outside the range of both ideal gas theory, commonly used to describe low density plasmas, and condensed matter, relevant to solids at low temperatures. A convenient way to place WDM on the phase diagram is using the definition of the coupling parameter Γ, which is the ratio of the Coulomb and kinetic energies. At the extreme end of the scale at high values of Γ we encounter strongly coupled condensed matter, i.e. room temperature solids with tightly bound ions often forming crystallic latices. Weakly coupled ideal plasma, where Coulomb interactions between ions are weak, appears at the top of the phase diagram with Γ less than unity. WDM then occupies the region in between, exhibiting properties of both ideal plasmas and correlated system similar to those found in condensed matter while ranging over wide span of thermodynamic conditions. Ions in this state of matter are strongly coupled and fluid-like with no long-range order, whereas electrons are fully or partially degenerate, i.e. quantum effects, normally neglected in ideal plasmas, become important in WDM. This state is therefore very hard to define and is poorly understood by current theory. Figure 1.1 shows a density-temperature phase diagram ranging from solid state physics to extreme states of matter over a variety of plasma conditions found in the laboratory or in astrophysical objects.

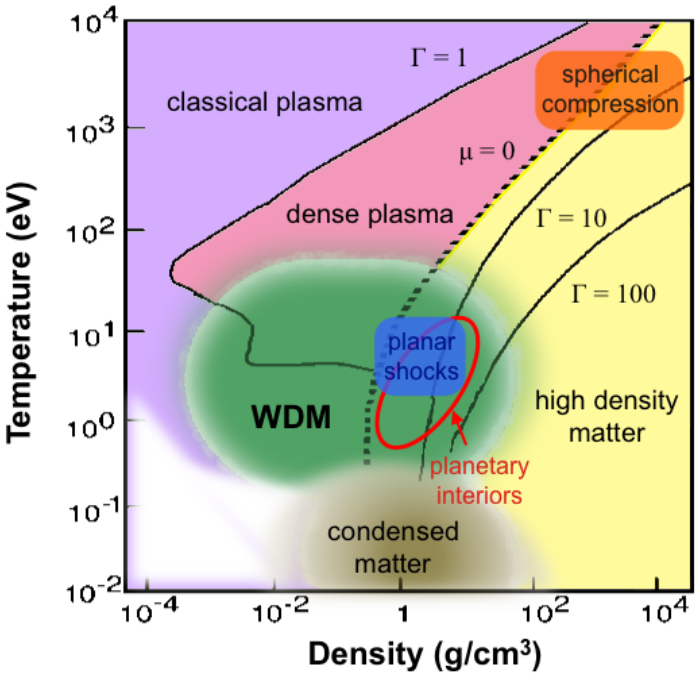

Figure 1.1: Phase diagram for the WDM regime. WDM lies between condensed matter (CM), hot dense matter (HDM) and ideal plasma (low densities), and overlaps the planar laser generated shocks in matter as well as the astrophysical conditions. Γ is the coupling parameter (ratio of Coulomb and thermal energy) so the $\Gamma = 1$ line separates the strongly and weakly coupled regimes and μ stands for the chemical potential where the $\mu = 0$ line signifies the area where the Fermi energy equals $k_B T$, below which we get Fermi degenerate matter.

The equation of state (EOS) of hydrogen and its isotopes is also important for inertial confinement fusion (ICF) research [4, 5]. The thermonuclear fusion yield is proportional to the Lawson criterion, which is the product of density and the confinement time [6]. In ICF the objective is to compress the deuterium-tritium (D-T) fuel down to sufficiently high densities to ignite the fusion reaction, while the confinement time is determined by the inertia of imploding matter. This is usually done in spherical compression of ablatively-driven capsules using high energy laser facilities such as Omega at the Laboratory of Laser Energetics, University of Rochester, or the National Ignition Facility (NIF) at the Lawrence Livermore National Laboratoy (LLNL) [7]. The two approaches are direct drive, where laser beams are used to directly ablate a plastic coating on the surface of the fusion fuel pellet driving a series of fast shock into the centre of the sphere; or indirect drive, where an external radiation source (laser or z-pinch) is used to irradiate a surface of a small gold cavity or hohlraum which heats up generating intense x-rays that will compress the D-T target inside

[4, 8]. Starting from cryogenic conditions the imploding D-T capsules transit through a range of extreme pressure and temperature states including WDM prior to ignition. In order to achieve an efficient fusion reaction this implosion is required to be highly uniform avoiding loss energy and/or confinement, which makes great demands on a detailed description of all phases during the implosion [9].

WDM is a common state of matter in astrophysical objects, for example: interiors of Jovian planets (also referred to as gas giants, e.g. Jupiter, Saturn, exoplanets), brown dwarfs, white dwarfs, low-mass stars, or crusts of old stars, all of which are predominantly composed of light elements such as hydrogen, helium or carbon. A detailed understanding of the thermodynamics of light elements under extreme conditions is therefore essential for the modeling of the evolution and inner structure of many astrophysical objects and especially giant gaseous planets and brown dwarfs [10, 11, 12, 13]. The current models rely on incomplete information to interpret the gravitational moments, total mass and spectroscopic measurements from telescopes and probes sent to Jupiter and Saturn. The full description of the structure of these planets remains uncertain in the absence of accurate EOS information for the strongly coupled degenerate matter within [14]. This means that study of hydrogen's EOS and structure under extreme conditions are of immense interest for interdisciplinary research including ICF development and laboratory astrophysics [15, 16].

To date, there is no fully consistent theoretical model for WDM. Powerful computational techniques and analytical theories have been employed to build reliable EOS tables. Possibly the most widely used EOS table for H/D is SESAME, developed at the Los Alamos National Laboratory, which is an example of a *chemical approach* [17, 18]. For astrophysical applications, these theories must tackle a number of grand challenges such as the existence of plasma phase transition, metallization, molecular-to-atomic transition, and melting of hydrogen at very high pressures [14]. However, to date there are many discrepancies and contradictions between the individual approaches, especially in the WDM regime which is covered only by interpolation in the *chemical models* [9].

A reliable experimental verification of the hydrogen and deuterium EOS is therefore of a great importance. WDM can be produced in the laboratory using fast shocks created by laser ablation [19, 20]. It is created commonly in planar shocks in laser-plasmas (solid-to-plasma transitions) or as an intermediate state during inertial confinement fusion (ICF) implosions. These laser experiments are capable of reaching temperatures of 10's of eV and pressures up to 100 Mbar, which are the conditions

that can be found in the planetary interiors. Alternatively, static compression techniques that employ diamond anvil cells (DAC) loaded with hydrogen or deuterium gas were developed to study the phases of solid hydrogen at very high pressures and lower temperatures under steady conditions forming a complementary study to the laser-shock experiments [21]. Both laser and static compression with a wide range of diagnostic techniques then allow us to probe a full range of thermodynamic and structural properties of dense hydrogen with a strong relevance to astrophysics and planetary science.

The main objective of this work is to examine the thermodynamic and structural properties of hydrogen and deuterium under conditions relevant to the interiors of giant gaseous planets like Jupiter. This is a largely experimental project carried out at the Omega laser facility, where cryogenic deuterium was compressed and heated by laser-produced shock waves. DAC static compression work was carried out at Oxford based laboratories and the Diamond Light Source at Harwell Science and Innovation Campus. The primary diagnostic technique used was x-ray Thomson scattering, spectrally resolved using crystal spectrometers. Complementary measurements were carried out using VISAR, SOP and Raman spectroscopy. Measurements of the thermodynamic quantities were then compared with a variety of theoretical models revealing important findings about the microscopic structure and compressibility of these highly degenerate systems.

1.2 Basic definitions

Systems created in experiments presented in this work span the full range of plasma conditions from Fermi degenerate to strongly coupled, even to high-temperature ideal plasmas. The transient region between solids and classical plasmas, WDM, is very difficult to define and its description bears elements of statistical plasma physics, condensed matter theory and atomic physics. It is therefore useful to define a set of classification criteria to describe these states and the transitions between them. This section will review some basic concepts and definitions taken from mostly statistical plasma physics that will be used throughout this work. It will become clear that many of the concepts from ideal plasma can be expanded to encompass the description of WDM.

Plasma is defined as a quazi-neutral system of mobile charged particles exhibiting collective behaviour. This means that the ions are at least partially ionized and as

a collective system, these free electrons and ions are capable of generating and interacting with electromagnetic fields. In ideal plasmas the interaction between the point particles is negligible and their collisions are ignored, i.e. collisionless weakly coupled plasma can be characterized as an ideal gas, from which we derive its statistical properties.

The motion of the charged particles in the system is then governed by the Maxwell-Boltzman velocity distribution. Based on this distribution of free particles it is easy to derive the screening length λ_s, over which a Coulomb field of a test particle is shielded by the charges surrounding it, which in this case is the Debye length for electrons:

$$\lambda_{De} = \sqrt{\frac{\varepsilon_0 k_B T_e}{e^2 n_e}}, \tag{1.1}$$

where k_B stands for the Boltzmann constant, T_e is the electron temperature, n_e is the number density of the electrons, e the Coulomb charge, and ε_0 stands for the permittivity of free space [22]. This then defines a radius of the Debye sphere enclosing a region of Coulomb interaction with potential $\phi(r) = (e/4\pi\varepsilon_0 r)\exp(-r/\lambda_{De})$, where r is the distance from the centre of the sphere. In a sense the Debye length is a measure of mobility of free particles in the plasma as for distances $< \lambda_{De}$ each particle moves in combined fields of equal numbers of oppositely charged neighbours and thus experiences no net force, i.e. charges effectively free inside the Debye sphere. At longer distances beyond the Debye length the interactions are weaker than the bare Coulomb interactions due to the effect of screening, i.e. the potential drops off more quickly [22].

Following from the kinetic theory we can derive the characteristic dispersion relation for the longitudinal Langmuir waves, which is the Bohm-Gross relation [23]:

$$\omega^2 = \omega_p^2 + 3k^2 v_{th}^2 (1 + 0.088 n_e \Lambda_e^3) + \left(\frac{\hbar k^2}{2m_e}\right)^2. \tag{1.2}$$

The first term ω_p corresponds to the characteristic oscillatory motion of the electrons as a response to charge displacement within the plasma, also referred to as the plasmon waves [24, 22]:

$$\omega_p = \sqrt{\frac{n_e e^2}{\varepsilon_0 m_e}}. \tag{1.3}$$

This expression bears an immense importance to the experimental investigation of plasmas. The electromagnetic radiation interacts with the electrons driving Langmuir waves within the plasma, which depend on the plasma frequency ω_p. Incident electromagnetic radiation with frequency lower than ω_p cannot penetrate into the plasma and is reflected back from its surface. As the plasma frequency depends on the electron density, we can define a critical density for a specific radiation energy (ω) over which the plasma is opaque to the radiation and the system is therefore *overdense*, with a critical density $n_c = \omega^2 \varepsilon_0 m_e / e^2$ [22].

The second term in equation 1.2 represents thermal oscillations and the third term includes degeneracy effects from Fermi pressure, introducing important quantities of the thermal velocity of electrons $v_{th} = \sqrt{k_B T_e / m_e}$ and the thermal wave length $\Lambda_e = h/\sqrt{2\pi m_e k_B T_e}$ [19]. The last term is the quantum shift [25].

A lot of scientific investigation is focusing on the study of microscopic properties of the transition from an ideal plasma to degenerate strongly coupled system. In this state, conventional theories that treat the inter-particle interactions as small perturbations, i.e. ideal collisionless plasmas, are no longer applicable [19]. As mentioned above, WDM can be characterized in the $T_e - n_e$ space through the coupling parameter Γ [26], which is the ratio of Coulomb to thermal energy (equation 1.4) and serves as a good reference to situate WDM between condensed matter and ideal plasma in the phase diagram (figure 1.1). The general definition of the coupling parameter for plasma obeying classical statistics is:

$$\Gamma_{\alpha,\beta} = \frac{Z_\alpha Z_\beta e^2}{4\pi\epsilon_0 a_{\alpha,\beta} k_B T_{\alpha,\beta}}, a_{\alpha,\beta} = \left(\frac{3\sqrt{Z_\alpha Z_\beta}}{4\pi n_e}\right)^{1/3}, T_{\alpha,\beta} = \frac{m_\alpha T_\beta + m_\beta T_\alpha}{m_\alpha + m_\beta}, \tag{1.4}$$

where Z is the charge of the particle and a is the interparticle separation for species α and β, i.e. electrons and/or ions. This definition is applicable to all types of interactions: electron-electron, ion-ion and electron-ion. The timescales relevant to this work are all at the hydrodynamic scale, i.e. at ns time scales and steady conditions (characteristic collision time of both electrons and ions are on the order of fs), so equilibrium is reached and a single temperature $T_e = T_i = T$ can be used for all interactions.

The ion-ion coupling parameter Γ_{ii} is often used as a reference for the state of matter, i.e. WDM can be defined as a system with Γ_{ii} greater than 1, which is a regime also known as *strongly coupled plasmas* [19]. In the condensed matter regime the ions are tightly bound so that the ion-ion coupling parameter is large, e.g. $\Gamma_{ii} > 175$ for

Coulomb/one-component plasma (OCP), reaching the crystallization limit [26, 19]. On the other end of the scale we find the low density plasmas that exhibit only very weak coupling with $\Gamma_{ii} \ll 1$ and can be fully understood using the ideal gas law. Coupling of the particles becomes significant at $\Gamma_{ii} > 1$. In such a strongly coupled plasma or WDM the Coulomb interactions between the particles determine the physical properties of the system.

As the density of the plasma increases to the point where the particle separation reaches their quantum oscillation wavelength $\lambda_{DeBroglie}$ the thermal motion of the electrons reduces and quantum effects become important as the electrons become degenerate. The Debye length reduces until it is comparable with the DeBroglie wavelengh of the electrons:

$$\lambda_{DeBroglie} = \Lambda_e = \frac{h}{\sqrt{2\pi m_e k_B T_e}}. \tag{1.5}$$

At this point the thermal distribution of the electrons begins to follow the Fermi statistics and equation 1.1 is no longer a correct expression for the screening length of the system. The highest occupied energy level in a fully degenerate electron gas system following the Fermi-Dirac distribution of particles is defined as the Fermi energy:

$$E_F = \frac{\pi^2 \hbar^2}{2m_e} \left(\frac{3n_e}{\pi} \right)^{2/3}. \tag{1.6}$$

Here T_e is the electron temperature, and n_e is the electron density, $h = 2\pi\hbar$ is Planck's constant, and m_e is the mass of the electron. The Fermi temperature is then $T_F = E_F/k_B$. When the thermal energy of the particles becomes comparable to the Fermi energy (equation 1.6) the degeneracy effects come to play [19]. The degree of degeneracy is described by the degeneracy parameter, a ratio of thermal and Fermi energies:

$$\Theta = \frac{k_B T_e}{E_F}. \tag{1.7}$$

This quantity is used to estimate the importance of quantum statistical effects in the system. In a degenerate plasma, the Fermi energy is larger than the thermal energy, i.e. $\Theta < 1$, and most electrons populate states inside the Fermi sea where the electrons cannot reduce the distance between them any further since multiple occupancy of those states by fermions is forbidden as a result of the Pauli's exclusion principle [19]. The electrons in WDM created in the laser shock experiments with solid or liquid targets are fully or partially degenerate.

In a highly degenerate state the Debye length, the scale over which mobile charge carriers screen out electric fields in ideal plasmas, is replaced with the Thomas-Fermi length, which depends only electron density n_e [27, 28]:

$$\lambda_{TF} = \sqrt{\frac{2\varepsilon_0 E_F}{3n_e e^2}}. \tag{1.8}$$

The Wigner-Seitz parameter r_s is another measure of electron degeneracy and coupling, see equation 1.9, where $a_B = 5.29 \times 10^{-11}$ is the Bohr radius and $d = (3/(4\pi n_e))^{1/3}$ is the inter-particle separation at a given electron density n_e. The values of r_s range between 2 and 6 for valence electrons in metals, a typical example of a fully degenerate electron system [26].

$$r_s = \frac{d}{a_B} \tag{1.9}$$

If the electron spacing becomes very small and $r_s < 1$, situation equivalent to a very large E_F reaching over the Coulomb potential, the electrons become free and form a uniform background around the ions. This results in very weak electron-electron coupling. The electron-electron coupling constant for system of degenerate electron is then redefined as [26]:

$$\frac{e^2/d}{E_F} = 0.543 r_s. \tag{1.10}$$

To account for partial degeneracy of the electron gas, the inverse of the screening length $\kappa_e = 1/\lambda_s$ should be calculated as $\kappa_e^2 = (4e^2 m_e)/(\pi\hbar^3) \int f_e(p) dp$, where $f_e(p)$ is the Fermi distribution [29]. It is more practical to use the Debye form with an effective temperature [30, 31]. Gericke *et al.* suggest the form of:

$$\kappa_e = \frac{1}{\lambda_s} = \sqrt{\frac{e^2 n_e}{\varepsilon_0 k_B T_e^{eff}}} \qquad \text{with} \qquad T_e^{eff} = (T_e^4 + T_F^4)^{1/4}, \tag{1.11}$$

which interpolates between the Debye and Thomas-Fermi screening length and yields results with less than 2% error for all densities [29]. More traditional alternative for the effective temperature (or classical fluid temperature) was proposed by Dharma-Wardana and Perrot, which was originally designed to bridge the transition regime between classical plasmas and fully degenerate electron systems by accounting both for thermal motion and the quantum effects of the electrons [31, 30]:

$$T_e^{cf} = \sqrt{(T_e^2 + T_q^2)}, \qquad T_q = \frac{T_F}{1.3251 - 0.1779\sqrt{r_s}}. \tag{1.12}$$

This approach was shown to reproduce finite-temperature static response of an electron fluid, valid for arbitrary degeneracy [30, 32]. Due to the larger mass, degeneracy effects play no role in ions for the physical conditions concerning this work.

1.3 Outstanding questions on planetary interiors

There has been a remarkable development in the understanding of the composition of the giant planets, mainly Jupiter and Saturn, during the past two decades. The chemical make-up of the deep atmospheric planetary layers have been accurately determined through spectroscopic data from telescopes and *in situ* measurements made by interplanetary probes and satellites [33]. Jupiter is composed mainly of H/He mixture with smaller quantities of heavier elements at pressures reaching ~ 10 Mbar and temperatures of a few eV deep inside its interior. Such conditions fall into the WDM regime, see figure 1.1.

Constraints on the internal structure of the planet have been mostly derived from its known mass, equatorial radius and the gravitational moments J_2, J_4 and J_6 [11], which were obtained from measurements made by the Galileo and Cassini-Huygens probes. A three-layer structure with a possible rock core surrounded by metallic and molecular hydrogen envelopes has been proposed, see figure 1.2. Jupiter therefore has a magnetic field generated by a dynamo of metallic hydrogen deep inside its interior. However, due to the poor knowledge of the EOS for hydrogen in the relevant conditions the present structural models are burdened with large uncertainties and many questions including the existence, size and composition of the inner core, the location and nature of the phase transition from molecular to metallic hydrogen and the possibility of phase separation of the H/He mixture are still a subject of scientific debate [34, 12, 35].

Molecular hydrogen at moderate temperatures ($\lesssim 10^5$ K/10 eV) dissociates and eventually ionizes undergoing a phase transition to a metallic phase once the pressure increases beyond ~ 1 Mbar creating a effective barrier between the He-rich molecular hydrogen layer in Jupiter and He-poor metallic hydrogen underneath as shown in figure 1.2 [33, 36]. It is however not clear whether the transition is continuous or discontinuous, first-order plasma phase transition (PPT). The density functional molecular dynamics (DFT-MD) simulations predict a continuous transition from the molecular to a dissociated regime in fluid hydrogen under the conditions of Jupiter's interior [37, 38, 12]. Other widely recognized models predict PPT [39, 40, 35]. Early

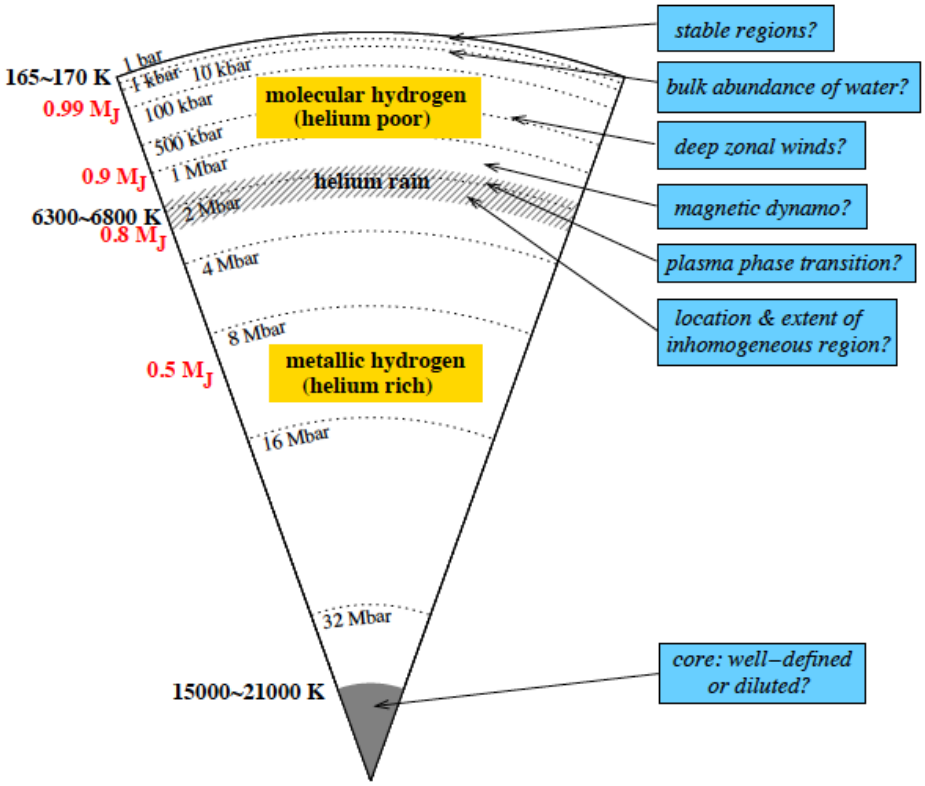

Figure 1.2: Jupiter's structure, after Ref. [36]. There are many unanswered questions about Jupiter's interior. The knowledge of EOS for H/He at the conditions deep inside the planet would help to answer those.

shock-compression experiments found no evidence of abrupt phase transition concluding that the dissociation of molecular fluid is likely to be continuous [41, 42, 43, 44, 45]. Later experimental evidence however supports the existence of PPT in hydrogen and deuterium [46, 47]. The presence of PPT provides an effective entropy barrier within the planet's interior that cannot be crossed by convection [48]. The PPT scenario therefore strongly supports the three layer model as it predicts a sharp separation of the molecular and metallic regions.

An interesting phenomenon predicted by theoretical models is H/He phase separation. Since He requires larger pressure than H to become ionized there is a possibility of a separation between He-rich and He-poor mixtures within the deep interior of the gas giants [49]. Although there is no EOS available for H/He, it is mostly agreed that this phase separation happens around the boundary of the metallic region [50, 51, 52]. Around this region He-rich droplets form within the metallic H fluid, grow rapidly and consequently fall towards the interior of the planet without being efficiently trans-

ported by convection [48]. This is also sometimes referred to as helium rain. This also remains the only viable explanation for the low atmospheric concentrations of He measured by the probes of the giant planets compared to the protostellar nebula from which the solar system formed.

Another mystery is the size and composition of the central core of the giant gaseous planets. Many evolutionary models predict that Jupiter (and Saturn) formed from a small rocky planetesimal, which acted as a seed for the planet to grow on top of [53]. Other theories assume that the core formed early in the centre of a very tenuous non-convective protoplanetary clump [54]. Its composition cannot be derived from the gravitational moments measurements. In fact its mass heavily depends on the EOS. Therefore hydrogen EOS determines if Jupiter has to have a rock core or not [34].

1.4 Laboratory astrophysics

1.4.1 Modeling of astrophysical objects

One of the growing applications of high energy density physics (HEDP) driven by the ICF research including high power lasers as well as wire array z-pinches is in laboratory astrophysics. High power lasers and z-pinches can be used as radiation sources for directly and indirectly driven ICF. Similarly, these experiments can be adapted to produce x-ray probes for absorption spectroscopy, x-ray scattering and photo-ionization experiments [19, 55]. Alternatively, plasma created in the HEDP experiments itself can be used to mimic astrophysical objects.

Both lasers and z-pinches can be used to simulate large scale astrophysical phenomena such as highly collimated outflows of energetic particles from active regions (e.g. protostars) or jets, collisionless shocks, gamma bursts, interiors of giant planets or supernova explosions [15, 16]. All these objects can be computationally modelled and compared with observations, however such numerical simulations and remote observations using astronomical telescopes have many limitations, and therefore the ability to recreate the same conditions in the laboratory on Earth and diagnose those directly with available instruments is priceless.

The actual astrophysical objects are massive spanning over many parsecs or even light years of distance and their evolution takes billions of years, yet their structure and evolution can be reliably modeled on length scales of a few μm to mm in a laboratory. Thanks to the same plasma conditions and dimensionless, i.e. scalable,

parameters (e.g. Sonic Mach number, Plasma beta, Reynolds number, Peclet number) gigantic astrophysical phenomena are governed by the same physics as small-scale experiments on Earth [34]. This work concentrates on the study of microscopic structure of highly compressed hydrogen isotopes at conditions identical to those found deep inside planets like Jupiter. The high pressures and temperatures can be recreated through ablative compression and heating using high energy nanosecond lasers. Complementary to the laser experiments, similar conditions at higher pressures, but lower temperatures can be achieved through static compression using diamond anvil cells.

1.4.2 Shock compression

The WDM conditions reaching solid densities, medium-to-high temperatures and pressures $\sim$ Mbar can be created using high power lasers. The general concept of such experiments will be outlined in this section. Direct laser irradiation leads to states reaching solid densities with relatively low temperature $1 - 100$ eV, which is perfect for WDM creation. Thus, a direct drive was chosen for this experiment. The Omega laser facility was used to provide a laser drive with typical irradiance of 10^{13} and 10^{14} W/cm^2. The infrared laser was frequency tripled giving 3ω wavelength of 351 nm and consisted of 6 pairs of 1 ns laser pulses staggered in time providing a 6 ns long constant intensity drive.

When an intense laser is focused upon a solid/liquid target a fraction of its energy is immediately absorbed creating a hot, highly ionized plasma, which rapidly expands away (timescale of a few picoseconds) from the solid surface into the vacuum. This process is referred to as ablation. This plasma further absorbs laser energy and is heated reaching very high temperatures. This low density hot plasma (corona) expands away from the solid surface into the vacuum creating a steep density gradient and ablation pressure against the cold material, which drives a strong single shock into the target. The rest of the laser energy propagates through the plasma, where it is being absorbed, until it reaches the critical density (n_c, see section 1.2) surface, into which the light can no longer propagate and is reflected back. The absorbed energy propagates further into the target through electron thermal conduction (low Z materials) heating the material within the propagating shockwave to WDM temperatures [56]. For the conditions relevant to this work, the inverse bremsstrahlung (IB) is the main process of absorption of the laser energy [57]. During this process the laser beam interacts with the electrons moving within the Coulomb field of the ions and causes them to oscillate. Since the electrons have some thermal energy and associated

velocity distribution they undergo random motion and collide with themselves and the surrounding ions. During these collisions, laser energy is transferred into thermal energy of the electrons as the extra laser-induced ordered oscillatory velocity gets randomized.

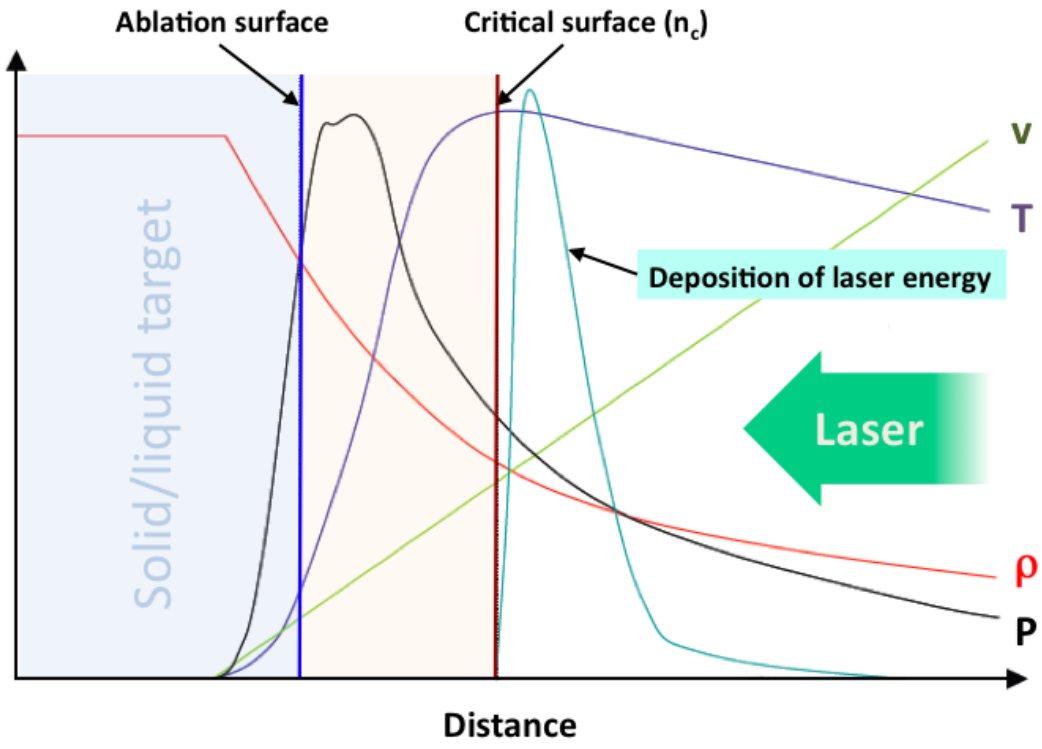

Figure 1.3: Diagram of interaction between a solid/liquid target and a laser showing ablation of the surface material. The laser light can only propagate through the plasma up to the critical density n_c at the critical surface, where it is reflected. The absorption of the laser energy increases with the density. Thus, the highest temperature is to be expected at the critical surface. The temperature then drops between the critical surface and the solid target. Heat from the critical surface is conducted down the temperature gradient towards the solid surface, where it generates more plasma, keeping the ablation process going. The cooling process due to the rapid expansion is balanced by laser energy deposition keeping the temperature of the low density corona roughly constant. The region between the ablation and critical surfaces is often referred to as conduction zone.

This collisional absorption mechanism dominates if the irradiance is kept below the limit of $I_L(W/cm^2) = 3 \times 10^{12} T_e(eV)/\lambda^2(\mu m) \sim 4 \times 10^{14}\ W/cm^2$ [58, 59]. This limit determines whether the electron thermal distribution is perturbed or not by the incident electric field, which in turn affects electron-ion collision frequency [59]. IB occurs mainly near the critical density and is therefore enhanced for shorter laser

wavelengths. At a given intensity, the plasma is much denser and cooler and hence much more collisional enhancing the IB process. Moreover, collective processes in the plasma are dampened due to the increased collisionality and are more weakly driven by short wavelength light [57]. Hence, shorter wavelengths are more advantageous as the laser light can propagate further into the plasma, closer to the cold material, and deposit its energy more efficiently. Laser absorption efficiencies reaching 80% can be expected in such experiments [60].

If the laser irradiance reaches over the limit of I_L, the nature of the laser plasma coupling changes and the incident radiation starts driving plasma waves within the target [60]. If the temperature increases too much, the efficiency of the collisional absorption is reduced [57]. Other absorption mechanisms such as the resonance absorption near the critical density n_c also take place [57, 61]. However, those interactions are a source of of many instabilities that can decrease the efficiency of laser light absorption by reflecting the incident radiation away from the target surface preventing it from reaching the critical surface, e.g. stimulated Brillouin and Raman scattering [57]. At higher intensities, generation of hot electrons can preheat the target region prior the arrival of the shockwave, reducing the shock pressure. Experimental evidence suggests that these effects are negligible when the irradiance is kept below I_L [62, 63].

The strength of the shock is often measured by the ablation pressure. A simple scaling expression can be obtained from basic principles to calculate the approximate value of the expected ablation pressure [34]:

$$P_a(Mbar) = 8.0(I/10^{14}(W/cm^2))^{2/3}\lambda^{-2/3}(\mu m), \tag{1.13}$$

which yields values of 3.5 Mbar and 16 Mbar for irradiances of 10^{13} and 10^{14} W/cm^2. These values are however likely to be slightly too high. A better estimate of the ablation pressure can be obtained using scaling expressions obtained in past experiments [64, 65, 66, 67, 68]. Considering that inverse bremsstrahlung is the dominant process of laser energy absorption in this experiment, the following expression has been used [58]:

$$P_a(Mbar) = 11.6(I/10^{14}(W/cm^2))^{3/4}\lambda^{-1/4}(Z_f t/3.5)^{-1/8}(A/2Z)^{7/16}, \tag{1.14}$$

where $A = 2$ is the mass number of the compressed material (deuterium), $Z = 1$ is its atomic number, $Z_f = 1$ the ionization degree, $\lambda = 0.35$ μm is the wavelength of the laser and $t = 6$ ns is the laser pulse duration. The introduction of parameter

t accounts for the IB process in under-dense plasma in front of the critical surface. Given this expression we should expect ablation pressures of 2.5 Mbar and 14 Mbar for 10^{13} and 10^{14} W/cm^2 laser drives respectively.

The main techniques used for the measurement of thermodynamic properties in such dense systems are x-ray scattering [19], shock velocity measurements made by velocity interferometer system for any reflector (VISAR) [69, 70] as well as temperature measurement inferred from streaked optical pyrometry (SOP) [71]. Additional diagnostic techniques such as x-ray absorption spectroscopy [72], femtosecond electron diffraction [73], proton and hard x-ray radiography are also being pioneered to improve the density measurement accuracy and to access high-Z materials [74, 75].

The temporal evolution of thermodynamic conditions in laser experiments described in this work is at the order of nanoseconds. Following from the Spitzer model [76] within this timescale the electron and ion temperatures are considered already equalized, since the electron and ion collision times are orders of magnitude smaller than the temporal resolution of the probes as well as the duration of the experiment:

$$\tau_e \approx 1/\nu_e = T_e^{3/2}/(2.91 \times 10^{-6} n_e \ln\Lambda) \sim 8.1 \times 10^{-16} \text{ s}, \tag{1.15}$$

$$\tau_i \approx 1/\nu_i = \mu^{1/2} T_i^{3/2}/(4.80 \times 10^{-8} Z^4 n_i \ln\Lambda) \sim 70 \text{ fs}, \tag{1.16}$$

where $T_e = T_i \sim 15$ eV, $n_e = n_i \sim 1.0 \times 10^{23}$ cm^{-3}, ionization $Z \sim 1$ and $\mu = m_i/m_p = 2$ for the deuterium experiment at the Omega laser facility. Here, $\ln\Lambda$ stands for the Coulomb logarithm. Even if more sophisticated models such as the Fermi Golden rule or the Coupled-mode energy-relaxation rate model by Dharma-wardana and Perrot [77] are used the equilibration times are of the order of 100's of ps [78]. The density and temperature gradients within the shocked material are also important to consider since the x-ray scattering signal is collected over the entire volume of the sample. The laser profile was smoothed with phase plates to avoid creation of hotspots that would result in instabilities in the shock (Chapter 3). Extensive 1-D hydrosimulations were carried out using the *LILAC* code [79, 80] prior the experiment to optimize the laser parameters that would generate an uniform shock.

There are other methods to generate WDM using high power lasers. Worth mentioning are experiments where laser-produced x-rays or protons are used to isochorically heat solid samples to WDM [81]. Similarly as in indirect drive ICF, high-Z material hohlraums can be used to efficiently convert incoming laser radiation into x-ray radiation due to a large number of allowed electronic transitions. These x-rays are

then used to create WDM conditions through shock compression instead of a direct laser drive [82]. Extreme conditions have been achieved by coalescing shocks within solid targets providing an excellent platform for x-ray scattering measurements [83]. Other high power facilities such as fast z-pinches and x-ray free electron lasers have been used to generate and probe WDM [44, 72, 84].

1.4.3 Static compression

Static compression experiments employing diamond anvil cells (DAC) form the basis of fundamental physics study and have over past 30 years revealed surprising structural complexity of compressed hydrogen. Through various diagnostic techniques the molecular bond structures, transitions between different structural phases, metallization, EOS and the melting curve in solid hydrogen are probed. This is a very active field of research with direct application to planetary science. The DAC experiments are at present time are capable of operating at up to $T \sim 1000 - 5000$ K (~ 0.5 eV) with laser heating of the samples and 350 GPa (3.5 Mbar) at 300 K. The conditions in DAC experiments are generally different to those created by laser-compression, but also very important to the fundamental research in physics of hydrogen and planetary science.

The DAC was first developed by Weir *et al.* [85, 86] as a new technique in the high pressure physics research and geoscience. Other materials such as sapphire have been used in similar applications, but diamond due to its strength and hardness is the material of choice to achieve the highest pressures reaching the Mbar range. Another advantage leading to the choice of the anvil material is the transparency to electromagnetic radiation in the infrared (IR), optical, ultra-violet (UV) and x-ray bands used as diagnostic probes [87]. The three main types of DAC systems are the piston-cylinder Mao-Bell cell, Merill-Bassett type and the Boehler-Almax (plate) cell [88]. A variant of cell type designed at Oxford was used in the x-ray scattering experiment at the Diamond synchrotron, see Chapter 6 and figure 1.4.

A typical DAC setup is shown in figure 1.4 two opposing diamond anvils, perfectly polished diamonds with a flat culets facing each other, compress a metal gasket (flat foil with a drilled hole) that contains the sample. Prior to the sample being loaded the gasket has to be preindented with the aligned diamond anvils to create the characteristic "bulged" shape which will contain the hydrogen/deuterium gas tight between the anvils. After that a hole of $\sim 50 - 200$ μm (depending on the desired pressure limit) is drilled in the centre of the indentation. Typical materials used as gaskets are: Rhenium, which is most common as it is strong yet very ductile allowing a plastic

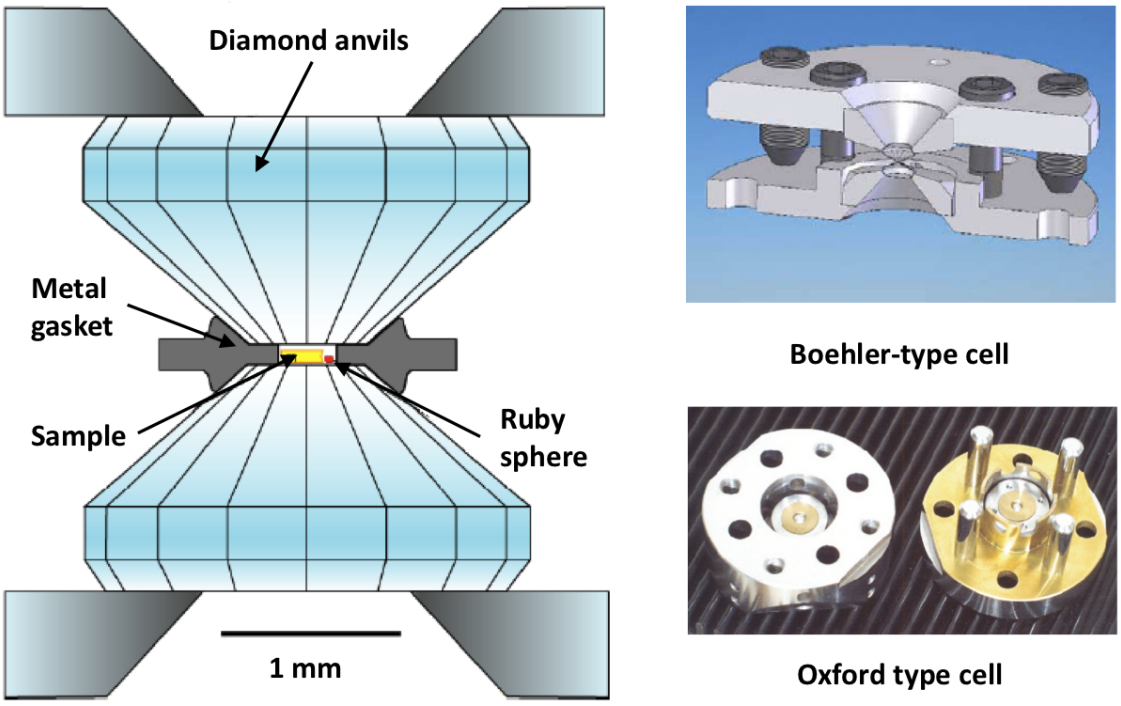

Figure 1.4: Schematic of a typical DAC setup including the diamond anvils, metal gasket, sample and a ruby sphere pressure reference. The figure also includes some example of different cell/gear box systems used. Images were taken from Ref. [88].

deformation during indentation and maintaining a reasonable thickness to high pressures; Tungsten, which is also very strong, but relatively brittle and has to be handled with caution; stainless steel Type 301, which is relatively soft, however acceptable for lower pressures and its main advantage is low chemical reactivity with the samples; and Beryllium, which is soft, but transparent to x-rays making it useful for diffraction experiments, however it is dangerous to handle. In the experiment described in this work Tungsten and stainless steel gaskets have been used.

The cell is then assembled by placing the gasket back on one of the diamond tips as before. When the diamonds touch the gasket, a birefringence effect with coloured fringes is visible under a microscope, which is an effect of strain within the diamonds under pressure. The cell is kept released (no birefringence observed) leaving a small gap between the diamonds and the gasket and placed inside a gas loading vessel. The sample is loaded with a pressure-transmitting medium, which helps to create close-to-hydrostatic conditions (homogeneous pressure throughout the system) and ideally also acts as a thermal insulator [89]. The cell is first flushed with the pressure medium (He condensed gas) and then with the experimental mixture (D_2-He or H_2-He

mixture) before it is loaded with the pressuarized gas using a compressed gas pump apparatus. The anvils are sealed inside the gas vessel after it has been filled with the gas at $\sim$ 30,000 psi (0.2 kPa) locking the sample within the gasket and the diamond anvils by compressing the DAC using a gear box. The pressure can then be further increased using a gear box to the GPa regime. Such experiments are characteristic for their small sample volume needed to achieve extreme pressures. The small sample size compensated by the brightness of the probe used to study the sample.

One or two small chromium-doped ruby (Al_2O_3: Cr^{3+}) spheres are also burried inside the gasket with the sample [90]. These act as a pressure reference, which was first introduced by Barnett *et al.* [91], who discovered the near-linear relationship of the spectral shifts of the optical fluorescence lines of ruby with increasing pressure. This secondary pressure scale is then used as a reliable pressure gauge in DAC experiments [92]. These measurements are relatively straightforward at $P < 100$ GPa and can be carried out on-line or off-line using a calibrated grating spectrometer coupled with an optical laser system, which can be focused onto the ruby spheres inside the gaskets under a microscope. This method is described in more detail in section 6.2.3.

Typical diagnostics used with such statically compressed samples include single crystal or powder x-ray diffraction at synchrotron facilities used to study the structure and the EOS of crystalline samples [21]. Alternatively, Raman or IR spectrocopy is used for finger-printing and structural studies of molecular substances through observation of energy shifts due to the vibrational and rotational modes of the molecular bonds [93]. Our group pioneered x-ray scattering from statically compressed samples, which was carried out at the Diamond Light Source synchrotron facility at the Harwell Science and Innovation Campus [3]. New experiments carried out at the Lawrence Livermore National Laboratory (LLNL) in California that combine both compression techniques, where statically pre-compressed DACs are further compressed and heated by laser ablation have also been reported and show to be a promising tool to probe the hydrogen EOS to even more extreme pressures and temperatures [94, 95].

1.5 Overview of previous experiments

The arrival of new facilities and diagnostic techniques during the last two decades brought something of a revolution on the experimental measurement of hydrogen and deuterium under extreme conditions. X-ray scattering as a diagnostic for dense plasmas was first suggested by Nardi *et al.* [96, 97] shortly followed by the first experimental evidence of scattering from indirectly irradiated and shock-compressed

Al foils with kilovolt Ti He-α laser-produced source [98, 99]. Spectrally resolved x-ray scattering from a radiatively heated Be plasma probed with Ti He-α x-rays was first demonstrated by Landen *et al.* [100] at the Omega laser facility. The first high accuracy measurement of electron temperature and density from non-collective scattering was performed soon after by Glenzer *et al.* [81, 101] marking the beginning of x-ray scattering as a standard EOS diagnostic. The first clear evidence of x-ray scattering measurement of plasmons was presented by Glenzer *et al.* [102, 103]. The first full measurement of the electron temperature and average ionization balance of nearly Fermi-degenerate CH plasma created by a direct laser drive shock-heating probed by Zn He-α was achieved at Omega the same year by Sawada *et al.* [104].

Spectrally resolved scattering using laser produced ultrafast Ti K-α x-ray pulse illuminating shock-compressed LiH creating WDM conditions relevant to planetary interiors was observed at the iconic experiment performed at the Titan laser facility by Kritcher *et al.* [83]. The first measurement of the ion-ion structure factor S_{ii} from an x-ray scattering measurement of warm dense Li was carried out at the Vulcan laser facility (RAL) by García Saiz *et al.* [105]. Faüstlin *et al.* [84] expanded the techniques of x-ray Thomson scattering to the DESY free electron laser (FEL) facility in Hamburg, where they were able to investigate ultrafast electron dynamics in a non-thermal state within a liquid hydrogen sample, which was isochorically and volumetrically heated to WDM state with moderate coupling using monochromatic x-rays from the FEL at 91.8 eV non-collective regime. Full review of x-ray Thomson experiments in high energy density systems as well the theory related to this work is presented in great detail in the review paper by Glenzer and Redmer [19].

The first extensive experimental study of the EOS of high pressure states in liquid deuterium were investigated by Da Silva *et al.* and Collins *et al.* [41, 42, 106]. In their experiment the Nova laser was used to shock-compress liquid deuterium to extreme pressures of 22 to 340 GPa. They were able to confirm a phase transition to metallic deuterium through the means of shock-reflective diagnostic with independent confirmation by radiography measurement and probed the deuterium Hugoniot through velocity interferometry measurements giving very high compression ratio ("soft" Hugoniot). Temperature of the shocked deuterium was obtained using multifrequency pyrometry. Although this Hugoniot measurement was later proven unreliable, this remain influenceful work within this field. The Mbar regime in fluid deuterium was probed through double shock-compression at the Omega laser facility by Boehly *et al.* [107].

An extensive study of the deuterium Hugoniot spanning a wide range of densities and pressures across the WDM regime by the use of VISAR diagnostic with quartz and Al pushers was performed by Hicks *et al.* [20, 108]. Alternatively, fast z-pinches including the Z-machine at Sandia National Laboratory have been used to accelerate flyer plates to shock compress cryogenic deuterium creating shock-heated states similar to those created in laser experiments. Knudson *et al.* [44, 109, 110] employed the velocity interferometry technique with an Al pusher to collecting a full set of deuterium Hugoniot measurements. Independent measurement by Belov *et al.* [111] confirmed these measurements using spherically converging shock wave excited by the denotation of condensed explosives to compress solid deuterium. Knudson himself later questioned [112] the quartz pressure standard that supported all of the quartz and Al pusher EOS used in the impedance-matching in order to obtain the deuterium Hugoniot in the previous VISAR experiments, shifting the Hugoniot further to the "stiff" end suggesting large systematic errors ($\sim 12\%$) in the deuterium density measurement.

Measurements by Celliers *et al.* [43] of shock reflectance vs. shock velocity observing an increase and subsequent saturation of the optical reflectance of shocked deuterium indicated a phase transition to a conducting state characteristic of a metallic fluid is reached at shock velocities ~ 20 km/s. The temperature of single-shock-compressed deuterium was determined from pyrometric measurements carried out by Collins *et al.* [113], who were able to use their results to prove that deuterium under these conditions is a degenerate Fermi-liquid metal. A full set of EOS measurement of deuterium Hugoniot were obtained by Bailey *et al.* [114] using simultaneous VISAR and time-resolved optical spectroscopy that provided a reliable temperature measurement along the Hugoniot. Comprehensive study of metallization of dynamically compressed hydrogen was carried out by Weir *et al.* [115, 116]. Progress in the study of metallization of hydrogen at high pressures was summarized in the review paper by Nellis [117]. Experiments carried out by Fortov *et al.* [46], who used the quasi-isentropic compression in plasma by series of reverberating shock waves to created extreme compression, observed the first direct experimental indication of a new phase transition to a metallic fluid in a strongly-coupled deuterium.

Static compression experiments have used the hydrogen/deuterium DACs to explore the low-temperature high-pressure EOS administrated by x-ray diffraction at synchrotron facilities. Among the first were Mao *et al.* [21] and Hemley *et al.* [118] with their x-ray diffraction experiments from single crystal hydrogen and deuterium probed the phase diagram up to 26.5 GPa at the National Synchrotron Light Source

in Brookhaven National Laboratory. Their work was extended by Loubeyre *et al.* [119, 120] who used the techniques of x-ray diffraction and optical Raman spectroscopy to measure the low temperature EOS of hydrogen up to 320 GPa. Excellent overview of high-pressure hydrogen structure in the static compression domain is summarized by Mao and Hemley in their review paper [121]. Most recent DAC experiments reported by Eremets and Troyan provide evidence of first-order transition (PPT) from molecular to a metallic state in pure solid hydrogen and deuterium at $260 - 270$ GPa and room temperature (295 K) [47]. The first experiment combining the techniques of static and dynamic compression of a hydrogen sample was carried out by Loubeyre *et al.* [94], where independent VISAR and pyrometric measurements provided pressure and temperature of pre-compressed hydrogen sample driven by the Vulcan laser.

1.6 Thesis outline and author's role in this work

Much like the rest of present experimental science, the research presented in this thesis is based on many generations of previous research and is a part of a large collaborative effort. This section is aimed to point out the contributions of the author to this project. Work of others presented in this work will be clearly referenced on all occasions and explicitly labelled by name when appropriate. The current chapter (Chapter 1) is aimed to provide a brief introduction to the field and research presented in this thesis. Although some of the calculations presented were carried out by the author, this is predominantly a literature review of previous work and the outstanding questions in the field and is thus mostly work of other scientists with all references to the relevant work included.

Chapter 2 is concepted as a theoretical background to the author's work. Content presented here is therefore taken entirely from a number of different sources, all of which have been acknowledged and the particular references to books, research papers and the work of individuals used have been identified within the text. Chapter 3 then provides an overview of the main experimental campaign at the Omega laser facility. Much of this work is done by a very large group of scientists and technicians at the Laboratory of Laser Energetics at the University of Rochester in the US. The diagnostics and laser set up was carried out entirely by the LLE staff. The target assembly was carried out by the LLE target fabrication laboratory overseen by Mark Bonino. The original experimental planning pre-2009 was done by Dr. Sean Regan (LLE) and Dr. Gianluca Gregori (Oxford). The author was in charge of planning of

the VISAR/SOP part of the Omega experiment. The planning of the XRTS part of the Omega project was then equally shared between the author and Dr. Sean Regan. The author was also closely involved in the laser drive and target development between 2009 and 2011 overseen by the project leader Dr. Sean Regan.

Data analysis on the laser pulse shape, x-ray streak camera and x-ray backlighter brightness was carried out by the author. The x-ray pinhole camera analysis (Chapter 2) was done by Dr. Sean Regan and Dr. Fred Marshall (LLE). The hydrodynamic simulations presented in Chapters 2, 4 and 5 are work of a number of individuals. The 1-D *LILAC* simulations, used in the planning stage of the Omega experiments, were run by Dr. Radha Bahukutumbi from LLE. The 2-D *DRACO* simulations were the work of Dr. Suxing Hu, LLE. The 1-D *HELIOS* simulations largely used to support the data analysis in Chapters 4 and 5 were carried out by the author using the Prism software. The DFT-MD simulations used to compute the deuterium EOS used in Chapters 4 and 5 done by Dr. Jan Vorberger and the final relevant analysis was based on theoretical consultations with Dr. Dirk Gericke, both from the University of Warwick. All references to these codes and underlying theory are included in the text.

Data analysis presented in Chapter 4 is entirely the work of the author. The XVIS program used to extract the phase shift from the VISAR data was written by Dr. Damien Hicks from the Lawrence Livermore National Laboratory. The VISAR and SOP work was supported by many helpful consultations with Dr. Tom Boehly, Dayne Frantanduono and Maria Barrios from the LLE. The data analysis in Chapter 5 are also the work of the author, with some of the earlier scattering spectra plotted by Dr. Sean Regan. The code used to fit the Compton peak and compute the thermodynamic conditions using the frequency sum rules of the dynamic structure factor was the work of the author. The spectral fits using the random phase approximation (RPA) and full profiles were done by the author using the XRS code by Dr. Gianluca Gregori. The calculations involving the composite scattering profiles and weighted averages using the 1-D and 2-D hydro simulation outputs in Chapter 5 are the work of the author. The contributions by other collaborators and referenced sources have been included in the chapters explicitly.

Chapter 6 then presents another type of an experiment on statically compressed hydrogen using diamond anvil cells. The experiment was a large collaborative effort of many teams of scientists at Diamond Light Source, Univesity of Oxford, DESY and Queens University Belfast, all closely involved individuals have been acknowledged in authors publication on this project [3]. The author was heavily involved in the

running of the experiment and data collection although the experiment had been planned by Dr. Gianluca Gregori and Prof. A. P. Jephcoat (Oxford, Diamond) prior the involvement of the author in the project. The cells have been prepared by Prof. Andrew Jephcoat and Dr. Annette Kleppe (Diamond). All data analysis, including the code used to calculate the downshifted scattering feature using the zero temperature RPA, presented in this chapter is the original work of the author.

Chapter 7 is a summary of the key results of this work. It includes conclusions and proposal of future work by the author, which have been peer-reviewed by the larger team of collaborators. Appendix A includes an overview of the acronyms, constants and common variables used. Appendix B provides a lengthly calculation of the dielectric function from the random phase approximation taken from other sources, which have been properly referenced. A list scientific publications by the author is given in Appendix C.

Chapter 2

Theoretical description of WDM

2.1 Introduction

As outlined in the previous chapter, WDM is a very complicated state of matter. Laying on the boundary between the descriptions of the ideal gas applicable to classical plasma of low density and the condensed matter theory used to understand crystalline solids its equation of state and microscopic staucture is very complicated. The correlations between the ions in WDM are important and it exhibits similar behaviour to liquids. Quantum effects have to be incorporated into the modelling of the electron species as they are fully or partially degenerate.

Due to its high density and relatively low temperature it is also a very difficult system to diagnose using traditional techniques such as optical laser interferometry, shadography, optical Thomson scattering or emission spectroscopy. X-ray scattering is introduced as a powerful diagnostic technique capable of penetrating deep inside the WDM sample and provide a full set of information of its state and microscopic structure [19].

This chapter outlines the theoretical understanding of WDM in present science. A brief description of theoretical models and simulations is provided. The theoretical description of the EOS of WDM is extremely challenging and many approximations are required resulting in many discrepancies between the individual approaches. The main models used to date include the analytical models such as Thomas-Fermi theory; *chemical models* that include some of the most widely used EOS tables such as SESAME [17] or the Saumon and Chabrier EOS [122, 123]; and more recently the computing power has reached a stage when theorists are able to include quantum and atomic physics calculations into their simulations, often based on the density-function theory molecular dynamics (DFT-MD) or path integral Monte Carlo (PIMC) simulations and created so-called *ab initio* or *physical models* [37, 38, 124, 125]. In this

work many of these models will be compared with experimental measurements from independent diagnostics in order to constrain the theoretical description of WDM.

2.2 Microscopic structure of WDM

2.2.1 Static and dynamic properties

For simplicity a one-component system (OCP) is going to be considered in order to derive some basic expressions to describe the structure of WDM. Here only ions are considered as individual charges or particles and electrons form a rigid neutralizing background of negative charges, which only provides charge neutrality. Such an approximation is valid when electrons are highly degenerate and effectively free as their wavefunctions are smeared out throughout the lattice satisfying the periodic Bloch functions [126, 127, 128]. It is also valid at high temperatures, when electrons are much more mobile than the ions and act as a spatially uniform background around the ions [126]. Internal structure of a static many-body system can be characterized in terms of correlation functions which give the probability of finding particles at a specific location in space at a certain time. The *pair correlation function* is defined as the conditional probability density of a pair of particles being separated by $\mathbf{r}$:

$$h(\mathbf{r}) = \frac{V}{N(N-1)} \langle \sum_{i \neq j=1}^{N} \delta(\mathbf{r} - \mathbf{r}_i + \mathbf{r}_j) \rangle, \tag{2.1}$$

where N is the total number of particles in the system with normalization:

$$\frac{1}{V} \int_V d^3 r h(\mathbf{r}) = 1 \tag{2.2}$$

The pair distribution function is therefore a statistical average of different configurations of positions of $\mathbf{r}_i$'s and $\mathbf{r}_j$'s. The *pair distribution function* is then defined as:

$$g(\mathbf{r}) = h(\mathbf{r}) + 1. \tag{2.3}$$

Here we assume that there always is one particle at some given distance, i.e. the distribution is even. The *density-density correlation function* of translationally invariant systems is then given by:

$$p(\mathbf{r}) = \langle \rho(\mathbf{r}) \rho(0) \rangle = \langle \rho(\mathbf{r} + \mathbf{r}') \rho(\mathbf{r}) \rangle = \frac{1}{V} \langle \sum_{i,j=1}^{N} \delta(\mathbf{r} - \mathbf{r}_i + \mathbf{r}_j) \rangle, \tag{2.4}$$

where the electron density operator and its Fourier transform are defined as:

$$\rho(\mathbf{r}) = \sum_{i=1}^{N} \delta(\mathbf{r} - \mathbf{r}_i), \qquad \rho_{\mathbf{k}}(\mathbf{r}) = \sum_{i=1}^{N} e^{-i\mathbf{k}.\mathbf{r}_i(t)}. \tag{2.5}$$

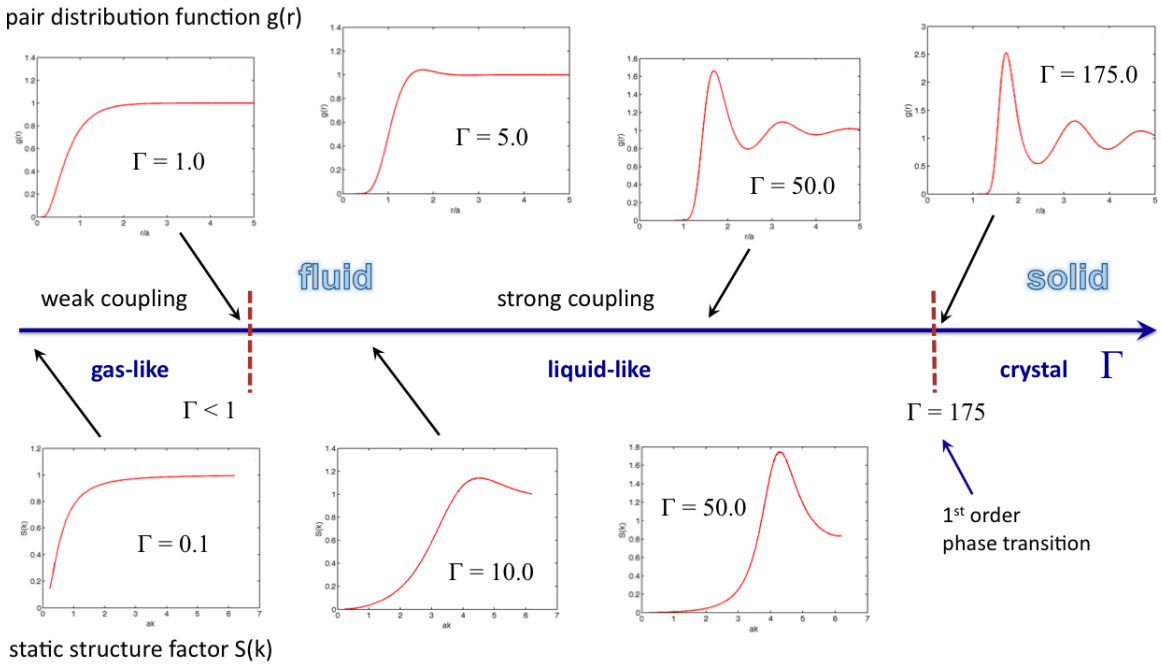

Figure 2.1: Pair distribution function ($g(r)$ vs. r/a) and static structure factor ($S(k)$ vs. ak), where a is the Bohr radius, as a function of coupling parameter Γ, equation 1.4. Plots of $g(r)$ and $S(k)$ were obtained from MD simulations by James Mithen.

It is clear that the density-density correlation function is related to the pair correlation function through the expression for the average density fluctuations of the ions. At this point we define the expression for the *static form factor*, which is the Fourier transform of spatial density distribution of the system of particles [26]:

$$S(\mathbf{k}) = \frac{1}{N}\langle \rho_{\mathbf{k}}(0)\rho_{-\mathbf{k}}(0)\rangle = 1 + \frac{1}{N}\langle \sum_{i\neq j=1}^{N} e^{i\mathbf{k}.(\mathbf{r}_i - \mathbf{r}_j)}\rangle \tag{2.6}$$

It is this quantity that gives the amplitude of scattering signal from the particles. The pair distribution function can then be linked to the static form factor through the Fourier transform of the pair correlation function, equation 2.1.

$$S(\mathbf{k}) - 1 = \frac{N-1}{V}\int d^3r e^{-i\mathbf{k}.\mathbf{r}}[g(\mathbf{r}) - 1] \tag{2.7}$$

This expression illustrates how the static structure of the system depends on the pair distribution of the particles [126]. The positions of the particles and hence the pair correlations can be obtained from the result of molecular dynamics or Monte Carlo simulations and the expression 2.7 can be used to calculate $S(\mathbf{k})$. Such a calculated scattering profile can then be compared with experimental scattering or diffraction spectra which directly measure $S(\mathbf{k})$.

In this work we are interested in the energy exchange between the electrons and photons, therefore we need to look at the frequency spectrum of the density fluctuations in the dense hydrogen/deuterium plasma. Thus, one has to go one step further to include time-dependence in the structure of the system. The *dynamic structure factor* (DSF) is therefore defined:

$$S(\mathbf{k},\omega) = \frac{1}{2\pi N}\int dt e^{i\omega t}\langle\rho_{\mathbf{k}}(t)\rho_{-\mathbf{k}}(0)\rangle, \tag{2.8}$$

where the space-time Fourier transform of the density operator is:

$$\rho(\mathbf{k},\omega) = \frac{1}{2\pi}\int dt e^{i\omega t}\rho_{\mathbf{k}}(t). \tag{2.9}$$

The dynamic density-density correlation function can then be expressed as

$$G(\mathbf{r},t) = \int\langle\rho_{\mathbf{k}}(\mathbf{r}+\mathbf{r}',t)\rho_{\mathbf{k}}(\mathbf{r}',0)\rangle d\mathbf{r}'. \tag{2.10}$$

The scattered signal is then generated by the density fluctuations in both space and time and its amplitude is determined by the dynamic structure factor (DSF), which is a space-time Fourier transform of the density-density correlation function $G(\mathbf{r},t)$, which describes the correlations between different points in the plasma [128]. It can be shown that the DSF is linked to the velocity distribution of the particles in the system through the density fluctuations of the charges [129, 126]. The effective potential of a particle submerged in a Coulomb field is reduced by the polarization screening of the surrounding charges. We can account for this effect by introducing the *effective quasi-particle density*:

$$\rho(\mathbf{k},\omega) = \frac{\rho^0(\mathbf{k},\omega)}{\varepsilon(\mathbf{k},\omega)}, \tag{2.11}$$

which is the definition of the *dielectric response function* $\varepsilon(\mathbf{k},\omega)$ [127]. Here, the "0" index marks the non-interacting particles. Since $\rho(\mathbf{k},\omega)$ and $\rho^0(\mathbf{k},\omega)$ are real quantities we have $\varepsilon(-\mathbf{k},-\omega) = \varepsilon(\mathbf{k},\omega)^*$. From here the link of DSF $S(\mathbf{k},\omega)$ to the dielectric function $\varepsilon(\mathbf{k},\omega)$ can be established:

$$S(\mathbf{k},\omega) = \frac{S^0(\mathbf{k},\omega)}{|\varepsilon(\mathbf{k},\omega)|^2} = \frac{1}{|\varepsilon(\mathbf{k},\omega)|^2}\int d^3v f(\mathbf{v})\delta(\omega - \mathbf{k}.\mathbf{v}). \tag{2.12}$$

This expression is known as the *fluctuation-dissipation theorem* and relates the spectrum of density fluctuations of charges in a many-particle system to the dielectric function [130]. EM radiation (x-rays) scatter from the electrons in the system, whose fluctuations can be described using these equations. The DSF then corresponds to the spectrum of the radiation scattered by the particles. The link to the dielectric functions then provides a measure of the electric and thermodynamic properties of the system.

2.2.2 The dynamic structure factor

According to the chemical model which separates the motion of the electrons and ions derived by Chihara [131, 132], the total electron-electron dynamic structure factor $S_{ee}^{tot}(k,\omega)$ breaks down into three different components, each corresponding to a different degree of correlation between the electrons and ions:

$$S_{ee}^{tot}(k,\omega) = |f_I(k) + q(k)|^2 S_{ii}(k,\omega) + Z_f S_{ee}^0(k,\omega) + Z_c \int \tilde{S}_{ce}(k,\omega-\omega')S_s(k,\omega')d\omega'. \tag{2.13}$$

This expression allows to account for contributions to the absorption and scattering of EM radiation from all electron species within the plasma or liquid metal [132]. This expression is valid in the regime where the energy of the incident EM radiation is higher than the ionization energy ($\hbar\omega_0 \gg E_I$) [58]. The first term represents the electrons whose motion is strongly correlated with the ions, thus this term relates to the ion-ion density correlation function S_{ii}, which reflects the thermal motion of the ions and/or the ionic plasma frequency and is related to elastic (Rayleigh) scattering of EM radiation [19]. The terms within the brackets correspond to the ion form factor $f_I(k)$ and the screening term $q(k)$, which describe the distribution of the electrons tightly bound to the nuclei and the free and valence electrons that dynamically follow the ion motion respectively.

The second term models the free electrons that do not follow the ion motion producing inelastic scattering due to the Compton effect [133]. Z_f is the number of delocalized electrons and $S_{ee}^0(k,\omega)$ is the high frequency part of the electron-electron correlation function already described in the previous section [26], see equation 2.16. The last term in the above expression includes the contribution of the inelastic scattering due to bound-free transitions of the core electrons [19]. Here Z_c denotes the

number of bound electrons, hence $Z_f + Z_c$ = atomic number of the neutral atom. $S_{ce}(k,\omega)$ is the dynamic structure factor of the core electrons undergoing Raman transitions to the continuum. $S_s(k,\omega)$ is the dynamic structure factor of a single ion, which modulates the contribution of the inelastic processes by the self-motion of the ions.

The ion feature

The theoretical calculation of the static ion structure factor $S_{ii}(k,\omega)$ for dense plasmas, where ion coupling is strong and weak coupling approximations such as the Debye-Hückel (equation 2.19) are not applicable, is very challenging for current theories and requires introduction of complicated quantum electron-ion potentials and/or screened models. In the simplified picture within the *frozen core approximation*, which treats the bound electrons in a simplified way neglecting the bound-free transitions (such that $lim_{k\to 0} f_I(k) = Z_c$) and treats the ions adiabatically, the frequency dependance in the ion-ion DSF is reduced to a delta function:

$$|f_I(k) + q(k)|^2 S_{ii}(k,\omega) = \left| Z_c + \sqrt{Z_f}\frac{S_{ei}(k)}{S_{ii}(k)} \right|^2 S_{ii}(k)\delta(\omega), \tag{2.14}$$

where $S_{ei}(k)$ and $S_{ii}(k)$ are the static electron-ion and ion-ion structure factors respectively [19]. Here, the screening function $q(k)$ in a fully ionized system is defined in terms of the partial structure factors in electron ion system as $q(k) = \sqrt{Z_f}S_{ei}(k)/S_{ii}(k) = Z(k_{De}/k)^2 S^0_{ee}$ [134, 29]. Corrections (e.g. screening) to S^0_{ee} will have a large impact on the intensity of the ionic feature through $q(k)$, which is particularly large for low-Z elements as the ratio of free to bound electrons increases. The ionic form factor $f_I(k)$ can be more precisely computed using the electron wavefunctions, e.g. Hatree-Fock self-consistent field method [135, 136, 130].

$S_{ii}(k)$ can be calculated through the one-component plasma (OCP) model, which is widely applied to dense plasmas with strongly coupled ions and highly degenerate electrons [27]. As described earlier, the model treats the ions as point-like particles interacting through Coulomb forces surrounded by a neutralizing, rigid and uniform background representing the electrons and neglects the electron-ion polarization effects. The positions of these ions and their total free energy energy can be computed through Monte Carlo (MC) or Molecular Dynamics (MD) simulations [137, 138]. For greater accuracy, the ions can be modeled as *Charged Hard Spheres* of finite size. Such models can be solved analytically. The screening of the charges is included as

a corrections through the linear screening approximation assuming weak electro-ion coupling:

$$S_{ii}(k) = \frac{S_{ii}^{OCP}}{1 + f_v(k) S_{ii}^{OCP}}, \tag{2.15}$$

where $f_v(k)$ is the screening correction to the bare ion-ion interaction and S_{ii}^{OCP} is the unscreened ion-ion structure factor calculated within the OCP model for finite-size ions [139]. In the most basic screened one-component plasma (SOCP) model the screening function $q(k)$ is derived from the Coulomb potential, which is only strictly valid for fully ionized systems. A more sophisticated approach employs pseudopotentials such as the empty core with a soft cut off which allows for negative screening extending the validity of the SOCPN ("N" for negative) model to partially ionized matter [29]. This is a well-known effect, where the bound electrons repel the valence electrons near the nucleus and reduce the effect of screening at short distances.

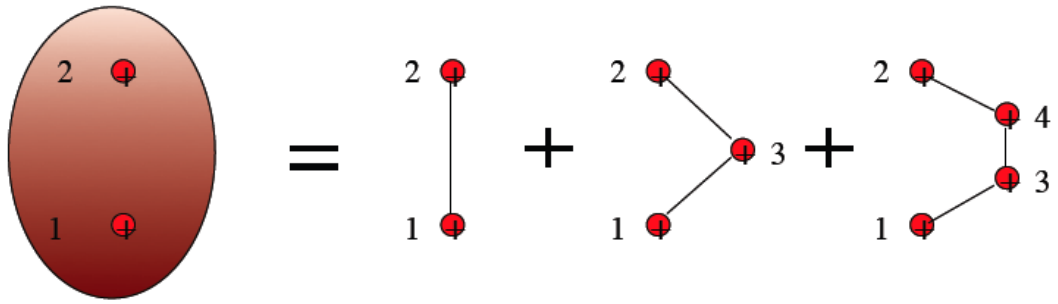

$$h(1,2) = c(1,2) + \int c(1,3)c(3,2)d3 + \int\int c(1,3)c(3,4)c(4,2)d3d4 + ...$$

Figure 2.2: Illustration of the HNC calculation process, after Ref. [126]. Here $c(r)$ denotes the direct correlation function introduced in the main text and $h(r)$ is the pair correlation function defined in the previous section.

The static structure factor can also be obtained from statistical theories including the integral equations for the pair correlation functions within the hypernetted chain (HNC) scheme [128, 26, 126]. In this approach the correlations between the ions are calculated in a series of steps. Going beyond weakly coupled theories (RPA or Debye-Hückel), which assume that the ions interact only with the surrounding field generated by the other charges, in the HNC approach direct interactions between the particles are considered by the means of the *direct correlation function* [126]. The calculation process is illustrated in figure 2.2.

In the first order, interaction of only two neighbouring bodies with specific effective potentials is considered. The second step then includes the interaction of the first pair with a third particle. Subsequently, more ions are gradually added modifying the total distribution of the particles. For homogeneous plasma, the interaction chain can be rewritten in the form of the Ornstein-Zernicke relation, which can be calculated analytically [126, 140]. In order to correctly account for short-range effects quantum pseudo-potentials were used in more advanced models to mimic diffraction and exchange effects in dense electron-ion systems [141, 142].

The choice of the effective potentials/screening as well as many approximations add uncertainty into the theoretical calculation of the ionic feature. It is often exhibited in reduction of the total intensity of the elastic peak in the scattering spectra, where many corrections such as the Debye-Waller factor have been suggested [139]. This uncertainty in determining the ionic feature makes the modeling of a full scattering profile that would include both the inelastic Compton and elastic Rayleigh scattering features difficult and inaccurate. In this work we therefore focus on the free electron feature in the scattering spectrum.

The free electron term

The free electron feature can be rewritten in terms of both ion and free electron contributions: $S_{ee}(k,\omega) = \frac{|q(k)|^2}{Z_f} S_{ii}(k,\omega) + S^0_{ee}(k,\omega)$, where the relationship between electron-ion and the ion-ion structure factors is $S_{ei}(k,\omega) = (|q(k)|/\sqrt{Z_f}) S_{ii}(k,\omega)$ [132]. These expressions derived in [131] are used as an intermediate step in the derivation of equation 2.13. The computation of $S^0_{ee}(k,\omega)$ is largely simplified by the fact that under the majority of WDM conditions the electron-electron correlations are weak and the non-linear interaction terms can be neglected.

The electron-electron structure factor, which describes the correlations within the electron species in the plasma, can be linked to the dielectric function from the Nyquist fluctuation-dissipation theorem introduced earlier, which states that if a thermodynamic system responds linearly to an external perturbation, then the amount it responds by is simply related to the fluctuation properties of the thermodynamic system [143]:

$$S^0_{ee}(k,\omega) = -\frac{\hbar}{1-\exp(-\hbar\omega/k_B T_e)} \frac{\epsilon_0 k^2}{\pi e^2 n_e} \operatorname{Im}\left[\frac{1}{\varepsilon(k,\omega)}\right] \tag{2.16}$$

Here $\varepsilon(k,\omega)$ is the electron dielectric response function, also known as the Salpeter electron feature [144] and can be derived through the Vlasov equation [129, 130]

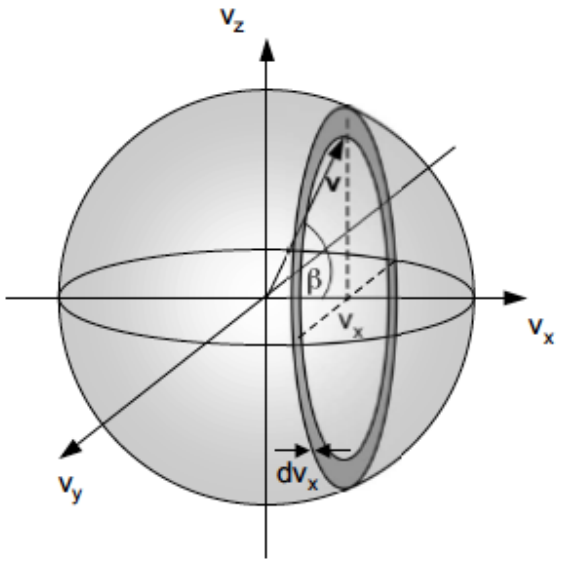

Figure 2.3: Volume element in three-dimensional velocity space (image from Ref. [19]). The number of electrons contribution to the velocity component v_x is given by the velocity distribution $f(v_x)$.

for classical collisionless plasmas or using the random phase approximation (RPA) for the degenerate case under the assumption that the interparticle interactions are weak [145, 146], described in a greater detail in the following section. This is an incredibly important relationship that links the measured scattering spectrum to the thermodynamic properties of the system. The finite temperature RPA provides the following form of the dielectric function [129]:

$$\varepsilon(k,\omega) = 1 - \frac{e^2}{\hbar\varepsilon_0 k^2} \int \frac{f(\mathbf{p}+\hbar\mathbf{k}/2) - f(\mathbf{p}-\hbar\mathbf{k}/2)}{\mathbf{k}.\mathbf{p}/m_e - \omega - i\nu} \frac{2d^3p}{(2\pi\hbar)^3}, \tag{2.17}$$

with $\nu \to 0^+$, where $\mathbf{p}$ is the electron momentum. The electron distribution function is then specified as the Fermi-Dirac distribution for degenerate electrons

$$f(\mathbf{p}) = \frac{1}{\exp\left(\frac{p^2/2m_e - \mu}{k_B T_e}\right) + 1}, \tag{2.18}$$

with μ being the chemical potential [130]. In the limit of $T \to \infty$, equation 2.18 reduces to the Maxwell-Boltzmann form correct for classical plasmas. Thus, for scattering from uncorrelated electrons, the form of the dynamic structure factor is given by the electron velocity distribution function, which in turn depends on the thermodynamic quantities of the medium [147, 19]. Due to the relationship between the electron-electron structure factor and the dielectric function, the shape of the free

electron Compton feature in the scattered probe radiation carries information of the electron density and temperature.

For collisionless plasma with weak ion-ion coupling a simple form for the electron static structure factor can be derived using the Debye-Hückel theory [148, 126]. Following from the relationship between the DSF $S^0_{ee}(k,\omega)$ and dielectric function $\varepsilon(k,\omega)$ derived from the fluctuation-dissipation theorem, equation 2.16, we substitute the Maxwell-Boltzmann distribution in the form for $\varepsilon(k,\omega)$ derived by Landau [129, 130], equation 2.17, and obtain the following expression for the static structure factor:

$$S_{ee}(k) \equiv S_{DH}(k) = \int d\omega S_{ee}(k,\omega) = \frac{k^2}{k^2 + k^2_{De}}, \tag{2.19}$$

where $k_{De} = 1/\lambda_{De}$ is the inverse of the electron Debye length, defined in equation 1.1. The pair correlation function can be then obtained from the inverse Fourier transform of equation 2.19, and corrected by the exponential form of the Debye shielding model giving the correct form: $g(r) = \exp(-\frac{k^2_{De}}{4\pi n_e r} e^{-r k_{De}})$. Although, this form was derived for weak coupling, the validity of the Debye-Hückel expressions can be applied to weakly collisional systems such as the free electrons in degenerate plasma.

States where electron-electron coupling becomes important $\Gamma_{ee} > 1$ are accessed in some experiments described in this work. In those cases the dynamic response of the system can no longer be described in terms of the pure RPA or Debye-Hückel theory. Coupling can however be introduced in terms of an additional parameter into the existing formulae: the *local field correction* $G(k,\omega)$, which is a measure of the effects of strong coupling due to higher order interaction terms and incorporates the short-range correlations, both neglected by the RPA or Debye-Hückel descriptions [26, 130, 139]. In the limit of small ω one can obtain the static local field correction $G(k)$. In the long-wavelength limit this is given by the compressibility rule and in the short-wavelength limit is calculated using a parametrized relation, which will be discussed in detail in Chapter 6 [26, 139, 149, 150]. The static electron structure factor is then given by:

$$S_{ee}(k) = \frac{k^2}{k^2 + k^2_{De}[1 - G(k)]}. \tag{2.20}$$

In the classical limit with low coupling, $G(k) = 0$ and the expressions for $\varepsilon(k,\omega)$ derived by the RPA or Debye-Hückel theories are recovered.

Bound-free transitions

The third term of the total dynamic structure factor shown in equation 2.13 expresses the bound-free transitions of the electrons. Calculation of this term requires a rather complicated atomic model due to the many corrections to the atomic structure imposed by the surrounding atoms and by the probe x-rays. The electronic states in a neutral atom are determined by the potential of the nucleus as well as other electrons in the vicinity of the atom. In plasmas one should expect that the atomic environment will change resulting in modifications to the electronic structure of the atoms.

In dense strongly coupled plasmas the ions are packed closer together, where the atomic potentials start affecting the electrons of the neighbouring ions, reducing the binding energy of the nuclei. This effect is also addressed as the *continuum lowering*. The magnitude of this effect depends on the total number of ions participating in the modification of the potential of a test ion, which is a function of the screening length of the Coulomb forces [19]. This effect has also been observed experimentally [151, 152].

The finite-temperature Thomas-Fermi model can be used to calculate the the lowering of the ionization potential in terms of an effective screening length as derived by Stewart and Pyatt [153]. However, an alternative approach employing a perturbative treatment of many-particle effects such as dynamic screening, Pauli blocking and statistical correlations applied to the bound states of the electrons has revealed that the binding energy stays almost constant while the continuum is lowered [154]. Subsequently the ionization energies are lowered with increasing density and untimately leads to pressure ionization of the outer electrons (Mott effect) when the higher bound states merge into the continuum [155]. Literature offers a broad range of models used to calculate the Compton interactions for the bound-free scattering and worth mentioning is the well-known *impulse approximation*, which assumes the potential between the charges does not change during their interaction so the final energy exchange is given by the initial and final states [156].

The bound-free term is small compared to the free electron-electron dynamic structure factor S_{ee} and the Raman band-width is comparable to the Compton feature [19, 157], thus this contribution generally yields only a weak background. In the case of hydrogen isotopes in the WDM regime, such a term can be completely neglected as the probability of occupancy of the core states and such transitions is very small. The bound-free contribution is therefore neglected in this work.

2.2.3 Random phase approximation (RPA)

The random phase approximation (RPA) is a widely used theory in condensed matter physics, nuclear physics as well as in dense plasmas. First derived by Bohm and Pines [145]. RPA accounts for the weak screened Coulomb interaction and is commonly used to describe the dynamic linear electronic response of free electron systems. The main assumption of the RPA states that in the high density limit the Coulomb interaction between the electrons may be treated as a perturbation [158]. The electrons then respond to an external perturbing potential, which is a sum of an external (Coulomb) potential and screening potential, oscillating at a single frequency ω [159] and is used within a self-consistent field approach to compute the dielectric function $\varepsilon_{RPA}(k,\omega)$, also called the *Lindhard dielectric function* [160, 161]. Going beyond basic perturbation theory, RPA sums over a infinite number of diverging higher order interaction terms which eventually average out providing a finite and sensible answer. Lindhard's approach is strictly valid only for $r_s \ll 1$, i.e. low coupling regime where electrons are effectively free such as highly degenerate or free electron gases.

The generally accepted way to derive the RPA is through a summation of leading-order chain Feynman diagrams in a dense electron gas [162]. This approach is illustrated in figure 2.4. The lowest order polarization interaction is represented by the "bubble", which is a function of the four-momentum $k = (\mathbf{k}, k_0)$, and involves excitation (left loop) and subsequent de-excitation (right loop) of an electron-hole pair as a response to disturbance of wavevector k and frequency k_0. The four-momentum entering each vertex is equal to that leaving, summing over the internal variable q. These electron propagators G_0 with four-momentum k and $k+q$ correspond to interactions through bare Coulomb potential $V(\mathbf{k}) = 4\pi e^2/|\mathbf{k}|^2$, marked as thin "wiggly" lines in figure 2.4. The dielectric function may then be connected to a response of the electron gas to an external probe or defined as a screened interaction of the electrons themselves. The screened response, in figure 2.4 denoted by thick "wiggly" line in the lower part of the diagram, may be obtained by summing over an infinite order of topologically distinct diagrams [158, 146].

The screened or effective interaction V_{eff} is the sum of of all orders of interaction terms of the bare Coulomb potentials:

$$V_{eff}(k) = V + V\Pi^0 V + V\Pi^0 V\Pi^0 V + ... \tag{2.21}$$

$$= \frac{V}{1 - \Pi^0 V} = \frac{V}{\varepsilon(k)} \tag{2.22}$$

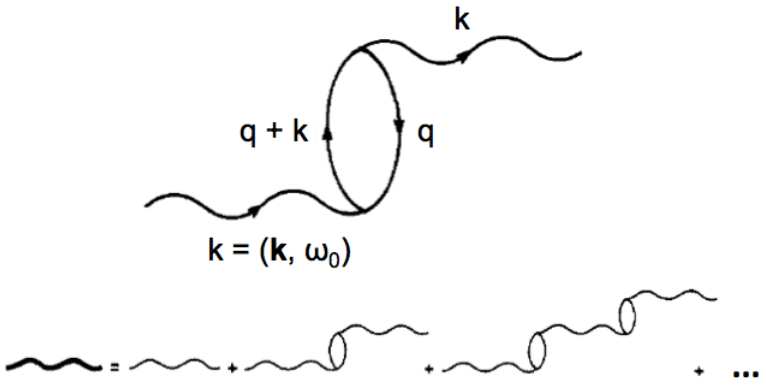

Figure 2.4: The "bubble" and the summation of polarization Feynman diagrams in the RPA, after Ref. [158].

The dielectric function has been introduced in term of the polarization Π, where Π^0 symbolizes the polarization 'bubble':

$$\varepsilon(k) = 1 - \Pi^0(k)V \tag{2.23}$$

The polarization function $\Pi^0(k)$ can then be computed from Feynman's rules:

$$\begin{aligned}
\Pi^0(k) &= -i\sum_{q\sigma}\int \frac{dq_0}{2\pi} G_0(q)G_0(q+k) \\
&= -i\sum_{q\sigma}\int \frac{dq_0}{2\pi}\left\{\frac{1-n_{\mathbf{q}}}{q_0-\epsilon_{\mathbf{q}}+i\eta}+\frac{n_{\mathbf{q}}}{q_0-\epsilon_{\mathbf{q}}-i\eta}\right\} \\
&\quad\times\left\{\frac{1-n_{\mathbf{q+k}}}{q_0+k_0-\epsilon_{\mathbf{q+k}}+i\eta}+\frac{n_{\mathbf{q+k}}}{q_0+k_0-\epsilon_{\mathbf{q+k}}-i\eta}\right\},
\end{aligned} \tag{2.24}$$

where $n_{\mathbf{q}}$ denotes occupation factors for non-interacting Fermi gas with electron energies $\epsilon(k) = \hbar^2k^2/2m_e$ and for Fermi-Dirac distribution at zero temperature is defined as:

$$n_{\mathbf{q}} = \begin{cases} 1 \text{ for } |\mathbf{q}| < k_F \\ 0 \text{ for } |\mathbf{q}| > k_F \end{cases}$$

with Fermi wavevector $k_F = (3\pi^2 n_e)^{1/3}$. The electron propagators contain the positive infinitesimal quantity η and the spin index σ simply multiplies the expression by 2 [158, 146]. The above equations have an analytic solution [163]. The explicit expression for $\varepsilon_{RPA}(k,\omega)$ can be found in Appendix B. RPA correctly predicts a number of properties of an interacting electron gas such as the plasmon oscillations, compressibility, specific heat, phonon dispersion, metal-insulator transitions, etc. [158].

2.2.4 Thomas-Fermi model

The Thomas-Fermi theory was developed as a semi-classical statistical model to approximate the distribution of electrons in an atom by replacing charge distribution in the plasma by a single average atom, which carries the average charge and population distribution. It is an average atom model, where a nucleus of charge Ze is placed in a centre of a sphere whose total charge is zero [148]. The spherically-symmetric potential $\phi(r)$ of the atom is assumed to slowly vary is space and falls to zero at the boundaries of the sphere. Thus, all bound and free electrons are considered degenerate and confined within the electrostatic field of the central atom and distributed statistically according to the Fermi-Dirac distribution [164]. Starting from Poisson equation:

$$\nabla^2 V(r) = 4\pi e[\rho_i(r) + \rho_s(r)], \tag{2.25}$$

where $\rho_i(r) = -en_e(r)$ is the impurity charge distribution and the screening charge $\rho_s(r) = -e[n_e(r) - n_0]$. The electron density is expressed in terms of Fermi wavevector $n_e(r) = k_F^3(r)/3\pi^2$ and n_0 is the equilibrium charge density [159]. The electron density is then calculated from the Fermi-Dirac distribution, equation 2.18. Following similar derivation as the for the Debye length [22], the Thomas-Fermi screening wavevector is obtained:

$$k_{TF}^2 = \frac{6\pi e^2 n_e}{\varepsilon_0 E_F}, \tag{2.26}$$

which reduces to the Thomas-Fermi screening length for a degenerate electron system introduced in the introduction section, equation 1.8. For a point charge impurity $\rho_1(k) = Q_i$ a screened interaction of the form of a Yukawa potential is reproduced $V(r) = -\frac{eQ_i}{r}\exp(-k_{TF}r)$. The Thomas-Fermi model only provides the static form of the dielectric function $\varepsilon_{TF} = 1 + k_{TF}^2/k^2$ and is not generally used to describe the dynamic response [159].

Although many models provide more accurate description of the local phenomena, the average atom model due to its simplicity is an ideal tool to link the electronic distributions to thermodynamic quantities such as pressure or density. The theory also provides a functional form for the kinetic energy of a non-interacting electron gas within a known potential as a function of the density of the system. Thomas-Fermi model is readily used in hydrodynamic codes for calculations of the ionization state in simulations of plasmas in inertial confinement fusion and astrophysics [164].

2.2.5 Frequency sum rules

The thermodynamic quantities such as the electron density and temperature can also be related to the electron-electron structure factor in terms its frequency sum rules. The main advantage of this approach is that these expression can be easily obtained giving exact expressions. Since $S_{ee}(k,\omega)$ is an even function, the odd frequency moments are by definition zero. The even moments can then be defined as

$$\Omega_{2n} = \int \omega^{2n} S_{ee}(k,\omega) d\omega. \tag{2.27}$$

The first three moments are then derived giving equations 2.28, 2.29 and 2.30 [165, 166].

$$\Omega_0 = S^0_{ee}(k) \tag{2.28}$$

$$\Omega_2 = (kv_t)^2 \tag{2.29}$$

$$\Omega_4 = 3(kv_t)^4 + \left(\frac{\hbar k^2}{2m_e}\right)^2 (kv_t)^2 + \omega_p^2 (kv_t)^2 [1 - I(k)] \tag{2.30}$$

Here $v_t = (k_B T_e/m_e)^{1/2}$ is the thermal velocity of electrons. The term $I(k)$ incorporates the effects of strong coupling. In the studied systems the value of $r_s = 2-6$ is small and the electron system is degenerate and weakly coupled. Thus in this semi-classical case the $I(k)$ term can be ignored.

The zeroth moment Ω_0 (equation 2.28) gives the total power in the fluctuation at a given scattering angle, i.e. the static structure factor. As previously shown, $S^0_{ee}(k)$ can be derived using the Debye-Hückel theory valid for weakly coupled electrons, this is a reasonable assumption for partially or fully degenerate electron system [167, 168]. In order to account for various degrees of degeneracy in the electron gas, an approach suggested by Gericke *et al.* [29], is chosen giving an expression for the static structure factor in terms of density and the effective temperature (equation 1.11) [169]:

$$S^0_{ee}(k) = \frac{k^2}{k^2 + \kappa_e^2}. \tag{2.31}$$

The second moment or *f-sum rule*, equation 2.29, is derived from conservation of particles in the system. This expression is exact and is valid for all degrees of degeneracy or coupling. Finally, the fourth moment, equation 2.30 includes the effects of pair correlations [165]. The second term in the expression for Ω_4 is very small compared to the rest and can in practice be ignored.

2.3 X-ray Thomson scattering from WDM

Diagnosing WDM is challenging since the temperature ($\sim$10 eV) is too low for x-ray emission from the plasma, yet the density is high above the critical density $n_c = \varepsilon_0 m_e \omega^2 / e^2$ for any optical laser to be used as a probe. Therefore x-ray Thomson scattering offers itself as an elegant solution to the problem. Typically the monochromatic x-rays are created from laser plasmas in the form of Ly-α ($n = 2$ to $n = 1$ transition in a hydrogen-like atom) or He-α ($1s^2 - 1s2p$ transition) using nanosecond lasers with intensities ranging between $10^{14} - 10^{15}$ Wcm^{-2} or as K-α inner shell emission (emission of a higher energy electron falling into the K-shell after the K-shell electron was knocked out of its position by a collision with another energetic particle) from ultra-short fs laser pulses creating x-rays in the range of $2-9$ keV [19]. Scattered radiation can be related to the dynamic response of the medium through it dynamic structure factor providing a direct measurement of its microscopic structure [133]. By careful analysis of the elastic and inelastic features of the x-ray scattering spectra a full range of the thermodynamic properties of WDM can be obtained from a single measurement [105, 83].

The primary investigative technique used in the experiments related to this work was x-ray Thomson scattering. Thermodynamic properties, namely density, temperature and ionization state can be accurately determined from the spectral features in the scattered signal. Thanks to the relation of the dynamic structure factor $S(k, \omega)$ and the scattering spectrum to the dielectric response function $\varepsilon(k, \omega)$ of the material (equation 2.16), which in return depends on the thermodynamic conditions of the system, all these quantities can be obtained simultaneously from a single spectrum. The scattering cross section can be expressed in terms of the dynamic structure factor $S(k, \omega)$, which is the Fourier transform of the total electron density distribution function:

$$\frac{d^2\sigma}{d\Omega d\omega} = \sigma_T \frac{k_1}{k_0} S_{ee}^{tot}(k, \omega), \tag{2.32}$$

where $\sigma_T = \frac{8\pi}{3} r_0^2 = 6.65 \times 10^{-25}$ cm^2 is the Thomson cross section with the classical electron radius $r_0 = e^2/(4\pi\varepsilon_0 m_e c^2) = 2.82 \times 10^{-15}$ m. The measured scattered power therefore is directly proportional to $S(k, \omega)$ and the scattering spectrum therefore contains information about the microscopic structure of the studied material [26, 130]. As the probe x-rays interact with the electrons in the sample, the oscillating electric field accelerates the charged particles in the plasma which reradiate. The scattering

wavevector k is defined (in the non-relativistic limit) as the difference between the wavevectors of the incident and scattered EM waves (see figure 2.5):

$$k = |\mathbf{k}| = |\mathbf{k}_0 - \mathbf{k}_1| = \frac{4\pi}{\lambda_0}\sin(\theta/2)\sqrt{1 - \frac{\omega_p^2}{\omega^2}} \tag{2.33}$$

where θ is the scattering angle, λ_0 and ω are the wavelength and frequency of the incident x-rays. The expression is multiplied by a factor to account for the final change in refractive index between the plasma and the vacuum, which can be neglected in the experiments described in this work. The scattering power P_S from N electrons with incident power P_0 into a frequency interval $d\omega$ and solid angle $d\Omega$ [133], i.e. the scattering spectrum is determined by:

$$P_S(\mathbf{R},\omega)d\Omega d\omega = \frac{P_0 r_0^2 d\Omega}{2\pi A} NS(\mathbf{k},\omega)d\omega \times \left|\hat{\mathbf{k}}_1 \times (\hat{\mathbf{k}}_1 \times \hat{\mathbf{E}}_0)\right|^2. \tag{2.34}$$

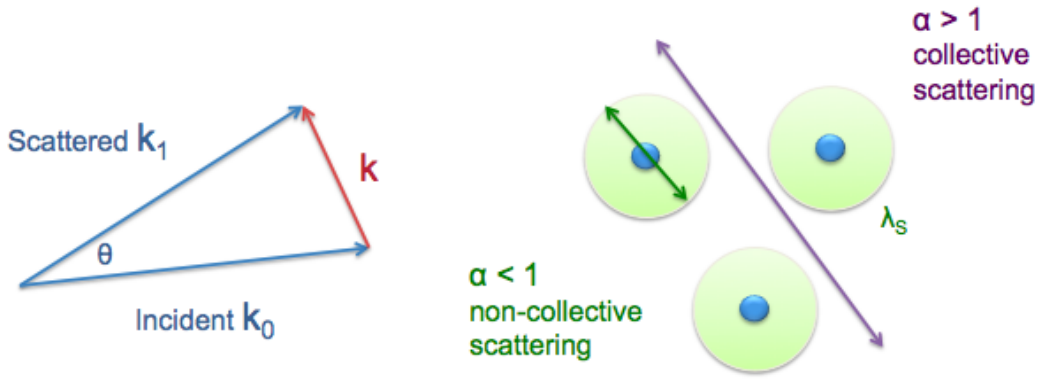

Figure 2.5: Schematic diagram of the Thomson scattering geometry.

The last term in equation 2.34 reflects the dependance of the scattered power on the polarisation of the probe radiation. For unpolarized x-rays from laser-plasma source the polarization term is $\left|\hat{\mathbf{k}}_1 \times (\hat{\mathbf{k}}_1 \times \hat{\mathbf{E}}_0)\right|^2 = (1 - \frac{1}{2}\sin^2\theta) = \frac{1}{2}(1 + \cos^2\theta)$. It is clear from the above expression that the geometry of the scattering experiments is very important. Depending on the energy of the probe, plasma conditions and the scattering angle the scattered x-rays carry information on the individual or collective behaviour of the electrons in the plasma. A classical scattering parameter α is defined to establish the limit between the collective and non-collective modes of scattering [144]:

$$\alpha = \frac{1}{k\lambda_s}. \tag{2.35}$$

For $\alpha < 1$ (figure 2.5) the scattering scale length $\lambda = \lambda_0/2\sin(\theta/2)$ is smaller than the plasma screening length λ_s and the x-rays scatter of the individual electrons. The measured spectrum resolves the non-collective properties of the material. If $\alpha > 1$ the scattered waves interfere over a larger distance than the screening length and the contributions add to a scattering signal from the collective motions of the electrons in the plasma. The screening length is the electron Debye length λ_{De} (equation 1.1) for classical plasmas and the Thomas-Fermi length λ_{TF} (equation 1.8) in the degenerate case. The screening length can also be calculated from the effective temperature [130], equations 1.11 and 1.12. This approach has been shown to reproduce the finite-temperature static response of an electron fluid correctly at various degrees of degeneracy.

The scattering parameter α also determines the total intensity of the scattered signal. Using the expression for the DSF derived from the Debye-Hückel theory, equation 2.19, the differential cross section from equation 2.32 can be rewritten in terms of α:

$$\frac{d^2\sigma}{d\Omega d\omega} \propto \frac{1}{1+\alpha^2}. \tag{2.36}$$

Thus, the strongest scattering signal should be expected for the non-collective regime. In order to obtain a reasonable collective scattering spectrum $\alpha > 2-3$ is required which reduces the total scattering amplitude by at least factor of 10. The total scattering spectrum is made up of independent contributions from bound and free electrons as described in a chemical model by Chihara [131, 132]. In the case of WDM hydrogen/deuterium the bound-free transitions in equation 2.13 can be neglected giving the form of the dynamic structure factor:

$$S(k,\omega) = |f_I(k) + q(k)|^2 S_{ii}(k) + Z_f S^0_{ee}(k,\omega). \tag{2.37}$$

The first term in equation 2.37 gives rise to the elastic Rayleigh scattering as the x-rays scatter off the combined mass of electrons and ions. At sufficiently high energies of the probe the incident photons can lose part of their energy during a momentum transfer upon an interaction with the free electrons due to the Compton effect [19]. The second term in equation 2.37 therefore reproduces the inelastic scattering contribution from the free electrons with a well defined energy downshift. The

thermodynamic conditions of the plasma will then determine the relative strength of the individual contributions to the total scattering spectrum.

2.3.1 Spectral features

The x-ray probe used in the laser-ablation experiments performed at the Omega laser facility at the University of Rochester was Cl Ly-$\alpha \sim 2960$ eV, which provides sufficient energy to observe inelastic scattering from WDM deuterium, with Compton recoil of $E_C = \hbar^2 k^2 / 2m_e \sim 17$ eV. Figure 2.6 shows analytically calculated scattering spectra for various plasma conditions in the collective and non-collective regimes. Significant differences resulting from both different geometrical arrangement as well as the thermodynamic conditions can be expected.

For $\alpha < 1$ (figure 2.5) the measured spectrum reflects the non-collective properties of the material. The frequency shift of a scattered photon by a free electron results from a combined effect of the Compton and Doppler effects [133]:

$$\Delta\omega = -\frac{\hbar^2 k^2}{2m_e} \pm \mathbf{k}.\mathbf{v}. \tag{2.38}$$

Therefore, the position and shape of the red-shifted Compton peak, see figure 2.6 (a), is given by the recoil of the free electrons undergoing thermal motion and therefore gives the free electron velocity distribution, i.e. the DSF is connected to the velocity distribution relation through the dielectric function (equations $2.16 - 2.18$). In the non-degenerate case $T_e > T_F$ the electrons follow the Maxwell-Boltzman velocity distribution and the electron temperature T_e can be obtained from the Doppler broadening of the inelastic peak, which has been demonstrated experimentaly [81]. When $T_e < T_F$ the degenerate system is defined by the parabolic Fermi-Dirac distribution reducing the sensitivity of the spectrum to T_e, the spectrum however becomes sensitive to the electron density $T_F \propto n_e^{2/3}$ [19]. X-ray scattering in the non-collective regime can be used to simultaneously measure the electron density and temperature, however the structure factors must be precisely calculated in order to retrieve the information from the spectral shapes in the experimental spectrum or the experiment has to be carried under specific conditions that constrain some of the measurable quantities, or with the help of independent EOS measurement (e.g. VISAR or SOP) [100, 104].

The collective motion of charges in the plasma are accessed by scattering when $\alpha > 1$ (figure 2.5). Following the Bohm-Gross dispersion relation for plasma (equation 1.2), where the first term shows that upon the interaction with the incident radiation

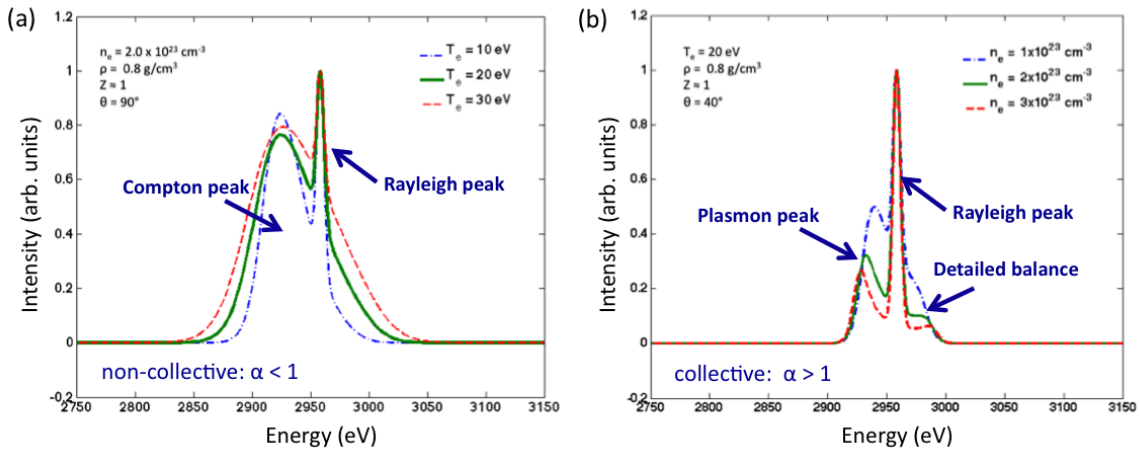

Figure 2.6: Simulated scattering spectra of shocked cryogenic deuterium probed with Cl Ly-α radiation at 2.96 keV during the Omega experiment, see Chapter 5 for further details on this experiment. The graphs show calculated x-ray Thomson scattering profiles for the (a) non-collective ($\theta = 90°$), (b) collective ($\theta = 40°$) regimes using varied temperature and density conditions.

the material undergoes oscillations (plasmon) at plasma frequency ω_p (equation 1.3), which depends on electron density n_e. This results in a pair of down and up-shifted peaks centered at the probe frequency, see figure 2.6 (b). Thus, the position of the plasmon peak depends on the n_e and therefore provides a very accurate measurement of the electron density [19]. The additional terms in equation 1.2 introduce additional shifts due to the thermal motion of the electron and Compton recoil. The thermal correction is however very small and the quantum shift is easily determined from the geometric configuration [58]. Reliable measurements of the electron density from the position of the plasmon peak in scattering spectra have been demonstrated [102, 83]. The imaginary part of the dielectric function determines the Landau damping of the Langmuir (plasmon) waves resulting in a finite width of the plasmon resonance, proportional to T_e, which can be therefore retrieved from the collective spectrum [129, 19].

An alternative temperature measurement is possible in the collective regime [19, 102]. Under the assumption that the plasma is in thermal equilibrium the principle of detailed balance can be exploited through the well-known relationship [128]:

$$\frac{S(\mathbf{k},\omega)}{S(-\mathbf{k},-\omega)} = e^{-\frac{\hbar\omega}{k_B T_e}}. \tag{2.39}$$

Here, the energy loss is given by $\omega = \omega_0 - \omega_f$. The intensity of the blue side

plasmon is reduced by the Boltzmann factor $\beta = -1/k_B T$ since the cross-sections of the scattering processes for the plasmon are equal to the statistical weights of the states accessed, i.e. the probability of the conduction band being occupied by an electron gaining an energy of $\hbar\omega$ is $p(v) = \exp(\beta\hbar\omega)/Z$, where Z is the partition function, whereas the probability of an electron falling into a state in the valence band by loosing energy $\hbar\omega$ is $p(c) = 1/Z$. Hence, the ratio of the Stokes and anti-Stokes components (positive and negative energies in the scattering spectrum) is $p(v)/p(c) = \exp(\beta\hbar\omega)$ [128].

The electrons that remain strongly bound to their nuclei are not excited by the scattering process as their ionization potential is higher than the Compton energy and therefore the x-ray photons scatter of them elastically producing the Rayleigh peak centered at the energy of the incident x-rays in the scattering spectrum. The amplitude of the elastic peak is sensitive to the number of strongly bound electrons and the microscopic properties that depend on S_{ii}. Hence, the average ionization state Z can be obtained from looking at the ratio of the amplitudes of the elastic and inelastic features. Since the ion-ion structure factor is sensitive to the ion temperature T_i, this quantity also has an impact on the shape of the scattering spectrum [19, 105].

The elastic Rayleigh peak is composed of the acoustic modes of the ionic plasma frequency, which are separated by less than eV of energy, [166, 170]. With current x-ray sources, such as those used in this work (Cl Ly-α $\sim$ 2960 eV: $\Delta E/E \sim 2 \times 10^{-3} \sim 6 - 10$ eV [103]), these features cannot be resolved and the ion-ion correlation function is approximated by its static value $S_{ii}(k, \omega) = S_{ii}(k)\delta(w)$ for purposes of these experiments [130].

The scattering parameter α can be easily manipulated by changing the energy of the probe or scattering geometry. The non-collective scattering in the backscatter geometry is an accurate measure of the electron temperature, where the collective scattering gives the rise to the plasmon peak that depends only on n_e. Thus, using collective scattering in conjunction with non-collective scattering provides complimentary measurements of all thermodynamic quantities simultaneously and can therefore be directly compared with various EOS models. The evolution of the plasma condition during a laser drive can then be probed by changing the relative temporal delay between the laser drive and the backlighter.

2.4 Equation of state

Crucial to understanding the properties of warm dense matter is the equation of state that links the internal energy of the system to the state variables (pressure, density, temperature, etc.). Classical plasmas can be described in terms of the ideal gas theory $E_{int}^{ideal} = 3Nk_BT/2$, however if strong coupling is present the Coulomb interactions have to also be included. Following the OCP model the Hamiltonian of the strongly coupled system can be computed giving:

$$\frac{E_{int}}{N} = \frac{3}{2}k_BT + \frac{1}{2V}\sum_{\mathbf{k}\neq 0} V_k[S(\mathbf{k}) - 1]. \tag{2.40}$$

The second term includes in equation 2.40 the Coulomb interaction through the Frourier transform of the Coulomb potential V_k, [126]. This expression shows that there is a connection between the structure factor and the internal energy of the system. If $S(\mathbf{k})$ is known, e.g. from scattering signal or theoretical calculation/simulation, the equation of state can be derived (the *virial* theorem):

$$\frac{P}{P^{ideal}} = 1 + \frac{1}{3}\frac{E_{int} - E_{int}^{ideal}}{Nk_BT}, \tag{2.41}$$

where $P^{ideal} = Nk_BT$ is the ideal gas pressure. This equation is valid if the pressure due to the ions is considered only. In real plasmas electron contribution also must be accounted for. An analogous derivation is possible for the electrons, however the electronic terms become more complicated as degeneracy and quantum mechanical corrections must be explicitly included [126]. The theoretical description of the EOS of WDM is extremely challenging as these models must correctly incorporate numerous phase transitions, quantum and coupling effects and structural changes. These require many theoretical approximations and immense computational power. All these complications result in disagreements between various approaches. Experimental validation of predictions made by theory is therefore essential.

The analysis of the EOS data in this work was based on three different theoretical EOS models: the SESAME EOS table [17], widely used for ICF applications; the model by Saumon and Chabrier (S&C) [122, 123] that spans over a wide range of conditions and is often used for astrophysical purposes; and density-functional molecular dynamics (DFT-MD) simulations of fluid hydrogen by our collaborators from the University of Warwick [37, 38, 171]. The S&C and DFT-MD tables apply to hydrogen and were adjusted to deuterium by accounting for the mass difference between the isotopes.

2.4.1 Chemical models

The *chemical picture* assumes the existence of independent bound configurations such as H atoms and H_2 molecules interacting via pair potentials. Electrons are treated as an uniform neutralizing background and are not individually included in the calculation of the EOS. These are purely classical and do not include any quantum corrections, which means such models break down at high densities where degeneracy effects in the electron species become important and material properties such as pressure ionization fail to be adequately described. Such models tend to do well for individual phases of molecular or atomic fluids, but at phase transitions mixing models must be implemented.

The SESAME table for deuterium is based on the *chemical model* by Kerley [17, 18] and includes many adjustments based on a variety of experiments. This multicomponent EOS considers three ideal phases of D (fluid, molecular solid and metallic solid) and includes dissociation, ionization, and linear (first-order) mixing of the combined molecular and atomic fluid phases. It was shown that SESAME underestimates the effects of strong coupling and many-body degeneracy in the nonideal plasma [9]. The SESAME tables used in this work were no. 5263 and 5265. Table 5263 is the original theoretically calculated EOS for deuterium based on the *chemical model* assumptions. This model is generally considered to give a "stiff" Hugoniot with lower compressibility of deuterium.

Table 5265 is no longer a pure theoretical model, but a modification of the older table 5263 to satisfy new experimental measurements [172]. The deuterium Hugoniot was significantly softened and there were many changes to the phase transitions in molecular deuterium. The table was adjusted to agree with new low temperature diamond anvil data of Loubeyre *et al.* [119, 120] making changes to the cold curve that softened it and moved the molecular-atomic transition to higher pressures. A new molecular-molecular phase transition was included. Remnants of the molecular-atomic transition persisting to finite temperatures also had to be removed. The finite temperature EOS was then brought into agreement with the Hugoniot data of Knudson *et al.* [44, 173, 109], and the data of Belov *et al.* [111] and Bonshov *et al.* [174]. The theoretical work of Lenosky *et al.* [175, 176] was used as a guide for changes to 5263 in bringing 5265 into agreement with the shock data. The thermodynamic consistency was maintained by integrating from the pressures to obtain the energies. It should be pointed out that the new impedance matching results by Knudson [112], which push the Hugoniot data back towards a "stiffer" curve, were not included.

The Saumon and Chabrier EOS (S&C) for hydrogen is entirely founded on theoretical results in the *chemical picture* [122, 123]. A free energy minimization method is used to determine the concentrations of atoms, molecules, protons, and electrons. The interactions between the independent H atoms and H_2 molecules are modeled through realistic pair potentials. For high densities a two-fluid model is used. The EOS consists of neutral species in the low-density low-temperature limit, in which the H^- and H_2^+ species are ignored, and fully ionized plasma in the high-density high pressure region, where the electron-ion interactions are weak and the plasma is described as linearly screened ionic fluid and partially degenerate electron gas. Partial ionization and molecular dissociation are handled through interpolation between these two limits. This model experiences difficulties at high densities where the pair potential principle fails and the system needs to be expressed in terms of the physical picture of quantum-statistical theory for interaction between electrons and nuclei. Pressure ionization therefore remains problematic in this model.

2.4.2 Physical models

With increasing computer power more sophisticated computational models became available to the scientists. In recent years, *ab initio* (first principles) simulations in the *physical picture* were developed treating both electrons and ions as elementary particle interacting through Coulomb potentials and included quantum effects into the calculation of EOS of H_2/D_2 and other materials [13]. Among the most widely used appeared the density-functional theory (DFT), which is well-established and very widespread quantum mechanical technique used in physics and chemistry to investigate the electronic structure (principally the ground state) of many-body systems, in particular atoms, molecules, and condensed phases of matter (e.g. WDM, crystalline solids and metals).

DFT provides insight into the exchange and correlation effects between interacting electrons in matter providing a very realistic picture of material properties. DFT has a broad range of applications, from calculation of magnetic moments and phonon dispersion curves of metals to phase transition parameters and binding energy curves (bond lengths, vibrational frequencies, chemical reaction energies, etc.) [126]. The main advantage of DFT is that it can be coupled with MD techniques for *ab initio* simulations of atomic and molecular processes on pico-second time scales (e.g. diffusion, chemical reactions, biological processes at an atomic level), which makes it an ideal technique to produce an EOS table applicable to the conditions relevant to

the giant gas planets as the electrons in these systems are either chemically bound or highly degenerate ($T \ll T_F$) [12].

The deuterium EOS was computed using first-principle DFT-MD simulations within the *physical picture* with electrons and ions handled as elementary particles [37, 38]. In this approach, the nuclei are treated by classical molecular dynamics simulations. Properties of the electrons are calculated via density functional theory using a Mermin functional that accounts for temperature effects within the electron subsystem in a statistical sense. The dynamics of ions and electrons is effectively decoupled with the Born-Oppenheimer approximation. This description of hydrogen avoids most approximations concerning the composition and mixing necessary in *chemical models* [37]. The Vienna Ab-initio Simulation Package (VASP) package [177] was employed for the DFT-MD simulations used to calculate the deuterium EOS for this work (simulation parameters are similar to Ref. [37]). VASP also allows for the application of the projector augmented wave (PAW) potential [178].

2.5 Hydrodynamic simulations

Hydrodynamic simulations were used to model the plasma evolution within the deuterium targets during the laser drive in application for the Omega experiments. Various simulations were used in the process of planning of the experiments as well as for the data analysis as comparison with the VISAR, SOP and x-ray scattering measurements. The three main codes used to support this project were 1-D hydro codes *LILAC* [79, 80], *HELIOS* [179] and 2-D *DRACO* code [180, 181]. The results of these simulations are discussed in Chapters 4 and 5.

LILAC is a 1-D hydrodynamics code predominantly used for modeling of the plasma conditions and warm dense matter in experiments carried out at the LLE, University of Rochester [79, 80]. The absorption of the laser drive is calculated through the ray-trace algorithm which models the inverse bremsstrahlung mechanism. Transport of radiation within the plasma is simulated through multi-group diffusion using the Los Alamos Astrophysical tables [182] or an average ion model which provides the opacity of the system [104]. The SESAME tables were used to input the deuterium EOS into the simulation [17, 18]. The electron transport in the *LILAC* simulations is modeled by the flux-limited Spitzer-Härm electron thermal-conduction model [183, 184]. More detailed description of the *LILAC* code can be found in Refs. [79, 80]. These simulations were run by Dr. Radha Bahukutumbi from

LLE and were used in the planning stage of the Omega experiments in order to optimize the laser drive and backlighter timing as well as the target design to achieve the desired WDM conditions and favourable timing of the x-ray scattering measurement.

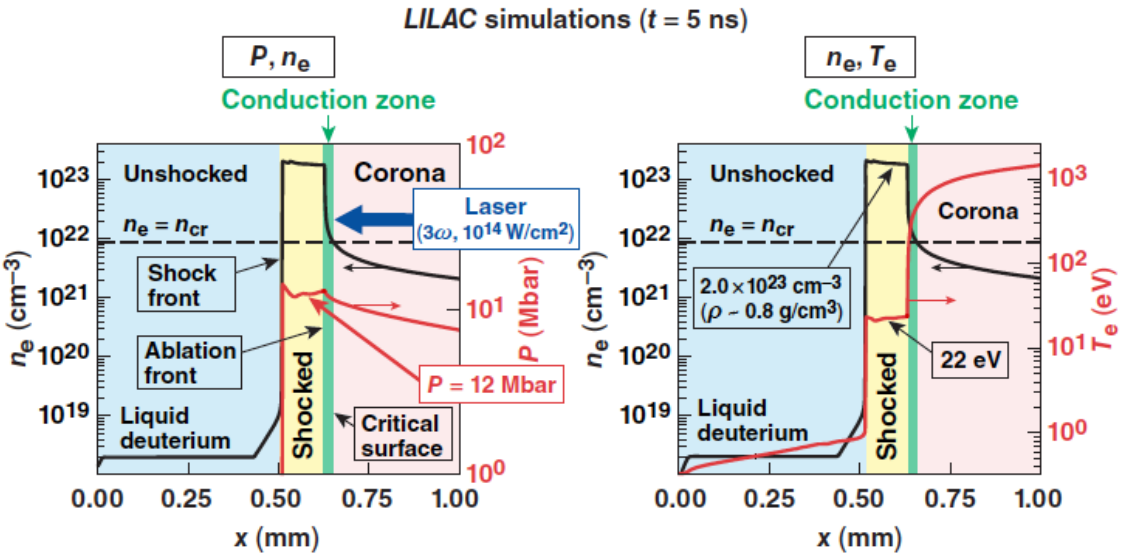

Figure 2.7: Plots of electron density, temperature and pressure generated from *LILAC* simulations for the higher intensity drive (10^{14} W/cm^2) experiments at Omega.

HELIOS 1-D radiation-magnetohydrodynamics code can be used to simulate the dynamic evolution of laser-produced plasmas and z-pinch plasmas [179]. The code supports three different target geometries: planar, cylindrical or spherical. The target is divided into spatial zones with the layer structure, material, density and other starting conditions specified upon the input. *HELIOS* allows an input of a real calorimetric measurements of laser drive intensity extracted from the experiment, otherwise simple "square" laser profile of a specific intensity is used. The code evolves the plasma within the Lagrangian hydrodynamics coordinate system in which the spatial grid moves with the fluid, i.e. cells maintain their mass ratio throughout the simulation.

In *HELIOS*, radiative transport can be calculated using either a multi-frequency flux-limited diffusion model or through a multi-frequency-multi-angle short characteristics model [179]. The diffusion transport model was selected for simulations in this work with 50 frequency groups. Spitzer thermal conductivity model was selected [184]. *HELIOS* supports the PROPACEOS (PRism OPACity and Equation Of State) EOS/multi-group opacity data tables as well as the SESAME EOS. Both equation

of state models are based on *chemical model* assumptions and provide the same result. In the simulations used to support the data analysis of the Omega experiments PROPACEOS was used, further information and results are shown in Chapters 4 and 5.

The 2-D radiation hydrodynamics code *DRACO* was developed at LLE (University of Rochester) for the purpose of both spherical implosion and planar-target simulations [185, 180]. The Lagrangian version of *DRACO* was used in this study. Laser absorption in the plasma corona by inverse bremsstrahlung was modeled by 3-D ray-tracing for Omega's port geometry [186]. The deuterium EOS was determined from the SESAME tables [17, 18]. The radiation transport model used was the multi-group diffusion model with input from the Astrophysics Opacity Table (AOT) 25 [182]. Further details on the multi-dimensional simulations and their applications can be found in Ref. [181]. The 2-D simulations were run by Dr. Suxing Hu, LLE. Their primary purpose was to provide greater accuracy simulations to complement the existing 1-D simulation to better understand the measurements form the Omega experiments.

Chapter 3

Laser experiment set up

3.1 Introduction

In this chapter, the technical details of the experimental set up for the experiments carried out at the Omega laser facility (LLE, University of Rochester) will be described in detail. The laser beam configurations, diagnostics, detectors, x-ray sources and targets will be introduced in the following sections. Representative data from the various target diagnostics will also be presented to complete the picture of the experiment. This is a complicated experiment that developed in many stages. The evolution of the target design, laser drive and x-ray backlighter as well as the diagnostics set up will be carefully explained throughout the chapter. This chapter is thus intended as a form of technical manual to the laser experiments within this work. More detailed analysis from the primary diagnostics and determination of the deuterium EOS will however be described in the following chapters, which will be probing deeper into the underlying physics of this experiment.

The main objective of this experiment is to provide an experimental verification of EOS models for WDM deuterium. This is achieved through an independent measurement of three different primary diagnostics including x-ray Thomson scattering (XRTS) [19], velocity interferometry (VISAR) [70] and streaked optical pyrometry (SOP) [71] which provide independent measurements of shock velocity, density and temperature respectively. The brightness of the x-ray backlighter, target alignment and the laser drive are monitored by a number of secondary diagnostics, also described in this chapter. A narrow-band x-ray source is created by line emission from laser-heated plastic foil doped with chlorine. The WDM conditions are created by 6 ns long high energy laser drive consisting of multiple beams at variable intensity.

3.2 Laser configuration

The 60-beam, 30-kJ Omega laser system was used to create the WDM conditions by launching a single shock inside the planar liquid deuterium target driven by laser ablation of rapidly expanding material from the laser-target interface [187]. Twelve of the Omega laser beams were used as a drive coming from the H14 side of the Omega chamber in the case of XRTS experiments and from the H7 side when VISAR was used, see figure 3.1. The x-ray source was then created by sixteen tightly focused *backlighter* beams incident on a chlorinated plastic foil on the H7 side of the target.

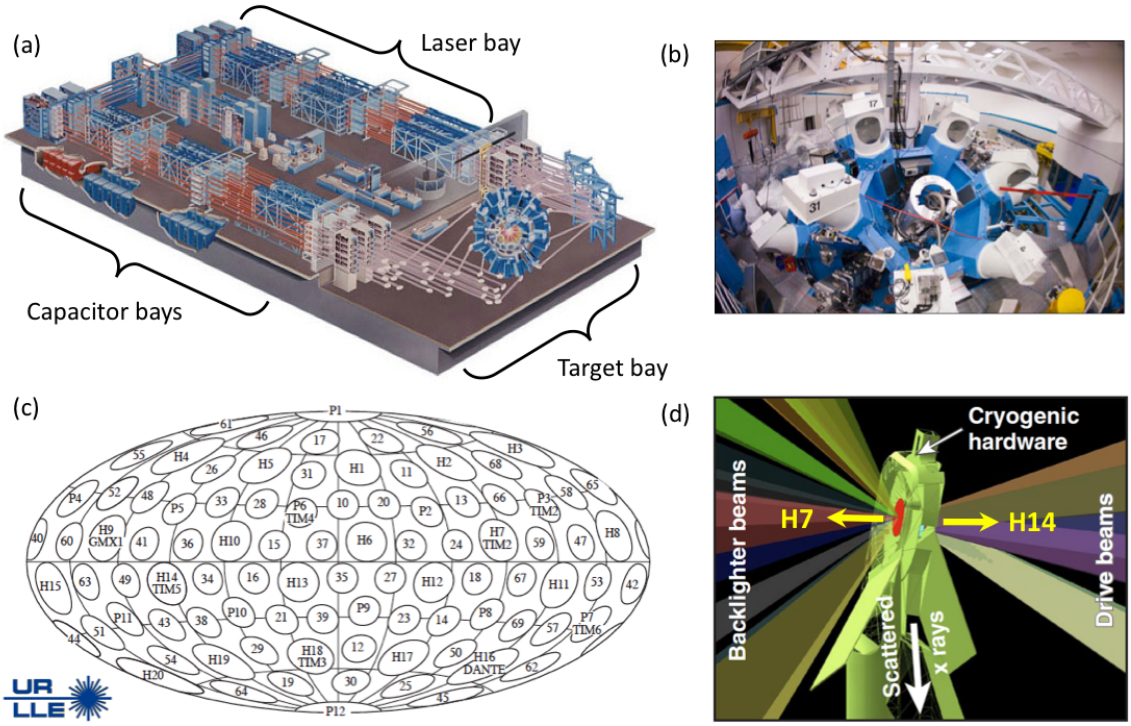

Figure 3.1: Schematic of the Omega laser system (a), photograph of the target chamber (b), schematic of port locations on the target chamber (c), and target set up with the laser drive and backlighter/scattering configuration (d). A constant intensity laser drive incident on the CH ablator compresses and heats the material inside a planar layer of liquid deuterium target creating WDM. Sixteen tightly focused beams irradiate a chlorinated plastic foil on the opposite side of the target. The scattered Cl Ly-α emission scattered at 90° down a scattering channel before it is detected with the GTS spectrometer [1]. Images were obtained from the LLE website.

The drive beams were frequency-tripled providing the 3ω ($\lambda = 351$ nm) laser output to increase the laser-plasma coupling efficiency [57]. The UV laser drive consisted

of six pairs of 1 ns laser pulses evenly divided into two cones around the target normal at angles of 23.2° and 47.8° and a flat intensity profile was created by phase plates and polarization smoothing [188]. These square pulses were then staggered in time forming a 6 ns constant drive with intensities of 10^{13} and 10^{14} W/cm^2. The higher intensity drive operated at the optimum energy output of the Omega system with $400 - 500$ J/beam. The $10\times$ lower intensity drive is then created by detuning of the frequency conversion crystals (FCC) lowering the conversion efficiency of the UV output of the laser. In the XRTS configuration the drive beams come from the H14 side of the Omega target chamber. For the higher intensity drive beams 16, 63, 29, 48, 33 and 54 are set to 420 J in each beam, whereas beams 34, 49, 36, 43, 38 and 41 are 300 J/beam coming at higher angle from the plane of the target, these energies are reduced to 42 J and 30 J respectively for the lower intensity drive. The drive beams are focused to $600 - 800$ μm spot size at 230 μm from the target chamber centre (TCC) towards H14. In the case of drive beams with a smoothed intensity profile the beam diameter on target is defined as the full width at the $1/e$ intensity of the super-Gaussian beam profile, see section 3.2.1. In the VISAR configuration the drive beams are switched to the H7 side to avoid a conflict with the ASBO/VISAR telescope located in port H14. The beam sets 11, 14, 32, 47, 68 and 69 at 42 J/Beam (UV) and 13, 18, 24, 59, 66 and 67 at 30 J/Beam (UV), both FCC detuned and focused at 770 μm from TCC towards H7, were used. Typical calorimetry measurements of the stacked laser drive are shown in figure 3.2.

Sixteen tightly focused 1 ns beams at 10^{16} W/cm^2 (200 μm focal spot diameter) then come from the H7 side and irradiate a 12 μm thick Saran foil creating a burst of narrowband Cl Ly-α x-rays at 2.96 keV, which are used as our x-ray backlighter probe. The beams used were: 13, 18, 24, 59, 66 and 67 in cone 1; 11, 14, 32, 47, 68 and 69 in cone 2; and 20, 53, 58 and 50 in cone 3 at 500 J/beam focused 1500 μm from TCC towards H7. The Ly-α radiation is emitted by highly ionized hydrogen-like atoms in the ablation plasma heated by the inverse bremsstrahlung process [19]. The backlighter lasers therefore operated at 3ω to maximize the conversion efficiency of the laser into x-rays by reducing laser backscattering instabilities [57]. No phase plates were used to smooth these beams, despite the possibility of improvement of the conversion efficiency, in order to achieve the highest possible intensity of the focused beams which both increases the conversion efficiency of the Ly-α and suppresses the He-like and Li-like satellites [103]. For the unsmoothed beams the focal spot diameter is defined by the perimeter encircling most of the laser energy. These x-rays

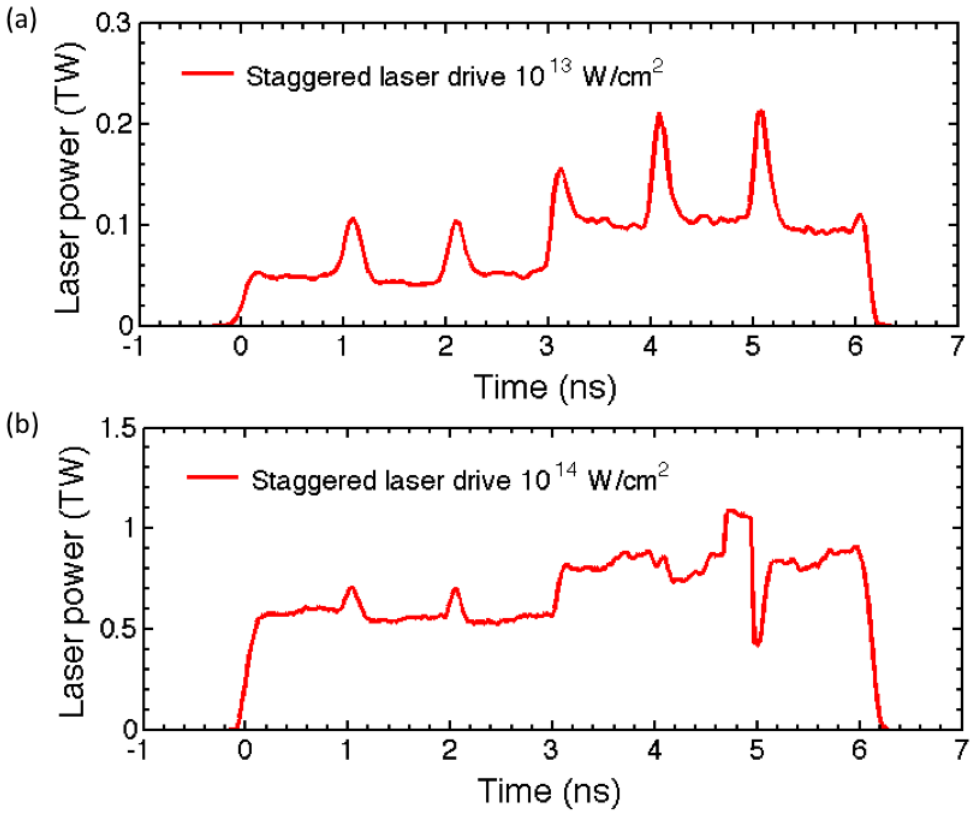

Figure 3.2: Typical profiles of laser power vs. time for low intensity drive at 10^{13} (shot 58571, July 2010) and high intensity drive at 10^{14} W/cm^2 (shot 54957, July 2009). The "spikes" in intensity are caused by temporal overlap of the individual 1 ns pulse pairs.

are collimated by a Ta pinhole 200 μm and scattered at 90° to a gated Thomson spectrometer (GTS).

The desired laser conditions including pulse shape, energy, frequency conversion, profile smoothing, timing, pointing and focusing were requested through the LLE shot request form (SRF) system. All the necessary jobs to ensure the desired laser set up were carried by the LLE engineers. The following sub-sections briefly outline some of the systems used in the process of delivering us the beams used in the experiment.

3.2.1 Beam profile and smoothing

Efficient creation of the desired WDM conditions require a uniform shock front to propagate through the cryogenic deuterium. However, non-uniformities in the laser drive in the form of intensity fluctuations (spikes) can result in undesired plasma instabilities in the ablation plasma resulting in hotspots that damage the uniformity

of the shock drive. At Omega, the drive beam profile was smoothed with combined use of the distributed phase plates (DPP) and distributed polarization rotators (DPR) [189].

The phase plates are two-dimensional arrays of transmitting areas of varied thickness placed just ahead of the focusing lens dividing the beam into multiple beamlets which break the spatial coherence and generate a characteristic speckled diffraction pattern that distributes the spatial intensity more evenly. The DPP's have no phase discontinuities of magnitude π, unlike previously used two-level phase plates of discrete rectangular or hexagonal subregions of either 0 or π where the far-field envelope is defined by the Fourier transform $sinc^2$ of the sub-regions and does not conform to a super-Gaussian shape required for high energy lasers such as Omega [190, 191, 192]. This design of phase plates builds on an earlier design for a continuous DPP which used a two-dimensional Fourier grating with random phase to produce a low-order super-Gaussian profile in the far field [190]. The improved design employed the phase-retrieval algorithm instead of a random noise removing phase discontinuities which then provides a smoothed speckled profile that supports higher-order super-Gaussian beam shape [191, 192]. The use of near-continuous phase plates also reduces scattering losses to a negligible level.

The function of the DPR's is to aid the beam smoothing in conjunction with the use of DPP's. The optical element itself is a 1 cm thick wedged birefringent potassium dihydrogen phosphate (KDP) crystal. The DPR splits the beam into the extraordinary (e) and ordinary (o) waves which travel travel in orthogonal directions with respect to one another at different speeds due to their different indices of refraction in the crystal. The KDP is oriented such that the vertex is halfway between the e and o axes. The speed difference between the e and o waves then results in a phase shift that prohibits the formation of interference fringes detrimental to the beam-smoothing process [189]. After the beam has passed through the DPP, there are many high intensity speckles ("hot spots") in the beam. With optimal alignment the DPR reduces this speckle pattern by a factor of $\sqrt{2}$ yielding a more evenly distributed intensity profile of the laser beam.

3.2.2 Frequency conversion

In order to achieve efficient energy coupling between the driver laser and the ablation plasma in the liquid deuterium target, third harmonic of the Omega laser output was used. By the use of the shorter wavelength of the drive and beam profile smoothing, which reduces sharp intensity peaks, the energy conversion efficiency of the ablation

process improves by significantly reducing the effect of plasma instabilities and electron pre-heating during the plasma formation [57]. Thus the drive intensity can be kept below the limit of $I_L(W/cm^2) \sim 4 \times 10^{14}\ W/cm^2$ as established in Chapter 1 [58, 59].

The frequency conversion crystals (FCC) are used to convert the fundamental wavelength of the Omega laser (1054 nm) to the second (527 nm) and third (351 nm) harmonic wavelength [193]. The FCC assembly contains a Brewster angle linear polarizer, an IR absorption glass, a UV absorption window and three KDP crystals. The crystals are 300 mm in diameter, the doubler and the first tripler have an average thickness of 12.2 mm and the second tripler is 8 mm thick. The crystal axes are oriented at the angle of $34.8° \pm 0.1°$ with respect to the incoming p-polarized beam as shown in figure 3.3. The IR absorber stops reflections from the coated polarizer surface. The UV absorption window is placed in the assembly to protect the polarizer from optical damage due to reflected UV light. It is made of type F-11 optical glass is designed to transmit IR radiation from the laser, but blocks any UV rays reflected from the target or optical surfaces [189].

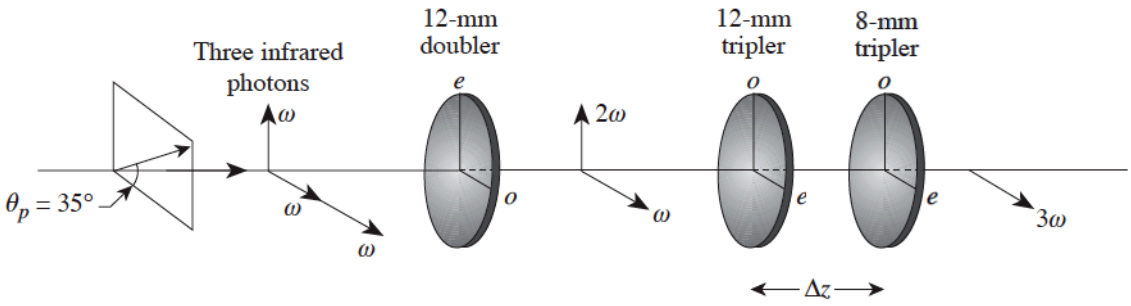

Figure 3.3: Schematic of the FCC assembly and crystal orientation, after Ref. [189].

The FCCs are located in the laser bay near the final image plane of the laser system under a thermally stable environment [189]. The energy conversion efficiency as specified by the Omega system performance is $70 - 80\%$ for 1 ns pulses. The conversion efficiency is a function of intensity, therefore it decreases for longer pulses. In our experiment, we achieve the maximum efficiency by staggering a series of 1 ns pulses. In order to achieve highly efficient harmonic conversion, the KDP crystals are tuned to the correct orientation with respect to the optical axis of the incident polarization vector and their e and o axes must be exactly orthogonal, as shown

in figure 3.3. The best-tuned position is found and calibrated for any particular temperature [189]. Lower output intensity of the laser can be achieved by detuning of the FCC plates by small adjustments of the relative rotation of the tripler crystals about the optical axis, which allows fine tuning of the e and o axes reducing generation of the third harmonic 3ω.

3.2.3 System alignment

The end-to-end alignment of the Omega IR and 3ω laser system is challenging as there is not sufficient power to operate the higher harmonics in continuous wave (cw) mode and the IR beam is poorly reflected by the UV transport optics in the target bay. The Omega alignment system therefore utilizes separate IR and UV lasers to align the optical systems [189, 194]. The IR alignment beam is a mode-locked cw 1054 nm Nd-doped yttrium lithium fluorine (Nd:YLF) laser and the UV optics are aligned with 351 nm cw laser that is injected into the system after the FCCs. Simultaneous alignment of both UV and IR optics is achieved using steering mirrors. The alignment procedures, carried out entirely by the LLE staff, are described in detail in reference [189].

3.2.4 Beam diagnostics

The UV energy measurement for each beam is carried out using the harmonic energy diagnostic (HED) [194]. Part of the energy in a beam (0.16%) is taken through a second-order Fresnel reflection off two uncoated optical surfaces just after the FCCs. The first uncoated surface "picks off" 4% of the beam's energy letting the remaining 96 % to pass to the target chamber. The second surface is mounted on a "flip-in" optic that redirects 4% of the radiation reflected from the first surface into an integrating sphere, which is kept under vacuum. The collected light is then transported through a fiber optic to a spectrometer outfitted with a CCD camera. The spectrometers are calibrated by conventional absorber/thermopile calorimeters used to measure the total energy in each beam before it enters the target bay [194]. An accumulative transmission of the target bay optical surfaces and substrates (these include: two UV high-reflector mirrors, a DPP, focusing lens, one vacuum window and a debris shield) is measured by the Omega Transport Instrumentation System (OTIS). This instrument consists of a CCD-based ratiometer embedded inside a reflective sphere inserted into the target chamber [194].

The temporal profile of the laser is measured by the diagnostic referred to as P510 streak camera [194]. The streak camera is outfitted with an external light source which provides a series of timing fiducials which are used to plot the measured intensity profile from the laser over a reliable temporal axis. This instrument is used to set and check the relative timing of the Omega beams. Moreover, the laser power measurement of P510 is calibrated, so the intensity on target can be extracted from the trace. Typical P510 output in the experiments described in this work are shown in figure 3.2.

3.3 Experimental diagnostics

A number of independent experimental diagnostics were used to collect data about the x-ray backlighter as well as the conditions in the shocked deuterium sample. This section will outline the technical details of these systems.

3.3.1 X-ray spectrometer (GTS)

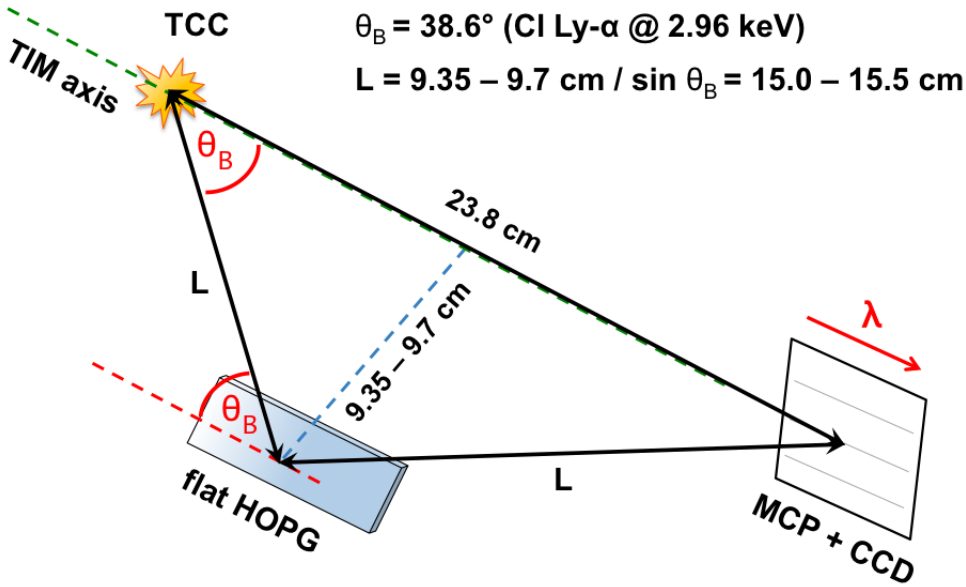

Figure 3.4: Schematic of the gated Thomson spectrometer (GTS) used in the x-ray scattering experiments on Omega.

The x-rays scattered at 90° are sent down the scattering channel where they are detected by the gated Thomson spectrometer (GTS), mounted inside the TIM 6 access

port P7 for diagnostics, see figure 3.1 (c). TIM stands for "Ten-Inch Manipulator" which is a diagnostic shuttle system that is used to position a variety of diagnostics near the TCC. The GTS is composed of a flat highly oriented pyrolytic graphite (HOPG) mosaic crystal [195, 196] coupled with an x-ray framing camera (XRFC), with a micro-channel-plate (MCP) combined with a CCD detector as shown in figure 3.4 [194]. The crystal was placed at the optimal Bragg angle of $\theta_B = 38.6°$ projecting the scattering spectra across the MCP camera which was placed 23.8 cm from the scattering target center, giving the spectrometer resolution of $\sim$ 12 eV/mm. The MCP has four individually powered strips charged in a sequence during the 1 ns backlighter providing an improved temporal resolution of the scattering measurement. The integration time of each strip was 250 ps. A Be blast shield was used to block any visible radiation and stop any debris from damaging the specrometer.

HOPG crystal

The use of hard x-rays in Thomson scattering to study WDM is crucial as only short wavelengh radiation can penetrate deep inside solid density plasmas due to the low critical density for lower energy probes, as discussed in Chapter 1. Also, short wavelengths have the advantage of short scattering scale length allowing us to access the non-collective regime, not available for radiation of lower energy, and can therefore probe the microscopic properties of the studied medium. Spectroscopic measurements with the use of these high-energy probes require the use of diffraction crystals, where the spacing of the atomic planes d is comparable with the probe wavelength, as a replacement for grating spectrometer that cannot be manufactured with sufficiently small grid spacing. The principle of Bragg's law is used in order separate the wavelengths by the spectrometer: $n\lambda = 2d\sin(\theta_B)$, where n is the order of diffraction.

The best spectral resolution is provided by so called *perfect* or *single* crystals such as Quartz, silicon or PET where all atomic planes in the block are arranged in parallel to the crystal surface with a unique value of $2d$. However, the reflectivity of these crystals is relatively low since the x-rays can only reflect from specific points in the lattice with no redundancy. For the purposes of x-ray scattering, especially in the case of hydrogen isotopes, signal levels of the scattered x-rays that can be detected are very low. Thus, *mosaic* crystals that exhibit significantly higher reflectivity are used. HOPG ($2d$ = 0.6708 nm) crystals are widely used in x-ray scattering experiments since their alternative crystalline structure increases their reflectivity. These crystals exhibit characteristic partially random alignment of the crystalline units around the

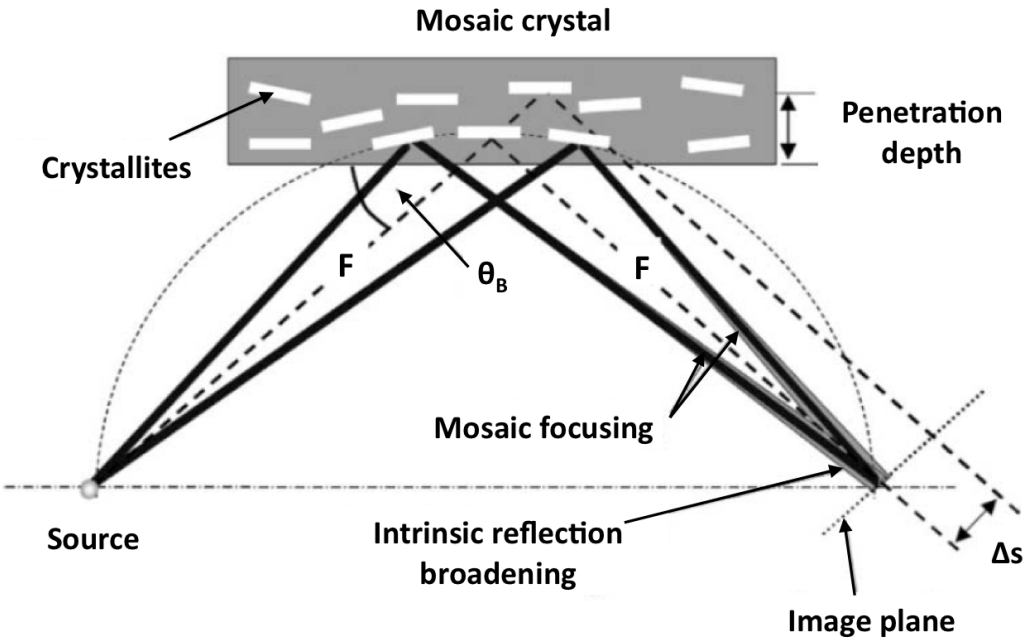

Figure 3.5: Schematic of typical structure of a highly oriented pyrolytic graphite (HOPG) mosaic crystal, after Ref. [195]. Mosaic focusing takes place if the distances F between the crystal and the source and the image plane are equal. Spatial smearing Δs in the image plane can result from penetration depth effects or from finite source size. Such a structure is achieved through a thermal treatment during the crystal manufacturing [195].

orientation of *perfect* crystals parallel to their surface [195] as shown in figure 3.5. These crystals have many interesting properties and advantages. Manufacturing of shaped *mosaic* crystals (e.g. cylindrical) is for example considerably cheaper than for *perfect* crystals.

The partial randomness of the orientation of the atomic planes causes a defocussing effect, also referred to as *mosaic spread*, in direction perpendicular to the diffraction plane, which causes "blurring" of the features in the x-ray signal. This *mosaicity* of the crystal is a direct reflection of the angular orientation of the individual crystallites, i.e. larger angular spread of the plane orientations from the perfect crystal plane position results in a more severe "blurring" effect reducing the crystal's spectral resolution. A simplified model defines the distribution of the orientation of the crystallites as a Gaussian function, which then provides the definition for mosaic spread as a FWHM of the Gaussian distribution, however more detailed studies have revealed a rather complex structure [197, 198].

HOPG crystal types are separated into groups according to their degree of mosaic-

ity ranging between 0.4° and 3.5°: ZYA, ZYB, ZYD and ZYH. The spectral resolution is reduced by the angular spread of the diffracted rays due to the mosaic spread. For the ZYA type we expect $(\Delta E/E)_\gamma \sim 4.3 \times 10^{-3}$ while it is $\sim 38.1 \times 10^{-3}$ for ZYH, i.e. ZYH crystal cannot be used to resolve spectral features in this experiment where the downshift of the Compton peak is expected to be ~ 17 eV. The expected depth broadening for the mosaic graphite crystals is $(\Delta E/E)_{depth} = \frac{\lambda_{mfp}}{2L} \times \cos^2(\theta_B) \sim 6.0 \times 10^{-5}$ (the penetration depth or mean free path of 3 keV x-rays is $\lambda_{mfp} \sim 30$ μm), which is negligible at these frequencies, i.e. the thickness of the crystal does not need to be kept small [199]. The integrated reflectivity expected for the HOPG crystals (ZYA, ZYH) for the Cl Ly-α line emission is ~ 3 mrad [199].

Mosaic crystals exhibit the very useful property of *para focusing*. Following from the principle of the Rowland's circle of radius F, a curved crystal surface placed on the circular perimeter will focus rays from a point source placed anywhere on the circle. Due to the random orientation of the atomic planes in a mosaic crystal, a fraction of the diffracted x-rays will always fall on the Rowland's circle, where they can be focused onto a detector [195]. Thus, this effect can significantly reduce the source broadening and improve the spectral resolution. The thickness and penetration depth of the crystal also have to be taken into account. Hard x-rays can penetrate deeper into the crystal finding a larger number of suitable planes to diffract from. As this increases the brightness of the measured signal, it also reduces the spectral resolution and can introduce unwanted features into the spectrum such as line broadening. This effect is smaller for crystals with a lower degree of mosaicity.

The experiment started with a ZYA crystal (25 × 50 mm, 2 mm thick) with mosaic spread γ of $0.4° \pm 0.1°$. This crystal gives an excellent resolution due to its low mosaic spread, however this comes at the expense of the reflectivity of the crystal, which was problematic for deuterium x-ray scattering measurements. The original HOPG crystal was therefore replaced with a ZYB type (25 × 50 mm, 2 mm thick) with $\gamma = 0.8° \pm 0.2°$ and resolution $(\Delta E/E)_\gamma \sim 8.7 \times 10^{-3}$, which is still negligible compared to the ray divergence through the Ta pinhole ($\sim 7.8°$). The thickness of the substrate on which the Bragg crystal was mounted changed throughout the various shots, thus the distance of the crystal surface from the TIM axis changes between the shots as shown in figure 3.4.

X-ray framing camera (XRFC)

LLE provide four x-ray framing cameras (XRFC) for two-dimensional, time-resolved x-ray imaging [200, 201]. Two of these cameras operate at a resolution of ~ 40 ps

and two with 80, 200, 300, 400, 500, or 1000 ps using interchangeable pulse-forming modules [194]. These cameras are operated from the TIM's available on the target chamber. Two cameras were used in these experiments: TIM 6 (port P7) operated XRFC4 joined with the GTS spectrometer, and XRFC1 inside TIM1 (port P3) was used to look at the temporal evolution of the emission from the plasma created by the backlighter laser beams incident onto the plastic foil.

The x-ray signal detected by the XRFC is amplified by the MCP which consists of a gold photocathode, coated on the MCP surface, micro-channels connected to a high voltage supply and a phosphor plate [202, 203]. The voltage supply is connected to up to four independent strips which can be engaged independently in time enabling sequential gating of the MCP. As the x-rays illuminate the Au cathode they liberate photoelectrons that are further accelerated down the channels and multiplied by a short high-voltage pulse propagated along the MCP strip line [194]. The two-dimensional image then forms as the electrons strike the phosphor plate producing an optical image.

The optical images were recorded with a charge-coupled device (CCD) camera consisting of a 4096×4096 array of 9 μm pixels [204]. The cameras are cooled to about -20°C during the experimental shots in order to reduce the dark-current noise in the chip. Remote electronic controls are used to change the MCP bias voltage and camera timing during the experimental day allowing the principal investigators to make flexible decisions about the data acquisition during the shot day.

A 8 mil (~ 200 μm) Be blast shield was placed in front of the GTS spectrometer. Additional read filters have been used to attenuate the incoming radiation and block any visible light from entering the camera. We have used 4 mil (~ 100 μm) Be or 1 mil (~ 25 μm) V filters for XRFC 4 inside TIM 6. The brightness of the measured signal was further reduced by applying a positive bias on the MCP camera strips. The quoted nominal value is $3\times$ reduction for every increase of 50 V. In the case of the cryo shots, where scattering signal levels were low, the bias was kept low at $0 - 50$ V. During foil shots for spectral calibration, when the signal is significantly higher as it is the direct radiation from the Saran target, the bias was increased to $250 - 400$ V depending on the shot. The inter-strip timing used was 250 ps.

3.3.2 Pinhole cameras

A series of x-ray pinhole cameras (XRPHC) are among the standard fixed diagnostics on Omega [194]. These are located at various locations around the target chamber and were used to view the radiation emitted from the backlighter foils during target

shots. The best view of the laser illuminated Saran foil was from ports H12 looking at an angle from the upper part of the target chamber ($\theta = 108.89°$, $\phi = 54.0°$) and H13, see schematic in figure 3.1 (c). These images were used to estimate the x-ray source size and the alignment of the backlighter beam during the cryo shots, see figures 3.6 and 3.7.

The x-rays are imaged using laser drilled Ta pinholes with diameter of 10 μm and thickness of 50 μm. The image magnification of XRPHC on port H12 is 4× with pinhole-to-target distance of 162 mm and pinhole-to-image distance of 648 mm. The time-integrated images are detected with charge-injection devices (CID) used in direct-detection mode (i.e. without phosphor) with a useful energy range better than $2 - 8$ keV. The CID chips are capable of recording images across 812×604 pixels with the useful central area corresponding to 800×600 pixels. The centre-to-centre spacing of the pixels is 38.5×38.5 μm [205]. The cameras are usually covered with a 25.4 μm thick Be window.

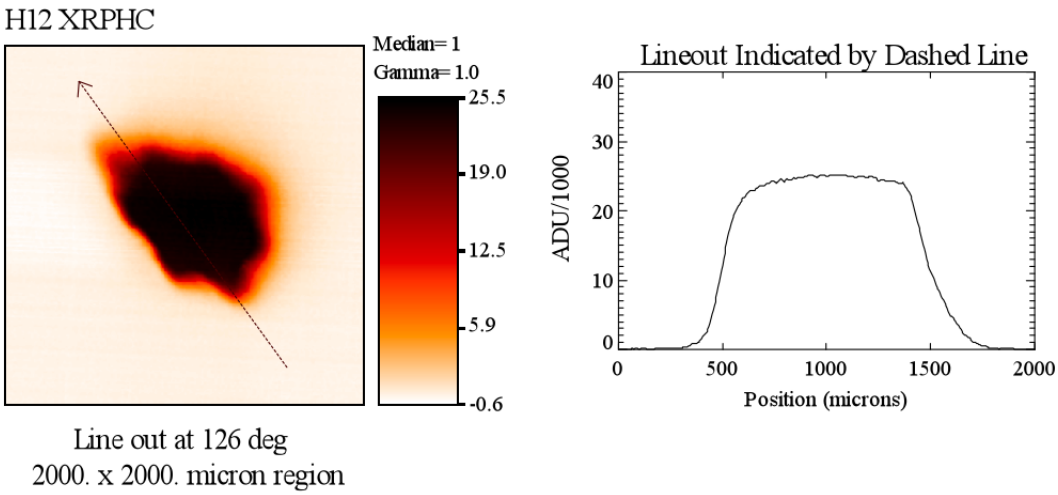

Figure 3.6: Analysed image from XRPHC in port H12 on shot 58571 (July 2010). Most of the XRPHC in this experiment seem to be saturated, which is not an issue since this diagnostic is simply used to identify the position and alignment of the backlighter laser spot. Badly aligned shots show a "star-like" shape of the spot.

A representative background-subtracted image from the H12 pinhole camera is shown in figure 3.6. Typically, the size of the plasma emission from the backligher spot as viewed from the laser side is $\sim 800 - 1000$ μm in diameter. The spot is assumed circular, so its size is taken along the longest axis of the projected circle. Since these images are not time gated, certain broadening of the laser spot due to

temporal expansion of the plasma from the foil should be expected, thus the actual backlighter spot is likely to be smaller during the scattering measurement.

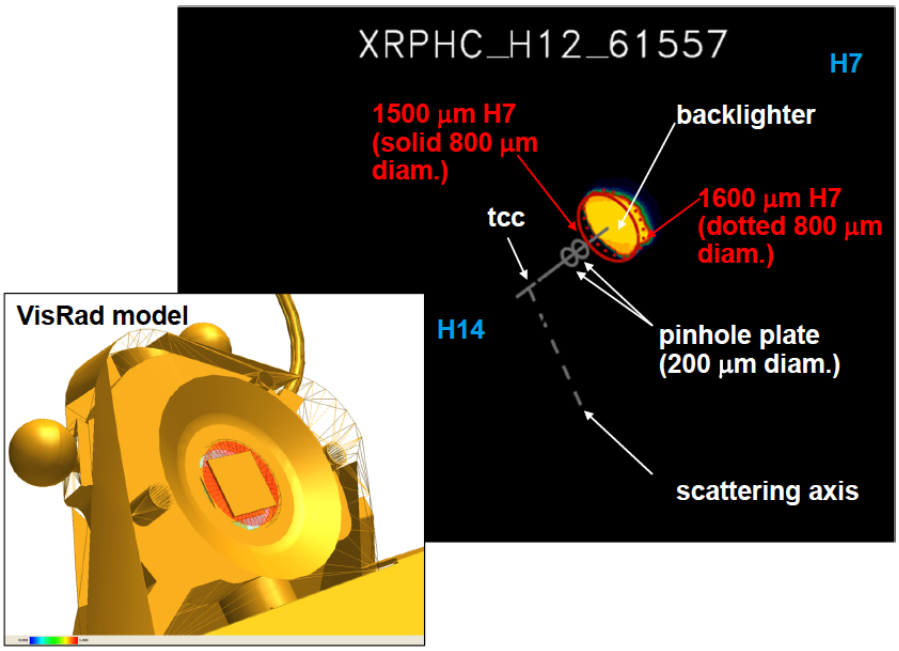

Figure 3.7: Analysed image from XRPHC in port H12 on shot 61557 (Mar 2011). In this case the image obtained from XRPHC located in port H12 identified target mis-alignment, where the cryo XRTS target was shifted $\sim$ 100 μm towards H7.

3.3.3 X-ray streak camera

The temporal evolution x-ray spectra emitted from the chlorinated plastic foil illuminated with the backlighter beams was measured with an x-ray streak camera (SIM Streak Camera A, SSCA) outfitted with a crystal spectrometer mounted in TIM 2 (port H3) pointing at 1500 μm / H7 (backlighter position) [206]. The camera includes a fourth-harmonic (263 nm) timing fiducial channel recorded simultaneously with the x-rays used for cross-timing of the x-ray emission with the laser pulse trigger to $\pm$ 25 ps [194]. The SSCA was protected with 4 mil ($\sim$ 100 μm) Be blast shield. The incoming x-rays were attenuated with an additional 1 mil ($\sim$ 25 μm) Be filter, which also acts as a block for visible radiation. This however resulted in saturated images in the first shots of the campaign. An additional 0.25 mil ($\sim$ 6 μm) Al filter was added to avoid saturation of the Cl lines.

The x-rays recorded by the streak camera are first converted into electrons by the photo-electric effect as they impact a Au cathode on a 0.5 mil ($\sim$ 12 μm) Be substrate.

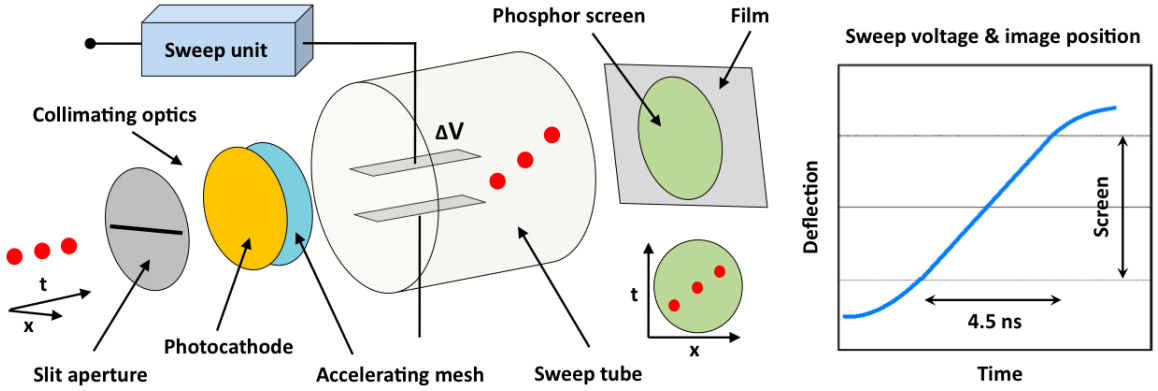

Figure 3.8: A schematic of a typical x-ray streak camera such as the one used in this experiment (SSCA). The photo-electrons liberated from the Au photocathode are accelerated inside the sweep tube by the sweep voltage (total SSCA ramp pulse is 2400 V) directed by the sweep unit, which sets the sweep speed of the electrons across the detector screen.

These electrons are accelerated by the cathode acceleration field (accelerating mesh) to 13 keV and subsequently focused and sweeped across an electron sensitive detector (a phosphor screen or MCP), which converts the signal to visible light, as a function of time [206]. A 1-dimensional image is created by a 250 μm wide slit aperture placed just before the photocathode. This image is then smeared across the detector plane as the electrons pass through a differential potential gradually varying in time, i.e. at earlier times electrons pass through a different potential than later ones causing them to impact the phosphor screen at a different location. This creates an 2-dimensional streaked image where one axis corresponds to one spatial dimension (a line out across the Cl spectrum) and the other to time. In our set up we used 115 ps/mm sweep velocity (speed 1 setting) and a fluorescent display which was 40 mm in diameter giving a temporal window size of $\sim$ 4.5 ns. A typical x-ray streak camera set up is shown in figure 3.8.

The optical output of the SSCA was recorded on Kodak T-max 3200 film (specially manufactured with no holes that could interfere with the recorded data). The film was then developed through rotary processing and digitized with a Perkin-Elmer PDS (photometric data system) Microdensitometer with a resolution of 50 μm/pixel. This device can be used to extract the information of the absolute intensity measured by the film through the use of a calibrated white lamp scanner fitted with adjustable ND filters and photomultiplier tube.

The spectrometer set up was similar to that of the GTS shown in figure 3.4. The Bragg crystal used was a flat RbAp ($2d$ = 2.6121 nm) mounted at $\theta_B = 8.7°$ with

additional rotation of $\phi = 0.65°$ to ensure a centered projection of the diffracted image into the slit of the streak camera. The central wavelength was thus 3.96 Å(3.14 keV) with a range of $3.19 - 4.67$ Å$(2.66 - 3.89$ keV), chosen such that the following Cl K-shell lines can be measured simultaneously: Cl He-α at 4.444 Å, Cl H-α at 4.188 Å, Cl He-β at 3.790 Å, Cl He-γ at 3.603 Å, Cl H-β at 3.535 Å, and Cl H-γ at 3.351 Å. The crystal was placed half way between the source and the slit of the streak camera separated by 19" ($\sim$ 48.26 cm). It should be noted that the SSCA is looking at the laser side of the Saran foil, which only gives a rough indication of the temporal x-ray backlighter profile without the effect of variable transmission of the foil as it is being ablated.

3.3.4 Velocity interferometry (VISAR)

The velocity interferometry system for any reflector (VISAR) was used to directly measure the shock velocity U_s in the deuterium sample from which the density and pressure in the shock could be inferred [207, 208]. The active shock breakout (ASBO) system is a line-imaging velocity interferometer used as a general purpose shock diagnostic at Omega [70]. This TIM diagnostic located inside the H14 port (TIM 5) is a two interferometer system (ASBO1 and ASBO2) capable of producing a continuous record of the shock velocity history as well as a 1-D image of the spatial profile of the shock [70]. The velocity measurement is obtained from a Doppler shift of a probe beam reflected from a moving shock surface (in transparent medium, i. e. deuterium), which reflects optical radiation due to its high level of ionization and over-critical density.

The main components of the VISAR diagnostic are: a probe laser, an imaging system and two Mach-Zehnder interferometers. The laser probe is a Spectra Physics frequency-doubled Nd-YAG laser ($\lambda = 532$ nm) that produces 8 ns pulses which can be stacked to provide up to $\sim$ 24 ns long trace, which is delivered to the VISAR through fiber optics [194]. The imaging system conveys the probe beam to the target, where it reflects back, and onto the output beam splitters (BS2) in the interferometers as shown in figure 3.9. Each interferometer produces a linear fringe pattern to the coherent laser beam imposed by a slight tilt of the output beam splitter. An optical delay element (etalon) is built within one of the interferometer legs, which introduces an additional optical path delay to the reflected probe beam which can be used to obtain the shock velocity from the phase shift in the fringe pattern. The output from the interferometers is detected with an optical streak camera which records images of the velocity trace with one spatial and one temporal dimension with 5 μm spatial

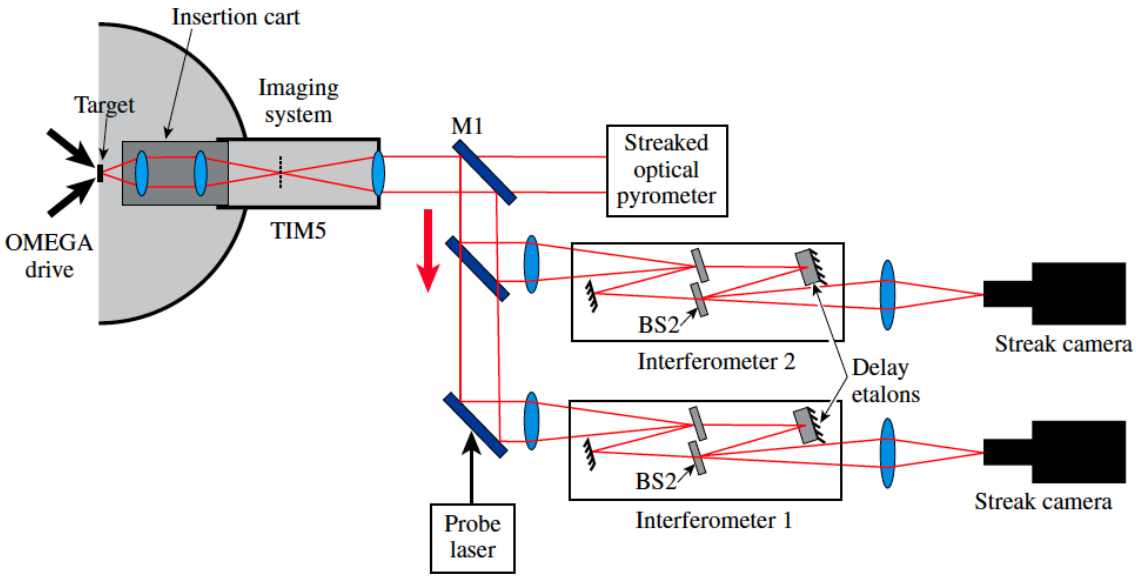

Figure 3.9: A schematic of the velocity interferometry system for any reflector (VISAR) at Omega as shown in Ref. [194].

and $\sim 10 - 50$ ps temporal resolution respectively. The streaked trace also includes two sets of timing fiducials imposed on the top and bottom edges of the data record. These are series of dots, laser pulses delivered by fiber optic, spaced by $\Delta t = 0.5$ ns. The dots on the top are a continuous trace used to keep track of the sweep velocity of the streak camera and the bottom of the image is then marked with 8 dots that synchronize the temporal measurement with the laser trigger (ASBO1: first fiducial at $t = 425$ ps and ASBO2: first fiducial at $t = -1150$ ps). All the etalons used are UV grade fused silica ($n = 1.4607$). The individual parts of the VISAR system, set up and alignment are described in more detail in reference [70].

The shock velocity measurement is obtained from the fringe shift measured by the two interferometer arms. The light going through the interferometer arm with the etalon will be delayed by time τ. The total optical delay is given by the translational offset of the etalon-mirror and the refractive delay in the etalon: $\tau = \frac{2h}{c}(n - 1/n)$, where h is the etalon thickness, n is the index of refraction and c is the speed of light [70]. This form is derived from the translation distance $d = h(1 - 1/n)$ which is calculated to place image plane as viewed through the etalon coincident with its initially determined null position (i.e. zero path delay with the etalon removed) [70]. The above expression for τ is approximate as the beam passes through the etalon at an angle, however for the purposes of the VISAR measurements it is accurate enough,

see Ref. [70] for further details. A fringe is formed by a constructive interference which will occur when $2v\tau = m\lambda$, where $m = 1, 2, 3, ...$, thus if $m = 1$ a shift by one fringe is observed. We can then define the velocity sensitivity of VISAR by velocity per fringe $VPF = \lambda/2\tau$.

In the simplest case when the probe light is reflected from a target/shock surface undergoing instantaneous acceleration to a velocity v its phase will change by a constant time-dependent term $\Delta\phi_D(t)$ as a result of a Doppler shift [69]. The phase-shifted signal will arrive through the shorter interferometer arm in time t_0, while it will take it $t = \tau$ to pass through the longer arm. In the time between, t_0 and $t_0 + \tau$ as the Doppler-shifted light arrives at the output beam splitter from the short arm and not yet the long arm, a linearly increasing fringe shift will be observed as the phase $\Delta\phi_D(t)$ develops, see figure 3.10 (a). After time τ passes, the signal from the longer arm fully catches up and the phase meters of both arms advance at a common rate and no further fringe shifting is observed [69].

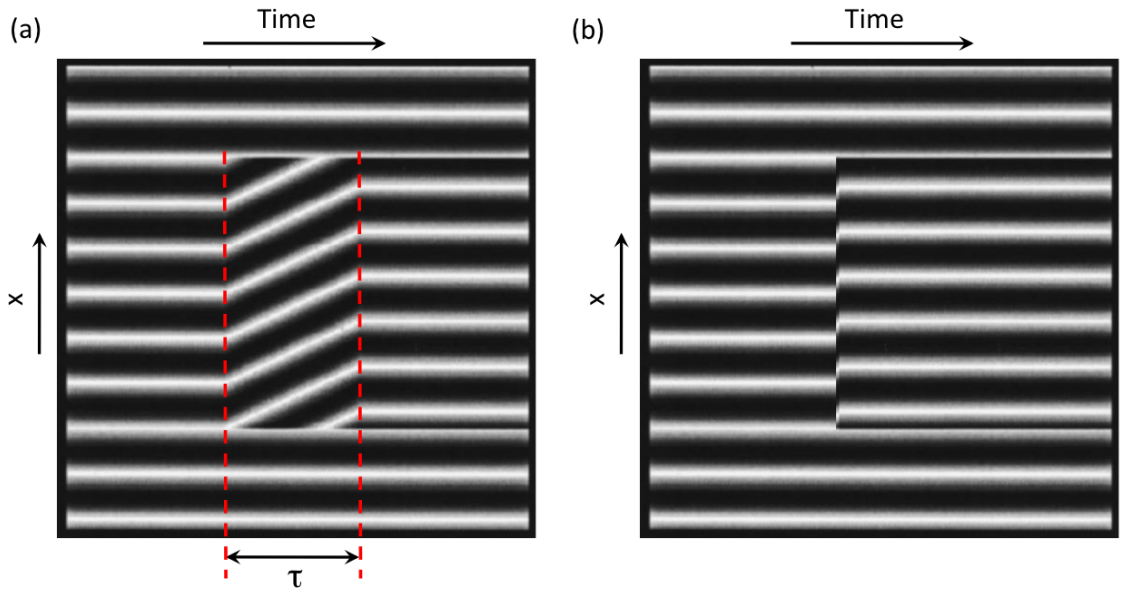

Figure 3.10: A simulated streak camera record of VISAR output in the case of simple acceleration (a) and discontinuous fringe pattern (b), after Ref. [69].

If the velocity of the target surface changes with time while the probe light reflects from it additional phase shifts of $\Delta\phi_R(t)$ are induced resulting in more fringe shifting. The shock velocity is then obtained from the total phase shift $\Delta\phi$ if the interferometer sensitivity is known: $v = VPF \times \Delta\phi/2\pi$. The temporal resolution of the velocity

measurement is limited by the transient time τ given by the delay between the interferometer arms as well as by the temporal resolution of the streak camera used. Rapid fringe movement during the transition time of the interferometer ($\tau = 15 - 50$ ps) thus results in discontinuous fringe shifts spanning across many fringes plus a fractional part, which in turn cause ambiguity in determination of the phase shift $\Delta\phi$ [70]. This is illustrated in figure 3.10 (b). The issues with fringe ambiguity are overcome by the use of two separate interferometers with different velocity sensitivity. The 2π discontinuities can be removed by matching the integer fringe shift from the two channels: $v_{1,2} = VPF \times \left(\frac{\Delta\phi}{2\pi} + m_{1,2}\right)$. Since both arms must measure the same velocity $v_1 = v_2$, the integer values of m_1 and m_2 from the two channels are matched to give a unique answer.

The etalon thickness and sweep rate of the streak camera in one of the interferometers are chosen based on expected shock velocity to reflect the best temporal and spatial (fringe shift) resolution of the recorded shock evolution. The second interferometer is fitted with a different delay element, giving it different velocity sensitivity, such that the velocity measurements from the independent arms carry different optical delays and can be matched to remove the 2π phase ambiguities observed in fast shock measurements resulting in observation of instantaneous fringe jumps greater than one fringe period. Care must be taken such that the VPF values corresponding to the two etalons used are not integer multiples of one another so that only one shock velocity can be matched from the two VISAR traces. A typical choice of velocity sensitivities would be 2.5 to 3.5 fringes in the first channel and 7 to 8 fringes in the second [70]. A different sweep rate can also be used to provide an independent verification of the time scale of the measurement.

The expected shock velocity, obtained from a number of hydro simulations using 1-D hydro codes *LILAC* [79, 80], *HELIOS* [179], was $30 - 50$ km/s. The sweep times chosen for ASBO1 and ASBO2 were 9 ns and 15 ns respectively, no delay was applied. Two complementary etalons were selected for both VISAR arms: etalon 5B ($h = 5.004$ mm, $\tau = 25.9$ ps, $VPF_{D_2} = 8.74$ km/s/fringe) was used in ASBO1 and 3A ($h = 3.095$ mm, $\tau = 16.02$ ps, $VPF_{D_2} = 14.1$ km/s/fringe) in ASBO2 with expected phase shifts by ~ 5 and ~ 3 fringes respectively. These values are computed using the corrected expression $VPF = \lambda/2\tau(1 + \delta)$, where term $\delta = 0.0318$ accounts for the dispersion of the etalon [209]. The phase shift was also corrected by the refractive index of deuterium ($n_{D_2} = 1.1379$), thus $VPF_{D_2} = VPF/n_{D_2}$. The full set of sample-dependent corrections to VPF can be found in Ref. [70].

3.3.5 Optical pyrometry (SOP)

Plasma created by laser driven shock will reach temperatures greater than 5000 K and thus will produce self-emission in the optical regime which can be linked to its temperature through the black body radiation relationship [210]. This radiation is measured by the streaked optical pyrometer (SOP) [71]. This instrument is absolutely calibrated such that emission temperature can be extracted from the measured data. SOP is generally used in conjunction with VISAR to obtain temporally and spatially resolved EOS measurements (shock temperature and velocity) from ablatively driven shocks at the Omega laser facility. A schematic of the SOP system used for the experiments described in this work is shown in figure 3.11.

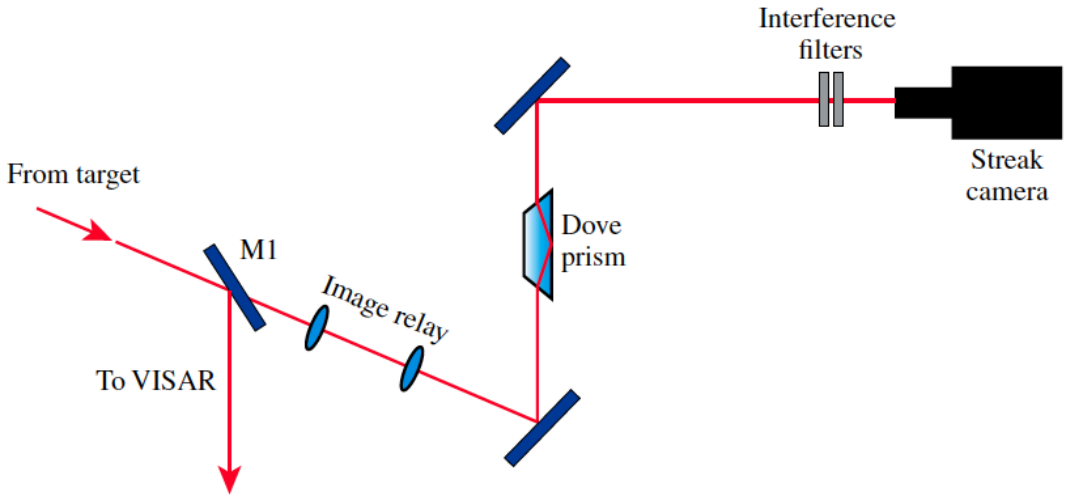

Figure 3.11: Layout of the streaked optical pyrometer at Omega as shown in Ref. [194].

The SOP optical system has been modified such that it can be used simultaneously with VISAR during target shots. The optical system takes a leak of the emission from the target through one of the periscope mirrors (M1) in the VISAR system and guides it through an image relay containing two lenses and two mirrors providing magnification of 20×, a Dove prism that rotates the image, and an interference filter pack into an optical streak camera [194]. Correction optics are used to compensate for refraction effects from the VISAR telescope at the wavelengths of interest. The various filter settings allow intensity measurements at multiple wavelength bands (blue channel at $400 - 500$ nm and red filter at $590 - 850$ nm). The responsivity of the pyrometer was calibrated using a lamp with a known emission profile traceable

to a National Institute of Standards and Technologies standard, which was placed inside the Omega chamber and viewed with the standard experimental configuration [194]. The spectral response was measured using a set of narrow-band filters.

The image is recorded by an optical streak camera (Hamamatsu C4187 with temporal windows of 2, 5, 10, 20, and 50 ns/image) coupled with an MCP intensifier with an P20 phosphor screen output and CCD (Photometrics CH350) camera with Thomson 7899 chip. The camera has an unbinned (raw) digital output of 2048×2072 array of 13.7 μm pixels (16-bit) [71]. The phosphor is the limiting resolution element giving an object-plane resolution of ~ 10 μm. The streak camera is outfitted with a slit of variable width providing various degrees of temporal resolution (0.5 mm slit gives ~ 170 ps integration time for 10 ns sweep). A more detailed description of the set up of the LLE SOP system can be found in Ref. [71].

The red channel with corresponding central wavelength of $\lambda_c = 684$ nm (the FWHM band of the normalized spectral responsivity of the red channel is $\sim 590-780$ nm, see figure 2 in Ref. [71]) was used in the experiments described in this work. The chosen slit width was $W_s = 100$ μm and the sweep speed window was set to 10 ns providing an excellent temporal resolution. No ND filters were used. The CCD image was compiled with 3×3 binning (B = 3) which generated a 682×691 pixel output. The gain setting 5 ($G = 19.0$) was used. The streak record of the SOP camera also includes two sets of timing fiducials equivalent to those used on the VISAR system. In the top continuous trace the dots are spaced by 506 ps, while the bottom 8 dot timing fiducial marks the laser time with the first fiducial at $t = -930$ ps. No delay to the timing fiducials was applied.

The SOP data can be used to provide an accurate measure of the temperature of the shocked material by comparing the emission intensity from the shock front at λ_c with the radiation distribution of a Planckian source. For the conditions in this experiment, the shock wave is optically thick to visible light, thus the brightness temperature of the self-emission radiation approaches the temperature of the material making the black/grey body approximation valid for shock temperature measurement [210]. Similar methods have proven to be reliable temperature diagnostics for shock-compressed deuterium [113, 114]. A detailed description of the analysis of the VISAR and SOP data will be provided in Chapter 4.

3.4 X-ray backlighter source

3.4.1 Spectral line profile

The x-ray probe selected for this experiment was a Cl Ly-α line at 2.96 keV ($\lambda_0 = 4.188$ Å) generated through laser irradiation of a chlorinated plastic foil (12 μm thick Saran or 5 μm thick Parylene D). The laser backlighter consisted of sixteen 1 ns beams at 10^{16} W/cm^2 (200 μm focal spot, 500 J/beam), which operated at 3ω maximizing the conversion efficiency of the laser into x-rays by reducing laser backscattering instabilities [57]. This line was selected due to its high conversion efficiency ($\eta_x \sim 0.2$ %) and narrow bandwidth ($\Delta E/E \sim 2 \times 10^{-3}$), sufficient for x-ray scattering measurements [103, 19, 211].

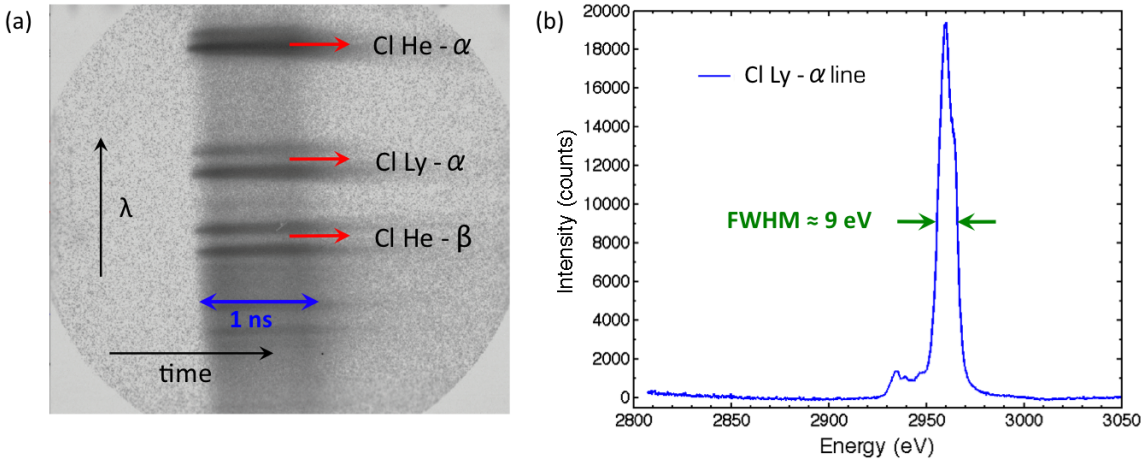

Figure 3.12: Cl Ly-α backlighter x-ray line at 2.96 keV created by laser illumination of the Saran foil at Omega: (a) shows the spectral trace recorded by the x-ray streak camera (SSCA) during shot 53908, Mar 2009, and (b) is the spectral measurement by the GTS spectrometer showing the full-width-half-maximum (FWHM) spectral width of the line is $\sim$ 9 eV (shot 54959, Jul 2009).

The Ly-α radiation is a result of the electronic transitions ($n = 2$ to $n = 1$, i.e. $1s - 2p$) in the K-shell of the highly ionized hydrogen-like Cl atoms in the ablation plasma heated by the inverse bremsstrahlung process [19]. The line itself consists of two fine structure components Cl Ly-$\alpha_{1,2}$ at energies of 2958 eV ($1s - 2p_{1/2}$) and 2962 eV ($1s - 2p_{3/2}$) respectively. The total width of the chlorine line consisting of both lines is $\sim$ 9 eV [103]. Additional dielectronic satellite lines, particularly on the lower energy wing of the resonance line, including Cl XVI ($2p^2 - 1s2p$) at 2928 eV and 2933 eV are also created, see figure 3.12, but the laser conditions are chosen such

that this emission is significantly reduced compared to the Cl Ly-α source. Typical spectra measured during the experiments is showed in figure 3.12.

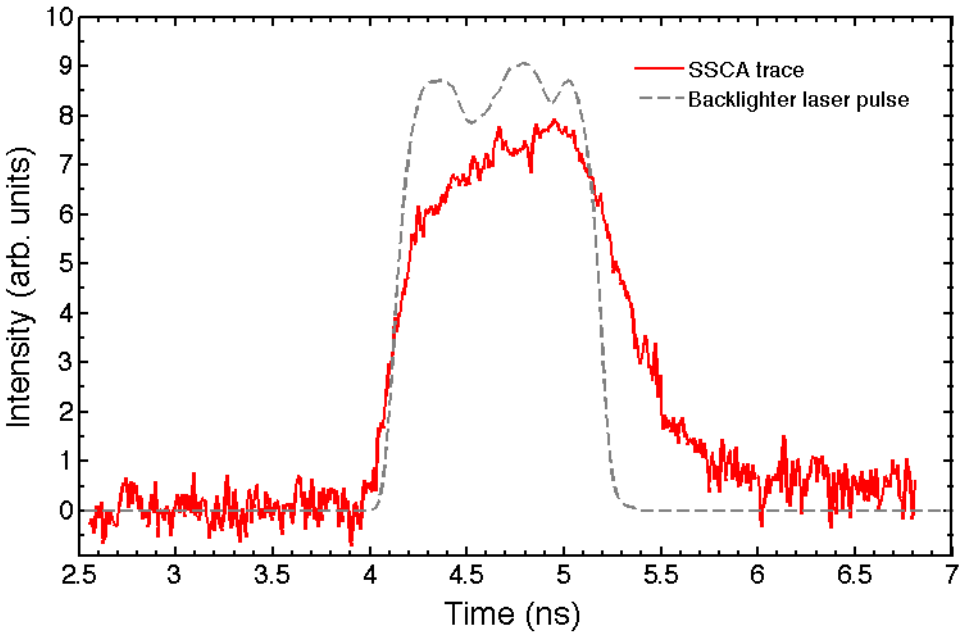

Figure 3.13: Temporal plot of the Cl Ly-α trace from SSCA overlayed with calorimetry measurement of the backlighter laser pulse during shot 61554 (Mar 2011). The backlighter pulse came on at 4 ns from the start of the high intensity drive.The duration of the streaked signal of the Cl Ly-α line is slightly longer than the backlighter laser pulse, showing a $\sim$ 0.5 ns long decreasing slope tail after the main signal, which can be a result of space-charge broadening in the streak camera as a result of saturation of the photocathode while operating the camera at a high signal level.

An important consideration was the minimization of the emission from the dielectronic satellites on the red wing of the Cl Ly-α line in order to resolve the Compton feature in the measured scattering spectra. Based on the previous work by Urry *et al.* [103] we were able to produce a bright narrow-band x-ray probe with minimal contribution from red-wing satellites. It was found that phase plates can improve the conversion efficiency by reduction of the backscattering instabilities, however a smaller spot size is needed to provided sufficiently high intensities [57]. It was found that the emission from Li-like satellites are significantly reduced at higher laser intensities [103]. At shorter laser wavelenths higher electron temperature and ionization in the backlighter foil is achieved suppressing the He-like emission [103]. These satellites however do appear later in time after the heater laser turns off and the plasma cools and the electronic population of the excited satellite states increase and therefore

time-gated measurements (using the GTS) are crucial to obtaining a clean scattering signal using the Cl Ly-α probe. Laser intensity and short wavelength were established as the crucial factors to achieve a good laser-target coupling and thus high conversion efficiency. We have used a frequency-trippled (3ω) backlighter laser at the intensity of 10^{16} W/cm^2 and focal spot of 200 μm.

Temporally resolved measurements of the Cl spectra were obtained using the x-ray streak camera (SSCA), described in the previous section. See figures 3.12 (a) and 3.14 for raw data. The streak camera measurements confirm a similar duration of the x-ray emission to the pulse length of the backligher beams, see figure 3.13. Preliminary shots with cryogenic targets showed that Ar condensation on the backlighter foil added an undesirable contamination of the emission spectra with Ar He-α radiation and its satellites with a significant burnthrough time for the Ar layer on the plastic foil which adds uncertainty to the scattering measurement, see figure 3.14. Thus a condensation shroud suspended over the target had to be used on all cryogenic shots minimizing the condensation of impurities particularly on the backlighter foil and the CH windows.

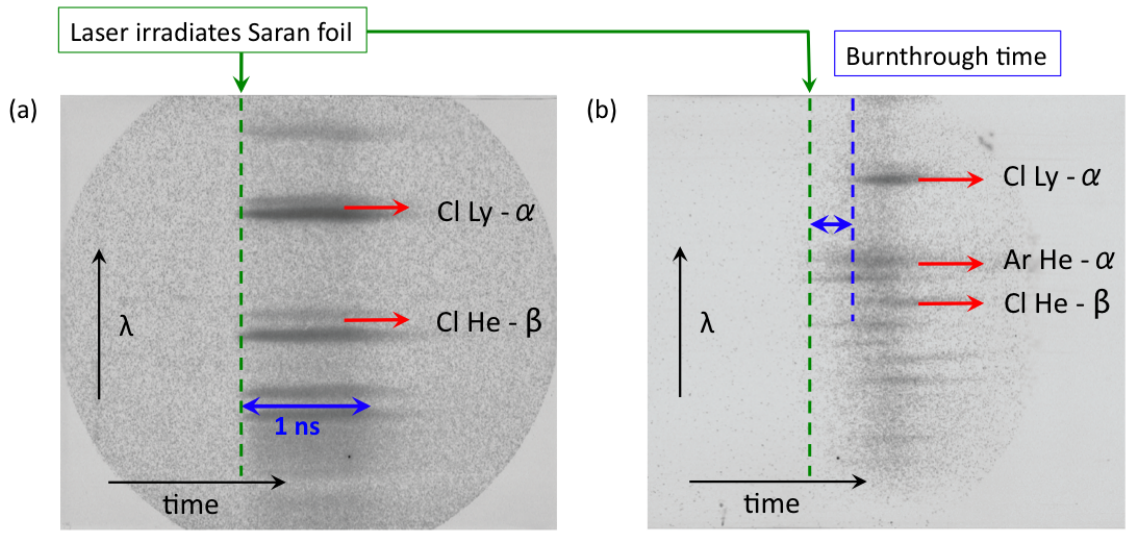

Figure 3.14: X-ray streak camera (SSCA) traces of the backlighter x-rays during shot 61554 (Mar 2011), when condensation shroud was deployed (a), and shot 53405 (Jan 2009) without shroud (b).

3.4.2 Photometrics

Due to the low cross section of the scattering process, high photon numbers in the x-ray probe are essential for successful scattering measurements. Other sources of noise in the signal including direct emission from the shock-heated deuterium plasma have to be considered. Intense x-ray sources (signal shot experiments with 10^{12} photons), closely coupled geometry (large solid angles) and high detection efficiency (highly reflective Bragg crystals, MCP) are required to achieve a large number of scattered photons. Furthermore, the scattered x-rays must overcome the bremsstrahlung emission reaching up to 10^{-7} J(eV sr)$^{-1}$ corresponding to 10^4 detected photons per eV [19].

The expected scattering signal can be approximated from known x-ray yield values, scattering fraction and the efficiency of the detector setup. With sixteen 500 J beams incident onto the Saran foil approximately $(E_L/h\nu)\eta_x \approx 3.4\times10^{16}$ 2.96 keV Cl Ly-α photons are created with conversion efficiency $\eta_x \sim 0.2\%$ [103]. The collimating Ta pinhole then selects a solid angle of $\Omega_p = 0.06$ sr, letting through only the photons which will scatter from the deuterium shock. The attenuation of the x-rays in dense plasma is assumed to be $\eta_{att} \approx 1/e$ [19]. Thus, the number of photons capable of effectively scattering from the deuterium is $(E_L/h\nu)\eta_x(\Omega_p/4\pi)\eta_{att} \approx 5.8 \times 10^{13}$ photons. Based on the *LILAC* simulations, we should expect electron density of $n_e = 2 \times 10^{23}$ cm^{-3}. The thickness of the deuterium sample is $l = 0.05$ cm. Then with the Thomson cross-section $\sigma_T = 6.65 \times 10^{-25}$ cm^2, we obtain the scattering fraction $ln_e\sigma_T = 6.7 \times 10^{-3}$ and the number of scattered x-rays from the deuterium shock is then $\approx 1.0 \times 10^{11}$.

The intensity of the inelastic scattering is also attenuated by its probability proportional to factor $(1+\alpha)^{-2}$, see equation 2.36, where $\alpha = 0.9$ is the scattering parameter in this experiment [19]. The solid angle of the crystal spectrometer is $\Omega_d = 0.03$ sr and the reflection efficiency of the HOPG crystal is estimated to be $R \approx 50\%$. The detection efficiency of the MCP detector at ~ 3 keV is $\eta_d \simeq 0.01$ [19, 212]. The intensity of the scattered x-rays is therefore reduced by $(\Omega_d/4\pi)R\eta_d = 1.3 \times 10^{-5}$ giving the total number of collected photons $\sim 1.4 \times 10^6$ photons, which is comparable to experiments by Glenzer *et al.* [81, 101, 102], Gregori *et al.* [213, 214] and García Saiz *et al.* [105]. Fractional reductions in the scattering signal should be expected since the actual thickness of the deuterium shock is predicted to be around 100 μm.

The sensibility of the scattered signal levels was checked against a direct measurement of the Cl Ly-α line. Shots 58571 (full D_2 cryo shot) and 58574 (spectral calibration shot) from July 2010 were compared. The integrated signal scattered

from the deuterium shock was $\sim 2.2 \times 10^4$ counts. The signal levels measured on the spectral calibration shot were then scaled by the scattering fraction $n_e \sigma_T l$ and by 3^6 accounting for the total applied bias on the MCP strips of 300 V (3× reduction for every increase of 50 V). The two signals agreed within an order of magnitude with $\sim 4\times$ ratio, which provides an excellent agreement considering the shot-to-shot variations and uncertainties in the signal scaling.

3.5 Targets

A number of different targets were used during the experimental campaign at Omega. The primary experimental data was collected from cryogenic targets filled with liquid deuterium, which were employed in the x-ray scattering and VISAR/SOP experimental configurations. A set of various foil targets (plastic and aluminium) were also used in shots designed to check the alignment and brightness of the x-ray backlighter, spectral calibration and flatfielding of the GTS spectrometer response. This section will provide a detailed description of the composition and alignment of the different target types.

3.5.1 Foil targets

12.5 μm thick chlorinated plastic (Saran) foils were used for spectral calibration and backlighter shot size check. These thin plastic foils were 3 mm in diameter and supported by a square 3 mm × 3 mm plastic frame (50 μm thick Mylar) with a 2 mm diameter through hole mounted on a thin stock. The spatial backlighter profile was measured using foil targets placed in a place of a backlighter foil as a part of the cryo targets, i.e. with its surface normal to the H7 port ($\theta = 79.19°$, $\phi = 90°$) placed at 1500 μm from TCC towards H7. The spectral calibration of the GTS spectrometer was carried out using the CH foil targets with beam line (BL) 17 target surface normal ($\theta = 154.97°$, $\phi = 162°$), which allows a direct viewing of the rear surface of the backlighter from TIM 6. Both types of targets are shown in figure 3.15.

In the final shots in August 2011, the Saran was replaced with 5 μm thick Parylene D foil of the same size. Parylene D has much larger concentration of chlorine than Saran and can thus be made thinner while keeping the same intensity of Cl Ly-α emission, which improved the signal levels in the x-ray backlighter as the use of the thinner foil minimizes the absorption of the x-rays before they reach the deuterium layer. In addition free-standing 12.5 μm thick Al planar foils (3 mm diameter, or 3 mm × 3 mm square), mounted directly on a stock and placed at TCC with

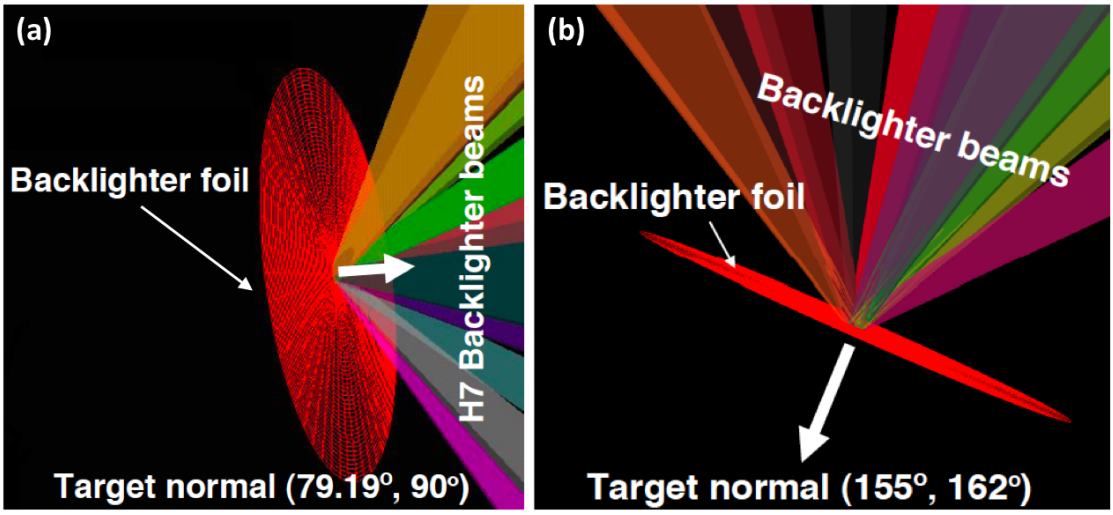

Figure 3.15: VisRad images of the chlorinated plastic foil (Saran) targets: the foils with H14 target normal (Y-TVS view), and (b) BL 17 target normal for spectral calibration (port H9 view).

BL 17 target surface normal, were used to check the flatfield response of the GTS spectrometer.

3.5.2 Cryogenic targets

The deuterium was kept inside a copper cryogenic cell, with 8 μm thick polyimide windows on either side, at pressure $P_0 = 20$ psi $\sim 1.38 \times 10^5$ Pa and cooled down to 18 K forming a liquid inside the target increasing its initial density to $\rho_0 = 0.175$ g/cm^3 [1]. The target was equipped with gold shields designed to block any direct x-ray emission from any other part of the target than the scattering channel, such that only scattered x-rays from the dense shock in the liquid D_2 can be measured. The cryogenic targets designed to hold and cool the deuterium fill to the liquid state were being developed and constantly improved throughout the campaign between March 2009 and August 2011. The targets were designed and build by Mark Bonino at the LLE. The schematic diagram of the cryogenic targets and the laser configuration for the XRTS and VISAR/SOP shots is shown in figure 3.16.

The main parts of the cryogenic targets are: Cu cooling finger connected to a Cu cryogenic cell, which holds the D_2 fill inside of it, two 8 μm Polyimide windows filling the 1.5 mm clear aperture in the Cu cell on the H7 and H14 sides confining the gas fill within (these are kept as large as possible to minimize the Cu ablation), 12 μm thick Saran backlighter foil (or 5 μm thick Parylene D) offset by 730 μm from the

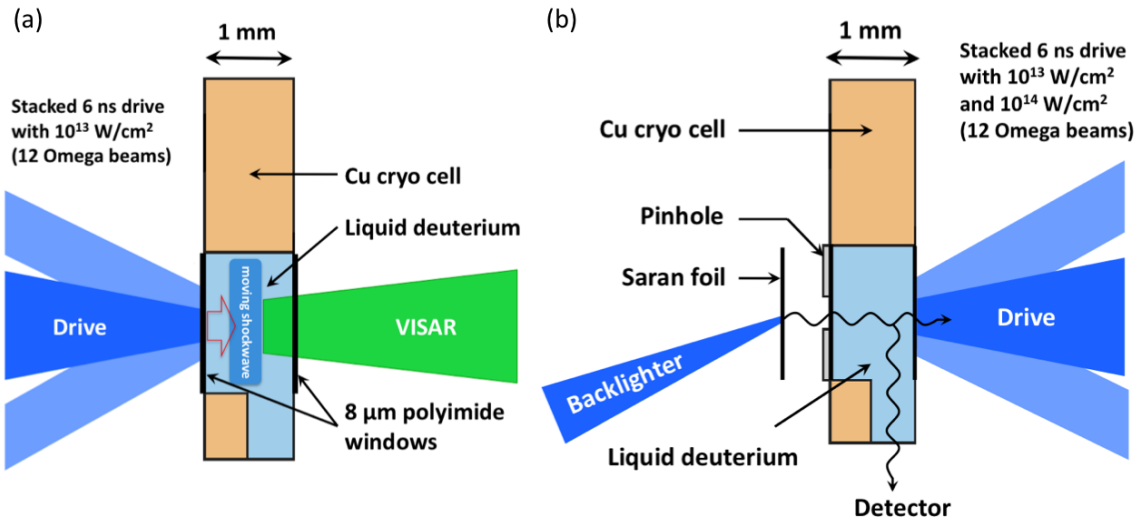

Figure 3.16: Schematic of the target set up with the laser drive with the VISAR laser (a) and the backlighter/scattering configuration (b). A constant intensity 6 ns laser drive incident on the CH ablator compresses and heats the material inside a planar layer of liquid deuterium target creating WDM. When VISAR is used, the laser drive 10^{13} W/cm^2 comes from the H7 side as the ASBO telescope is located in the H14 port (the backlighter foil and Ta pinhole are not needed in this configuration). In the XRTS experiment, sixteen tightly focused beams irradiate a Saran backlighter with 10^{16} W/cm^2 from the H7 side while the 10^{13} and 10^{14} W/cm^2 laser drive comes from the H14 side. The scattered Cl Ly-α emission scattered at 90° down a 500 μm wide scattering channel before it is detected with the XRFC outfitted with a HOPG crystal spectrometer [1].

H7 Polyimide window, 200 or 400 μm diameter Ta pinhole (designed to collimate the backlighter x-rays) positioned on the H7 side between the backlighter foil and plastic window of the cryo cell, 500 μm wide scattering channel machined into the bottom of the Cu cell pointing towards TIM 6 with a direct view of the TCC, Au (100 μm thick)/Fe (50 or 100 μm thick) radiation shields coated with 20 μm Parylene, fill tube connecting the the cryo cell with a gas reservoir (Cu coil/cylinder) bent out of the cell such that it does not obstruct the view of the scattering channel, and square wedges at the top and side of the cryo cells used for alignment purposes. A more detailed diagram of the cryo target is provided in figure 3.17.

On targets designed for the VISAR shots only, the backlighter foil and Ta pinhole were removed and additional sliver of Al coating was added to the edge of the Polyimide window in order to aid reflection of the VISAR laser during the diagnostics alignment, see figure 3.17. In some of the XRTS shots the scattering channel was

narrowed by adding a 250 μm thick Au slit plate intended to block direct emission from the corona as shown in figure 3.17. During the target cooling procedure a shroud surrounding the target is used to minimize the condensation of the residual particles inside the vacuum chamber depositing on top the target (particularly Ar atoms can be a particularly harmful contaminant of the x-ray signal if illuminated with lasers, x-rays or energetic particles). The shroud is extracted shortly before the target shot is taken.

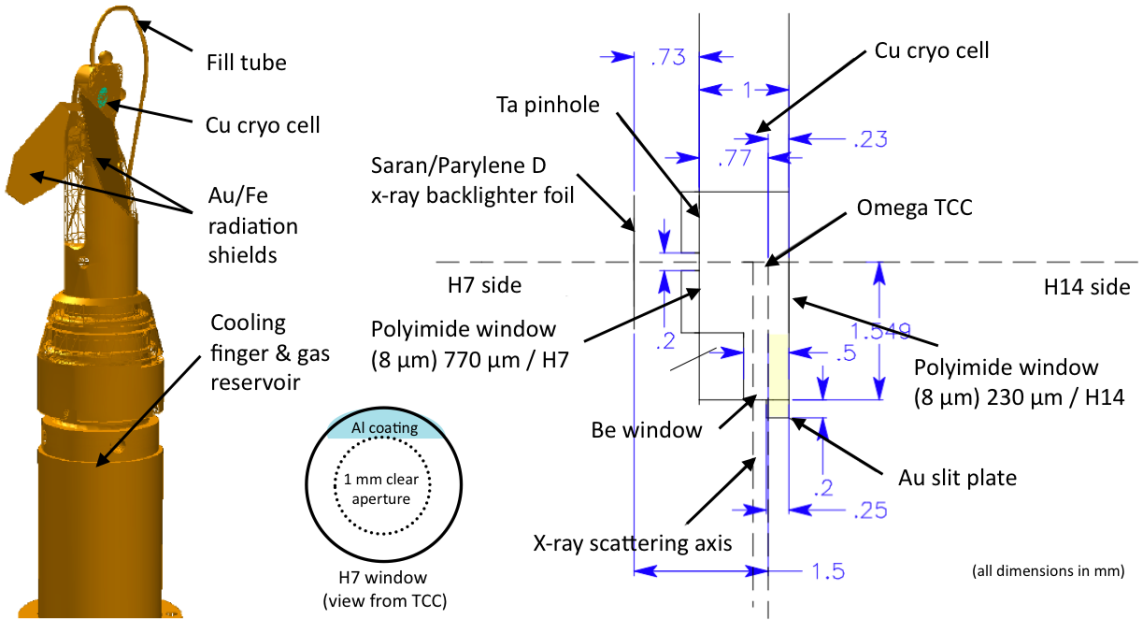

Figure 3.17: Schematic drawing of the D_2 cryogenic target used at Omega with dimensions.

The original design has been upgraded multiple times. Ideally, as the temperature of the Cu cryo cell is lowered below 20 K the liquid D_2 layer should start forming and one observes a bubble of deuterium gas passing across the view of the ASBO telescope as it escapes back through the fill tube into the gas reservoir only leaving the dense liquid within the target. The first targets have experienced problems with the phase transition from gas to liquid in the deuterium fill. It was thought that the deuterium fill was either lost or that the thermal coupling of the system was insufficient to form the liquid layer. Sometimes, less than half of the targets formed a liquid inside.

This was at first tackled by creating a larger gas reservoir (the Cu coil was replaced with a cylinder) that provided a better heat gradient between the gas reservoir and the cryo cell. The bolts used to hold the cell together were also removed to improve

the thermal contact within the cell itself. Further improvements were needed as it was found that liquid was forming inside the fill tube, which was cooling too rapidly, which was blocking the way of the escaping gas bubble during the condensation process inside the cell. On some shots the fill tube was wrapped in a copper foil connected to the heat reservoir and the temperature of the reservoir was slightly raised to create a smoother thermal gradient. The thermal contact between the fill tube and the Cu cell was finally improved, which avoided the formation of a vapour lock in the fill tube preventing the D_2 gas bubble from escaping and the liquid deuterium formed in majority of the targets.

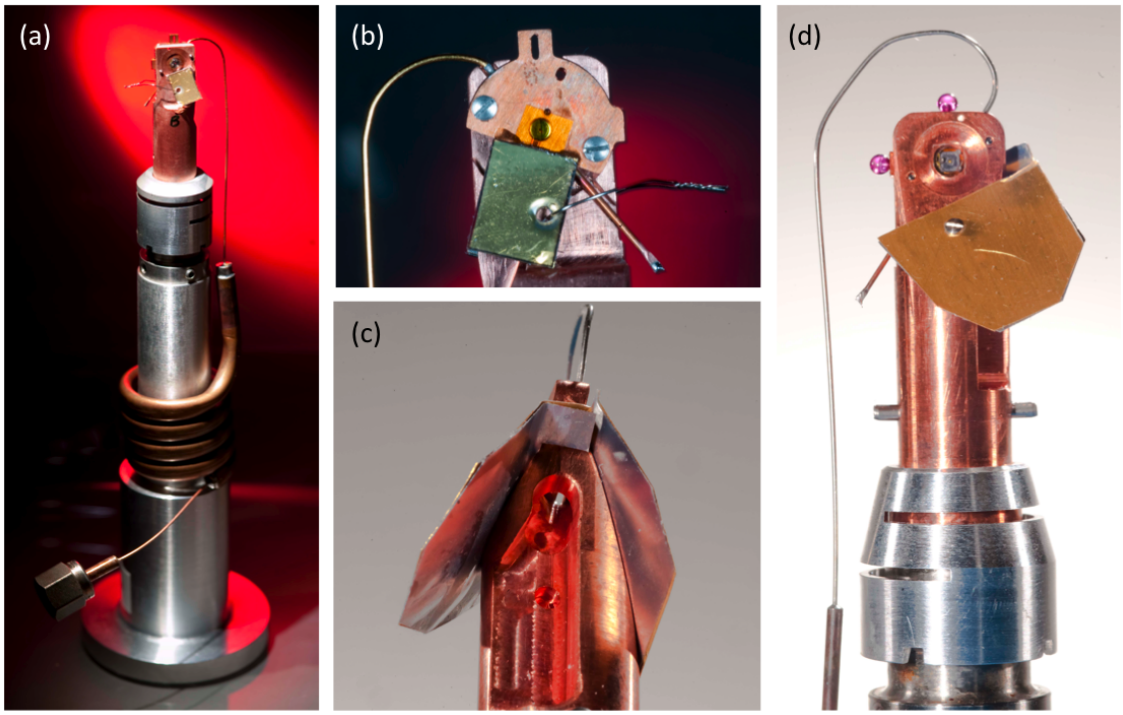

Figure 3.18: Photographs of the D_2 cryo targets: (a) older target (full size, 2009), (b) close up on cryo cell with alignment wedges (old target, 2009), (c) close up on scattering channel (new target, 2011), (d) new target with square wedges on the top and right side of the Cu cold finger structure replaced with ruby tooling balls, i.e. fiducial spheres used for improved target alignment (2011).

Furthermore, the Au/Fe shields designed to block direct view of the ablation plasma from the GTS spectrometer were enlarged in the later target designs. The final size of the shields was 20 mm $\times$ 20 mm. The original alignment square wedges were later replaced with larger spheres as alignment fiducials, which significantly improved the efficiency and reliability of the alignment process. The Prism VisRad

cadding software was used design and optimize the laser illumination of the targets. Since this software is capable of visualizing the target from any port on the Omega chamber, which is loaded into the base of the package, it has also been used to draw up the target alignment procedures using the X and Y target viewing system cameras. The photographs of the original and final cryo targets are shown in figure 3.18.

3.5.3 Target alignment procedures

All of the foil targets (CH and Al) are inserted in the vacuum chamber using the target positioner (TPS) 2 arm lowered from port 7 ($\theta = 27°$, $\phi = 270°$). The cryogenic targets with D_2 fill are the delivered using cryo carts 4 and 6 (planar cryo) from port 1 at the top of the chamber. The targets are aligned primarily using the X and Y target viewing system (TVS). The X TVS is located in port 75 ($\theta = 120°$, $\phi = 270°$) while Y TVS is in port 68 ($\theta = 111°$, $\phi = 0°$) and together they provide two near-orthogonal views of the TCC. The cryo targets are also viewed through the ASBO telescope looking from H14, which can be focused to view the Ta pinhole inside the target, which provides additional alignment reference (i.e. the pinhole is centered in the ASBO view) and is primarily used to view the phase transition of deuterium gas turning liquid while being cooled inside the target chamber. Figure 3.19 shows a schematic view of the alignment system with respect to the target chamber.

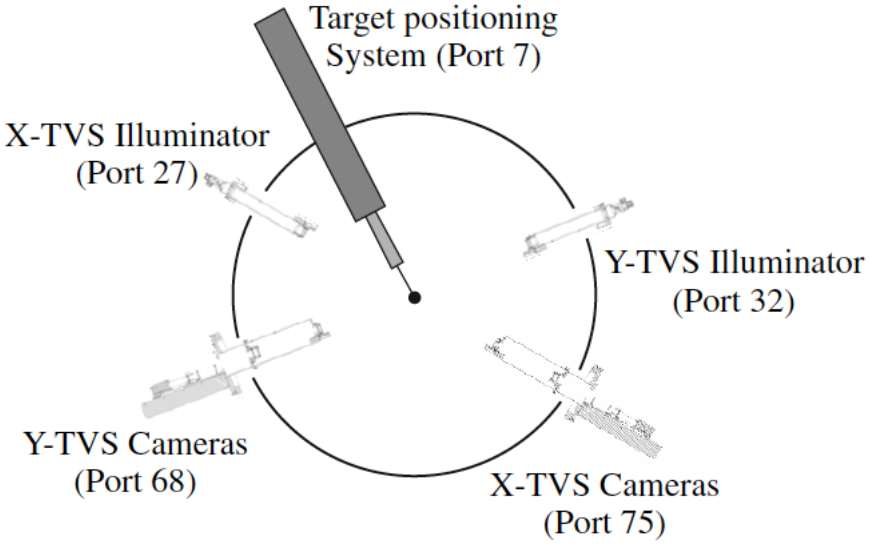

Figure 3.19: A schematic view of the target viewing system (TVS) on Omega, after Ref. [215].

Each foil target is first mounted on the TPS 2 and inserted to a position near TCC where its position is adjusted until the target disk is visible in the TVS narrow views. A series of rotations then follows such that the correct target normal is achieved. The TVS monitors are overlayed with alignment reticles obtained from VisRad (marked red over the screen), which need to correctly overlap with the shadow of the target recorded by the cameras in both X and Y views. The target is in a correct position only when both views agree with the alignment reticles. Figure 3.20 features the example of TVS views of the 3 mm square Saran disk targets, mounted on TPS 2, centered at 1.5 mm to H7, with target surface being normal to the TIM 6 / XRFC / GTS view axis ($\theta = 154.97°$, $\phi = 162°$), for spectral calibration shots. Similar procedures including individual TVS monitor reticles are provided for the H7 normal plastic foils used to check the spatial profile of the backlighter and Al foils on flatfielding shots.

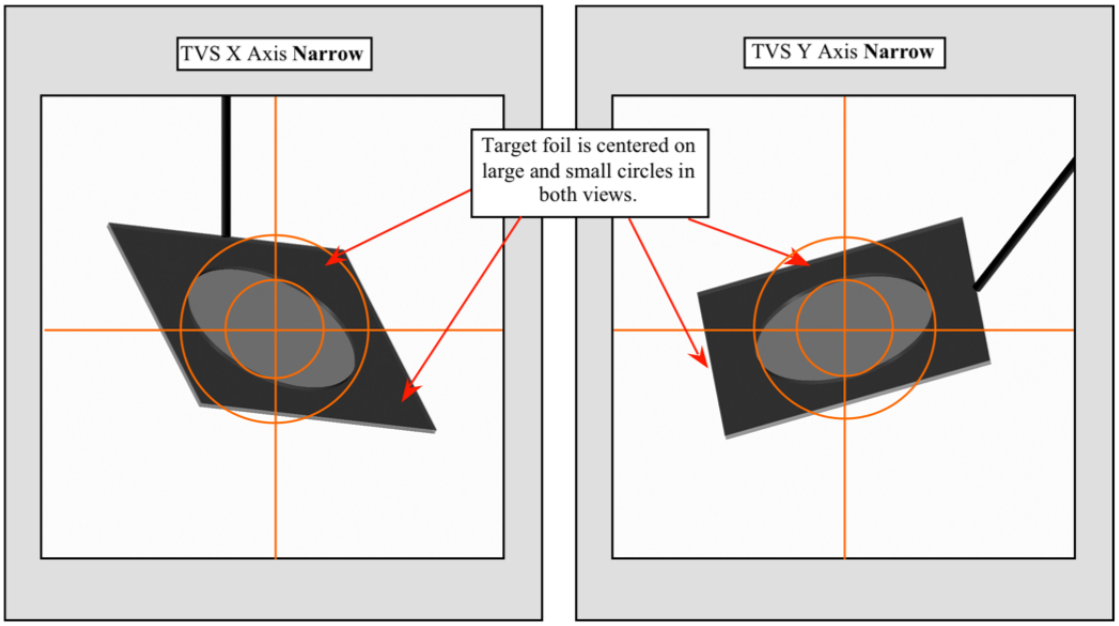

Figure 3.20: View of the TVS screens during the foil (surface normal to BL 17/TIM 6, $\theta = 154.97°$, $\phi = 162°$) alignment.

Each cryo target is individually metrologized (the distance between the alignment fiducials is measured) by the target fabrication staff and the output values are compared with the VisRad model prior the experiment. The metrologized values for each target are uploaded to the TVS alignment system monitors. A standard alignment procedure is carried out by the LLE staff on each shot to position the planar cryogenic

XRTS or VISAR/SOP targets, normal to the H7−H14 axis. The alignment procedure is started with a planar grid target mounted on TPS 2, inserted TCC, which is used to align the ASBO telescope in TIM 5. The ASBO interferometer view is used to align and focus the telescope on the center of the grid. Just like for the foil targets the alignment reticles are loaded on the TVS monitors once the cryo target is placed near the TCC. Cryogenic Target Handling System (CTHS) translation axes are used align the target to its reticles, as shown in figure 3.21.

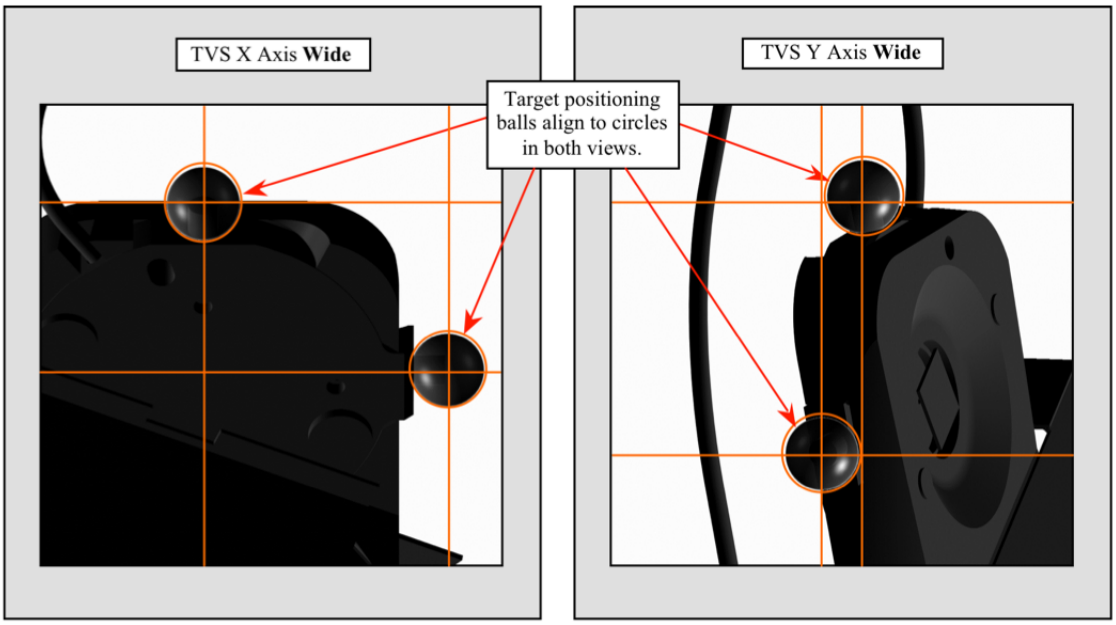

Figure 3.21: View of the TVS screens during the alignment of the new D_2 cryo targets.

The alignment is carried out with the condensation shroud lowered (target is being cooled at this point) and the target is viewed through windows along the X and Y TVS axes. Finally, the beamline reticles are loaded for the current shot configuration to confirm that all configured beams intercept the target. The ASBO telescope view is used to confirm target fill and carry out fine adjustments to the target alignment. Finally, the shroud is removed while final alignment adjustments are being made to correct for any possible target drift before the shot is taken.

3.6 Target shots

Shots with different target and beam configurations were taken as a part of the same campaign to ensure the completeness of the data sets and add a solid ground for analysis and conclusions to be drawn from the experiment.

Cryo VISAR shot

During the full VISAR shot, the planar deuterium filled is properly cooled to form a liquid layer inside. These cryo targets have the backlighter foil and Ta pinhole removed and the H7 side Polyimide window is coated with a thin Al layer for ASBO alignment. The target is driven by 12 drive beams from the H7 side while the VISAR probe beam is sent from port H14, where the ASBO telescope is located, to reflect from the critical surface of the moving shock front providing the velocity measurement. ASBO is thus run during the target shots. Lower intensity laser drive (10^{13} W/cm^2) was designed for the purpose of these shots in order to avoid "blanking" of the VISAR diagnostic, which is expected to occur at shock velocities exceeding ~ 70 km/s due to fast electrons and hard x-rays being formed that can cause ionization of the material before the shock front.

Cryo XRTS shot

The full XRTS planar cryo targets are used including chlorinated plastic backlingter foil and Ta pinhole placed just outside the H7 Polyimide window. Both the drive beams (from H14 side) and backlighter beams (from H7 side) are fired on the target and the GTS spectrometer collects the scattering spectrum from the shocked deuterium sample to infer n_e, T_e and Z. The laser drive in these shots is set to both intensities (10^{13} and 10^{14} W/cm^2) in order to probe different plasma conditions. The ASBO/VISAR telescope is used only to confirm the presence of liquid deuterium in planar cryo cell and fine adjustments in pinhole alignment as is retracted during the target shot.

Cold shot

A cold shot is a scattering test of an undriven target with an identical set up to the full XRTS planar cryo target. However, only the backlighter beams (from H7) side incident on the chlorinated plastic backlighter are switched on. GTS is set to collect background scattering signal, which should not show any features due to the low density and no ionization in the deuterium sample (the probability of a measurable scattering signal is negligible in this setting). The GTS data serves as a background reference for the scattering data from shocked deuterium.

Spectral calibration

A free-standing Saran/Parylene D foil was placed at TCC and irradiated with laser beams to calibrate the intensity and spectral position of the Cl Ly-α line on the GTS spectrometer. In order to measure the direct emission from the chlorinated plastic foil by the spectrometer a different beam configuration was used. The port directly opposite TIM 6 is laser no. 17 (BL 17), thus the Saran foil was tilted such that its surface is now normal to BL 17 to face TIM 6 and the original backlighter configuration was switched to beams 11, 13, 22, 20, 56, 68, 15, 17, 10, 26, 28, 31, 37, 46, 55 and 61 (500 J/beam focused 1500 μm from TCC). This shot was repeated on each shot day to provide a calibration for each unique configuration of the diagnostics such as the crystal or detector position, which may vary on the different days. A small systematic shift in position of the line from the full XRTS shots was observed which could be traced to the 1.5 mm shift in position of the signal source between the two types of shots.

Backlighter spatial profile check

These shots were used to check the spatial profile of the backlighter on each day, primarily to check the correct focus and pointing of the backlighter laser beams. The plastic (Saran or Parylene D) foil targets are illuminated by the H7 side beams just like in the deuterium shots. The primary diagnostics used in these shots were the x-ray pinhole cameras, which were checking for a small circular plasma ablation spot. If a star-shaped profile or a significant shift in position of the spot was observed, the beam alignment would have to be adjusted.

Flatfield check

These shots were designed to check the first order flatfield spatial response of the GTS spectrometer including the changes in reflectivity of the different areas of the HOPG crystal as well as the variations in sensitivity of the MCP/CCD detector. The Al foils placed at TCC were illumnated by beams coming from the BL 17 side, such that the radiation emitted from the rear surface of the target could be viewed directly from TIM 6, where the GTS spectrometer system is placed. The beams used were 25 and 64 with 250 J/beam (UV - FCC detune) and 200 μm spot size, focused at TCC.

Chapter 4

VISAR/SOP experiment at Omega

4.1 Introduction

The main traditional techniques used for the measurement of thermodynamic properties in WDM are shock velocity measurements made by velocity interferometer system for any reflector (VISAR) [69, 70] in conjunction with temperature measurement inferred from streaked optical pyrometry (SOP) [71]. VISAR has been used to obtain the pressure and density of the shocked deuterium by use of impedance matching (IM) techniques [109, 110, 20]. Such methods require a pusher with well-known EOS, usually quartz or aluminum, that transfers the shock created by laser ablation into the studied medium and is used to determine the Hugoniot through a known pressure standard [44, 107]. However, this standard has recently been questioned [112], suggesting that higher than expected errors in the density measurements of deuterium are possible, thus impacting the EOS studies in regime relevant to interiors of giant planets and ICF [20, 110].

This chapter presents a novel approach which bypasses the need for a pressure reference by a direct comparison of the shock velocity measured by VISAR and an independent SOP temperature measurement with theoretical models. It is found that the EOS based on *ab initio* simulations is the only one that can provide a consistent interpretation of both measurements. Of course, such consistency checks cannot prove that a given data and simulation set gives the correct conditions in the sample and produces a correct EOS. On the other hand, any inconsistencies clearly rule out the theoretical or simulation model applied. Moreover, consistency between experimental data and theoretical predictions strongly increases our confidence in the measured data. Here, we will apply this new method to deuterium under conditions where many EOS points from different experimental approaches already exist to prove that

the method is able to obtain EOS data without the uncertainties related to the use of pressure standards.

4.2 Experimental set up overview

The experiment was carried out on the 60-beam, 351 nm, Omega laser system [187]. The experimental set up is outlined in figure 4.1. The deuterium gas is fed into a copper cryogenic cell at pressure $P_0 \approx 1.38 \times 10^5$ Pa and cooled down to $T_0 = 18$ K undergoing a phase transition to the liquid state with an initial density of $\rho_0 = 0.175$ g/cm^3. The 8 μm thick polyimide window acts as an ablator when its surface is irradiated by 12 of the Omega beams which are staggered in pairs over a period of 6 ns in order to form a drive with an average intensity of 10^{13} W/cm^2. This launches shock waves into the planar deuterium target creating WDM conditions within the shocked material. The beams are evenly divided into two cones around the target normal at angles of 23.2° and 47.8° and smoothed with phase plates and polarization smoothing [188].

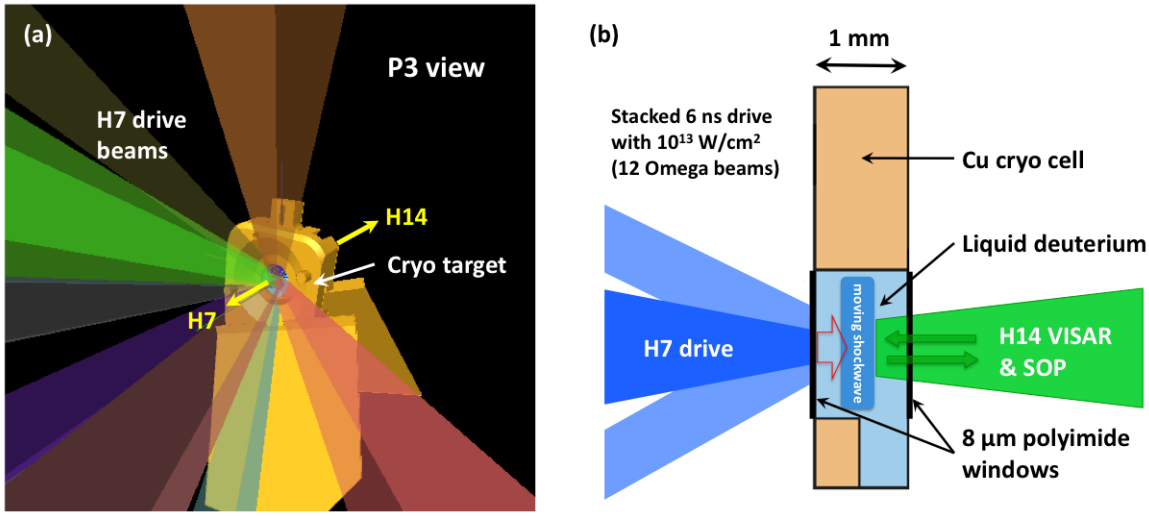

Figure 4.1: Schematic of the target set up with the drive and VISAR beam configuration: VisRad image of the port P3 view of the target with the H7 driver beams (a) and a schematic layout of the planar cryo cell with driver beams and diagnostics (VISAR,SOP) (b). The planar copper cryogenic cell is filled with D_2 gas and cooled down to 18 K forming D_2 liquid inside, which is then compressed by laser ablation from drive beams incident on the polyimide window.

VISAR was used to directly measure the shock velocity U_s in the deuterium sample. The line-VISAR system at Omega, operating at 532 nm, is a two interferometer

system such that the velocity measurements from the independent arms with different optical delays can be matched to remove the 2π phase discontinuities in fast shock measurements [70]. The SOP diagnostic recorded self-emission from the shock front in a narrow wavelength band around $\lambda_c = 684$ nm [71].

4.3 Hydrodynamic simulations

1-D *HELIOS* and 2-D *DRACO* hydrodynamic simulations were carried out to support the experimental planning (correct etalons in the VISAR interferometers had to be chosen based on the expected velocity) and to provide a reference for the analysis of the VISAR and SOP data [179, 180]. In the later simulations, obtained after the experiment where the shock velocity as measured by VISAR was found to be 16.9 ± 0.9 km/s jumping to 23.0 ± 1.0 km/s at 3 ns (see the following section for details), the actual laser power measurement from the P510 diagnostic was used as an input for these simulations to better reflect the plasma evolution during the stacked laser drive, see figure 4.2 (a). As is apparent from the figure the temporal overlap of the individual beams was not perfect resulting in a "spiky" intensity profile which could have an effect on the spatial and velocity profile of the shockwave. The summary of the *DRACO* and *HELIOS* results are shown in figures 4.2, 4.3 and 4.4.

Figure 4.2 shows the results of the 2-D *DRACO* simulations for the laser drive in shot 56736, when the VISAR and SOP were deployed during our experiments on Omega in January 2010. From the simulations, it is clear that initial velocities around 20 km/s should be expected. However, the 2D simulations seem to predict an erratic velocity profile at later times due to the sudden intensity variations in the laser drive. Another simulation was thus run to verify this result for the shock velocity using the 1-D *HELIOS* code. With the same laser input we obtained shock velocities reaching ~ 30 km/s, which just like in the 2-D simulations were significantly higher than the velocity measurement from VISAR, but the velocity profile was significantly smoother. It is known that 1-D and 2-D simulations always predict a higher shock speed because there is no route for the energy to diffuse along the missing dimensions. One thus has to reduce the energy input drive to reproduce the experimental values. The velocity fluctuations in the *DRACO* simulations seem to be happening on a very short time scale, which might be a result of the heat transport model, i.e. the choice of the flux limiter. *HELIOS* has a much smaller limiter than *DRACO*, thus the heat conduction is effectively more important in *HELIOS* which would smear out the spikes in the laser drive.

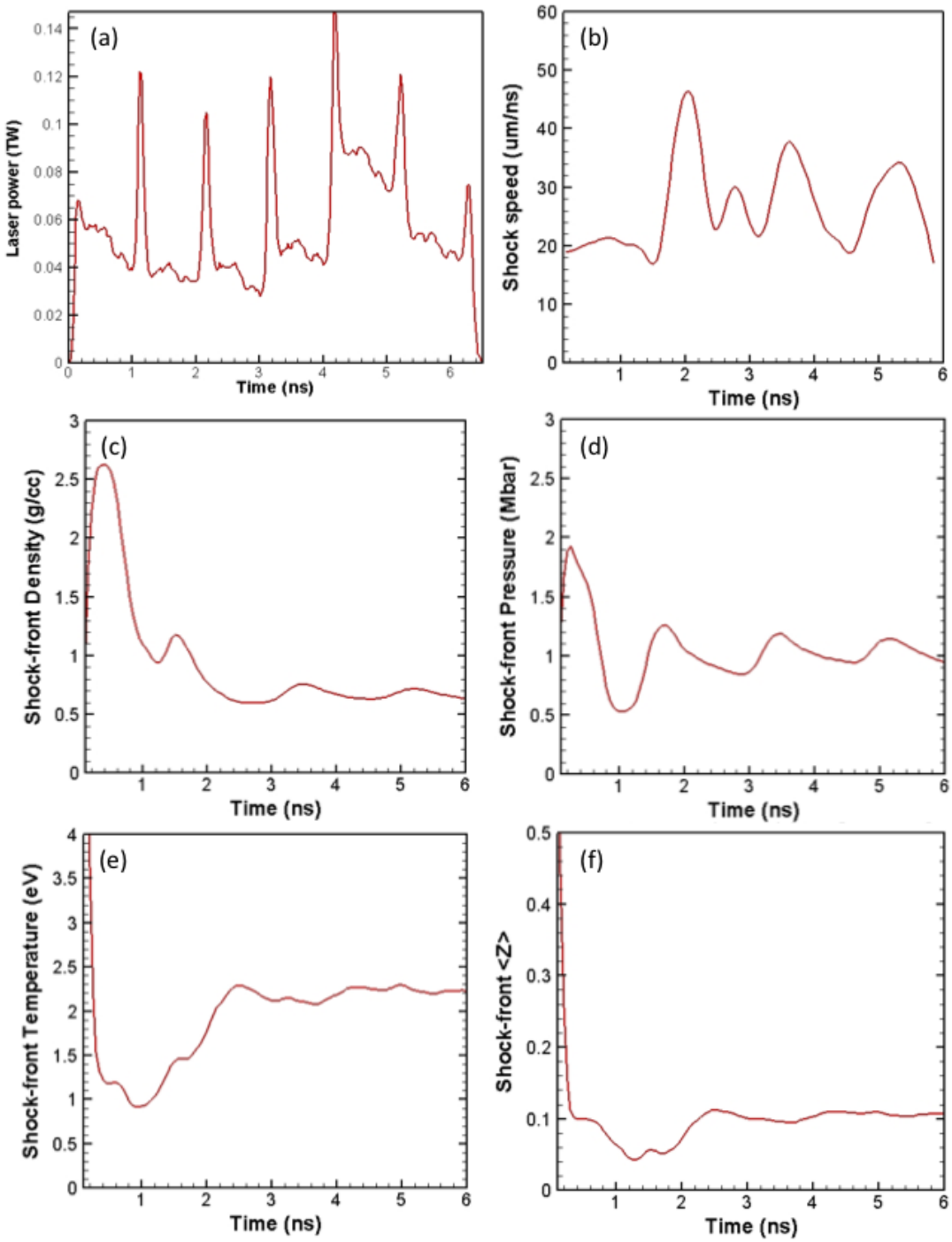

Figure 4.2: Results of 2-D *DRACO* hydrodynamic simulations: (a) laser power (Omega shot 56736) input, (b) shock-front speed, (c) density, (d) pressure, (e) temperature, and (f) ionization (Z).

In order to account for power losses due to reflection of the laser drive at the critical surface of the ablation plasma (expected $\sim 20\%$), the calorimetry measurement from

shot 56736 was multiplied by a constant of 0.75. The resultant shock velocity profile is much more steady and closer to the measured values with initial shock velocities around 18 km/s increasing to $\sim$ 25 km/s after 2 ns and temperatures of $\sim$ 2 eV. Nevertheless, these values were still slightly high. In order to match the measured shock velocity perfectly, the laser drive input was changed to a simple 6 ns square pulse at 3 TW/cm^2 ($\sim$ 70% reduction), producing much lower velocities ($\sim 16 - 19$ km/s) as shown in figure 4.3. In the *HELIOS* simulations the shock surface temperature was found to be around 1 eV, which is in better agreement with the SOP temperature measurement of $\sim$ 0.6 eV.

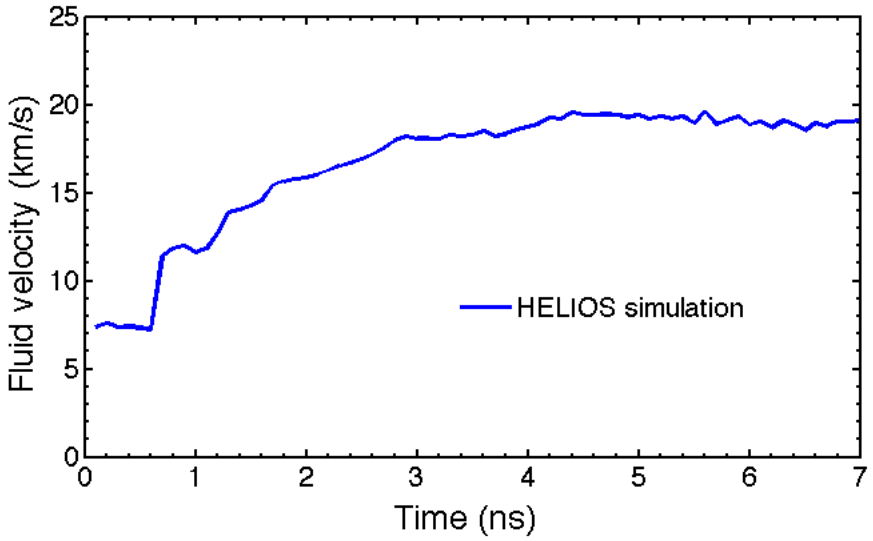

Figure 4.3: Shock velocity from 1-D *HELIOS* hydrodynamic simulations.

Furthermore, the predicted ionization state estimated from the 2-D *DRACO* simulations ($Z \sim 0.1$) is rather low for the temperatures $\sim$ 1 eV, which is a result of the use of the SESAME equation state, which is not expected to get the ionization right in this regime as it underestimates the quantum effects and pressure ionization in WDM. Another important consideration is the time the shock takes to break out from the CH/Polyimde ablator layer of the target. The 1-D *HELIOS* simulations estimate the time it takes to $\sim$ 0.6 ns, whereas raw data from the VISAR shows that the shock becomes reflective just over 1 ns after the start of the drive. Although this difference is not big, it is still significant and points out the fact that the simulations most likely overestimate the shock speed inside the CH layer.

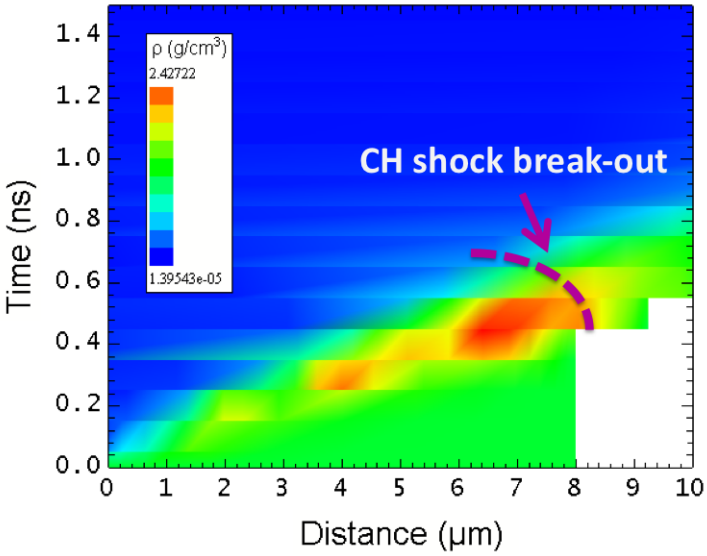

Figure 4.4: Mass density plot from 1-D *HELIOS*. Shock inside the CH (Polyimide) layer breaks out (8 μm distance) after about 0.6 ns, i.e. at this time all of the CH has been burned off. After this time the laser beams drive the deuterium directly.

4.4 VISAR analysis

The raw VISAR data contained a phase shift from which a plot of the shock velocity as a function of time could be extracted. This information was then used to obtain the values for additional thermodynamic conditions within the shock (WDM deuterium) including pressure and density. This section describes the whole VISAR analysis process step by step.

4.4.1 Phase extraction

The phase shift due to the Doppler effect in the VISAR laser probe was extracted from both interferometer arms (ASBO1 and ASBO2) using the XVIS program written in IDL by Dr. Damien Hicks from the Lawrence Livermore National Laboratory, which is a standard package used for VISAR analysis at the Omega laser facility [216]. This software is capable of loading multiple image formats and operates through a graphical interface aiding the data visualization and includes corrections for the camera rotation and shear in the image output from the streak camera. It is used to obtain the unwrapped phase from both the data and reference (background) images/fringe patterns which are then used to obtain the absolute phase shift and thus the shock velocity.

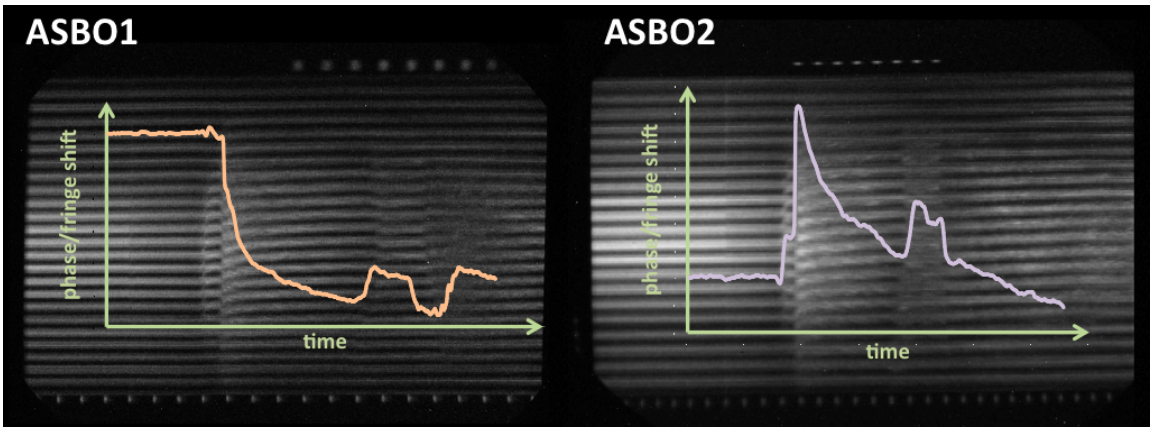

Figure 4.5: Raw VISAR data in the form of HDF images from both interferometer arms (ASBO1 and ASBO2) were input into XVIS (IDL program developed by Damien Hicks), used to calculate the wrapped phase (fringe shift) across a selected area. This was done for both the data and reference (background) images. This phase contains 2π discontinuities that still need to be removed to obtain the correct shock velocity. The light dots on the top and bottom of each trace are the timing fiducials.

XVIS calculates the phase shift in the fringe pattern over a selected area of the image. Care must be taken that the selected area starts and ends at a centre of a fringe (horizontal) and the largest possible number of fringes should be selected to improve the statistics of the phase extraction procedure. The same area must be selected in both the data image and the reference (background streak with no velocity shifts). The phase is extracted through the Fourier transform method (FTM) first developed by Takeda *et al.* [208]. The recorded fringe intensity pattern can be represented as a real function:

$$S(x,t) = B(x,t) + A(x,t)\cos[\Delta\phi(x,t) + 2\pi f_0 x + \delta_0], \tag{4.1}$$

where $B(x,t)$ is the slowly varying background intensity and $A(x,t)$ represents the fringe amplitude such that $|A| \leq B$ [70]. The term $2\pi f_0 x + \delta_0$ corresponds to the linear phase ramp of the background fringe pattern with spatial frequency f_0 and phase offset δ_0 due to imperfections in the interferometer optics and distortions introduced by the streak camera [70]. The desired information about the velocity of the shock is then contained in the phase modulation superimposed on the carrier wave $\phi(x,t)$. Taking the spatial Fourier transform of equation 4.1 yields:

$$s(f,t) = b(f,t) + c(f - f_0, t) + c^*(f + f_0, t), \tag{4.2}$$

which effectively separates the background function $b(f,t)$ from the phase information contained in c. In the next step of the FTM analysis an appropriate filter is applied to select the c-lobe which contains the positive frequencies. The reverse Fourier transform then generates a complex function:

$$D(x,t) = C(x,t)\exp[2\pi i f_0 x + \delta_0]. \tag{4.3}$$

The *wrapped* phase function W bound by the interval $[-\pi,\pi]$ is then extracted:

$$W[\Delta\phi(x,t) + 2\pi f_0 x + \delta_0] = \arctan[\mathrm{Re}(D), \mathrm{Im}(D)]. \tag{4.4}$$

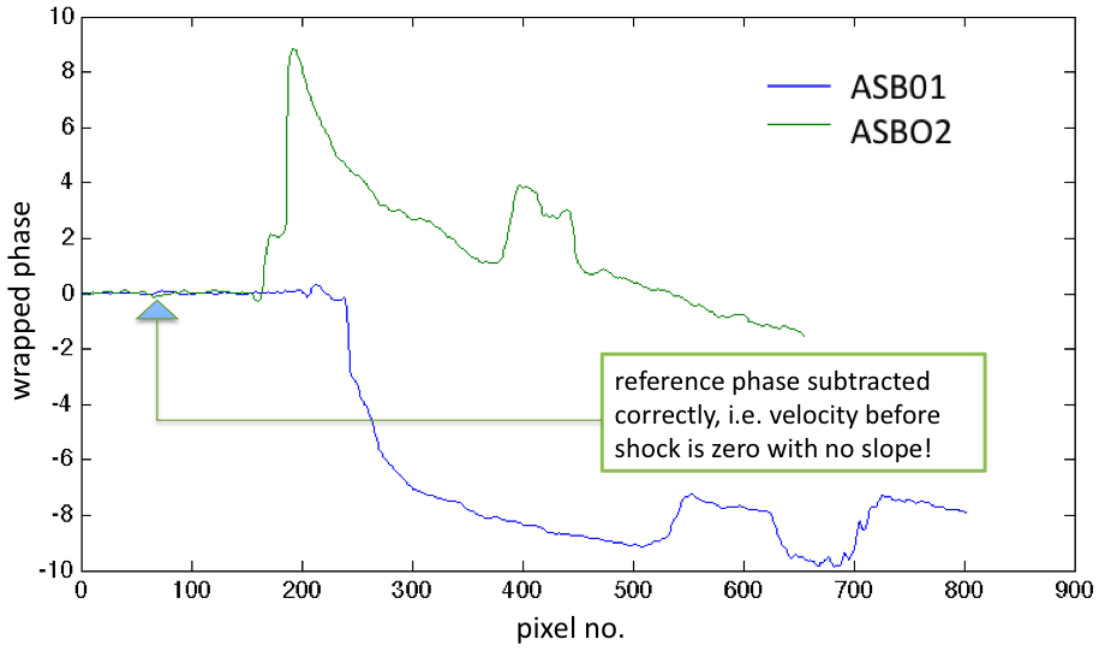

Figure 4.6: Wrapped phase from two interferometer arms ASBO1 and ASBO2 extracted using the XVIS program during the analysis of Omega shot 56736 in Jan 2010. At this stage the 2π phase jumps have not yet been removed and the correct time base is not yet imposed on the plots, i.e. the phases do not overlap yet.

Finally, phase shift due to the moving shock front is extracted by subtracting the background $2\pi f_0 x + \delta_0$ and removing the 2π discontinuities resulting from instantaneous fringe jumps across many periods. Figure 4.5 shows raw VISAR data from shot 56736 (Jan 2010) overlaid with the *wrapped* phase extracted from the XVIS analysis. During the analysis in this work, the phase profile was extracted from both data and reference using XVIS. These data sets were then input into a Matlab script used to subtract the background, remove the 2π discontinuities, calculate the shock velocity

and set a correct time base. A plot of the background subtracted phase is shown in figure 4.6. It should be noted that XVIS outputs values for $\varphi = \Delta\phi/2\pi$, i.e. the actual number of fringes shifted.

4.4.2 Time scale

The timing fiducial markings on the top and bottom of each streaked VISAR trace are used to identify and plot the correct time scale for the velocity data. The bottom time fiducials mark the start of the laser drive at $t = 0$ (ASBO1: $t_0 = 0.4$ ns and ASBO2: $t_0 = -1.15$ ns) while the trail of top timing fiducials is spaced by $dt = 0.506$ ns. Figure 4.7 shows marks both sets of timing fiducials as well as the direction of time flow on the ASBO 1 and 2 traces. Note that these images are reversed from top to bottom effectively swapping the positions of the timing fiducials.

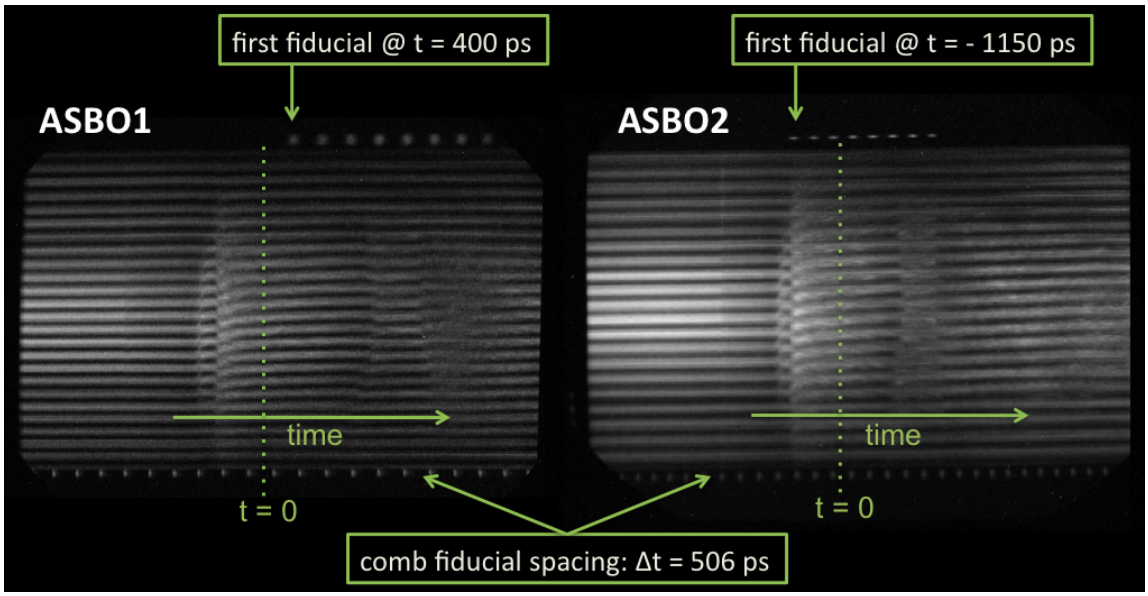

Figure 4.7: Raw VISAR streaked images from both interferometer arms (ASBO1 and ASBO2) with the timing fiducial and the direction of the temporal axis marked on them. The marked time $t = 0$ refers to the absolute laser time (Omega facility), thus since the laser drive started at $t = -3$ ns, $t = 0$ corresponds to 3 ns.

The lineouts of the fiming fiducials are shown in figure 4.8. The position of t_0 (x_0) was found at pixel no. 570 for ASBO1 and 445 for ASBO2 respectively. To maximise the accuracy of the pixel spacing of the top time fiducial trail, the value is averaged over all dots across the whole image: $\Delta x = (x_1 - x_2)/(\text{no. of peaks} - 1)$, where x_1 and x_2 are the pixel number positions of the first and last fiducials in the trail respectively. The streak camera sweep rate $a = dt/\Delta x$ is then found to be

0.0106 ns/pixel for ASBO1 and 0.0158 ns/pixel for ASBO2. The temporal axis for each interferometer arm is then given by $t_{1,2} = a_{1,2} \times (\text{pixel no.} - x_{0_{1,2}}) + t_{0_{1,2}}$.

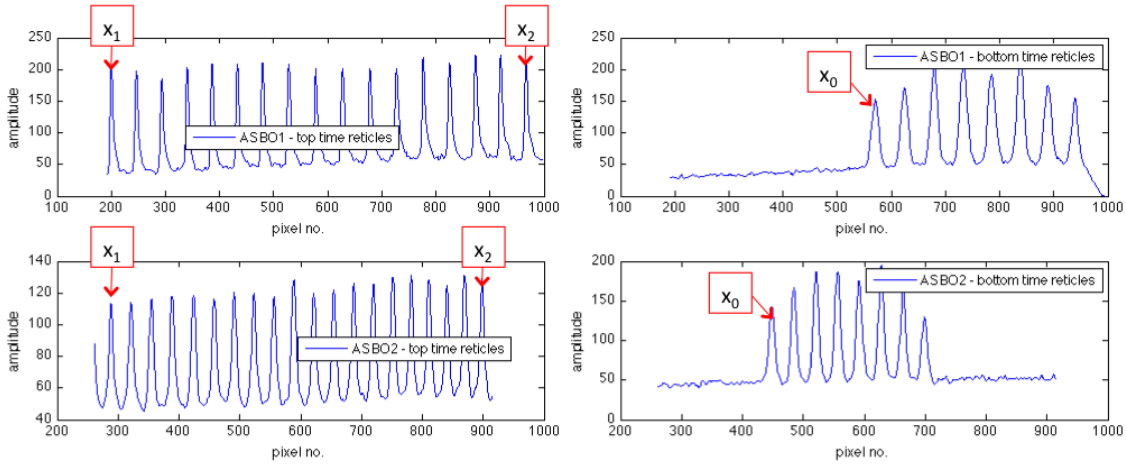

Figure 4.8: Lineouts of top and bottom timing fiducials for ASBO1 (top plots) and ASBO2 (bottom plots) with marked positions of x_0 (t_0), x_1 and x_2.

4.4.3 Velocity measurement

It is at this stage when the 2π discontinuities are removed from the phase output of XVIS. As described in the VISAR set up section in the previous chapter, etalons with specific values of velocity per fringe (VPF) are chosen for this experiment based on anticipated shock velocities. The chosen etalons for ASBO 1 and 2 had $VPF_1 = 8.74$ km/s/fringe and $VPF_2 = 14.1$ km/s/fringe. The phase shift is also corrected by the refractive index of deuterium ($n_{D_2} = 1.1379$), thus $VPF_{D_2} = VPF/n_{D_2}$. Both interferometer arms are looking at the same shock and therefore they ultimately have to measure the same shock velocity. Also, the 2π discontinuities happen at discrete jumps corresponding to one fringe period. Thus the velocity can be found from the following relationship:

$$v_{1,2} = \left(\frac{\Delta\phi_{1,2}}{2\pi} + m_{1,2} \right) \times \frac{VPF_{1,2}}{n_{D_2}} = \frac{VPF_{1,2} \cdot (\varphi_{1,2} + m_{1,2})}{n_{D_2}}, \tag{4.5}$$

where $m_{1,2} = 1, 2, 3, \ldots$ are integers varied until the condition $v_1 = v_2$ is satisfied. The 2π discontinuities were matched with $m_1 = 2$ and $m_2 = 1$ giving initial shock velocity of 16.9 km/s which increases to $\sim$ 23 km/s at $\sim$ 2 ns from the start of the laser drive, see figure 4.9. Another possible velocity match for the two interferometer arms happened at the second bump in velocity corresponding to $\sim$ 50 km/s (instead

of 23 km/s), which was discarded as such velocities were not possible for such a low intensity laser drive (maximum velocities predicted by the hydrodynamic simulations reached up to ~ 30 km/s, which is already an overestimate).

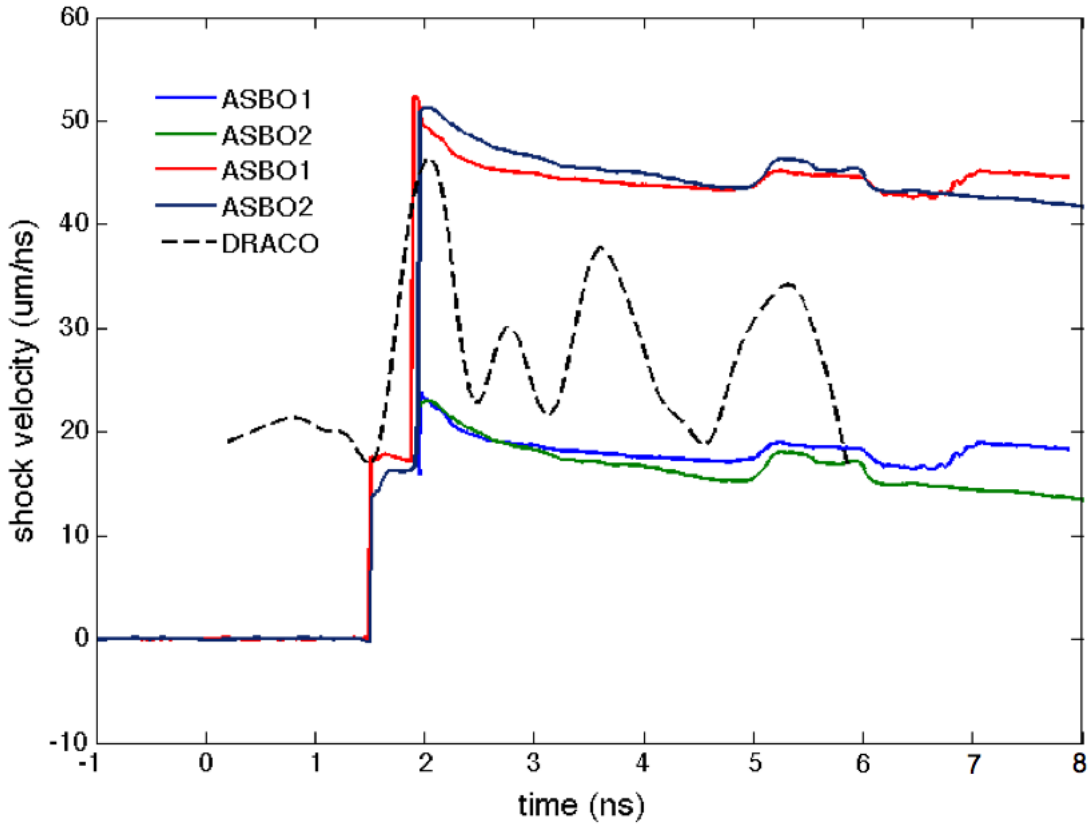

Figure 4.9: Calculated velocity profiles from phase shift obtained for Omega shot 56736 (Jan 2010). Two possible velocity matches of the ASBO 1 and 2 interferometer arms are shown along with 2-D *DRACO* simulations. The lower velocity trace is favoured as it is more probable given the intensity of the drive.

Error analysis

Following the equation 4.5 for shock velocity, assuming independent error contributions from φ, VPF and n_{D_2}, we obtain the error on the velocity trace from the following expression:

$$\sigma_v = \sqrt{\left(\frac{VPF}{n_{D_2}} \cdot \sigma_\varphi\right)^2 + \left(\frac{\varphi + m}{n_{D_2}} \cdot \sigma_{VPF}\right)^2 + \left(\frac{VPF(\varphi + m)}{n_{D_2}^2} \cdot \sigma_{n_{D_2}}\right)^2} \tag{4.6}$$

The output from XVIS also provides the upper and lower limit on phase $\varphi = \frac{\Delta\phi}{2\pi}$ such that one standard deviation of the phase trace is $\sigma_\varphi = (\varphi_{upper} - \varphi_{lower})/2$. The second term in equation 4.6 is small since the error on VPF $\approx 5\%$ giving $\sigma_{VPF} \approx 0.05$, this error is associated with the resolution of the streak camera, i.e. the streak camera can only resolve fringe jump within 5%. The third term is then associated with error on the measurement of deuterium refractive index, which was considered to be $\sim 1\%$. The final error trace was then calculated using equation 4.6 and plotted in figure 4.15. The measurement of the initial shock velocity was thus 16.9±0.9 km/s increasing to 23.0±1.0 km/s.

4.4.4 Hugoniot plots

Additional thermodynamic conditions including the shock pressure P_s and density ρ_s were obtained from the velocity measurement from VISAR by applying the single shock Hugoniot equations, which must be satisfied for a set of know initial conditions ρ_0, P_0 and T_0, to various EOS tables. Only the initial velocity of 16.9 ± 0.9 km/s was used for this analysis as this value is certain to lay on the Hugoniot with known initial conditions, the second velocity is subject to intensity variation in the laser drive which could result in additional effects such as preheat of the unshocked material before the shock changing the initial conditions to unknown values.

This analysis is based on three different theoretical EOS models: i) the SESAME tables [17], widely used for ICF applications; ii) the model by Saumon and Chabrier (S&C) [122, 123] that spans a wide range of conditions and is often used for astrophysical purposes; and iii) density-functional molecular dynamics (DFT-MD) simulations of fluid hydrogen [37, 38, 171]. The details of these tables were described in section 2.4. The Hugoniot relations are derived from jump conditions stating that mass flow (equation 4.7), momentum (equation 4.8) and energy (equation 4.9) are conserved across a single shock front [210]. The equations in this form are independent of the

EOS model used, which enter into the Hugoniot problem through the relationship for the internal energy E.

$$\rho_0 U_s = \rho(U_s - U_p) \tag{4.7}$$

$$P - P_0 = \rho_0 U_s U_p \tag{4.8}$$

$$PU_p = \frac{1}{2}\rho_0 U_s U_p^2 + \rho_0 U_s (E - E_0) \tag{4.9}$$

The particle velocity U_p (velocity of the material behind the shock front, i.e. the *piston velocity*) in shock compression experiments is usually found from the measured shock speed U_s and the EOS of a standard material by IM [217, 210]. The Hugoniot relations $P = \rho_0 U_s U_p$ and $\rho = \rho_0 U_s/(U_s - U_p)$ are then used to determine the pressure and density of the shocked material [42, 109, 110, 108]. As no pressure standard pusher (quartz or aluminum) was used in our set up, the conditions behind the shock front could not be inferred directly from these equations as U_p is unknown. Instead, we calculate them by comparing with an EOS table (SESAME tables no. 5263 and 5265, S&C, DFT-MD). The S&C and DFT-MD tables apply to hydrogen and were adjusted to deuterium by accounting for the mass difference between the isotopes.

Two SESAME tables for deuterium were compared in this work: table 5263 is the original calculated EOS based on the chemical model assumptions, more recently table 5265 was released. This table is no longer a pure theoretical model, but was modified to satisfy new experimental measurements, including the diamond anvil data of Loubeyre *et al.* [119, 120] and Hugoniot data of Knudson *et al.* [44], etc. The Hugoniot was significantly softened and there were many changes to the phase transitions in molecular deuterium. It should be pointed out that the new impedance matching results by Knudson [112], which push the Hugoniot data back towards a "stiffer" curve, were not included.

The conditions behind a single shock are inferred from the tabulated EOS by finding combinations that satisfy the Hugoniot relation for the specific initial conditions (ρ_0, P_0 and E_0):

$$E - E_0 + \frac{1}{2}(P + P_0) \times \left(\frac{1}{\rho} - \frac{1}{\rho_0}\right) = 0. \tag{4.10}$$

This equation is derived from equations 4.7, 4.8 and 4.9 for a single shock and is thus in this form independent of the EOS. The exact values along the Hugoniot curve for each EOS table are found through an interpolation routine written in Matlab.

Since the shock velocity in this case is well below 100 km/s, radiative effects in the energy balance are not important and the energy conservation holds in this case with no corrections [210]. Sets of U_p and U_s values along the Hugoniot are then compared to the VISAR velocity measurement which identifies the correct set of shock conditions on each Hugoniot:

$$U_s = \frac{P - P_0}{\rho_0 U_p} \tag{4.11}$$

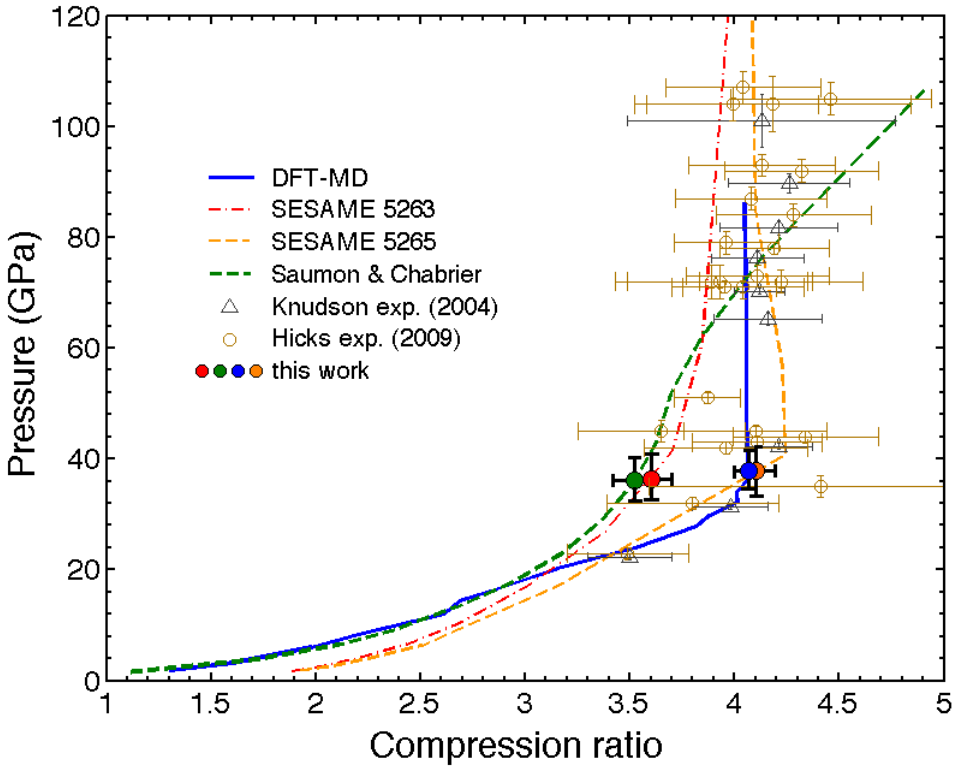

Figure 4.10: Hugoniot curves as function of compression ratio ρ/ρ_0 calculated from the SESAME 5263 table [17] (red dot-dashed line), SESAME 5265 (yellow thin dashed line), S&C [122, 123] (green thick dashed line) and our DFT-MD [37, 38] (solid blue line) EOS models for deuterium. The initial conditions are: $P_0 \sim 1.38 \times 10^5$ Pa, ρ_0 = 0.175 g/cm^3 and T_0 = 18 K. The conditions extracted from each model for the shockwave traveling at U_s = 16.9 km/s are marked by red, green, and blue circles, respectively. The error bars on these points are propagated from the uncertainty in the VISAR measurement by satisfying the Hugoniot condition for the extreme velocity values.

Figure 4.10 shows Hugoniot curves calculated from the three EOS models. The DFT-MD Hugoniot as shown here is in good agreement with other DFT-MD results [218, 124]. For each EOS, we plot the point on the corresponding Hugoniot where

the predicted U_s is equal to the experimentally measured value. The data show that the greatest differences between the models indeed occur near the shock speed investigated ($U_s = 16.9 \pm 0.9$ km/s). At this U_s, the models yield similar pressures but quite different compression ratios. In particular, the EOS based on DFT-MD is much softer. Each of the densities for a particular EOS along with the associated values of P_s and temperature T_s are summarized in table 4.1.

4.4.5 Spatial profile of the shock

It is possible to obtain an accurate measurement of the shock size in 1-D from the line-VISAR trace since the ASBO telescope is exactly focused onto a target grid prior the experiment defining its resolution and width of the view. The telescope view is calibrated to 16 grid spacings, each of which has width of 63.5 μm giving the full ASBO view (edge-to-edge) = 1016 μm. From the laser set up (using phase plates) we know the laser spot size is about 600 μm in diameter. Traces from ASBO 1 and 2 observe two shock fronts, see figure 4.11. The first shock was significantly curved, probably due to irregularities in laser beam pointing and/or slight target misalignments which could result in non-uniform spot size. Otherwise, the shock in D_2 was very flat. The full view of ASBO1 was 720 pixels and the first shock profile spanned across 363 pixels $\approx$ 508 μm, the second shock profile was 570 pixels $\approx$ 798 μm. ASBO2 view was 715 pixels, where first shock and second profiles were 405 pixels $\approx$ 567 μm wide 610 pixels $\approx$ 854 μm respectively. Thus, the shock diameter was found to grow from 530 ± 50 μm to 830 ± 30 μm.

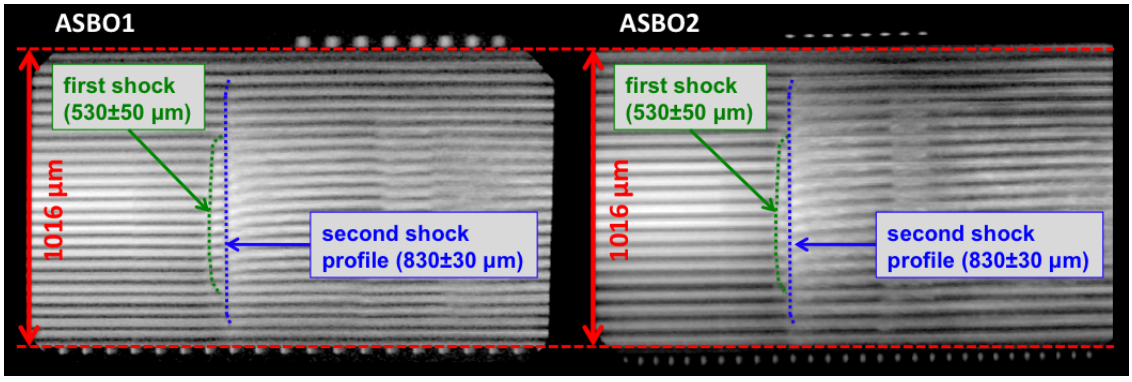

Figure 4.11: Raw data from the Omega VISAR system (shot no. 56736) showing variable shock front profile. The total width of the field of view in both ASBO 1 and 2 is 1016 μm.

4.5 SOP analysis

The streaked optical pyrometer was used to record a temporal evolution of the self-emission at a narrow wavelength band ($\sim 590-780$ nm) centered at $\lambda_c = 684$ nm. In the case of a highly opaque emitter the self-emission from the surface approaches the limit of Planckian (black body) radiation and the emission intensity at a known wavelength can be used as an accurate measure of temperature [210, 71]. The temporally resolved SOP data can also be used in conjunction with the VISAR trace to verify the temporal evolution of the laser drive plasma formation. 10 ns sweep window was chosen to provide the maximum resolution across the entire 6 ns laser drive.

4.5.1 Time scale

The temporal axis of the SOP trace was determined using the same procedure as described in section 4.4.2. The log plot of the streaked image is shown in figure 4.12.

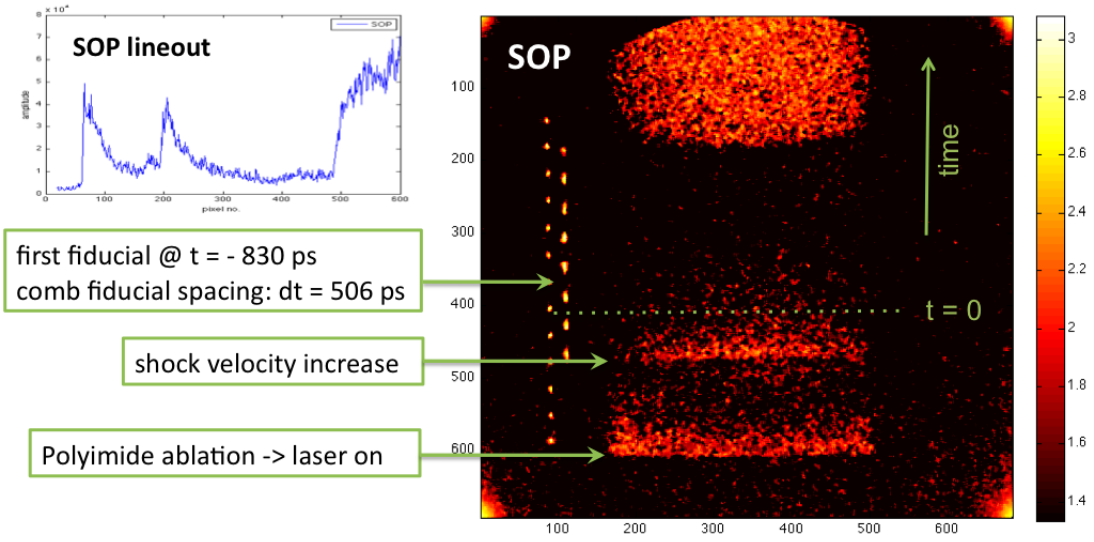

Figure 4.12: Log plot of the raw data (HDF image) from the Omega SOP system (shot no. 56736) showing shock self emission at $\sim 590-780$ nm (red filter). The image is plotted over pixel number and the time $t = 0$ refers to the absolute laser time, thus since the laser drive started at -3 ns, $t = 0$ corresponds to 3 ns. Inserted image shows a full window intensity lineout across the SOP trace vs. pixel number.

The position of x_0 was found at pixel no. 205 in the SOP trace, corresponding to $t_0 = -830$ ps (the error in the position of the timing fiducials is $\sim \pm 100$ ps). Just like in the VISAR case, the pixel spacing of the temporal fiducials was averaged over all dots across the whole image: $\Delta x = (x_1 - x_2)/(\text{no. of peaks}-1)$, where

x_1 and x_2 are the pixel number positions of the first and last fiducials in the trail respectively. The SOP camera sweep rate $a_{SOP} = dt/\Delta x$ is then found to be 13.8 ps/pixel, where $dt = 506$ ps. The temporal axis for each interferometer arm is then given by $t = a_{SOP} \cdot (x - x_0) + t_0$, with x being the pixel number.

4.5.2 Temperature measurement

The SOP data can be used to measure the temperature of the shocked material by comparing the measured emission intensity with a black body radiation distribution. For the conditions in this experiment, the shock wave is optically thick to visible light. The value for absorption/emission Planck mean opacity $\kappa_P \cong 2\times10^6$ cm^2/g was obtained from 1-D *HELIOS* simulations (for the lower intensity drive at 10^{13} W/cm^2) [179, 219]. The transmission of radiation is then given by:

$$I(x) = I_0 e^{-\kappa_P \rho x}, \tag{4.12}$$

which then for the given density of ~ 0.72 g/cm^{-3} and shock thickness $x \sim 0.005$ cm gives $I(x) = e^{-7200} \approx 0$, which means that the optical depth of this shock is large and no optical radiation can transmit through it. In the first order approximation, the brightness temperature of the self-emission radiation therefore approaches the temperature of the material making the black body distribution appropriate for shock temperature measurement [210, 220]. Similar methods have proven to be reliable temperature diagnostics for shock-compressed deuterium [113, 114].

The SOP camera records a calibrated intensity trace in ADU units, where signal in a single pixel is given by:

$$I = \frac{B\Delta x W_s \Omega_{lens}}{\eta M^2} \int_{\text{all }\lambda} d\lambda T_x(\lambda) L_s(\lambda) SR(\lambda), \tag{4.13}$$

where T_x is the product of the transmission/reflection spectrum of the optical elements in the SOP system and $SR(\lambda)$ is the wavelength-dependent sensitivity of the streak camera measured in [ADU/(energy/pixel)] [71]. The integration constant is then composed of binning of the CCD B (i.e. in our case $B = 3$ for 3×3 binned CCD), pixel size $\Delta x = 13.7$ μm, slit width $W_s = 100$ μm, solid angle Ω_{lens} of the $f/3.3$ telescope, streak camera sweep rate $\eta = 1/a_{SOP}$ (pixel/ps) and the system magnification $M = 20$ [71].

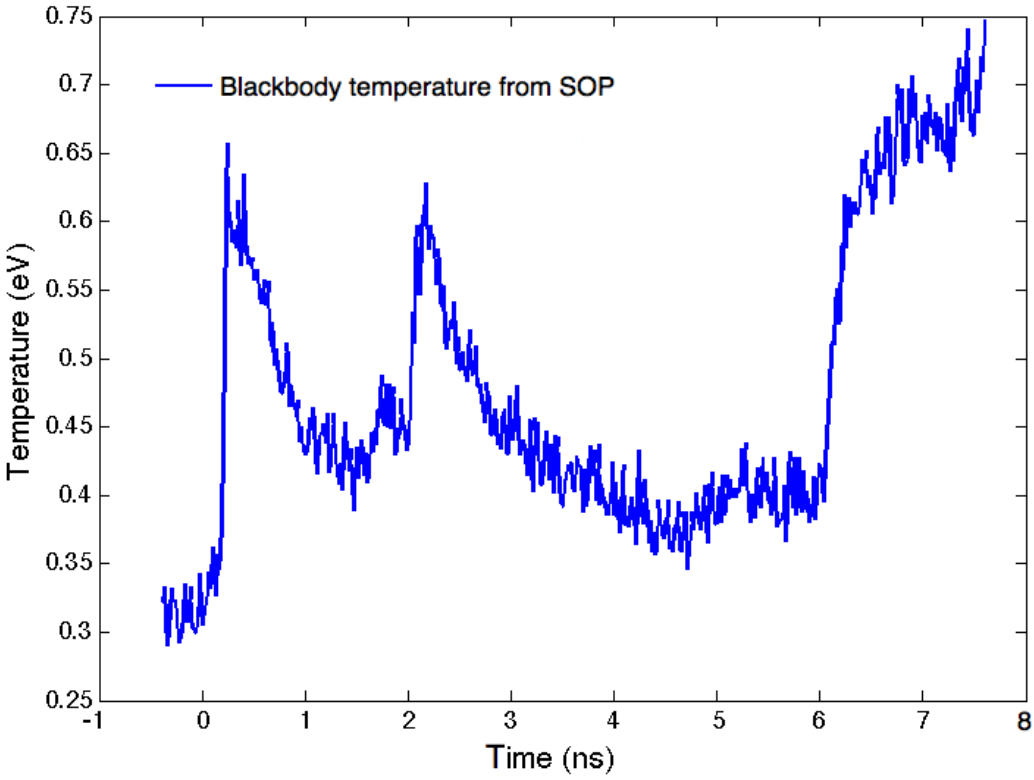

Figure 4.13: Black body shock surface temperature trace from SOP diagnostic with correct time scale. The beginning of the time scale corresponds to the start of the laser drive.

The source radiance $L_s(\lambda)$ is then taken to be the radiance given by Planck's law:

$$L(\lambda, T) = \frac{2hc^2}{\lambda^5} \frac{1}{\exp(hc/\lambda T) - 1}, \tag{4.14}$$

where h is Planck's constant, c is the speed of light, λ is the wavelength of the radiation, and T is the temperature of the Planckian source, i.e. black body radiation [71]. Since the the spectral band detected by the SOP system is narrow (red filter: ($\sim 590 - 780$ nm, centered at $\lambda_c = 684$ nm) the wavelength dependance of the SOP can be approximated by a δ function and thus the black body temperature can be easily obtained from integrating equation 4.13:

$$T = \frac{T_0}{\ln(1 + A/I)}, \tag{4.15}$$

where $T_0 = hc/\lambda_c = 1.818$ eV for the red filter.

Since the response of the SOP system is absolutely calibrated the constant A is known for the specific settings used:

$$A = A_0 \cdot \frac{BW_sG}{\eta M^2}, \tag{4.16}$$

where A_0 = 11340 ADU/ps/mm for the red channel with no ND filters used. We used gain setting no. 5 corresponding to G = 19.0. The calculated black body temperature for our SOP trace for Omega shot 56736 (Jan 2010) is shown in figure 4.13.

A more appropriate approximation to be used here is the *grey body* distribution, which does not rely on the assumption that the shock is optically thick at all wavelengths like the black body distribution does. The reduced reflectivity of a *grey body* emitter increases the emissivity of the surface and thus changes the temperature measurement. The *grey body* radiates energy having the black body distribution reduced by a constant factor related to the reflectivity of its surface. According to Kirchhoff's law of thermal radiation, the absorptivity and emissivity of a grey body are equal at any given temperature and wavelength and the constant A black body distribution is thus reduced by a constant $(1 - R)$, where R denotes the reflectivity [210, 71]. Based on previous reflectivity measurements by Celliers *et al.* [43], we can expect the reflectivity of the deuterium shock surface to be $\sim 0.4 - 0.5$, see figure 4.14.

The values for reflectivity of WDM deuterium at relevant conditions were calculated by our collaborators Dr. Jan Vorberger and Dr. Dirk Gericke from the University of Warwick. They used the Kubo-Greenwood formula to obtain the optical properties of the shocked material from snapshots of our DFT-MD simulations [143, 221, 124]. At the given wavelength, the result is R = 0.45 for a pressure of P = 37.5 GPa. Figure 4.14 shows that this value of reflectivity is in a good agreement with other DFT-MD data and measurements by Celliers *et al.* [43]. Moreover, at the pressures of interest, the reflectivity is weakly dependent on the wavelength of the emission, making it a robust diagnostic. Using the calculated value of R, the temperature estimate is T_{sop} = 0.57±0.05 eV (8% instrument error [71]), consistent with the temperature value directly inferred from the DFT-MD EOS table (T_s = 0.66±0.09 eV). The full grey body temperature trace with R = 0.45 from SOP intensity measurements is shown in figure 4.15.

A similar treatment is not possible for the EOS data from SESAME or S&C. In the S&C case, we calculated the dynamic collision frequency in the Born approximation using the free electron density as given by the S&C EOS in order to obtain the conductivity and dielectric function within a Drude approximation [222, 124]. The

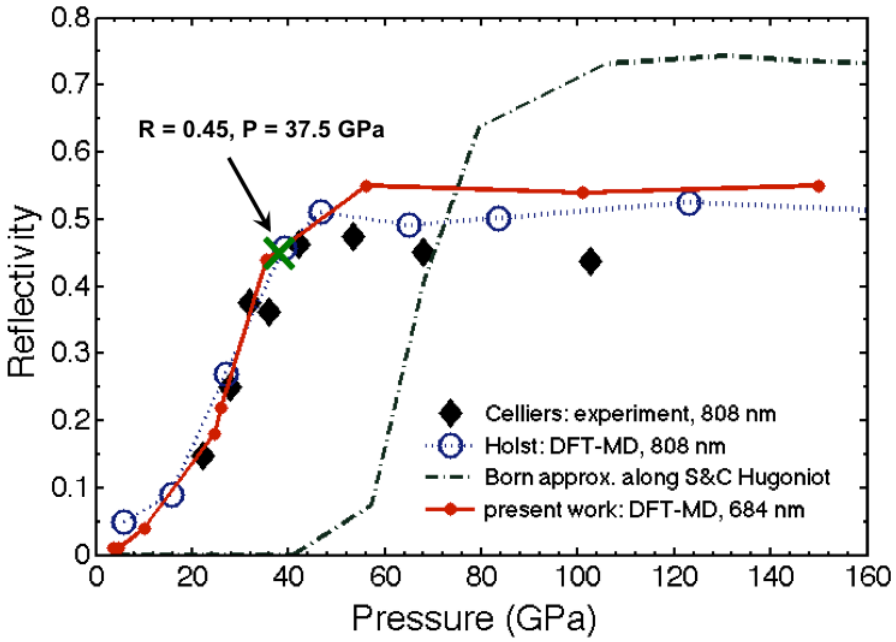

Figure 4.14: Reflectivity of the shocked material versus pressure along the Hugoniot. Reflectivity values are calculated from present DFT-MD simulations for 684 nm, from DFT-MD by Holst *et al.* for 808 nm [124], and using the Born-Mermin approach along the S&C Hugoniot. Measured optical reflectivities of shocked liquid deuterium obtained at the Nova laser facility by Celliers *et al.* are also shown [43].

obtained value of $R \sim 10^{-4}$ reflects the fact that, contrary to DFT-MD, the S&C EOS predicts rather low ionization for this shock condition. Consequently, the SOP temperature given by S&C EOS is $T_{sop} = 0.47 \pm 0.04$ eV (see table 4.1), which lies outside the error bars of the theoretical prediction ($T_s = 0.75 \pm 0.09$ eV). Although our VISAR measurement does not provide an absolute value of reflectivity, relative reflectivity changes can be obtained. Using the refractive indexes of ambient polyimide and deuterium, neglecting absorption, we can expect an initial reflectivity of at least 10% which means that the S&C value for R is three orders of magnitude too low. Reflectivity data from SESAME were not available and therefore no temperature comparison was possible.

Error analysis

The error in the temperature measurement as given by equation 4.15 is influenced by the uncertainties in the source, transmission measurements, sweep rates, fits and signal-to-noise ratio of the SOP calibration [71]. The error in T_0 is estimated to be $\sim$ 1% dominated mainly by the wavelength dependance on the source and the

transmission measurements. The $G \cdot A_0$ product is affected by uncertainties in the source (1%), transmission measurements ($< 1\%$), signal-to-noise ratio (5%), calibration sweep rate ($< 1\%$), and the error in estimate of the gain (2%) giving a total error of $\sim 5.5\%$ [71]. The error in sweep rate is negligible in this case as the variation in spacing of the timing fiducials is very small ($< 1\%$). Magnification was observed to deviate less than 1% [71]. Overall estimated error in the brightness temperature measurement for a 3×3-binned CCD is approximately 8% for shock waves radiating at the order of few eV when SOP is used at its best focus [71].

4.6 Results and discussion

The VISAR system produces a continuous record of the shock velocity history as well as a 1-D image of the spatial profile of the shock. VISAR registered a variable velocity profile with an initial value of 16.9 ± 0.9 km/s. The shock diameter was found to grow from 530 ± 50 μm to 830 ± 30 μm. Since the long driver pulse was realized by staggering of different beams, slight errors in spatial alignment and temporal overlap could have produced a non-uniform spot size and variable shock velocity.

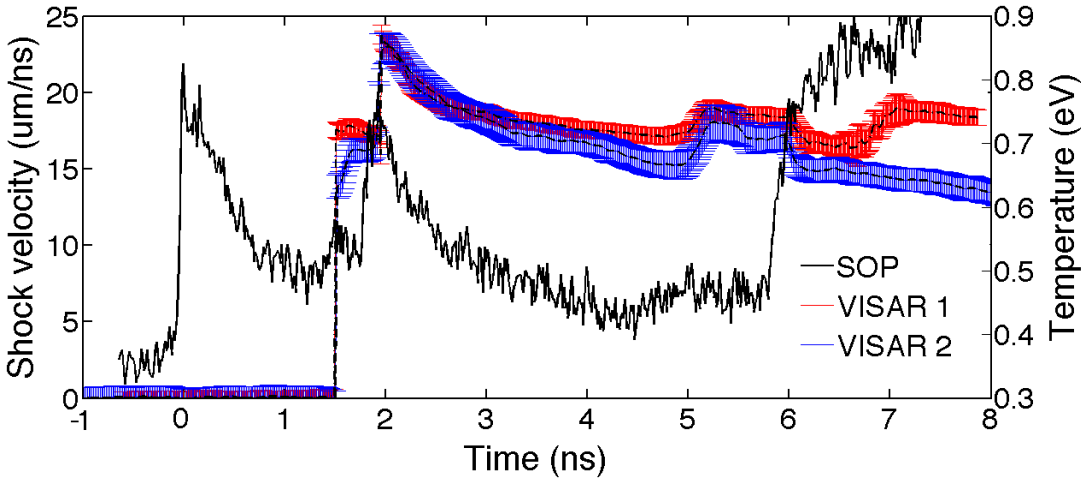

Figure 4.15: Plot of the calculated velocity measurement from the two VISAR arms (red and blue traces) and the temperature of the emitting shock front calculated from the SOP measurement fitted with the grey body approximation using reflectivity of 0.45 obtained from DFT-MD simulation (black solid line). The shock forms at $t = 0$ ns as soon as the laser pulse hits the surface of the target, which is instantly observed by SOP. The shockwave becomes reflective $\sim$1.5 ns later when VISAR records the signal.

Figure 4.10 demonstrates that the calculated Hugoniot varies significantly in the

compressibility of deuterium for the different models within the region of interest. The pure chemical models show much lower compressibility in this regime that the physical ones. The original SESAME is known to give a *stiff* EOS, whereas the EOS from DFT-MD is *softer* with noticeably greater compressibility. The pressure ionization/dissociation happens much earlier for DFT-MD producing abundance of free electrons and thus generating high reflectivity of deuterium at lower pressures. At some point the chemical models catch up and dissociate at higher pressures at about the same parameters for S&C and SESAME (as can be seen in the similar Hugoniots). This is consistent with DFT-MD being more compressible for lower pressure and S&C being more compressible for higher pressures.

Table 4.1: Summary of results: thermodynamic conditions within the shockwave obtained from the measured shock velocity (16.9 ± 0.9 km/s) and calculated Hugoniots from three EOS models: SESAME [17], S&C [122, 123], DFT-MD [37, 38]. Reflectivity data from SESAME were not available.

EOS table	Shocked conditions		
SESAME 5263	P_s = 35.9±4.5 GPa	ρ_s = 0.63±0.02 g/cm^3	T_s = 0.63±0.09 eV
SESAME 5265	P_s = 37.9±4.6 GPa	ρ_s = 0.72±0.02 g/cm^3	T_s = 0.68±0.09 eV
S&C model	P_s = 35.7±4.2 GPa	ρ_s = 0.62±0.02 g/cm^3	T_s = 0.75±0.09 eV T_{sop}=0.47±0.04 eV
DFT-MD	P_s = 37.5±3.9 GPa	ρ_s = 0.72±0.01 g/cm^3	T_s = 0.66±0.09 eV T_{sop}=0.57±0.05 eV

The consistency of the theoretical models' predictions is then checked against an independent temperature measurement by the SOP diagnostic, see table 4.1. Only the DFT-MD calculations are consistent with the SOP temperature measurement. It can therefore be concluded that only the *ab initio* DFT-MD model was able to satisfy the constrains set by the shock velocity and temperature measurements. The S&C model, on the other hand, is not consistent with both data sets. This is not a surprising result

since it is known that the chemical models tend to underestimate the ionization of the system in this regime. The DFT-MD predicts very high ionization state $70 - 100\%$ for temperatures around 0.6 eV, which is consistent with the experimental results of Celliers *et al.* [43], which show that at the given shock velocities near saturation of the reflectivity signal was observed indicating maximum ionization.

The conditions inferred by combining VISAR, SOP, and EOS models yield a degeneracy parameter (ratio of thermal and Fermi energies) of $\Theta = T_s/T_F \sim 0.05 < 1$ and an ionic coupling parameter $\Gamma_{ii} = e^2/4\pi\epsilon_0 a k_B T_s \sim 21 \gg 1$, where ϵ_0, a, and k_B are the vacuum permittivity, inter-particle separation and Boltzmann's constant, respectively. This confirms the creation of a strongly coupled, degenerate plasma at conditions relevant to the interiors of giant planets. In this region, the applicability of the chemical models is questionable [37] but DFT-MD simulations provide a reliable description of such states [105]. Introducing SOP as a tool for temperature measurements together with VISAR diagnostics has made it possible to validate the EOS without relying on pressure standards. The higher compressibility of hydrogen as indicated by the DFT-MD has serious implications for Jupiter's structure, in particular on the size of its core, the required concentration of heavier elements, and the location of the molecular to metallic transition [14, 12].

Chapter 5

X-ray Thomson scattering (XRTS) experiment at Omega

5.1 Introduction

Recently, the new technique of x-ray Thomson scattering (XRTS) has rapidly expanded within the field of high energy density physics as the high power radiation is capable of penetrating deep inside WDM states reaching solid densities and higher, beyond the critical density regions through which the conventional optical probes cannot propagate [81, 104, 105, 19]. Here, a full set of thermodynamic conditions including the temperature and density measurement as well as information on the microscopic properties such as the ionization, inter-particle collisions and quantum effects can be extracted from a scattering spectrum [19, 223, 3].

This work presents the first XRTS measurement from deuterium being developed at the Omega laser facility. The validation of the deuterium EOS comprises the use of complementary but independent techniques, both experimentally and theoretically. In the experiments described in this chapter the value of scattering parameter was $\alpha = 0.6 - 1$ falling to the boundary of collective and non-collective scattering regimes making the XRTS measurement sensitive to both electron density and temperature. XRTS data was compared to previous experiments carried out with independent VISAR and SOP diagnostics which were able to confirm a correct treatment of the physical conditions in these experiments based on the density-functional molecular dynamics (DFT-MD) simulations [2, 37, 38, 171]. The scattering measurement confirmed the earlier experimental and theoretical findings and added an insight into the microscopic structure of the WDM deuterium creating a unique self-consistent study of deuterium EOS. This chapter presents a detailed overview of the development of XRTS as a probe to diagnose EOS of cryogenic D_2 at high-energy laser facilities.

5.2 Experimental set up overview

The 60-beam, 30-kJ Omega laser system was used to create the WDM conditions by launching a single shock inside the planar liquid deuterium target driven by laser ablation of rapidly expanding material from the laser-target interface [187]. The deuterium was kept inside a copper cryogenic cell with 8 μm thick polyimide windows on either side and cooled down to 20−18 K forming a liquid inside the target increasing its initial density to $\rho_0 = 0.175$ g/cm^3, see figure 5.1 [1]. The target was equipped with gold shields designed to block any direct x-ray emission from any other part of the target than the scattering channel.

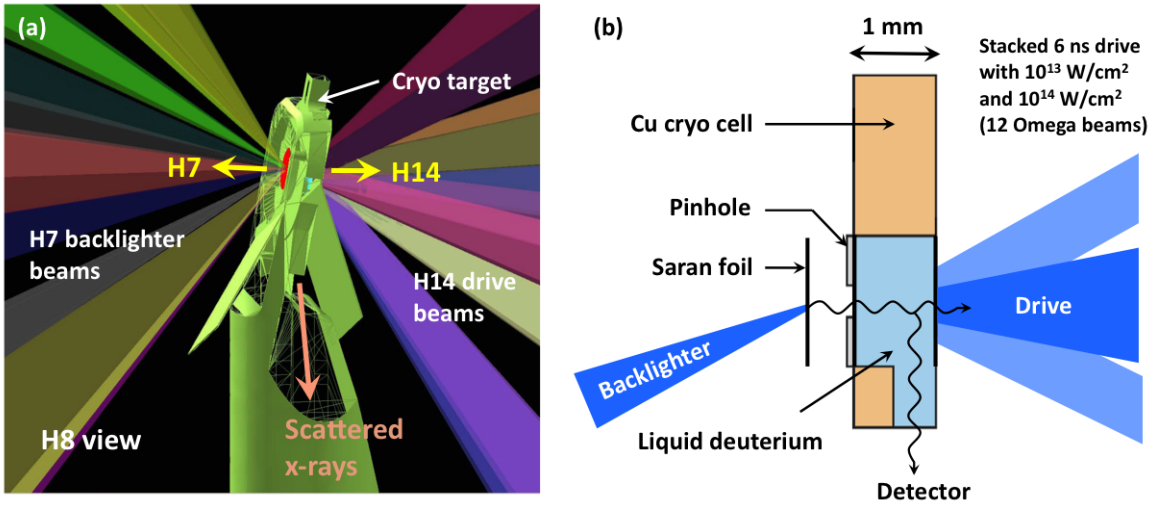

Figure 5.1: Schematic of the target set up with the laser drive and backlighter/scattering configuration: VisRad image of the port H8 view of the target with the H7 backlighter and H14 drive beams (a) and a schematic layout of the planar cryo cell with driver and scattering channel leading to GTS spectrometer (b). A constant intensity 6 ns laser drive incident on the CH ablator compresses and heats the material inside a planar layer of liquid deuterium target creating WDM. Sixteen tightly focused beams irradiate a saran backlighter with 10^{16} W/cm^2. The scattered Cl Ly-α emission scattered at 90° down a 500 μm wide scattering channel before it is detected with the XRFC outfitted with a HOPG crystal spectrometer [1].

The drive beams were frequency-tripled providing the 3ω ($\lambda = 351$ nm) laser output to increase the laser-plasma coupling efficiency [57]. The UV laser drive consisted of 6 pairs of 1 ns laser pulses evenly divided into two cones around the target normal at angles of 23.2° and 47.8° and a flat intensity profile was created by phase plates and polarization smoothing [188]. These square pulses were then staggered in time forming 6 ns constant drive with intensities of 10^{13} and 10^{14} W/cm^2. The higher

intensity drive operated at the optimum energy output of the Omega system with $400 - 500$ J/beam. The lower intensity drive is then created by detuning of the frequency conversion crystals (FCC) lowering the conversion efficiency of the UV output of the laser.

Sixteen tightly focused 1 ns beams at 10^{16} W/cm^2 (200 μm focal spot diameter) then come from the opposite side and irradiate a 12 μm thick saran foil creating a burst of narrowband Cl Ly-α x-rays at 2.96 keV, which are used as our x-ray backlighter probe. The Ly-α radiation is emitted by highly ionized hydrogen-like atoms in the ablation plasma heated by the inverse bremsstrahlung process [19]. The backlighter lasers therefore operated at 3ω to maximize the the conversion efficiency of the laser into x-rays by reducing laser backscattering instabilities [57]. No phase plates were used to smooth these beams, despite the possibility of improvement of the conversion efficiency, in order to achieve the highest possible intensity of the focused beams which both increases the conversion efficiency of the Ly-α and suppresses the He-like and Li-like satellites [103]. These x-rays are collimated by a Ta pinhole 200 μm and scattered at 90° to a gated Thomson spectrometer (GTS). The measurements of the Cl Ly-α line and its satellites are described in Chapter 3, section 3.4. The direct spectral measurement of the probe line reveals a full-width-half-maximum (FWHM) of ~ 9 eV with a Gaussian-like spectral profile.

The GTS is composed of a highly oriented pyrolytic graphite (HOPG) mosaic crystal (ZYB, 25 × 50 mm, 2 mmm thick) [195] coupled with an x-ray framing camera (XRFC), with a micro-channel-plate (MCP) combined with a CCD detector. The crystal was placed at the optimal Bragg angle of $\theta_B = 38.6°$ projecting the scattering spectra across the MCP camera which was placed 23.8 cm from the scattering target center, giving the spectrometer resolution of ~ 12 eV/mm. The MCP has four individually powered strips charged in a sequence during the ns backlighter providing an improved temporal resolution of the scattering measurement. The integration time of each strip was 250 ps. A Be blast shield was used to block any visible radiation and stop any debri from damaging the specrometer. A detailed desciption of the GTS set up is provided in section 3.3.1.

5.3 Hydrodynamic simulations

The analysis of the scattering spectra from the WDM deuterium driven at both intensities 10^{13} W/cm^2 and 10^{14} W/cm^2 was supported by a series of 1-D and 2-D simulations using the *HELIOS* and *DRACO* codes [179, 180]. Conditions within

the shockwave were found to be $T_e \sim 1-5$ eV and $n_e = 1.0-2.0 \times 10^{23}$ cm^{-3} when deuterium is driven by the lower intensity laser at 10^{13} W/cm^2. For the higher intensity drive at 10^{14} W/cm^2 the expected shocked conditions are $T_e = 15-20$ eV and $n_e \sim 1.0 \times 10^{23}$ cm^{-3}. According to the DFT-MD simulations near full ionization ($Z = 0.7-1$) should be expected at such conditions, which is consistent with previous measurements of optical reflectivities of shocked liquid deuterium obtained at the Nova laser facility by Celliers *et al.* [43].

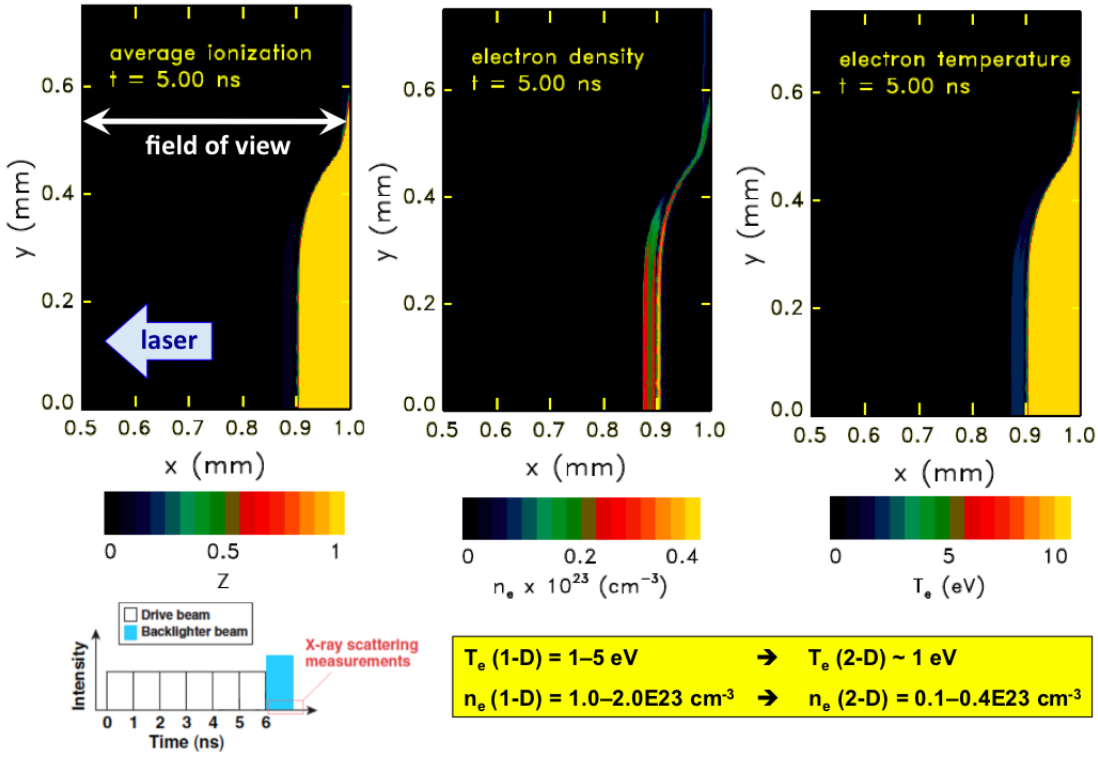

Figure 5.2: Result of 2-D *DRACO* simulations for the low intensity drive at 10^{13} W/cm^2. The inserted figure shows a schematic of the 6 ns staggered laser drive and the scattering measurement starting at 6 ns.

The results of the 2-D *DRACO* simulations with the lower intensity drive input showed that a narrow shock wave (< 50 μm) with a relatively low temperature (~ 1 eV) and high density (~ 0.7 g/cm^3) travelled at velocities just under 20 km/s, which is consistent with the previous measurement from VISAR and SOP using the same intensity drive. This however also means that by the time the scattering measurement is taken between 6 and 7 ns from the start of the 10^{13} W/cm^2 drive the shock has only travelled just under 200 μm into the 500 μm wide scattering channel leaving a significant amount of unshocked deuterium within the field of view of the GTS

spectrometer. This bulk of cold material can thus contribute to the total scattering spectrum adding an undesired impurity to the measurement of the shock conditions. *DRACO* predicts somewhat low ionisation levels for the shocked deuterium ($Z \sim 0.1-0.3$) for these conditions, typical for the SESAME EOS used in the code. Contour plots of the shocked conditions of the *DRACO* for the low intensity drive at 10^{13} W/cm^2 are shown in figure 5.2.

The 2-D simulations predict significantly faster and hotter shock for the higher intensity drive at 10^{14} W/cm^2, see figure 5.3. This time the scattering measurement is taken between 4 and 5 ns from the start of the laser drive, when the shock has travelled to the edge of the scattering channel leaving very little unshocked material within the field of view of the scattering measurement. Thus the contribution from the cold scatter is considered negligible. The shock is also much wider (almost 100 μm) potentially resulting in a stronger scattering signal. The shocked conditions in this case are: $\rho \sim 0.7 - 0.8$ g/cm^3, $T_e \sim 5 - 15$ eV, $Z = 0.5 - 1$.

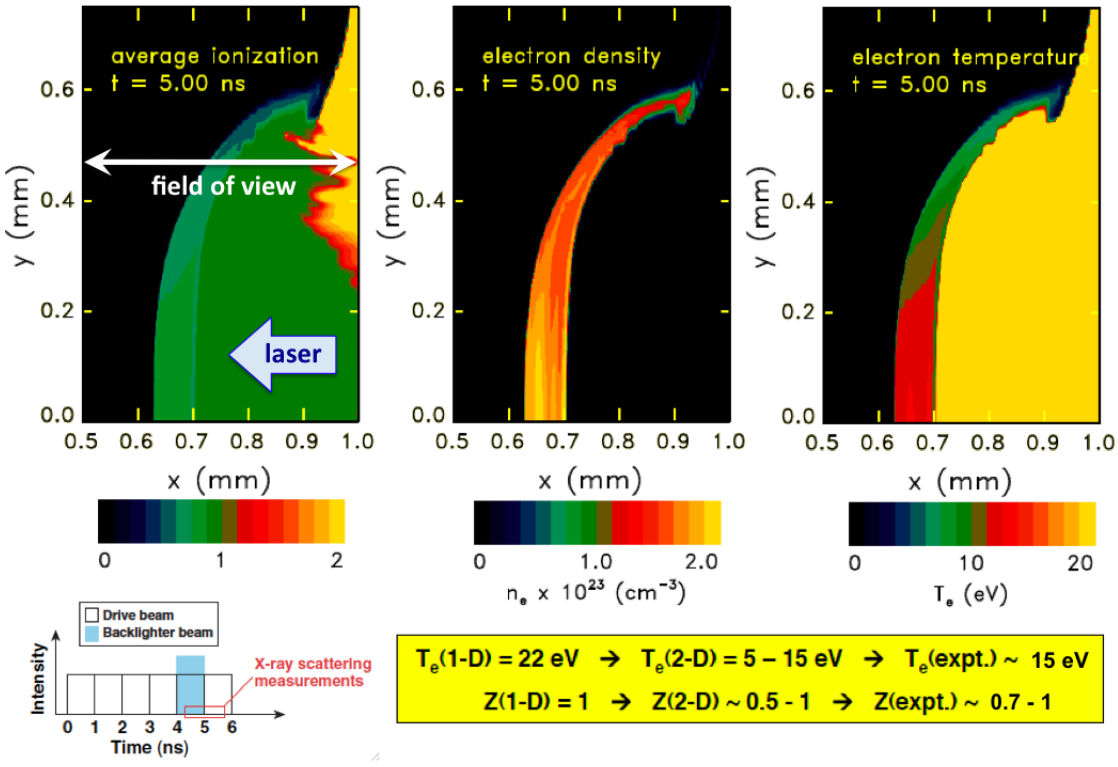

Figure 5.3: Result of 2-D *DRACO* simulations for the high intensity drive at 10^{14} W/cm^2. The inserted figure shows a schematic of the 6 ns staggered laser drive and the scattering measurement between 4 and 5 ns.

1-D radiation-hydrodynamics simulations using the *HELIOS* code [179] were run

to compare conditions within the various zones with corresponding plasma conditions, which vary significantly throughout the target as can be seen in figure 5.4. These simulations are then used to investigate the relative contributions of these zones to the total scattering signal, which will be described in more detail later in this chapter. An actual calorimetry measurement of the laser drive was used as an input into the *HELIOS* simulations with 70% of the input energy being absorbed by the plasma, which accounts for power losses due to reflection of the drive at the critical surface.

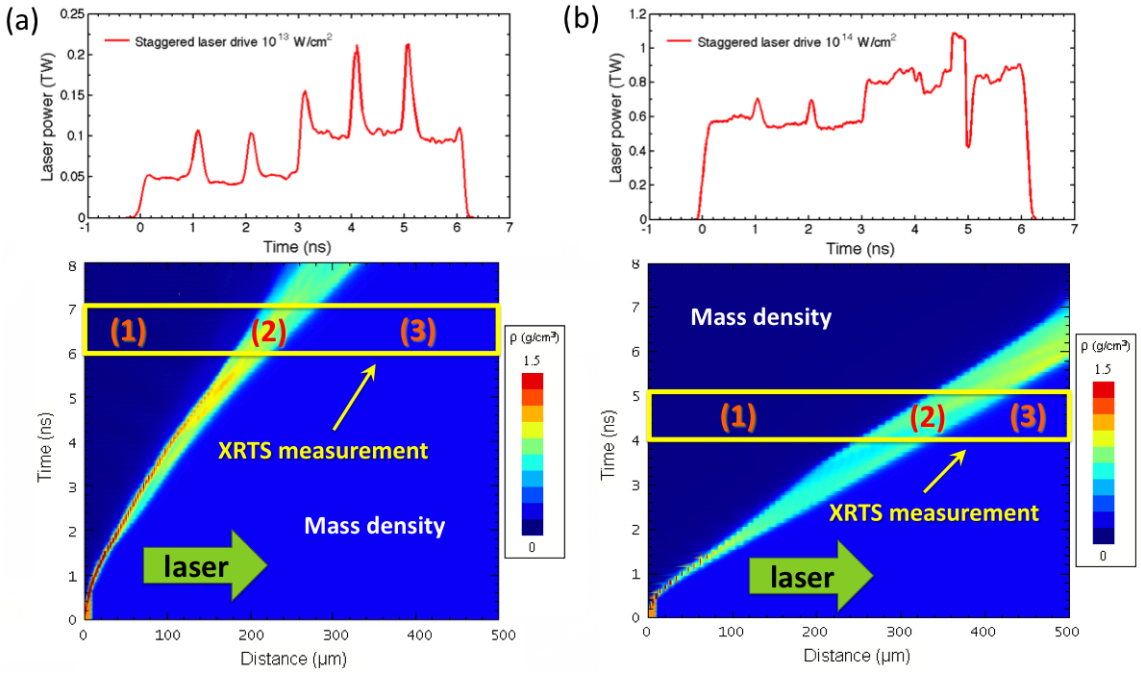

Figure 5.4: Result of 1-D hydro-simulations using the *HELIOS* package for the laser drive (a) at 10^{13} W/cm^2 (shot 58571, Jul 2010) and (b) at 10^{14} W/cm^2 (shot 54957, Jul 2009). The scattering measurement was taken taken at $\sim$ 6.5 ns for the lower intesity drive and between 4 and 5 ns from the start of the laser drive when higher intensity drive was used, both cases are marked by the rectangular box. The three regions within the field of view of the spectrometer correspond to the low density corona (1), dense shocked material (2), and unshocked cold deuterium (3).

The 1-D simulations carried out for the lower intensity drive at 10^{13} W/cm^2 were cross-checked with previous VISAR and SOP measurements to constrain the margin of the simulation [2]. The shock velocity in the simulation was below 20 km/s matching well with the VISAR measurement of 16.9 ± 0.9 km/s. The shock surface temperature was found to be $\sim$ 1 eV, which is in a reasonable agreement with the SOP measurement of 0.57 ± 0.05 eV. The simulations also predict a somewhat high ionization for these conditions of $Z = 0.5$ or higher. Simulations with the higher

intensity drive input predict a hotter plasma than for the lower intensity drive giving the following shocked region conditions: $\rho \sim 0.6 - 0.7$ g/cm^3, $T_e = 16 - 25$ eV, $Z \sim 0.9$, which is consistent with earlier *LILAC* simulations used for the planning of the experiment [79], see figure 2.7 and description in Chapter 2.

5.4 Spectral plots

Based on the geometrical set up of the GTS spectrometer, shown in figure 3.4, we obtain the spectrometer dispersion of ~ 12 eV/mm. With 9 μm $\times$ 9 μm pixels we thus obtain the relation ~ 0.2 eV/pixel (2×2 binning) needed to plot the spectra obtained in the Omega experiments. The position of the Cl Ly-α line at 2960 eV was found from the spectral calibration shots, when direct emission from the backlighter foil was measured, giving the spectral offset.

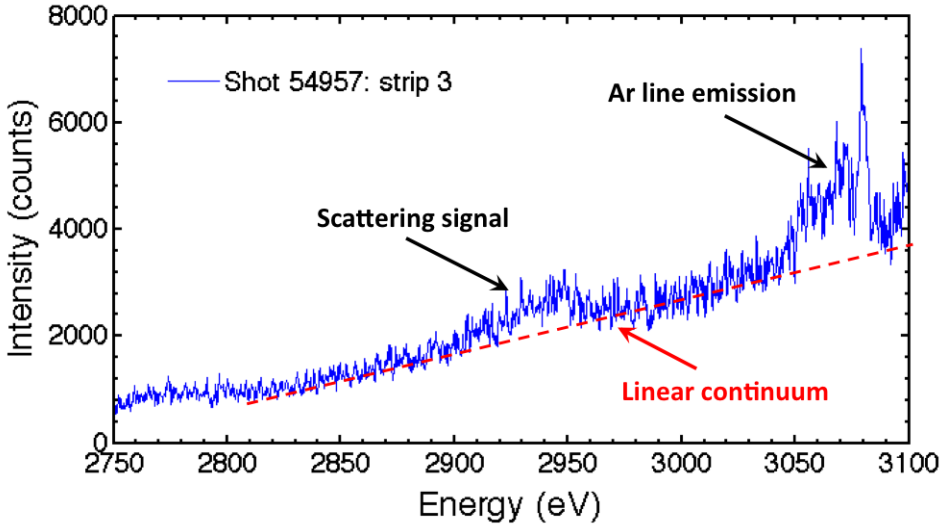

Figure 5.5: An example of raw scattering spectra when Saran backlighter was used (shot no. 54957, Jul 2009). With the lower intensities the GTS detector responds linearly to the incoming x-rays and the scattering spectrum can be obtained by a simple subtraction of the linear continuum.

In the earlier shots, when the Saran backlighter was used, the intensity of the scattered x-rays was relatively low. An example of a lineout of such a spectrum is shown in figure 5.5. All of these spectra exhibited a sloped background continuum increasing in intensity towards the Ar He-α emission lines. At these low intensities of the measured x-rays the intensity response of the detector can be considered linear and indeed it has been found that these continua can be fitted with a linear function,

which can be used to extract the intensity gradient in the spectra and obtain a flatfield response by simple continuum subtraction.

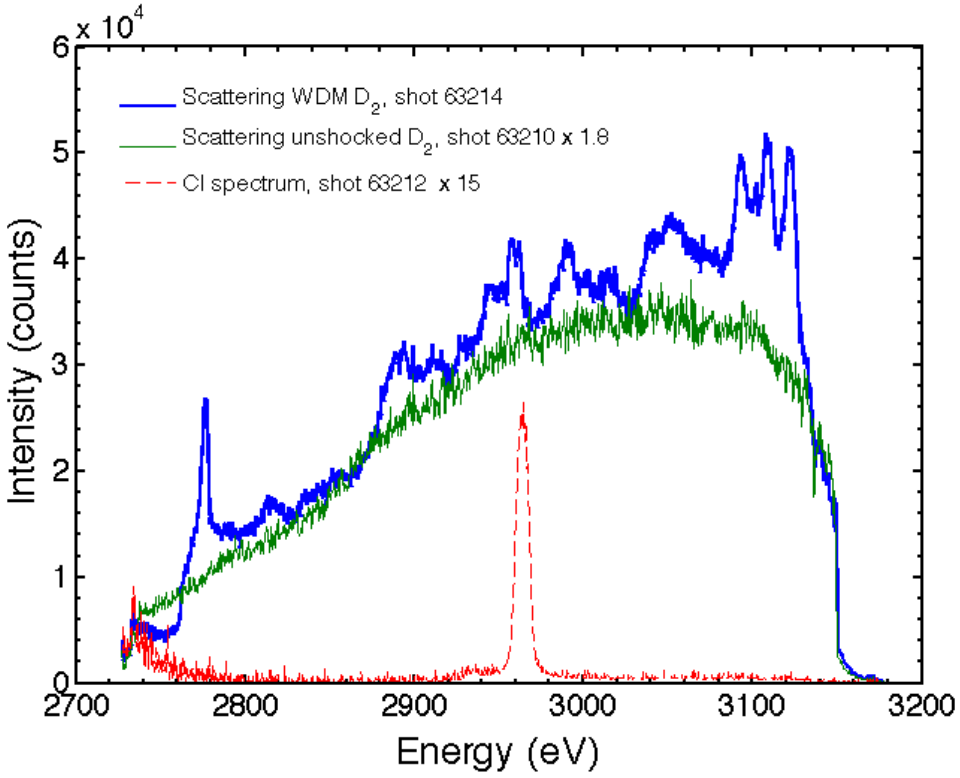

Figure 5.6: An example of raw D_2 WDM scattering spectrum when Parylene D backlighter was used (shot no. 63214, Aug 2011) overlayed with spectra from unshocked D_2 scattering from a cold shot (no. 63210) and the Cl spectral calibration shot (no. 63212).

Similar treatment was not possible for the later shots, when the Parylene D backlighter was used, which significantly increased the intensity of the generated and scattered x-rays. At these intensities "flatfielding effects" due to changes in spatial reflectivity of the HOPG crystal and variation in sensitivity of the MCP/CCD detector become apparent. Figure 5.6 shows lineouts from shocked deuterium scattering shot (no. 63214), cold shot (no. 63210) and spectral calibration shot (no. 63212). There is a strong non-linear continuum below the scattering signal itself. The unshocked deuterium (cold shot) does not produce any obvious scattering signal as is expected due to low densities and temperatures within the sample. The shocked D_2 spectrum shows a characteristic pattern (or "bumpy" profile) on top of the continuum which is a result of the "flatfielding effects", which have to be removed along with the continuum before the scattering data can be analyzed.

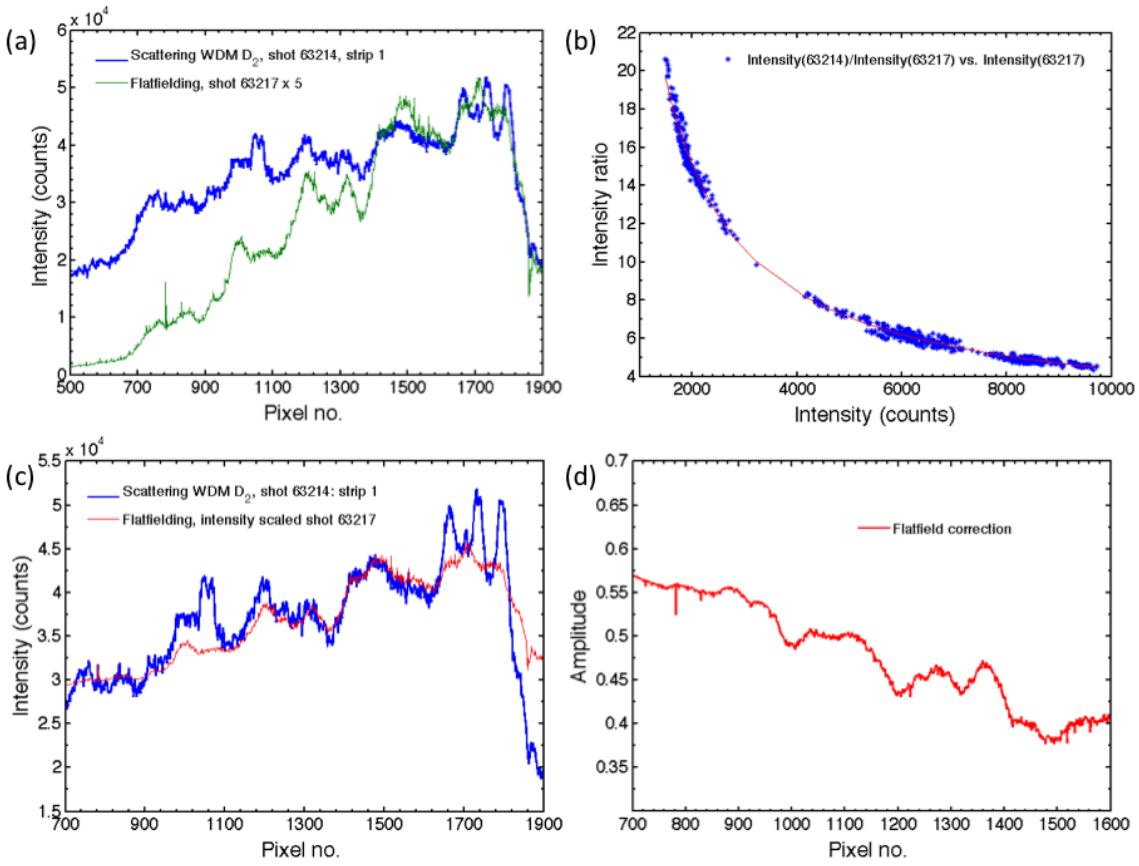

Figure 5.7: Flatfielding analysis procedure. Part (a) shows lineouts of the D_2 scattering spectrum (shot no. 63214) overlayed with a scaled Al flatfield spectrum (shot no. 63217), part (b) shows the non-linear intensity scaling of the detector response (intensity ratio of shots 63214 and 63217 vs. intensity of shot 63217 data), (c) shows the intensity scaled Al flatfield spectrum (shot no. 63217) matched to the deuterium spectrum from shot 63214, and (d) is the peak normalized flatfield correction for the deuterium spectra.

In order to obtain a flatfield spectrum with no features on top of the scattering spectrum a spectral or *flatfielding correction* has to be devised. For this purpose a direct emission from a laser driven Al foil is used, which should exhibit no spectral features in the spectral region of interest under these conditions and thus makes an ideal reference for the flatfield spatial response of the GTS spectrometer. First, points where no line emission or scattering spectra should be observed (i.e. this should be a featureless or flat part of the D_2 spectrum) are selected in both Al flatfielding spectrum (shot no. 63217) and the WDM D_2 scattering spectrum (shot no. 63214), i.e. pixels 733 to 929 and 1120 to 1626, see figure 5.7 (a). The Al spectrum exhibits a large dynamic range of intensities. For such a high intensity gradient the detector

response can no longer be assumed linear. This intensity-dependent response has to be quantified before the deuterium and Al spectra are directly compared.

In the next step, a ratio of the D_2 and Al spectral intensities is plotted as a function of the Al spectral intensity I_{Al} and fitted with a power law relationship (red line) of the form $fit = a \times I_{Al}^{b} + c$, see figure 5.7 (b). The power law relationship with the correct coefficients ($a = 2.568 \times 10^4$, $b = -0.9942$ and $c = 1.698$) is then used to obtain an intensity scaled Al flatfielding spectrum I_{ff} which can be perfectly matched to the deuterium spectrum as shown in figure 5.7 (c). From this point it is easy to obtain the flatfield correction in the form of 1/intensity scaled Al spectrum (63217) normalized to the peak intensity (flatfield corr. $= 1/I_{ff}/max(I_{ff})$), see figure 5.7 (d). This flatfield correction is then multiplied with the deuterium scattering spectrum removes both the continuum background as well as the flatfielding features ("bumps") in the spectrum. The flatfield-corrected spectrum is shown in figure 5.13.

5.5 XRTS analysis

A number of different approaches were employed in order to extract the information about the thermodynamic conditions within the shocked deuterium from the measured scattering spectra. Since under the conditions of the experiment and given the geometry of the scattering measurement, the scattering parameter $\alpha \sim 0.6 - 1$ falls into the non-collective scattering regime. Thus the shape of the downshifted Compton peak is given by the velocity distribution of the electrons and governed by equations 2.17, 2.18 and 2.38 as explained in Chapter 2. It is therefore the shape of the Compton feature that carries the information about the temperature and density of the plasma.

The ionization state of the plasma can then be extracted from the ratio of the Compton and Rayleigh peak intensities which are proportional to the number of free/delocalized and bound electrons in the sample respectively. This analysis was problematic in particular for some of the earlier data sets, where a weaker x-ray probe was used and the scattering data was very noisy making the fit to the absolute intensities difficult. Impurity scattering from cold deuterium also adds complications to the analysis of the state of the WDM deuterium in these experiments. In the following sections a number of different approaches to obtain the information about the conditions within the shocked deuterium sample and their results are outlined.

5.5.1 Fitting with frequency sum rules

The shape of the Compton feature is proportional to the electron-electron structure factor $S_{ee}(k,\omega)$ which can be linked to the frequency sum rules as shown in equations 2.27 to 2.31 which in turn depend on the thermodynamic properties of the plasma as described in section 2.2.5. Since these expressions are exact for the semi-classical regime, i.e. for free particles with weak coupling, they can be used to easily obtain the dynamic structure factor for the free electrons. This is the simplest approach to obtain the electron temperature and density from the spectral shape fitting to the Compton feature. The strength of of this method is its simplicity and the exact results for the electron density and temperature based a number of known expressions which can be easily linked to the integrated amplitude of the inelastic peak only.

In this approach, the Compton peak is first fitted with an appropriate curve $g(\omega)$ which matches well with the experimental measurement. This fit is then integrated in a fashion analogous to the sum rules as $\int \omega^{2n} g(\omega).d\omega$, see equation 2.27 in section 2.2.5. The best fitting function for the data sets for both drive intensities was found to be of a Gaussian form:

$$g(\omega) = C.\exp\left(-\frac{\omega-\omega_0}{2\sigma^2}\right), \tag{5.1}$$

where C is an arbitrary constant matching the amplitude of the Compton peak in the scattering spectra, where the Rayleigh peak is rescaled to an amplitude of 1, $\omega_0 = E_0 e/\hbar$ where $E_0 \approx 2940$ eV corresponds to the downshifted position of the inelastic feature with the Compton recoil $E_C = \frac{\hbar^2 k^2}{2m_e} \sim 20$ eV, around which the Gaussian fit is centered. The width of the Gaussian is then determined by the constant σ which can be linked to the velocity distribution of the electrons, e.g. $\sigma = k\sqrt{E_F/m_e}$, where E_F is the Fermi energy (equation 1.6) for degenerate electrons or $\sigma = k\sqrt{k_B T/m_e}$ for classical plasma.

Before the analysis could be carried out the profile of the x-ray probe had to be deconvolved from the spectral fits. The Cl Ly-α has a roughly Gaussian profile with FWHM or $\sigma_i \sim 9$ eV, so the deconvolution of two Gaussians simply gives the value for $\sigma^2 = \sigma_{conv}^2 - \sigma_i^2$, where σ_{conv} corresponds to the width of the Gaussian fit to the scattering data. Each deconvolved Gaussian fit to to the data sets was then integrated and linked to the exact results for the frequency sum rules of the dynamic structure factor for free electrons, equations 2.28, 2.29, 2.30 and 2.31. The various degrees of degeneracy in the electron gas were included by the approach suggested by Gericke *et al.* [29] which gives an expression for the static structure factor $S_{ee}^0(k)$ in

terms of density and the effective temperature as shown in equation 1.11 in section 1.2 [169]. The moments of the frequency-integrated fits to the Compton peak can then be linked to the exact expressions for the semi-classical frequency sum rules which only depend on the electron density n_e, temperature T_e and the instrument spectral response function constant K:

$$K \cdot \int g(\omega).d\omega = S^0_{ee}(k) = \frac{k^2}{k^2 + \kappa_e^2}, \tag{5.2}$$

$$K \cdot \int \omega^2 g(\omega).d\omega = (kv_t)^2, \tag{5.3}$$

$$K \cdot \int \omega^4 g(\omega).d\omega = 3(kv_t)^4 + \omega_p^2(kv_t)^2. \tag{5.4}$$

Here $v_t = (k_B T_e/m_e)^{1/2}$ is the thermal velocity of electrons and the screening length of the electrons is then found through interpolation of the Debye and Thomas-Fermi screening lengths and is of the form $\kappa_e = 1/\lambda_s = \sqrt{e^2 n_e/\varepsilon_0 k_B T_{eff}}$, where the effective temperature is denoted as $T_{eff} = (T_e^4 + T_F^4)^{1/4}$ [29], see equation 1.11. The instrument constant K is eliminated from the equations 5.2 to 5.4 by taking the ratios of the equations leaving the electron density n_e and temperature T_e the only unknowns. The integrated plots are found through numerical integration using the trapezium rule and the values of n_e and T_e are obtained by numerically solving the simultaneous non-linear equations 5.2 to 5.4 using the iterative Newton-Raphson method [224] by finding the roots to equations:

$$\frac{m_e}{\left(k^2 + \frac{e^2 n_e}{\varepsilon_0 k_B T_e ff}\right) \cdot k_B T_e} - R_1 = 0, \tag{5.5}$$

$$\left(T_e^4 + \left[\frac{\hbar^2 (3\pi^2 n_e^{2/3})}{2 m_e k_B}\right]^4\right)^{1/4} - T_{eff} = 0, \tag{5.6}$$

$$\frac{m_e^2}{\left(k^2 + \frac{e^2 n_e}{\varepsilon_0 k_B T_e ff}\right) \cdot \left(3k^2 k_B^2 T_e^2 + \frac{e^2 n_e k_B T_e}{\varepsilon_0}\right)} - R_2 = 0. \tag{5.7}$$

These equations were derived from ratios of the equations 5.2, 5.3 and 5.4, where R_1 is the ratio of the right hand side expressions in 5.2 and 5.3 and R_2 is the ratio of the right hand side expressions in 5.2 and 5.4 respectively. Equation 5.6 was derived from the expression for the effective temperature T_{eff} in equation 1.11 by substituting

for the Fermi energy E_F (equation 1.6). The derivatives of equations 5.5 through 5.7 with respect to T_e, T_{eff} and n_e were found using the symbolic maths function within the Matlab code.

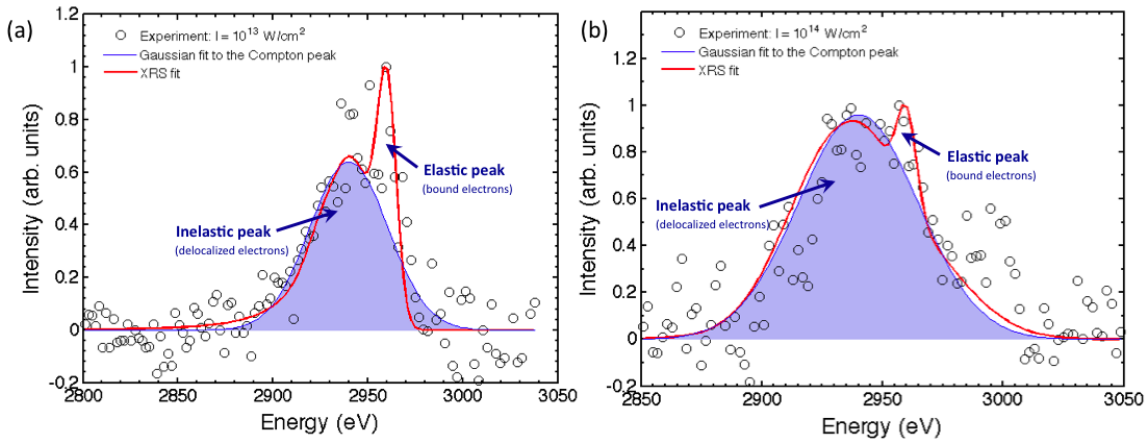

Figure 5.8: Gaussian fits (highlighted blue plots) to the Compton peak for (a) lower intensity shot at 10^{13} W/cm^2 (shot 58571, Jul 2010) and (b) higher intensity shot 10^{14} W/cm^2 (shot 53906, Mar 2009). The scattering data were binned by 10 pixels to better reflect the true resolution of the HOPG crystal spectrometer and also smooth the data. The data sets were also overlayed with calculated profiles from x-ray scattering (XRS) code (red line) which computes the Compton feature using the RPA and also includes the ionic feature.

Examples of the Gaussian fits to the scattering data obtained for the 10^{13} W/cm^2 and 10^{14} W/cm^2 intensity shots are shown in figure 5.8. The blue highlighted plots show the integrated area under the best fit (Gaussian) to the inelastic Compton feature. The sum rules analysis then provided the values for the electron density and temperature in the lower intensity drive experiments of $n_e = 1.7 \pm 0.4 \times 10^{23}$ cm^{-3} and $T_e \sim 13 - 20$ eV, where $T_F \approx 12$ eV. Based on these values the DFT-MD simulations predict $Z \sim 0.7 - 1$ and $\rho \approx 0.7$ g/cm^3. This density is in a good agreement with the previous measurements from VISAR, however the temperature is very high and disagrees with the SOP measurement. The high electron density suggests high levels of degeneracy, which would imply that the semi-classical approach of the sum rules which is strictly valid for classical plasmas is not applicable in this case and thus gives an incorrect answer for the electron temperature. The inclusion of the strong coupling effects was attempted by the use of a non-zero value for the static local field correction by substituting the values for $I(k) = 0.1$ ($G(k) = 0.45$) calculated from molecular dynamics simulations that employ the OCP model, however the improvement to the temperature calculation was marginal.

For the higher intensity drive the sum rules provide the electron density $n_e = 0.9 \pm 0.3 \times 10^{23}$ cm^{-3} and temperature $T_e = 11 - 29$ eV. The DFT-MD simulations then predict $Z \approx 0.8 - 1$ and $\rho \approx 0.3$ g/cm^3 for these conditions. These values seem more reasonable and agree with the 1-D and 2-D hydro simulations. Since these conditions would correspond to lower levels of degeneracy, the sum rules should be more applicable in this regime. The approximate error bars on n_e and T_e were found by fitting the Gaussian plots to the upper and lower bounds of the noise levels in the inelastic scattering spectra. The consistency and applicability of the sum rules analysis in the regime accessed in the Omega experiments is however questionable and thus these values should be considered as approximate rather than final results.

The plots in figure 5.8 also include calculated profiles from a more sophisticated x-ray scattering (XRS) code (red curves) which computes the shape of the inelastic peak (delocalized electrons) using the finite temperature RPA while the elastic ionic peak (bound electrons) is calculated using the screened one-component plasma (SOCP) model which uses the input of the same temperature and density as the Gaussian fits as well as ionization state of the plasma [139]. These plots are only used to visualize both elastic and inelastic features and to compare the shape to the pure Gaussian fits to the Compton peak, which are in a good agreement with XRS. In particular in the lower intensity shots, the XRS code predicts a very low ionization state of $Z \sim 0.1$ which is in a direct contradiction with previous findings from SOP and DFT-MD described in the previous chapter. This discrepancy is attributed to a poor fit to the Rayleigh peak since the data is very noisy and/or to impurities in the measured signal due to scattering from the unshocked/cold material.

5.5.2 RPA fits to the Compton peak

Another unique approach to analyze the inelastic feature in the scattering data was employed in this work in order to increase the reliability of the measured thermodynamic quantities. The Compton peak in the measured spectra was fitted with a curve corresponding to the velocity distribution of the free electrons based on a more sophisticated calculation than the previously used frequency sum rules of the electron-electron structure factor. These fits were computed using the XRS code which utilizes the finite temperature random phase approximation (RPA) for a specific sets of thermodynamic conditions (T_e and n_e) until the correct fit to the data was reproduced [139].

Due to the thermal motion of the free electrons the downshifted Compton line E_C is broadened through the Doppler effect ($\Delta\omega = -E_C \pm \mathbf{k}.\mathbf{v}$), i.e. the Compton

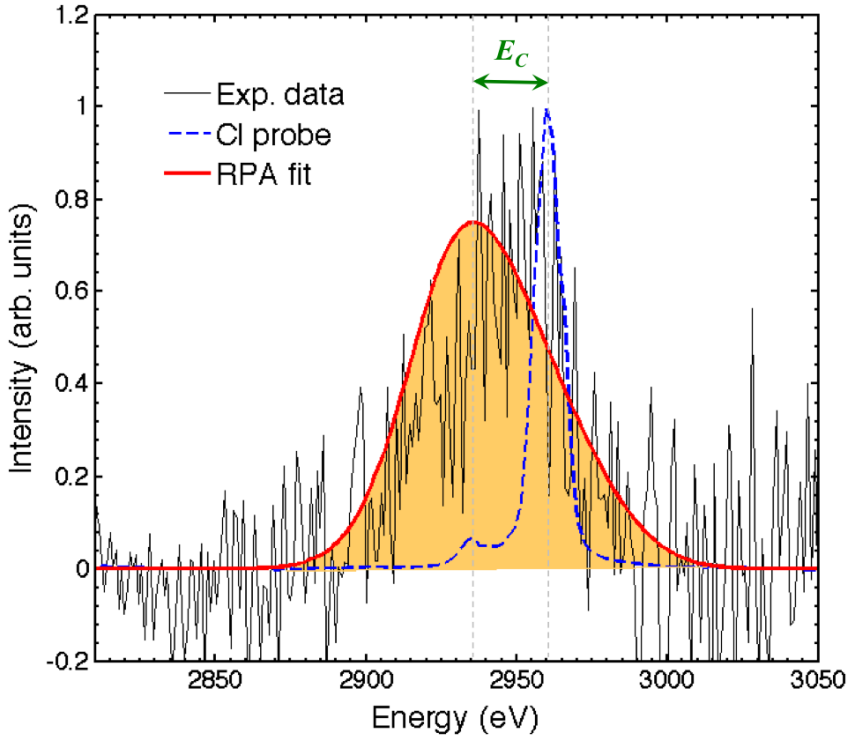

Figure 5.9: RPA fit to the experimental data obtained for higher intensity laser drive at 10^{14} W/cm^2, centered at the classical position of the Compton peak dowshifted by $E_C = \hbar^2 k^2 / 2m_e = 17$ eV. This figure shows the best calculated fit to the scattering data at $T_e = 15$ eV and electron density at $\sim 0.3 - 1.0 \times 10^{23}$ cm^{-3}.

feature in the scattering spectrum reflects the velocity component of the free electrons in the direction of the scattering vector **k** [19]. As said before, the x-ray scattering in the non-collective regime probes the velocity distribution function of the electrons. In a degenerate system the spectrum of the Compton line is governed by the Fermi distribution making its spectral width proportional to $(E_F)^{1/2}$ and hence $(n_e)^{1/3}$ providing an electron density measurement. Whereas, for the classical case the x-rays are scattered by free electrons following the Maxwell-Boltzmann distribution making the Compton line width sensitive to the temperature of the system [19].

It is found that the Gaussian-like profile provides the best fit to the measured Compton line. The Gaussian profile corresponds to the Maxwell-Boltzmann distribution suggesting that the width of the inelastic scattering feature is dominated by the Doppler broadening due to temperature. In order to account for the instrument function the spectrum of the probe x-rays with FWHM $\sim$ 9 eV was convolved with the RPA calculated profile. An example of the scattering spectra of the shock compressed

deuterium by the high intensity drive at 10^{14} W/cm^2 (shot 54957, Jul 2009) is shown in figure 5.9. The conditions used to calculate the theoretical fit in figure 5.9 were $T_e = 15 \pm 10$ eV and $n_e \sim 0.8 \times 10^{23}$ cm^{-3} giving $r_s = 2.7$ and $\Theta = 2.2$, which corresponds to partially degenerate weakly coupled electron gas in a regime with strong validity of the RPA. In this geometry (non-collective scattering), we are limited to identifying the upper bound for the electron density, which is dictated by the limit of full degeneracy being reached for $T_e \ll T_F$ when the Compton profile changes shape to the parabolic Fermi-Dirac distribution, making the density measurement less precise than that of temperature.

A number scattering spectra from different shots were compared. The intensity of the laser drive and timing of the backlighter varied between 10^{13} and 10^{14} W/cm^2, and 3 to 6 ns delay from the start of the drive respectively. The spectra measured between 4 and 5 ns from the start of the drive at the higher intensity, figure 5.9, provided a clear measurement T_e and n_e from a single RPA fit. For the lower intensity drive the XRTS measurement was carried out at the end of the laser drive at 6 ns, yet the slower shock wave did not propagate through the entire width of the scattering channel leaving a large amount of cold material within the field of view of the spectrometer.

Just like when the sum rules approach was applied, the RPA fits to the scattering data from the lower intensity drive at 10^{13} W/cm^2 (shot 58571, Jul 2010) provided a temperature measurement of $T_e > 10$ eV, which is inconsistent with the SOP temperature measurement for the same laser conditions. This is most likely result of a significant contribution of the cold scattering to the measured data set. Thus, a more sophisticated analysis, which includes bound-free contribution from the unshocked material, is required as the simplified expression 2.37 is only applicable for nearly fully ionized deuterium. This analysis will be described in more detail in the next section.

5.5.3 Composite scattering profiles

As mentioned above, a single RPA calculated profile cannot be used for the lower intensity drive shots as the bulk of the molecular deuterium adds a contribution of the bound-free transitions to the total scattering spectrum. If one wishes to fit both the inelastic electron and elastic ion features using the XRS code [139, 166, 29] to include these transitions in the scattering spectrum for the lower intensity drive, a very low ionization state (around 10%) has to be assumed, which is not physical. The previous results from SOP and DFT-MD simulations suggest very high ionization of around 70% for these conditions, which is consistent with reflectivity measurements

by Celliers *et al.* [43] which show that around the shock velocity of 20 km/s the reflectivity of deuterium reaches its maximum suggesting near full ionization in this region. This discrepancy is resolved once one looks at the individual contributions to the total scattering signal from different regions within the field of view of the spectrometer.

The output of the *HELIOS* simulation was used as an aid to extract the individual contributions from different spatial zones within the 500 μm side scattering channel. The simulations in figure 5.4 show that x-rays can scatter over a very wide range of plasma conditions, which can be separated into three main regions contributing to the total scattering signal. For the lower intensity drive at 10^{13} W/cm^2, these are: the dense shocked material (mass density $\rho \sim 0.7 - 0.8$ g/cm^3, $T_e = 0.7 - 5$ eV, $Z = 0.6 - 1$), hot expanding corona of low density behind the shock ($\rho \sim 0.05 - 0.005$ g/cm^3, $T_e = 50 - 500$ eV, $Z = 1$) and the bulk of cold unshodked material before the shock-wave ($\rho = 0.175$ g/cm^3, $T_e = 18$ K, $Z = 0$).

The output of the simulations was then used to calculate a synthetic scattering profile expected for each region. Each profile was computed using the XRS code which computed a full scattering profile including the downshifted Compton feature, calculated using the finite temperature RPA, and the elastic Rayleigh peak, where bound electron response $|f_I(k) + q(k)|^2 S_{ii}(k)$, see equation 2.13, is obtained from the screened one-component plasma model where screening term $q(k)$ is allowed to vary to become negative (SOCPN) [139, 166, 29]. These calculated profiles were then each weighted by their mass density and relative volume to scale the relative contributions to the total signal:

$$S_{tot}(k, \omega) = \sum_j \rho_j \cdot w_j \cdot S_j(k, \omega), \tag{5.8}$$

where ρ_j, w_j and $S_j(k, \omega)$ is the mass density, width and a scattering profile of zone j respectively. These profiles were then added up and overlapped with the experimental scattering spectrum with an excellent agreement. All these fits for shot 58571 (Jul 2010) are shown in figure 5.10.

This result confirms that the scattering spectrum measured for the lower intensity drive cannot be fitted with a single calculated profile due to the significant contribution of the cold scattering. The conditions within the shocked region in the *HELIOS* simulation were $\rho \sim 0.7 - 0.8$ g/cm^3, $n_e = 1.0 - 2.0 \times 10^{23}$ cm^{-3}, $T_e \sim 1 - 5$ eV and $Z = 0.6 - 0.9$ (conditions on the shock front: $\rho \approx 0.7$ g/cm^3, $n_e \sim 1.0 \times 10^{23}$

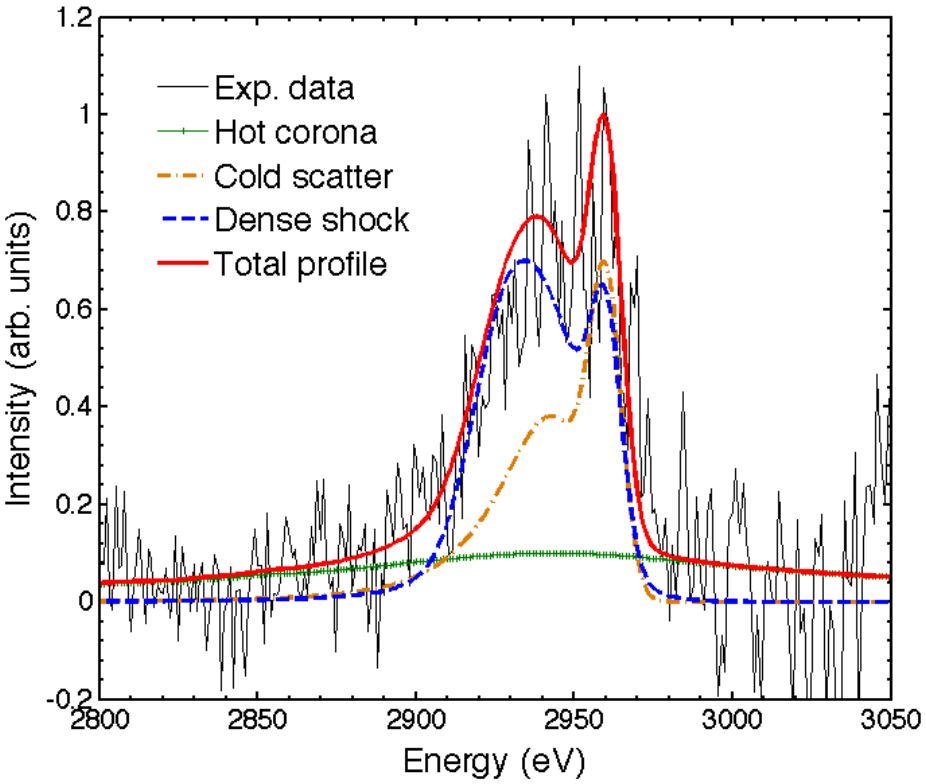

Figure 5.10: Experimental data obtained for lower intensity laser drive at 10^{13} W/cm^2 (shot 58571, Jul 2010) overlayed with calculated plots for the hot expanding corona of low density (cross-dashed/green line), cold deuterium (dot-dashed/gold line) and the dense shock (dashed/blue line). Each contribution was weighted by its mass density and relative volume. The total composite profile (thick/red line) was obtained by adding all of the weighted contributions and scaling it to overlap the data.

cm^{-3}, $T_e \sim 1$ eV and $Z = 0.3 - 0.7$). This is in a good agreement with previous VISAR and SOP measurements and the DFT-MD simulations ($\rho = 0.72$ g/cm^3, $n_e \sim 2.0 \times 10^{23}$ cm^{-3}, $T_e = 0.6$ eV and $Z \sim 0.7 - 1$) [2]. Thus, once the cold contribution to the scattering signal is removed, the x-ray scattering measurement provides a self-consistent EOS measurement with independent diagnostics supported both by hydro and DFT-MD simulations.

The same analysis was applied to the shots with higher intensity laser drive at 10^{14} W/cm^2, figure 5.4 (b). The shock as modeled by the hydro simulations is hotter than for the lower intensity drive giving the following shocked region conditions: $\rho \sim 0.6 - 0.7$ g/cm^3, $T_e = 16 - 25$ eV, $Z \sim 0.9$. This time the simulations show that by the time the scattering measurement is taken between 4 and 5 ns from the start of the laser drive the shock wave has travelled right to the end of the scattering channel

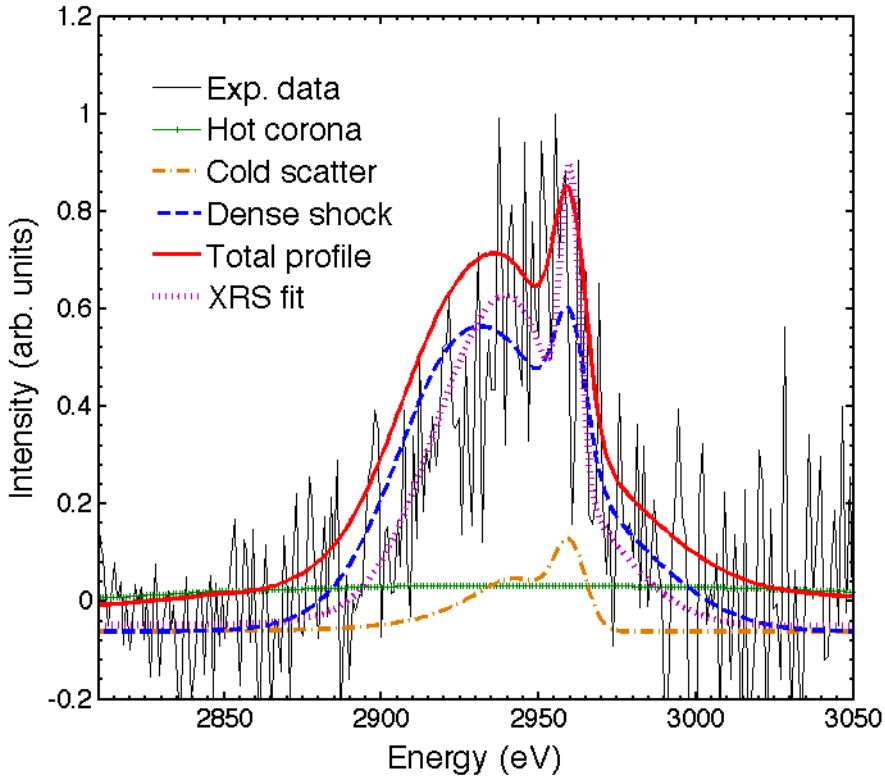

Figure 5.11: Experimental data obtained for higher intensity laser drive at 10^{14} W/cm^2 fitted by weighted calculated plots for the hot expanding corona of low density (cross-dashed/green line), cold deuterium (dot-dashed/gold line) and the dense shock (dashed/blue line) and the composite profile (thick/red line) obtained by adding all of the weighted contributions and scaling it to overlap the data. This figure also shows the best single calculated fit calculated using XRS to the scattering data at $T_e = 15$ eV and electron density at 0.8×10^{23} cm^{-3} (dotted/purple line).

leaving almost no cold material within the field of view of the spectrometer. This confirms that the contribution to the scattering from the cold deuterium is negligible and the scattering profile from the low density corona has no significant influence on the overall shape of the scatterings spectrum. The measured spectrum can thus be reliably fitted with a single calculated profile using the XRS code including both the Compton and Rayleigh features providing a single measurement of the electron density, temperature and ionization as shown in figure 5.11 (dotted/purple line).

5.5.4 Single calculated profiles using XRS code

It has been shown in the above section that for the higher intensity drive scattering spectra, it is possible to fit a single calculated scattering profile to the data sets as

the impurities from the scattering from the cold unshocked material and the expanding corona behind the shock provide a negligible contribution to the total measured spectra. One can then assume that the conditions obtained from such a calculated fit corresponds to the plasma conditions within the bulk of shocked WDM deuterium. A single calculated plot using the XRS code computing the full scattering profile using the finite temperature RPA and the SOCPN model to compute the Compton and Rayleigh components [139, 166, 29] is shown in figure 5.11 (dotted/purple line).

These single calculated scattering profiles are thus used to analyze the scattering spectra from the higher intensity drive (10^{14} W/cm^2) Omega shots for both old and new target design. These results are compared with 1-D and 2-D hydrodynamic simulations as well as the EOS data obtained from the DFT-MD simulations. The noise levels within the measured spectra are also used to obtain the error margin for the measurement of the various plasma conditions including the electron temperature T_e, density n_e and the average ionization state Z. All spectral fits are calculated using the XRS code using the RPA and SOCPN models to compute the full scattering profiles including the elastic and inelastic parts. In the later experiments a new function in the XRS code (version 3), which allows a manual input for the value (intensity) of the ion-ion static structure factor S_{ii}, is also used.

Error analysis using single calculated profile

In the case of the higher intensity drive, the scattering signal is dominated by the shocked material and other contributions such as cold material are small. The noise levels in the data can then be used to estimate the error in the measurement of the theromodynamic conditions. Since, on top of the statistics and instrument response, a gradient in plasma conditions within the field of view the spectrometer can give rise to a spatialy and temporaly integrated scattering signal reflecting a range of values of electron temperature and density.

Error bars were obtained by fitting to $\pm\sigma/2$ (σ stands for one standard deviation) of the noise levels of the Compton peak with the calculated scattering profile with different thermodynamic conditions. For shots at the 10^{14} W/cm^2 drive using the original target design with the Saran backlighter, we obtained electron temperatures of 15 ± 2 eV and 20 ± 10 eV, see table 5.1. The best fit for electron density ranged between 0.2 and 1.0 $\times 10^{23}$ cm^{-3}. One of such plots for one of the high intesity drive shots is shown in figure 5.12.

These conditions obtained from the analysis of the scattering spectra are in a good agreement with the 1-D and 2-D hydrodynamic simulations which predict tem-

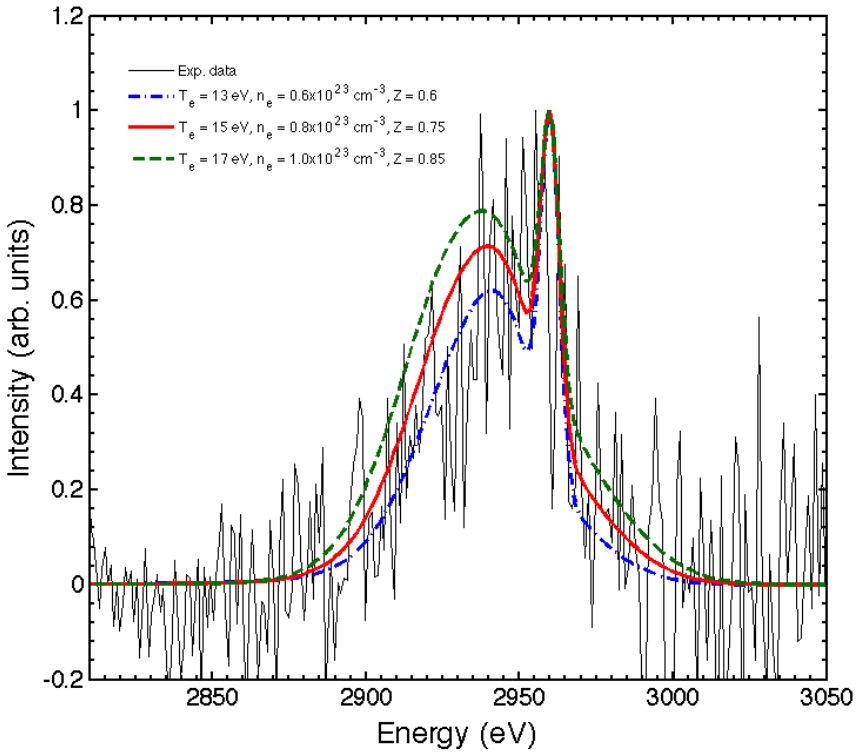

Figure 5.12: RPA fit to the experimental data obtained for higher intensity laser drive at 10^{14} W/cm^2 (shot 54957, Jul 2009). This figure shows plots at $n_e = 0.6 - 1.0 \times 10^{23}$ cm^{-3} for different values of electron temperature (13, 15 and 17 eV), with the best fit at 15 eV.

peratures in the range of $15 - 25$ eV and electron densities $\sim 1.0 \times 10^{23}$ cm^{-3}. The predicted ionization state was high $Z = 0.7 - 1$, which is consistent both with the experiment as well as the DFT-MD simulations.

Improved signal-to-noise ratio

The final scattering data set has been obtained on a high intensity shot at 10^{14} W/cm^2 (shot 63214, Aug 2011) when a new target design with a different set of alignment reticules and Parylene D as a new backlighter foil material. With Parylene D the x-ray backlighter probe was significantly brighter and a 10× stronger scattering signal was observed, see figures 5.5 and 5.6. These upgrades in the target design thus significantly improved the signal-to-noise ratio and constrained the error bars in the scattering measurement.

2-D hydrodynamics simulations of the experiment were performed with the *DRACO* code with the higher intensity drive input as described in section 5.3, the results of

these simulations are shown in figure 5.3. These results predict a peak compressed mass density $\rho \sim 0.8$ g/cm3, $T_e \sim 5 - 15$ eV, and $Z \sim 0.5 - 1$ for the shocked liquid deuterium. Since the measured scattered x-ray spectrum is spatially integrated, it includes contributions from shocked, unshocked liquid deuterium and the decompressed plasma behind the dense shock with a large range of different plasma conditions.

An equivalent spatial integration was applied to the 2-D simulation to calculate the average plasma conditions as would be seen by the scattering measurement. Since the simulations were run in cylindrical geometry and given that the total number of scattered photons is proportional to the number of particles in the scattering volume, the mass density and volume averaged values for electron density, thermal velocity ($v_t = (k_B T_e/m_e)^{1/2} \propto T_e^{1/2}$) and ionization were obtained from the following generalized relationship:

$$< F_n >= \frac{\int F_n(r,z).\rho(r,z).rdrdz}{\int \rho(r,z).rdrdz}, \tag{5.9}$$

where $F_1(r,z) = n_e(r,z)$, $F_2(r,z) = T_e^{1/2}(r,z)$ and $F_3(r,z) = Z(r,z)$ while z denotes the dimension along the H7−H14 axis and r is the dimension along the radius of the cryo cell. The average temperature is thus obtained from the thermal velocity since the observed Doppler broadening of the inelastic peak in the scattering spectrum is given by $\Delta E \sim k.v_t \propto T_e^{1/2}$. The averaged thermodynamic quantities obtained from the *DRACO* simulation are $n_e \approx 0.5 \times 10^{23}$ cm^{-3}, $T_e \approx 3$ eV and $Z \approx 0.3$ respectively. These values were then compared with the scattering measurement and served as input parameters for DFT-MD simulations.

The incident spectrum of the Cl Ly-α emission is shown in figure 5.13 (a) and the scattered spectrum is shown in figure 5.13 (b). The incident spectrum is measured by directly irradiating a Parylene D foil target on a separate laser shot. The scattered spectrum has a strong Rayleigh peak around 2960 eV and a distinct Compton downshifted feature. The splitting of the Cl Ly-α emission is observed in the scattered spectrum, but not in the incident spectrum, due to differences in the amount of source broadening in each measurement (i.e. the backlighter plasma is bigger than the scattering volume). Scattered x-ray spectra were calculated using the x-ray scattering (XRS) code, which uses the finite temperature RPA with static local field correction [26, 139] to obtain the shape of the inelastic (Compton) feature.

On the other hand, as discussed in Ref. [105], the elastic scattering intensity strongly depends on the degree of ion-ion correlations in the plasma via the ion-ion static structure factor $S_{ii}(k)$. In order to constraint the value for S_{ii} we have

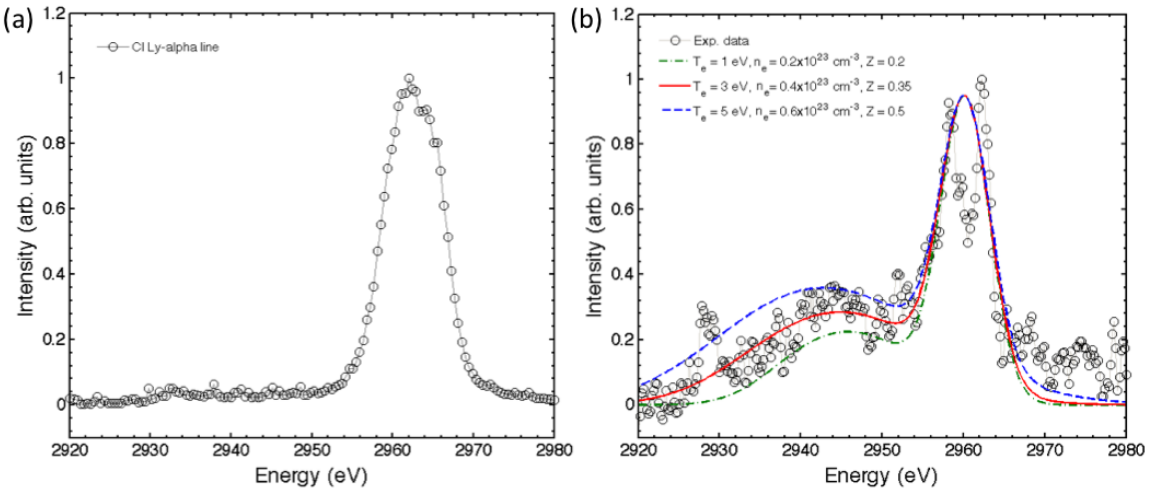

Figure 5.13: Measurement of (a) Cl Ly-α emission incident on shocked liquid deuterium (shot 63212, Aug 2011) and (b) Cl Ly-α emission scattered from shocked liquid deuterium (shot 63214, Aug 2011). The scattered spectrum has a strong Rayleigh peak around 2960 eV and a Compton-downshifted feature. The splitting of the Cl Ly-α emission is observed in the scattered spectrum, but not in the incident spectrum, due to differences in the amount of source broadening in each measurement. The scattered spectrum was fitted with the x-ray scattering (XRS) code and $T_e = 3 \pm 2$ eV, $n_e = 0.4 \pm 0.2 \times 10^{23}$ cm^{-3} and $Z \sim 0.35 \pm 0.15$ were inferred.

performed DFT-MD simulations using the VASP package [178, 37]. The simulations indicate that for the average plasma conditions (see figure 5.14), there are weak correlations (i.e. no visible peaks or valleys in the plot of the $S_{ii}(k)$ vs. k) in the deuterium plasma, with S_{ii} close to unity at the scattering wavenumber relevant for this experiment ($ka = 2.1$).

The plots in figure 5.13 were thus created using a new more advanced version of the XRS code, where the input to the calculation of the scattering spectra as well as T_e, n_e and Z also included a fitting parameter I_{ii}^{fit}, which determines the overall intensity of the Rayleigh peak. This means that $|f_I(k) + q(k)|^2 S_{ii}(k) = I_{ii}^{fit}$ has been set equal to the value given by that parameter. However, since $f_I(k)$ and $q(k)$ are both non-zero and determined by the specific calculation, this is equivalent to forcing $S_{ii}(k)$ to be equal to a constant value. If I_{ii}^{fit} is used, the static model (OCP or SOCP) is not used and S_{ii} is always given by $S_{ii} = I_{ii}^{fit}/|f_I(k) + q(k)|^2$ and provided as an output after each XRS calculation. The input values were varied until the output of the XRS calculation agreed with $S_{ii} = 1$ as predicted by the DFT-MD simulations. The best fit to the scattering measurement was found for $T_e = 3$ eV, $n_e = 0.4 \times 10^{23}$ cm^{-3}, $Z = 0.35$ and $I_{ii}^{fit} = 0.3$ with no local field correction ($G(k) = 0$) giving

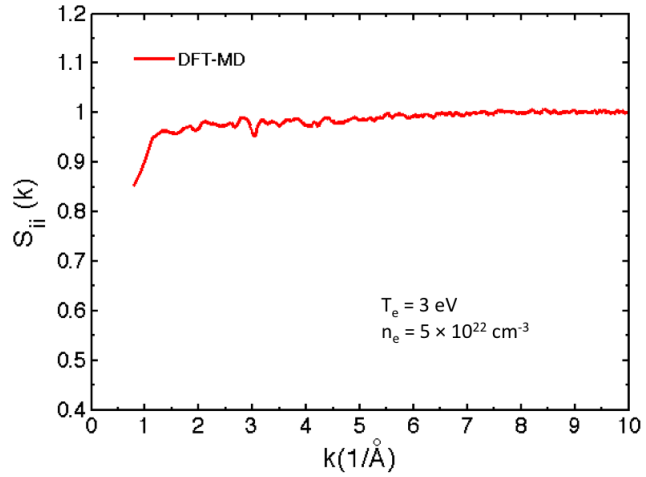

Figure 5.14: Ion-ion static structure factor $S_{ii}(k)$ from DFT-MD simulations for the average plasma conditions obtained from the 2-D *DRACO* simulations with the higher intensity drive.

$S_{ii} \approx 0.95$, which is in good agreement with DFT-MD simulations.

The effective temperature can be estimated using the relations in equation 1.12 giving $T_e^{cf} = 5.2$ eV for the conditions obtained from the scattering measurement above. This value can be substituted instead of temperature in the relationship for the Debye length, equation 1.1, obtaining a screening length λ_s valid in the moderate coupling and degeneracy regime. This then gives the scattering parameter $\alpha = 1/k\lambda_s = 0.57$. In addition to Doppler broadening proportional T_e, the width and position of the inelastic feature are also dependent on the density contribution n_e for our value of scattering parameter $\alpha \approx 0.5 - 0.6$. This allows us to bracket the electron density and estimate the ionization charge based on the initial mass density of the sample. The simulated scattering spectra computed using XRS were used to find the error margin from the noise levels providing the range of plasma conditions $T_e = 3 \pm 2$ eV, $n_e = 0.4 \pm 0.2 \times 10^{23}$ cm^{-3} and $Z \sim 0.35 \pm 0.15$. These values are in agreement with the *DRACO* simulations, see figure 5.3.

5.6 Results and discussion

In conclusion, this work reports the first experimental observation of non-collective, inelastic x-ray scattering from shocked liquid deuterium. A full set of thermodynamic conditions including the electron temperature T_e, electron density n_e and an average ionization Z were inferred from the line shape of the elastic (Rayleigh) and inelastic

(Compton) components in the measured scattering spectra. 1-D and 2-D hydrodynamic simulations utilizing equation of state models relevant to inertial confinement fusion research and planetary interiors indicate that the predicted average state of the probed plasma is in close agreement with the x-ray scattering measurements. This is a significant step towards measuring all the thermodynamic variables needed for EOS research including pressure P, mass density ρ, electron density n_e, electron temperature T_e, and ionization Z by combining simultaneous inelastic x-ray scattering observations with shock velocity measurements (VISAR) and optical pyrometry (SOP).

The electron densities and temperatures measured in the various experiments, including both VISAR and SOP as well as x-ray scattering runs, ranged between 0.3 and 2.15×10^{23} cm^{-3} and $0.6-20$ eV, a set of WDM conditions directly relevant to the interiors of giant gaseous planets [2]. A full set of the measured thermodynamic conditions obtained from all the experiments employing different diagnostics (XRTS, VISAR and SOP) and simulations are summarized in table 5.1. There is an observable difference in temperature between the higher drive experiments and between the earlier and later experiments, which is attributed to the different target design with more efficient cooling system, different backlighter and alignment system which can all contribute to different plasma conditions being created during the experiment.

The conditions inferred from the scattering measurements yielded a range of values for the degeneracy parameter (ratio of thermal and Fermi energies) of $\Theta = T_e/T_F \sim 0.1-2.5$, Wigner-Seitz parameter $r_s = d/a_B \sim 2-3$ and an ionic coupling parameter $\Gamma_{ii} = e^2/4\pi\epsilon_0 dk_B T_e \sim 0.6-10$. The analysis confirms that the state of matter created falls into the WDM regime of moderately-to-strongly coupled, partially or fully degenerate plasma at conditions equivalent to the interiors of giant planets. Previous experiments and simulations suggest that the DFT-MD simulations provide an accurate description of such states [2, 105] in favor of chemical models such as SESAME table [17] or the Saumon and Chabrier EOS model [122].

It should be noted that the conditions measured by x-ray scattering are not strictly the Hugoniot conditions as measured by VISAR and SOP. An Al or quartz pusher is generally used during shock velocity measurement experiments, which maintains a steady shockwave with homogeneous conditions and minimizes the effects of preheat resulting from strong laser drives. However such a pusher cannot be used during scattering experiments as the stray scattering from the pusher itself would be significantly stronger than the signal from the deuterium and would render this measurement impossible. Thus, in this experiment no pusher was used. The only reliable velocity

Table 5.1: Summary of results. Data set no. 1 is from the previous experiment, where density and pressure were obtained from a VISAR measurement combined with DFT-MD EOS and temperature directly measured by SOP for lower intensity drive (10^{13} W/cm^2) with additional density and pressure measurements (ρ = 0.72 g/cm^3 and 37.5 GPa). Data set 2 includes the shock front conditions extracted from the HELIOS simulations for the low intensity 10^{13} W/cm^2 (with ρ = 0.72 g/cm^3), which are comparable with the VISAR and SOP measurements. Cases 3 to 6 correspond to XRTS measurements of n_e, T_e and Z. Data set no. 3 was from XRTS measurement carried out at 6 ns from the start of the lower intensity drive (equivalent to the VISAR/SOP experiment). Measurements 4, 5 and 6 were obtained from XRTS between 4 and 5 ns during the higher intensity drive at 10^{14} W/cm^2. Data set 6 was obtained when the new target with the Parylene D backlighter foil and new alignment reticules was used.

Experiment	Electron density (n_e)	Temperature (T)	Ionization (Z)
1. VISAR&SOP low I drive	$2.15\times10^{23} \pm 20\%$ cm^{-3}	0.57 ± 0.05 eV	$0.7 - 1$
2. HELIOS (shock-front) low I drive	$\sim 1.0 \times 10^{23}$ cm^{-3}	~ 1 eV	$0.3 - 0.7$
3. XRTS low I drive	$1.0 - 2.0 \times 10^{23}$ cm^{-3}	$1 - 5$ eV	$0.6 - 0.9$
4. XRTS high I drive	$\sim 0.2 \times 10^{23}$ cm^{-3}	20 ± 10 eV	~ 0.9
5. XRTS high I drive	$0.8 \pm 0.2 \times 10^{23}$ cm^{-3}	15 ± 2 eV	$0.6 - 0.85$
6. XRTS high I drive	$0.4 \pm 0.2 \times 10^{23}$ cm^{-3}	3 ± 2 eV	0.35 ± 0.15

measurement could be taken at the start of the lower intensity drive when the effects of preheat from the laser drive are not significant and this measurement can still lie on the principal Hugoniot. A significant preheat from hard x-rays and energetic particles generated at the laser-plasma interface would change the conditions downstream complicating the velocity measurement and at extreme levels even results in blanking of the VISAR diagnostic. The scattering measurement for the 10^{13} W/cm^2 is then taken at a much later time when the shockwave travelled the maximum distance

within the scattering channel, when the principal Hugoniot conditions are no longer satisfied. The scattering measurement is thus consistent with previous measurements by VISAR and SOP but not identical. The previous VISAR and SOP measurements agreed with the DFT-MD equations of state, however due to the large error bars XRTS is unable to resolve the difference between the physical and chemical models.

The total measured scattering signal consists of contributions from all areas of the scattering channel including any remaining cold material, the dense shock itself and the coronal plasma behind the shock. The intensity of the scattering signal depends on the total number of scatterers and is thus proportional to the electron density and the total volume of the sample. The hot coronal plasma therefore contributes very little due to its low density and only offsets the total signal intensity by a small amount (due the extreme broadening of the signal due to the high temperatures). The scattering from the dense shock depends mainly on the width of the shock and the maximum density achieved. The proportion of the scattering impurity from the cold material is then given by the position of the shock with respect to the edge of the scattering channel at the time of the measurement. If the total volume of the cold material is large enough it can create a significant contribution even at lower density. Since the shockwave created during the lower intensity drive only travelled at ~ 20 km/s and by the time the XRTS measurement was carried out it only reached just over 100 μm into the 500 μm wide scattering channel, much of the cold material remains within the field of view of the spectrometer and the measured scattering signal contains a significant contribution from impurity scattering of unionized matter. Under such conditions, the XRTS analysis was aided by hydro simulations.

In the case of the higher intensity drive at 10^{14} W/cm^2 VISAR cannot be used at all since without a pusher or filter material the preheat is too strong and VISAR blanks immediately. Thus conditions in these experiments are never on the principal Hugoniot. The shockwave created in these experiments is however much faster and thicker, which means that it has travelled to the edge of the scattering channel by 4 ns from the start of the laser drive and the dense region from the majority of the probe x-rays scatter is much bigger resulting in a stronger scattering signal originating from a single shocked region and all the other contributions from the corona and cold material are negligible. Such scattering signals could therefore be successfully fitted with a single calculated profile reliably retrieving the shocked conditions.

Chapter 6

X-ray scattering measurement from hydrogen DAC

6.1 Introduction

A central feature of planetary research and laboratory astrophysics is the creation of extreme high-pressure, high-temperature states of hydrogen and helium. At solid densities and high pressures (above a few GPa) degeneracy and strong inter-particle coupling start to play an important role in determining the equation of state (EOS) of hydrogen, which is still largely unknown in this regime. To date, most experimental efforts have concentrated on creating high density and temperature conditions in fast shocks created by laser ablation [19, 20]. State-of-the-art EOS measurements of laser-driven shocks on pre-compressed H and He samples, which employ specifically designed diamond anvil cells (DAC) that can be used in conjunction with high power laser drive, have been demonstrated using Velocity Interferometer System for Any Reflector (VISAR) diagnostics [94, 95].

While the laser driven dynamic compression reaches higher pressures, DACs that compress the samples statically can be used to create steady state conditions, under which the sample exists in long-term equilibrium, which are more representative of the planetary interiors than laser-shock experiments [21]. X-ray Thomson scattering (XRTS) [81] is capable of providing more EOS information, such as electron temperature, density and ionization state, and VISAR is less applicable at higher pressures while XRTS can still be used in such conditions, making it the preferred method for measurements of the dynamic response of highly compressed H. This chapter thus presents the first XRTS data from statically compressed hydrogen using the diamond anvil cells carried out at the Diamond Light Source (DLS) synchrotron facility at the Harwell Science and Innovation Campus in the UK.

6.2 Experimental setup overview

This proof-of-principle experiment was conducted on the I15 (Extreme Conditions) beamline at DLS, see figure 6.1 (c). The schematic of the experimental set up is shown in figure 6.1 (a).

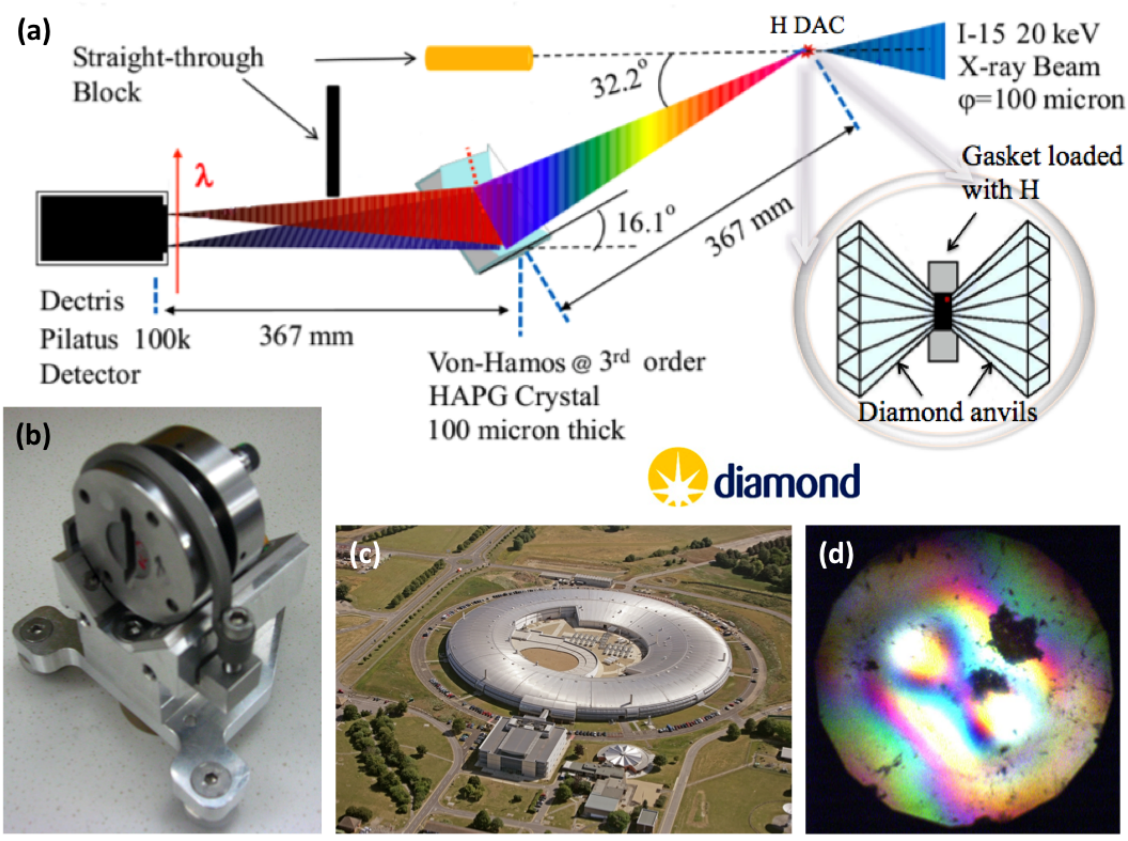

Figure 6.1: Diamond experiment layout including (a) a schematic of the apparatus arrangement with the cylindrically bent HAPG crystal spectrometer in Von Hamos geometry, (b) photograph of the Oxford cell holding the diamond anvils with hydrogen gas load, (c) photograph of the Diamond synchrotron facility (from the DLS website) and (d) microscope view of the compressed H DAC gasket interior with colourful birefringence effect resulting from the strain within the diamond anvils.

The hydrogen gas loaded inside a 0.1 mm thick steel gasket with diameter of 250 μm was compressed using a diamond anvil cell and probed by monochromatic 19 952 eV ($\sim$ 20 keV) x-rays from the synchrotron. The inelastic x-ray scattering spectra from hydrogen DACs at $P_1 = 2.8$ GPa (liquid phase) and $P_2 = 6.4$ GPa (solid phase), probing the phase transition of fluid hydrogen to a polycrystalline solid, were observed in Von Hamos geometry using a curved highly annealed pyrolytic graphite (HAPG)

mosaic crystal [195] coupled with a photon-counting detector (Pilatus 100k). Any radiation coming from the direct line of sight was blocked with a set of thick tungsten beam blocks. The straight-through beam stop was a tungsten rod, up to 3 mm in diameter, and $\sim$ 18 mm long and with a concave cone at the beam side to absorb any side scatter. The scattering angle was $32.2\pm1.1^{\circ}$, corresponding to a regime where the magnitude k of the scattering wavevector ($k = 5.59\pm0.19\times10^{10}$ m^{-1}) is comparable to the Thomas-Fermi screening wavenumber of the electrons ($k_{TF} = 1/\lambda_{TF} = 1.7 \times 10^{10}$ m^{-1}) giving the scattering parameter $\alpha = 0.3$ corresponding to the non-collective scattering regime. The DAC was positioned with 20 μm accuracy, corresponding to an uncertainty of 10 μm ($\sim$ 1 eV) at the detector plane.

The pure hydrogen gas was loaded in the cell prepared by Prof. Andrew Jephcoat using a high pressure apparatus at Oxford. The steel gaskets are first pre-indented using the aligned diamond anvils and a 250 μm hole is drilled at its centre using precision needle drill. The DAC is then reassembled with two ruby spheres loaded within the gasket and the diamond anvils are pushed closer together only leaving a small gap for the hydrogen gas to fill the gasket. The prepared cell is then loaded inside a pressure cylinder used for gas loading connected to a compressed gas pump. During the gas loading process the cylinder is first flushed with pure hydrogen gas at 10 000 psi multiple times to ensure that no air particles remain inside. When all impurities have been removed the hydrogen gas is loaded at 30 000 psi. When the desired pressure is achieved and holds steady, the DAC is manually closed (leaving no gap for the gas to escape again) by turning the screws in the gear box connected through the gas loading cylinder, which can be operated from the outside. When done, the gas loading cylinder is released and the fully loaded hydrogen DAC is ready for experiments.

Before the compression the gasket had a diameter of 250 μm, after compression its diameter decreased to 200 μm an upon release the pinhole was left deformed into and oval shape with long and short axes of $\sim$ 114 μm and $\sim$ 137 μm resulting in slight sample area/volume variation between $\sim 49.2 \times 10^3$ μm^2 for the uncompressed sample and $\sim 31.4 \times 10^3$ μm^2 for H DAC under pressure.

Beamline I15 (Extreme Conditions) operates at optimal energy range of $20 - 80$ keV providing a collimated (beam size $\sim$ 10's of μm), narrowband x-ray probe with a photon flux at sample of 10^9 ph/s at 50 keV. The layout of the beamline set up is shown in figure 6.2. The beamline uses an Si(111) double crystal monochromator to provide the narrow wavelength band incoming x-ray beam with a divergence-limited bandpass/energy resolution of $\Delta E/E \approx 10^{-3}$ (theoretical best $\sim 10^{-4}$). The 1^{st} and

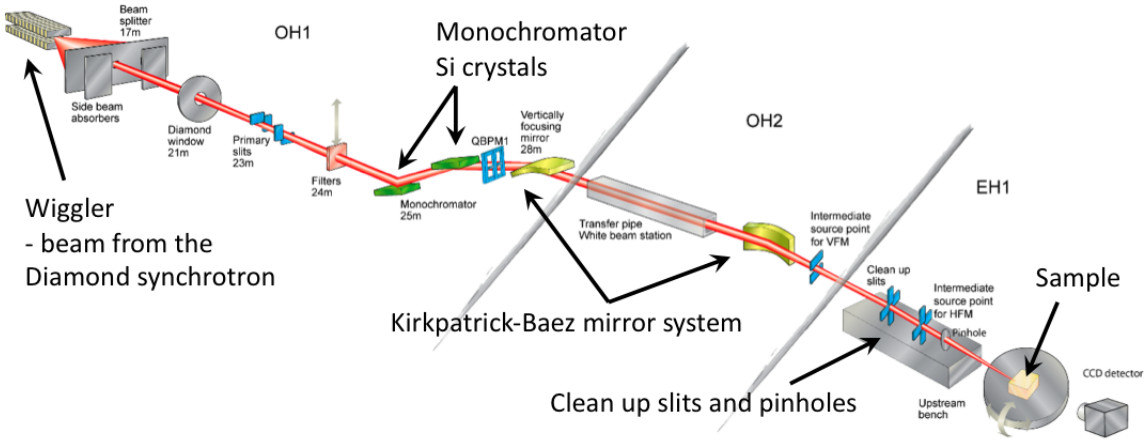

Figure 6.2: Schematic of a layout of the I15 beamline at the Diamond Light Source including the collimating and monochromatic optics systems (image taken from the DLS website).

2^{nd} crystal dimensions are $172 \times 50 \times 70$ mm^3 and $170 \times 20 \times 5$ mm^3 respectively. The monochromator uses cryogenic nitrogen cooling. The large Kirkpatrick-Baez mirror system is used for vertical and horizontal focusing and for rejection of high photon energies. The vertical focusing mirror (VFM) and horizontal focusing mirror (HFM) operate in white and monochromatic beam. The different coatings of the HFM provide a set of cut-off energies at a constant reflection angle. The purpose of the secondary, micro-focusing mirrors (small Kirkpatrick-Baez mirror system) is to provide a focal spot size of the order of 10 μm (FWHM) in the monochromatic beam.

6.2.1 Von Hamos HAPG spectrometer

The crystal spectrometer used in the DLS experiment was set up in the Von Hamos focusing geometry as shown in figure 6.3. In order to obtain a higher signal collection, the HAPG Bragg crystal was curved along the sagittal (non-dispersive) plane with a radius of curvature of $R = 107$ mm. The best focusing in both sagittal and meridional (dispersive) directions is thus achieved when the source-to-crystal and crystal-to-detector are both equal to the Von Hamos focusing length $F = R/\sin\theta_B \sim 384$ mm, where $\theta_B = 16.1°$ is the Bragg angle for the third order diffraction of the 20 keV probe radiation [103, 225]. The spectral resolution of the spectrometer is then given by:

$$\frac{\Delta E}{\Delta y} = \frac{E_0}{2F\tan\theta_B} \approx 94.2 \text{ eV/mm}, \tag{6.1}$$

where y refers to the spatial distance on the detector plane along the dispersive direction and $E_0 = 20$ keV.

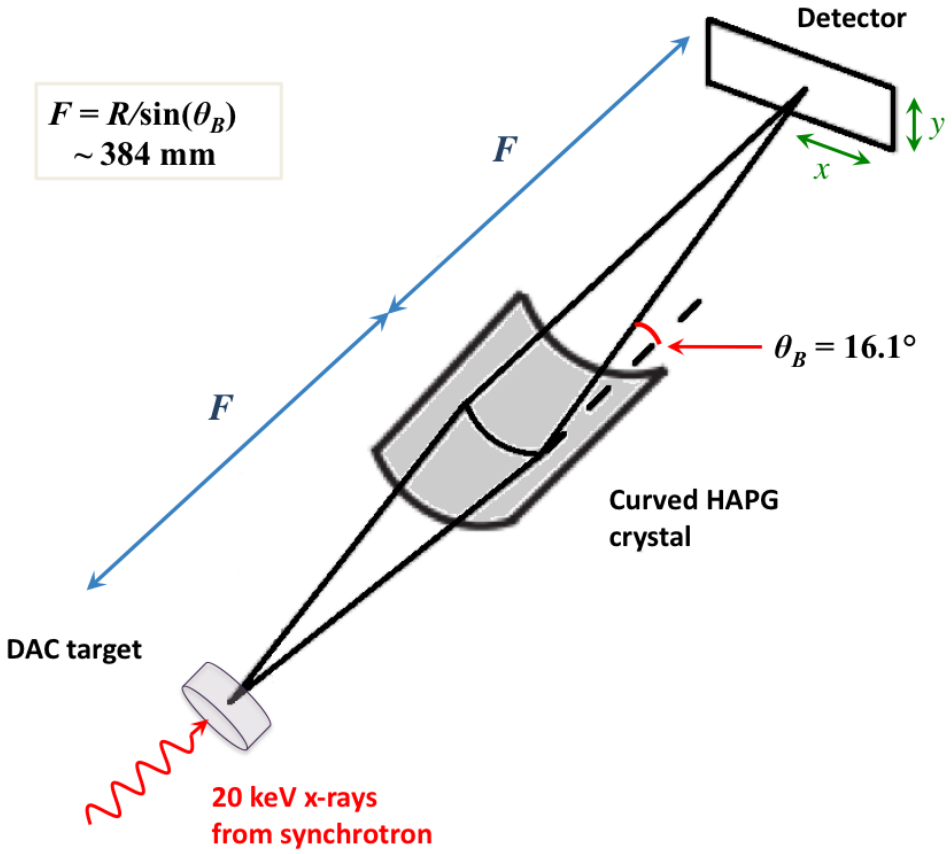

Figure 6.3: The x-ray HAPG crystal spectrometer designed to detect the scattering signal from the hydrogen DAC sample was set up in the focusing Von Hamos geometry to maximize the intensity of the collected data.

The cylindrically bent crystal is used to focus the scattered radiation in the non-dispersive direction (x), which increases the intensity of the measured signal. The flat surface is then placed along the dispersive dimension (y) satisfying the Bragg condition for the third order diffraction of the ~ 20 keV probe and thus selecting the desired range of wavelengths for the scattering measurement. For technical reasons the detector plane was placed perpendicular to y with its base mounted on the optical table. The source (DAC target) and the centre of the PILATUS detector chip were placed close to the cylindrical axis of the HAPG crystal. The crystal spectrometer thus operated in the mosaic focusing mode where the dispersive dimension also acts as if bent reducing the blurring effect of the source size [101, 199]. This effect was described in more detail in section 3.3.1.

Highly annealed pyrolytic graphite (HAPG) is a similar mosaic graphite crystal to the highly oriented pyrolytic graphite (HOPG) described in section 3.3.1. The main advantage of a HAPG crystal is its much lower mosaicity and with it a better energy resolution similar to Si(111) Bragg crystal and with an integral reflectivity comparable or higher than that of Ge(111) [226, 195]. For large mosaicity a photon has to penetrate much deeper into the crystal before it reaches a crystallite with the correct alignment to reflect from. For crystals with small mosaicity the reflection occurs closer to the crystal surface as the crystallites at the surface screen the crystallites in the depth [226, 195]. Since the reflections do not occur deeper within the crystal the depth broadening effect, described in section 3.3.1, is reduced which in turn improves the energy resolution of the crystal. The thin HAPG crystal was chosen for this experiment, as opposed to the thicker HOPG type with much larger mosaic spread, primarily due to the high energy of the probe. At energies as high as 20 keV, the depth broadening becomes significant due to the larger penetration depth of the x-rays into the graphite [199]. This means that the crystal must be kept thin with a low mosaicity while its reflectivity is still reasonable, which makes the HAPG type an excellent candidate.

6.2.2 PILATUS detector

The PILATUS detector is a novel type of x-ray detector, which has been developed at the Paul Scherrer Institut (PSI) for the Swiss Light Source (SLS). PILATUS detectors are two-dimensional hybrid pixel array detectors, which operate in single-photon counting mode, see figure 6.4 [227]. Each hybrid pixel consists of a preamplifier, a comparator and a counter. The preamplifier enforces the charge generated in the sensor by the incoming x-ray; the comparator produces a digital signal if the incoming charge exceeds a predefined threshold and thus, together with the counter, one obtains a complete digital storage and read-out of the number of detected x-rays per pixel. The PILATUS 100k detector consists of a single module and has 487×195 pixels with a pixel size of 0.172 mm. The active area spans over 84×34 mm^2. Each pixel contains a charge-sensitive preamplifier and shaper, a single-level comparator with a 6-bit individual threshold adjustment, a 20-bit counter with a count rate of ~ 1.5 MHz/pixel/s.

These detectors exhibit several advantages compared to current state-of-the-art CCD and imaging plate (IP) detectors. The main advantages of the photon-counting detectors include: no readout noise, superior signal-to-noise ratio, faster read-out time of 5 ms, a better dynamic range of 20 bit, high detective quantum efficiency and

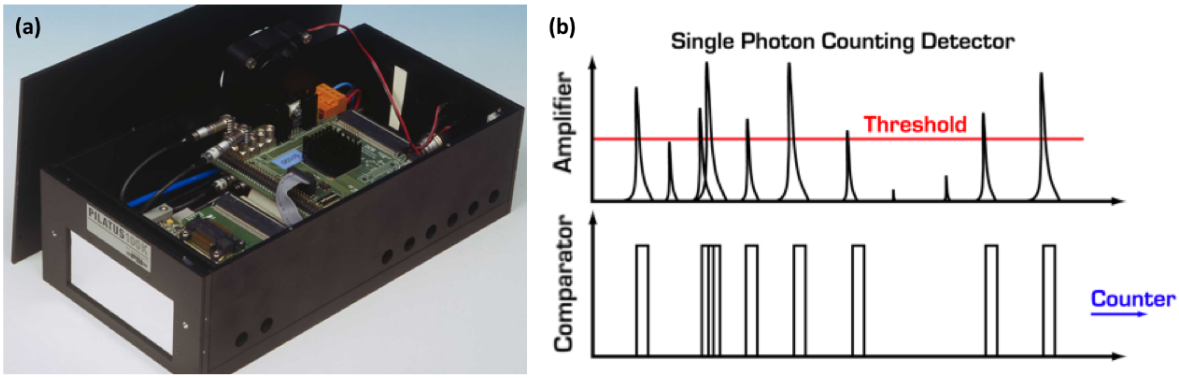

Figure 6.4: The PILATUS 100k photon-counting x-ray detector. Part (a) shows a photograph of an exposed PILATUS 100k detector used at the DLS experiment and part (b) is the graphic representation of the photon-counting detection procedure, after Ref. [227].

the possibility to suppress fluorescence by a energy threshold that is set individually for each pixel. The short readout and fast framing time allow for diffraction data to be taken in continuous mode without opening and closing the shutter for each frame [227].

In the case of the integrating detectors (such as CCD's or IP's), charge is accumulated and then converted. In the case of single photon counting we have an amplifier, an energy threshold for each pixel and a comparator, which sends only those pulses to the counter which are higher than the energy threshold. This thus removes the read-out noise and dark current. A schematic view of the photon counting procedure is shown in figure 6.4 (b). This increases the sensitivity of the detector to weak x-ray signals making it particularly suitable for the study of weak diffraction phenomena such as diffuse scattering.

6.2.3 Pressure and density measurement

The pressure within the anvil cell was measured through the well known relationship for the spectral shift of fluorescence of chromium-doped ruby (Al_2O_3: Cr^{3+}) under pressure [92]. An example of this spectral shift is shown in figure 6.5 (b). One or two small ruby spheres were buried inside the anvil cell together with the hydrogen sample, as shown in figure 6.5 (a), and the fluorescence was measured using an optical laser and a calibrated spectrometer. Ruby is a popular choice for pressure sensor material in DAC experiments due to its high fluorescence intensity and a relatively large pressure shift ($\sim$ 0.365 nm/GPa) [90]. It is chemically inert and thus does

not react with the sample within the gasket. The pressure response of ruby is well documented to high pressures. The I15 beamline operates a blue Laser Quantum solid state laser operating at 473 nm for the ruby measurement. The spectral response of the ruby through optical luminescence was measured using the HR-320 spectrometer from Horiba Jobin Yvon coupled with a CCD detector.

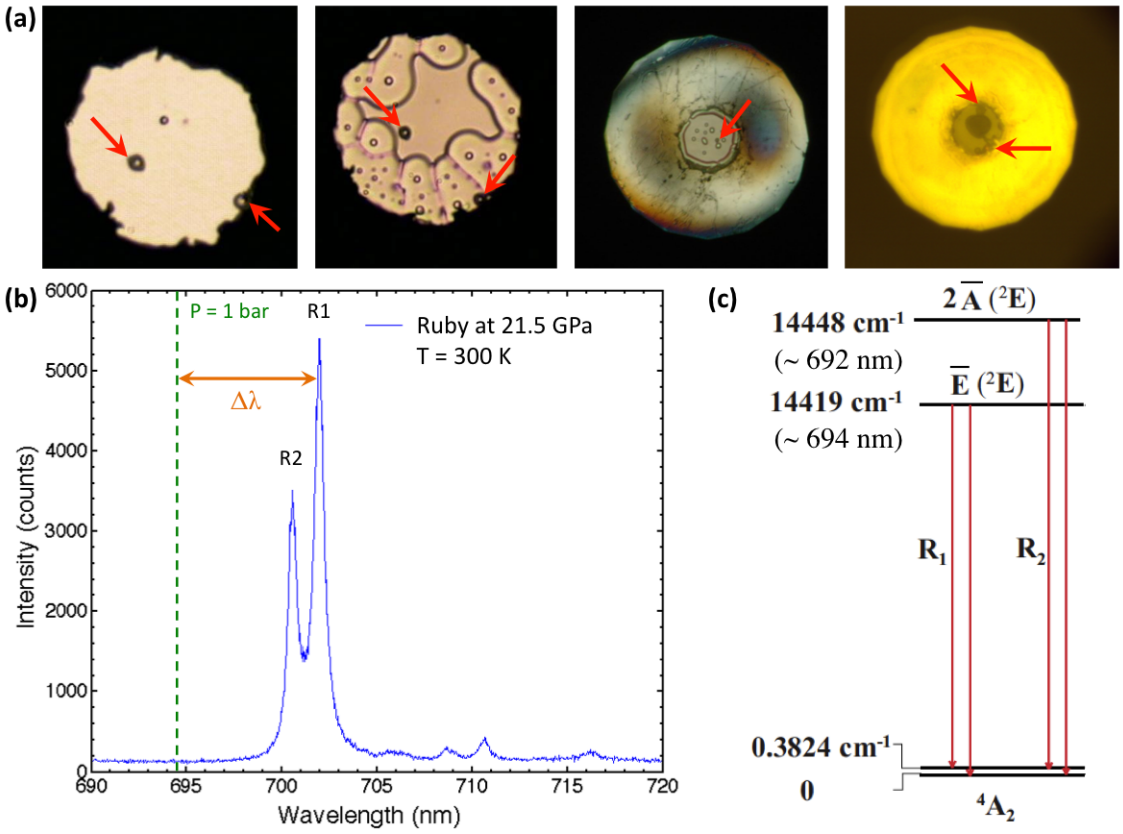

Figure 6.5: Pressure and density measurements of hydrogen DACs. The top images (a) show photographs of the hydrogen loaded gaskets ranging between pressures of 2 and 8 GPa the images show a formation of a solid hydrogen crystal (different cells and systems were used in each picture). The red arrows point out the location of the ruby spheres within the gasket. Image (b) then shows an example of ruby fluorescence spectrum with both R1 (higher intensity) and R2 (lower intensity) lines taken at 21.5 GPa. The position of the R1 line at zero pressure applied at 300 K is marked by the dashed green line, while the arrow points out the redshift of the line for ruby at 21.5 GPa. Part (c) includes a schematic of the transitions between the initial $2\overline{A}$ and $\overline{E}$ and final states $^4A_2$ giving rise to the R1 and R2 emission lines of Cr^{3+} in Al_2O_3: Cr^{3+} (ruby), after Ref. [228].

The Cr^{3+} ions occupy a trigonal site in a sapphire Al_2O_3 lattice as an impurity replacing Al. The effects of the trigonal distortion, crystal-field effects and spin-orbit

coupling due to the impurity give rise to strong absorption bands in the green (U band) and blue (Y band) spectral ranges, which gives ruby its characteristic red colour [228]. Electrons optically excited (e.g. by a laser) into the broad U and Y bands non-radiatively decay into the metastable $2\overline{A}$ and $\overline{E}$ states. From these states the electrons decay radiatively into the $^4A_2$ ground state, see figure 6.5 (c). At room temperature (300 K) and ambient pressure (1 bar) ruby thus has two sharp emission lines R1 and R2 at 694.2 and 692.8 nm respectively, emitted by the Cr^{3+} ions.

The ruby fluorescence lines R1 and R2 shift towards longer wavelengths with increasing pressure due to a combination of complicated mechanisms. Their description is beyond the scope of this thesis but details on these processes can be found in Refs. [229, 230, 231, 92]. The pressure measurement using the ruby gauge was first introduced and calibrated against the Decker equation of state for NaCl up to 19.5 GPa by Barnett *et al.* [91] and Piermarini *et al.* [232] who found the approximate linear relationship of the spectral shift of the R-lines to pressure. An improved relationship was suggested by Mao *et al.* [233], where the fluorescence is calibrated against the room temperature isotherms of Cu and Ag. The following equation was thus devised for quasi-hydrostatic conditions:

$$P = A \cdot \left[\left(1 + \frac{\Delta\lambda}{\lambda_0} \right)^B - 1 \right], \tag{6.2}$$

where pressure P is in GPa, $\lambda_0 = 694.24$ nm is the ruby R1 at ambient conditions (1 bar and 300 K), $\Delta\lambda$ is the R1 line wavelength shift in nm, and constants $A = 248.4$ GPa, $B = 7.665$ for quasi-hydrostatic conditions [233]. This quasi-hydrostatic scale was calibrated up to 80 GPa, above this pressure the scale was extrapolated. For non-hydrostatic conditions (at pressures > 100 GPa) $A = 380.8$ GPa and $B = 5.0$. Since then other calibration scales for ruby have appeared [234, 235, 236]. These scales were then united in the review article by Syassen [92]. A new revised pressure scale, based on equally weighted least-squares fitting method to fit the combined data for pressures up to 150 GPa, was proposed:

$$P = A \cdot \left(\frac{\lambda}{\lambda_0} - 1 \right) \left[1 + B \left(\frac{\lambda}{\lambda_0} - 1 \right) \right], \tag{6.3}$$

where λ is the redshifted wavelength of the R1 line, $A = 1870$ GPa and $B = 5.9$. This expression deviates by less than 1.5% for the three calibrations [234, 235, 236] in the pressure range $0 - 150$ GPa [92]. There is little difference to Mao *et al.* [233] scale for pressures < 50 GPa, thus both scales can be used for the purposes of the DAC experiments described in this work.

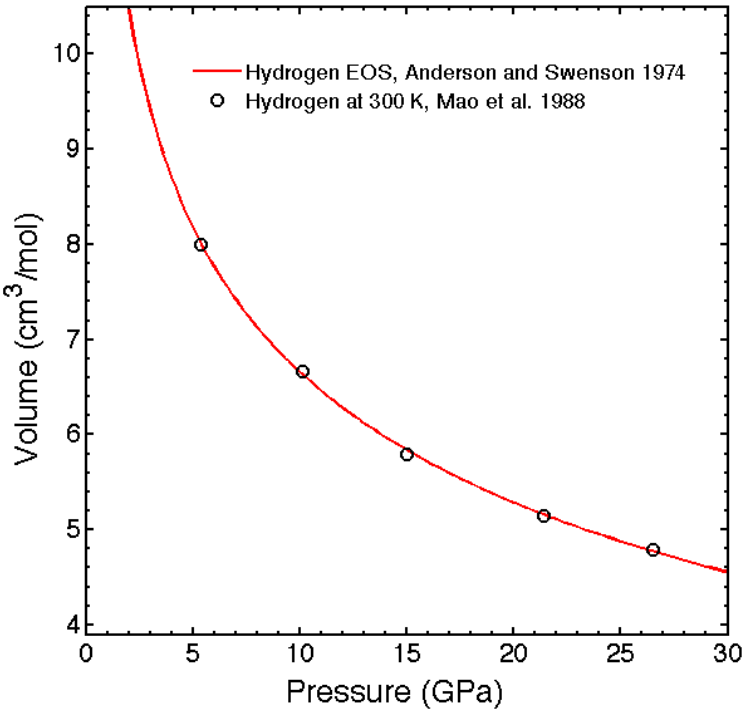

Figure 6.6: The hydrogen EOS measurements as presented by Mao *et al.* in Ref. [21] (black circles). The data is fitted with a modified power-series based on the Birch relation (red line) giving the Anderson and Swenson hydrogen EOS [237].

Since the pressure and temperature of the hydrogen in the anvil cell are known (room temperature, T = 300 K) the electron density could be determined from the equation of state (EOS) data for compressed hydrogen experimentally determined by Mao *et al.* in Ref. [21] using x-ray diffraction technique, where a unit-cell volume of a substance can be accurately measured. Their measurements of pressure and density of hydrogen are shown in figure 6.6. The best fit to this experimental data was found to be the hydrogen EOS by Anderson and Swenson [237], which employ a modified power-series based on the Birch relation fitted to their original data obtained from piston-displacement experiments. The density (ρ_n in cm^3/mol) information was read off the plots provided in Refs. [21] and [237], see figure 6.6. The electron densities were then found from simple relations $n_e = N_A/\rho_n$, where $N_A = 6.022 \times 10^{23}$ is Avogadro's number. The number densities were found to be 6.0×10^{22} cm^{-3} for P_1 and 7.9×10^{22} cm^{-3} at P_2 at which hydrogen is fully degenerate (see table 6.1). The rest of the quantities in the table were calculated from the known values for the electron density.

Table 6.1: Physical parameters in compressed hydrogen. The Wigner-Seitz radius given by $d = (3/(4\pi n_e))^{1/3}$ is the inter-particle spacing at electron density n_e and a_B is the Bohr radius.

	$P_1 = 2.8$ GPa (liquid)	$P_2 = 6.4$ GPa (solid)
Brueckner parameter, $r_s = \frac{d}{a_B}$:	2.99	2.74
Fermi energy, $E_F = \frac{\pi^2\hbar^2}{2m_e}\left(\frac{3n_e}{\pi}\right)^{2/3}$:	5.6 eV	6.7 eV
Degeneracy parameter, $\theta = \frac{k_B T}{E_F}$:	0.0046	0.0039
Plasma frequency, $\omega_p = \left(\frac{n_e e^2}{\varepsilon_0 m_e}\right)^{1/2}$:	9.12 eV	10.4 eV

6.3 Scattering data analysis

Pure air scatter (background, i.e. scattering signal obtained when the sample was removed keeping all other conditions the same) images were subtracted from the 1800 sec exposure PILATUS 100k spectra of empty and H loaded DACs at pressures of 2.8 and 6.4 GPa. Line-outs of 50×195 pixels were taken (exactly the same pixels for each image). The total intensity of each scattering spectrum (empty cell, and H loaded DAC at 2.8 and 6.4 GPa) was scaled by readings of the ring current, the electron current in the storage ring, which is proportional to the total x-ray output from the synchrotron, and x-ray intensity readings from a diode placed just before the DAC for each shot, which provided an additional intensity corrections due changes in the apparatus alignment during the experiment.

This was necessary as the electron current in the synchrotron gradually decreases between the fills into the storage ring (done $\sim$ every day) resulting in lowering of the x-ray probe intensity. The intensity of the Diamond beam is also attenuated by any adjustments in energy and position of the I15 beamline x-ray optics that may occur between taking the shots. The dispersion was found from the Pilatus images of relative shifts in energy of the measured spectra by varying the wavelength of the I15 beamline giving a spectral resolution of $\sim$ 17 eV/pixel. The absolute energy calibration was found using the Pd-edge absorption, see figure 6.7 (b).

6.3.1 Spectral calibration

The I15 beam line output was set roughly to the desired 20 keV narrow band x-ray source using a set of monochromating crystals as described above. However, the exact energy of the probe x-rays was unknown as thus had to be measured exactly in order

to correctly calibrate the measured spectra. The dispersion as calculated from the geometrical set up of the HAPG crystal spectrometer was estimated to be ~ 94.2 eV/mm = 16.2 eV/pixel (with 0.172 mm pixels).

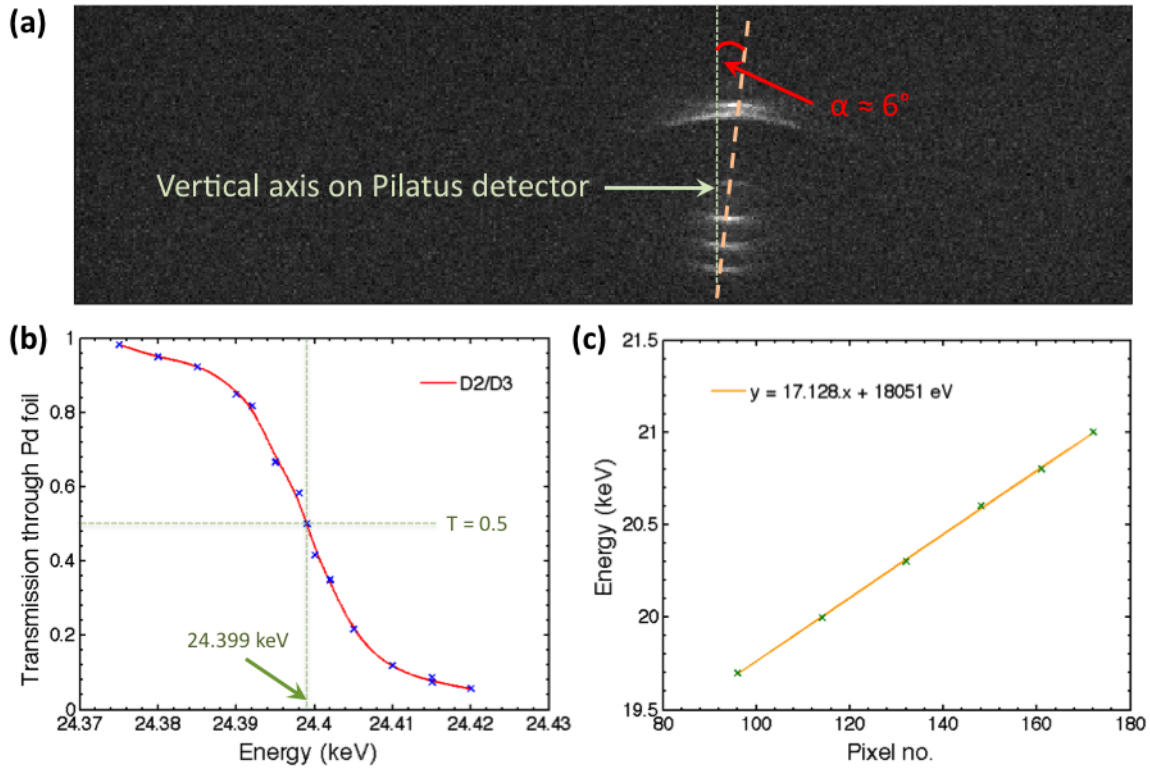

Figure 6.7: The energy calibration of the HAPG crystal spectrometer. Image (a) shows overlayed data sets for various energies in the $19 - 21$ keV range showing the system dispersion as well as an obvious $\sim 6°$ tilt in the spectra direction away from the vertical direction, (b) shows transmission scan across the Pd K-absorption edge at 24.351 keV, and (c) shows the linear fit to the dispersion calibration obtained from part (a).

The actual dispersion of the spectrometer was calibrated using the Diamond facility capability to change the energy of the output x-ray beam from the synchrotron. The narrow energy band radiation was selected using a set of monochromatic crystals, while the roughly calibrated system would provide the approximate energy of the beam. The alignment of the monochromatic crystals was then varied to provide different beam energies ranging between 19 and 21 keV (as read by the I15 beamline control system). The overlayed spectral images obtained for the different beam energies are showed in figure 6.7 (a). The experimental verification of the dispersion calibration exhibits a good linear fit to the pixel location of the various energies within

the $19 - 21$ keV range giving the dispersion of ≈ 17.1 eV/pixel (see figure 6.7 (c)), which is a good agreement with the theoretical value and the difference is attributed to the uncertainty in the system alignment.

Prior any manipulation all data images are also subtracted by background/air scattering for a given exposure time and probe energy. Despite the best efforts aligning the Bragg crystal the spectral axis as seen in the detector plane (Pilatus 100k chip) is not parallel to the vertical axis, but exhibits a slight tilt of $\alpha \approx 6.7 \pm 0.05°$, see figure 6.7 (a). All measured data therefore have to be corrected for this tilt by rotating the image before spectral lineout can be taken prior the analysis.

The offset of the spectrum was obtained from the Pd K-shell absorption edge (24.351 keV). A set of photodiodes before (D2) and after (D3) 47 μm thick Pd foil was used to measure its transmission through the experimental measurement of the D2/D3 intensity ratio while scanning through a range of beam energies across the Pd edge. Figure 6.7 (b) shows the transmission curve across the energy range of $24.375 - 24.42$ keV (these numbers correspond to the system energy values, not the actual calibrated energy). The transmission T = D2/D3 = 0.5, assumed to be the central energy of the Pd K-shell absorption edge at 24.351 keV, while the DLS system read 24.399 keV, which corresponds for 48 eV shift towards the lower energy. This means that all spectra (plotted using the relationship in figure 6.7 (c)) have to be offset by this shift in order to obtain the correct energy axis. Thus the 20 keV beam as set by the beamline systems was in fact 19.952 keV. Uncertainties in the synchrotron energy (as determined using a Pd filter) were also found to be within ± 1 eV, which is comparable to the energy error due to target/DAC positioning, see above. This error estimate was obtained from the variation in the D2 and D3 diode readings.

6.3.2 Data reduction

The scattering spectra obtained from the diamond anvil cells loaded with compressed hydrogen were dominated by the Compton scattering from the diamond anvil obscuring the hydrogen data of much lower intensity. The weak scattering signal from hydrogen compared to the diamond is a result of the small sample volume needed to achieve high compression of the hydrogen gas within the larger anvils (the x-rays travel through 4 mm of diamond while the thickness of the H sample is only 0.1 mm) and the fact that each C atom has many more electrons to scatter from than the H atoms.

In order to compensate for the dominant scattering from the diamond, we retrieved the hydrogen scattering data in the form of a ratio of spectra from hydrogen

at P_1 and P_2 through a careful reduction analysis procedure using the measured signal referenced to the empty cell. The ratio of the 2.8 GPa to 6.4 GPa spectra was computed using the following equations. The empty cell scattering spectrum corresponds to:

$$I_0 = B \cdot S_{anvil} \tag{6.4}$$

And the scattering spectrum of hydrogen loaded DAC at pressures $P_1 = 2.8$ GPa (liquid hydrogen) and $P_2 = 6.4$ GPa (polycrystalline solid):

$$I_{P_1} = A_{P_1} \cdot (S_{anvil} + S_H^{P_1}), \tag{6.5}$$

$$I_{P_2} = A_{P_2} \cdot (S_{anvil} + S_H^{P_2}), \tag{6.6}$$

where A and B are calibration constants, which depend on the absolute response of the measuring apparatus and their ratio is a well defined quantity given by the ratio of average background noise levels of the empty and H loaded DAC spectra, and S_{anvil}, $S_H^{P_1}$ and $S_H^{P_2}$ are the dynamic structure factors proportional to the total spectral intensity of the scattering signal from the diamond anvils only and hydrogen at pressures P_1 and P_2, respectively. The expressions 6.4, 6.5 and 6.6 can then be combined to give the experimentally determined ratio of the scattering signals from compressed hydrogen at the two pressures (liquid and solid phases) linked to the known response of the empty cell:

$$\frac{S_H^{P_1}}{S_H^{P_2}} = \frac{(B/A_{P_1})(I_{P_1}/I_0) - 1}{(B/A_{P_2})(I_{P_2}/I_0) - 1} \tag{6.7}$$

Since the quantity on the RHS of equation 6.7 is directly obtained from the experimental data using the measured spectra from the empty cell and the DACs loaded at the two pressures, the ratio $S_H^{P_1}/S_H^{P_2}$ is well defined.

6.3.3 Data smoothing

The quantity on the RHS of equation 6.7 was obtained directly from the experimental data using the lineouts from the PILATUS spectra of empty and H loaded DACs at pressures of $P_1 = 2.8$ GPa and $P_2 = 6.4$ GPa providing the ratio of the scattering spectra at the two different pressures. The result gave a noisy spectrum. Therefore various Matlab codes were developed to smooth the spectral ratio which included

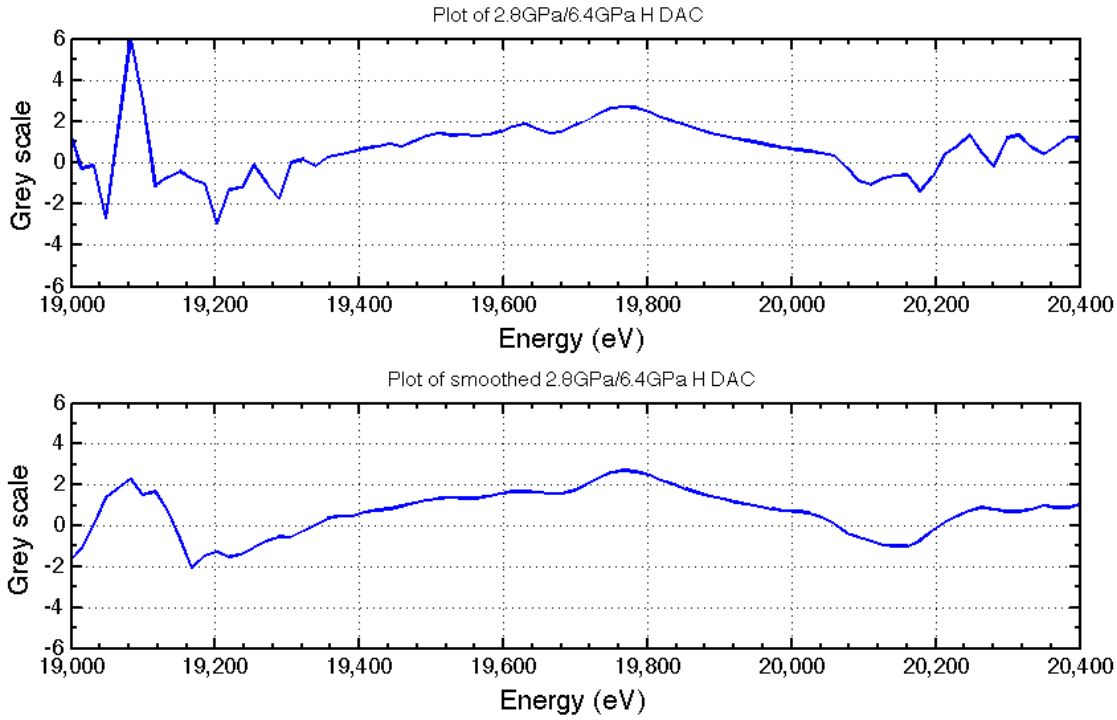

Figure 6.8: Comparison of original spectral ratio of H DAC data signals obtained from equation 6.7 before (top plot) and after (bottom figure) the Savitzky-Golay smoothing filter was applied.

the low pass filter, high frequency noise filter employing the fast Fourier transforms (FFT) and the Savitzky-Golay smoothing method [238].

The Savitzky-Golay code turned out to be the most effective for our data, see figure 6.8. This method makes use of the least-squares technique that fits a high order polynomial to the data, which essentially performs a local polynomial regression (of degree n) on a distribution (of at least $n+1$ equally spaced points). The main advantage of this method is that it preserves the shape including the maxima, minima and width of peaks unlike the other methods mentioned above. The code employed a moving window of adjustable size, over which a polynomial of a higher order (also adjustable) was fit, and the newly computed values were then averaged to draw the new smooth plot [239]. The optimal polynomial order for this plot was $n = 4$. This filter preserved the shape of the scattering spectra between 19.5 keV and 20 keV, while it reduced most of the strong peaks outside this range, where no scattering signal was observed, but the background subtraction of small values resulted in high amplitude spikes.

6.4 Local field correction (LFC) measurement

The principle of local field correction (LFC) $G(k, \omega)$ was outlined in section 2.2.2 in part describing the free electron term in the scattering spectrum. LFC characterizes the strong coupling effect between free electrons through measuring the difference between the bare Coulomb interaction and the screened response. These effects result from the higher interaction terms, which become important under the conditions of the Diamond experiment. The LFC incorporates the short-range correlations neglected by the RPA into the expression for the free electron-electron structure factor, equation 2.20. The effect of non-zero values of LFC therefore manifests itself through spectral shifts of the Compton feature in the scattering spectrum, which is a measurable quantity. Local field correction can be linked to dynamic properties of the compressed material, namely the isothermal compressibility and conductivity, thus a non-zero value of LFC has a direct impact on the EOS.

The most common assumption used in computing the LFC is to describe it as a weak function of frequency, i.e. the static local field correction (SLFC): $G(k, \omega) \rightarrow G(k)$. Various approaches to calculate the SLFC are summarized in Refs. [26, 240] including the long-wavelength limit expression $G(k \rightarrow 0)$ given by the compressibility rule and the short-wavelength $G(k \rightarrow \infty)$ limit where LFC is written in terms of the electron-electron pair distribution function at $r = 0$ as suggested by Kimball [149, 150]. For simplicity, in this work we concentrate on the description of static LFC in the limit of $k \rightarrow \infty$, which can be calculated by the simple parametric expression provided in its explicit form in Refs. [26, 139]. The static local field correction already gives a considerable improvement to the RPA, although the full dynamic local field correction (DLFC) may be necessary for the correct modelling of strong coupling at frequencies $\omega \gtrsim \omega_p$, where ω_p is the electron plasma frequency (equation 1.3) [240].

6.4.1 LFC from Compton spectral shift

Since we only obtained the ratio of the scattering signals of hydrogen at the two different pressures $S_H^{P_1}/S_H^{P_2}$ (see equation 6.7), the dynamic structure at a given pressure has to be retrieved from this ratio using a known result for the other pressure. This is a ratio of signals from liquid and solid hydrogen with significant structural differences. In the next step, the experimentally determined ratio was multiplied by a synthetic spectrum to obtain a dynamic response of fluid hydrogen. The inelastic scattering response from solid hydrogen at $P_2 = 6.4$ GPa was calculated using a code that implemented the zero temperature RPA described in section 2.2.3 and Appendix

B. The spectrum for liquid hydrogen at $P_1 = 2.8$ GPa (solid blue line in figure 6.9) was then retrieved from the experimental ratio (see equation 6.7) multiplied by the calculated spectrum for solid hydrogen.

P_2 has been chosen for the calculated spectrum, because at the higher pressure we have polycrystalline solid hydrogen (hexagonal close packed) [241]. The electrons are effectively free as they satisfy the Bloch functions for electronic motion inside the periodic potentials within the crystalline lattice of localized ions, i.e. the electrons are weakly coupled with $G(k) = 0$. Since, in our experiment, k lies outside the Brillouin zone boundary, the lattice does not influence scattering from the electrons. This phase is also more degenerate (lower degeneracy factor $\Theta = k_B T/E_F$) resulting from higher Fermi energy making the effects of finite temperature less important. Therefore the calculation of the scattering spectrum for P_2 can be justifiably carried out using the random phase approximation (RPA) at T = 0 K [163].

The electron-electron dynamic structure factor for electrons interacting via Coulomb forces is given by the fluctuation-dissipation theorem (equation 2.16), for $k_B T \ll \hbar\omega$:

$$S_H^P(k,\omega) = \frac{\varepsilon_0 \hbar k^2}{\pi e^2 n_e} \cdot \mathrm{Im}\left[\frac{-1}{\varepsilon(k,\omega)}\right] \tag{6.8}$$

where n_e is the electron density, e the electron charge, ε_0 the permittivity of free space, k is the magnitude of the change in wavevector due to the scattering and ω is the inelastic energy exchange. The dielectric function $\varepsilon(k,\omega)$ relates to the electron susceptibility $\chi(k,\omega)$ as $\varepsilon(k,\omega) = 1 - (e^2/\varepsilon_0 k^2) \cdot \chi(k,\omega)$ [240]. The electron susceptibility can also be written as:

$$\chi(k,\omega) = \frac{\chi_0(k,\omega)}{1 + \frac{e^2}{\varepsilon_0 k^2} G(k,\omega)\chi_0(k,\omega)} \tag{6.9}$$

where χ_0 is the Lindhard susceptibility at T = 0 K and $G(k,\omega)$ is the local field correction [240]. For $G(k,\omega) = 0$, $\chi(k,\omega) = \chi_0(k,\omega)$ and the pure RPA is reproduced. The inelastic spectrum for solid hydrogen at $P_2 = 6.4$ GPa can therefore also be calculated theoretically from equation 6.8 using the dielectric function $\varepsilon(k,\omega)$, calculated from RPA using the equations in Appendix B (with $G(k,\omega) = 0$). The experimental spectrum for $P_1 = 2.8$ GPa is then obtained from this calculated profile multiplying by equation 6.7. In the case of the fluid hydrogen at $P_1 = 2.8$ GPa, the inelastic spectral response can also be calculated, but due to strong coupling effects affecting the position of the free electron peak the local field correction have to be included in the calculation.

The resultant synthetic spectrum for P_1 is overlapped with the experimentally deduced profile (blue line in figure 6.9) with $G(k)$ as a fitting parameter in equation 6.9. We obtained a good overlap of the experimental spectrum with the synthetic profile for $G(k = 5.59 \pm 0.19 \times 10^{10}\ \mathrm{m}^{-1}, \omega \sim 130\ \mathrm{eV}) = -9 \pm 1.5$ (red-dotted line in figure 6.9). The error in the measurement of $G(k, \omega)$ was determined from the uncertainty in the scattering angle $32.2 \pm 1.1°$ given by the uncertainty in the sample and crystal position, which then translates into error in determining the scattering wavevector $k = 5.59 \pm 0.19$ x $10^{10}\ \mathrm{m}^{-1}$. The value of k enters the calculation of the spectral profile and thus changes the position of the experimental plot in figure 6.9. The values of $G(k, \omega)$ of -7.5 and -10.5 respectively were obtained by carrying out the same fitting technique for the two spectra calculated using extreme values of k.

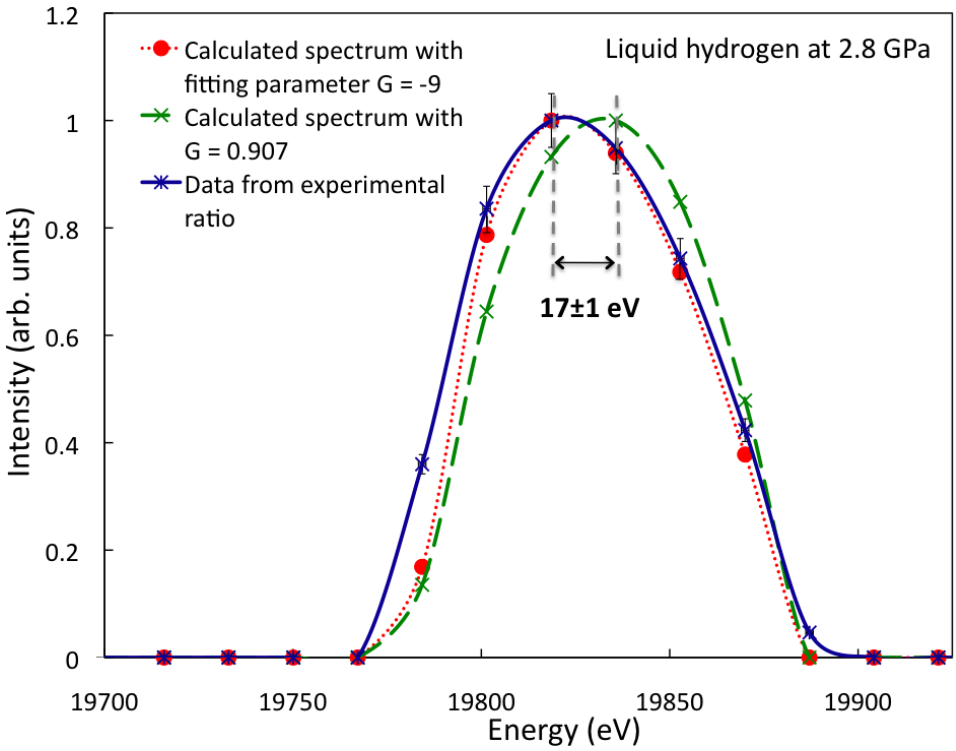

Figure 6.9: Normalized plots of the electron-electron feature of the scattering spectrum for H at 2.8 GPa. The solid blue line is the inelastic response of liquid hydrogen at $P_1 = 2.8$ GPa obtained from the experimentally determined spectral ratio of hydrogen at the two different pressures $S_H^{P_1}/S_H^{P_2}$ (see equation 6.7). The red-dotted line is the calculated spectrum for liquid hydrogen at P_1 using fitting parameter $G(k, \omega) = -9$ with the spectral shift overlapping the experimental spectrum. The green dashed line then corresponds to another calculated profile for hydrogen at P_1 using the static LFC calculated from the Utsumi-Ichimaru theory [242] using equations 6.10 to 6.14 which is $G(k) = 0.907$ for the relevant conditions.

6.4.2 Comparison with Ichimaru LFC

In the previous section the local field correction was retrieved from an experimentally measured spectral shift of the inelastic scattering signal. In this section, this value is compared to a theoretically calculated value for $G(k,\omega)$. Among the best theoretical descriptions available to us at present time is the parametric form of the Utsumi-Ichimaru equations in the short wavelength limit ($k \to \infty$) of the static approximation, i.e. $G(k,\omega) \approx G(k,\omega=0) \equiv G(k)$ [242, 26, 139]:

$$G^0(k) = AQ^4 + BQ^2 + C + \left[AQ^4 + \left(B + \frac{8}{3}A\right)\cdot Q^2 - C\right] \times \frac{4-Q^2}{4Q} \ln\left|\frac{2+Q}{2-Q}\right|, \tag{6.10}$$

where $Q = k/k_F$, A = 0.029,

$$B = \frac{9}{16}\gamma_0 - \frac{3}{64}\left[1 - g_{ee}(0)\right] - \frac{16}{15}A, \tag{6.11}$$

$$C = -\frac{3}{4}\gamma_0 + \frac{9}{16}\left[1 - g_{ee}(0)\right] - \frac{16}{5}A, \tag{6.12}$$

where the electron-electron pair correlation function at $r = 0$ is denoted as:

$$g_{ee}(0) = \frac{1}{8}\left[\frac{z}{I_1(z)}\right]^2, \tag{6.13}$$

with $z = 4(4/9\pi)^{1/6}(r_s/\pi)^{1/2}$, $I_1(z)$ being the modified Bessel function (first kind) of the first order ($n = 1$) and r_s denoting the Wigner-Seitz parameter defined in Chapter 1, equation 1.9. The parameter γ_0 is evaluated in the following way accounting for both exchange and Coulomb-correlation effects [139]:

$$\gamma^0(r_s) = \frac{1}{4} - \frac{\pi(4/9\pi)^{1/3}}{24}\left[r_s^3\frac{d^2E_c(r_s)}{dr_s^2} - 2r_s^2\frac{dE_c(r_s)}{dr_s}\right], \tag{6.14}$$

where the correlation energy $E_c(r_s)$ is obtained from the parametrization:

$$r_s\frac{dE_c(r_s)}{dr_s} = b_0 \cdot \frac{1 + b_1 r_s^{1/2}}{1 + b_1 r_s^{1/2} + b_2 r_s + b_3 r_s^{3/2}} \tag{6.15}$$

substituting for $b_0 = 0.0621814$, $b_1 = 9.81379$, $b_2 = 2.82224$ and $b_3 = 0.736411$.

This expression is particularly applicable in the regime $k \sim 2k_F$, with the Fermi wavenumber expressed as $k_F = (3\pi^2 n_e)^{1/3}$, relevant to the conditions of this experiment ($r_s \approx 3$, $k/k_F \approx 4.6$), where the Utsumi-Ichimaru theory correctly reproduces the peak structure associated with discontinuity in momentum distribution at the

Fermi surface [242]. This simple analytic expression for the static local field correction was obtained from parametrization of numerical data obtained from Green's-function Monte Carlo (GFMC) simulations which included exchange and Coulomb-correlational effects in the degenerate electron fluid [242, 26, 139].

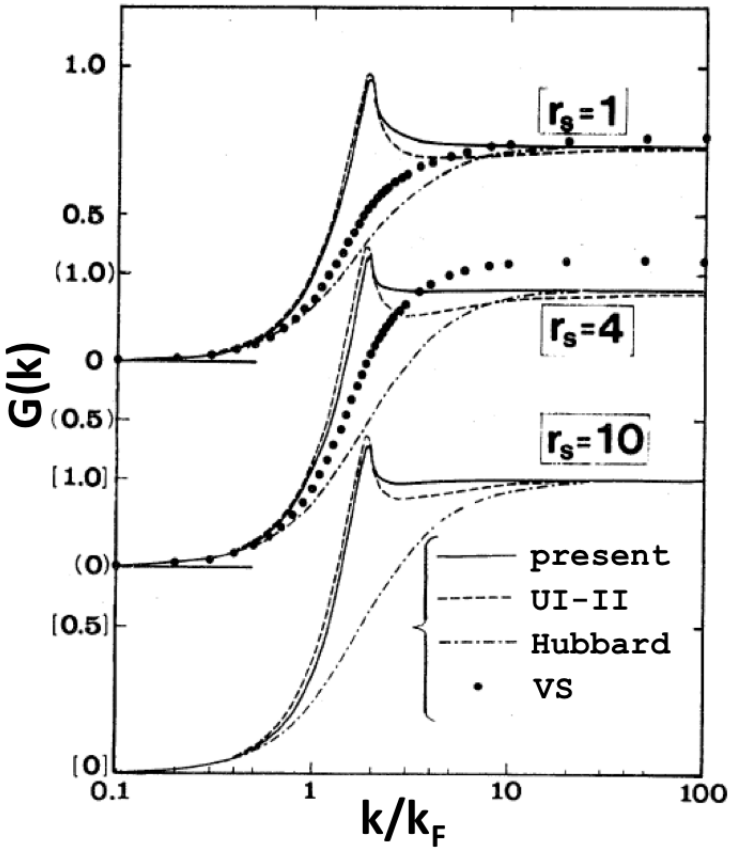

Figure 6.10: Static local field correction $G(k)$ at $r_s = 1$, 4 and 10 evaluated using various theoretical methods, after Refs. [242, 26]. The solid line (marked as "present") corresponds to the parametric relation presented in equation 6.10 by the current Utsumi-Ichimaru theory. The dashed line marked as "UI-II" is an earlier result from Utsumi-Ichimaru from 1980. Two earlier schemes from Hubbard (1958) and Vashishta and Singwi (1972) which do not correctly reproduce the peak structure at $k \sim 2k_F$ are also included for comparison [26]. The parameters of this experiment are $r_s \approx 3$, $k/k_F = 4.6$ giving an Utsumi-Ichimaru value for $G(k) = 0.907$.

Figure 6.10 shows the original plots of $G(k)$ calculated using equations 6.10 to 6.15. In case of liquid hydrogen at $P_1 = 2.8$ GPa ($r_s = 2.99$, $k/k_F \approx 4.6$), the theoretical value of the static local field correction was estimated using the Utsumi-Ichimaru equations to be $G(k,\omega) \approx G(k) = 0.907$ [26], and the spectrum calculated using this value of G corresponds to the dashed green line in figure 6.9.

Figure 6.9 shows that there is a noticeable shift of $\sim 17 \pm 1$ eV between the peaks of the calculated spectrum using the Utsumi-Ichimaru theory and the data obtained from the experiment (obtained from the experimental ratio $S_H^{P_1}/S_H^{P_2}$, equation 6.7, assuming a nearly free electron gas for the solid H calculated spectrum). This indicates a rather large deviation between the experiment and the theoretical prediction, which may be a result of our assumptions breaking down in the case of liquid hydrogen, where the electrons are no longer free and short range correlations can become important.

6.5 Results and discussion

For the first time inelastic x-ray Thomson scattering from statically compressed hydrogen was observed allowing us to measure the dynamic response of the compressed medium within a diamond anvil cell [81, 130]. The liquid at 2.8 GPa and solid at 6.4 GPa phases of hydrogen were studied, as they were expected to exhibit significant differences in their structure. This was a very challenging experiment, where the weak inelastic signal from fluid hydrogen had to be retrieved from scattering spectra dominated by the signal from the diamond anvils through a sophisticated data reduction analysis. This proof-of-principle experiment has proven that it can provide useful information on microscopic structure of statically compressed hydrogen in DAC [3].

This experiment obtained the first experimental measurement of the local field correction $G(k = 5.59 \pm 0.19 \times 10^{10}\ \mathrm{m}^{-1}, \omega \sim 130\ \mathrm{eV}) = -9 \pm 1.5$ retrieved from a spectral shift of the inelastic scattering feature [26, 240]. This large value of LFC suggests that under the conditions of this experiment the electron-electron coupling, negligible in previously presented experiments, plays an important role in this highly degenerate fluid (degeneracy parameter $\Theta = k_B T_e / E_F \approx 0.004$). The measured value for the local field correction $G(k, \omega)$ obtained from the spectral shift of the Compton feature shown in figure 6.9 was compared with theoretical model for the static LFC by Utsumi-Ichimaru, which determines the screening function of the degenerate electron liquids at metallic and lower densities, giving us the value $G(k, \omega) \approx G(k) = 0.91$ for the conditions within the liquid hydrogen sample at $\mathrm{P}_1 = 2.8$ GPa [26] finding a very large deviation between the theoretical prediction and the experimentally obtained value. However, since $\omega \sim 130$ eV is significantly larger than plasma frequency $\omega_p \sim 10$ eV, static approximations, such as that of Utsumi-Ichimaru, may not be applicable here which could be the reason for the breakdown of the theoretical description when it was compared with the experiment.

Isothermal compressibility of ideal gas is $\kappa_0 = -\frac{1}{V}\left(\frac{\partial V}{\partial P}\right)_T = 1/P = 3.57 \times 10^{-10}$ Pa^{-1}. Following from equation 2.5 in Ichimaru Ref. [26], we obtain the expression for the local field correction for OCP in terms of the system compressibility for the limit of small k:

$$\lim_{k\to 0} G(k) = \frac{k^2}{k_{TF}^2}\left(1 - \frac{\kappa_0}{\kappa}\right). \tag{6.16}$$

We thus obtain the approximate value of compressibility of hydrogen at 2.8 GPa: $\kappa = 1.94 \times 10^{-10}$ Pa^{-1} giving the compressibility ratio $Z = \kappa/\kappa_0 \sim 0.54$. Although this approach is not strictly correct as conditions of this experiment do not satisfy the small k limit ($k^2/k_{TF}^2 \sim 10$), at least this expression gives a rough indication that the compressibility of degenerate fluid hydrogen can be obtained in this experiment. The value for Z quoted above is comparable with previous experiments by Stewart [243], who used the piston displacement method to reach pressures in hydrogen samples of up to 2 GPa at low temperatures (4 K). Stewart measured the compression ratio $V/V_0 = 0.445$ for hydrogen, where V and V_0 were measured values for sample volume at $\sim$ 2 GPa and ambient pressures respectively. Since under atmospheric pressure hydrogen behaves like an ideal gas ($Z = \kappa(1\text{ atm})/\kappa_0 = 1.001$) one can relate this compression ratio directly to the compressibility ratio with ideal gas as a reference: $V/V_0 \approx \kappa/\kappa_0 = Z$, since $\kappa_0 = 1/P = V/Nk_BT$.

Our findings indicate a much stronger effect of correlations than suggested by fluid theories to date. This is important since the local field correction can be linked to dynamic properties of the compressed material, namely the isothermal compressibility and conductivity having a direct impact on EOS. These results were summarized in the publication by Falk *et al.* [3].

Chapter 7

Summary, conclusions and future work

The comparison of experimental measurements of the thermodynamic conditions to theoretical models is the backbone to understanding the complicated interaction and structural processes in WDM. This work presents the first experimental measurements of x-ray Thomson scattering from hydrogen and deuterium at extreme conditions relevant to the planetary interiors and ICF created both via laser-driven shock compression as well as static compression by diamond anvil cells obtained from experiments at the Omega laser facility (LLE) and the Diamond synchrotron respectively. In the case of warm dense deuterium a full set of thermodynamic conditions including density, pressure and ionization state were inferred directly from the XRTS measurement. The scattering measurement from statically compressed hydrogen using the DAC technique then provided the first direct measurement of the local field correction which measures the effects of strong coupling in dense electron fluids. The shocked deuterium under WDM conditions was also supported by an independent shock velocity (with inferred density and pressure) and temperature measurements using the Omega VISAR and SOP systems. All of the experimental results have been compared to a number of standard theoretical models, equation of state tables and computer simulations. On many occasions theoretical models were also used to support the data analysis. A self-consistent approach between the independent XRTS, VISAR and SOP diagnostics was found when the DFT-MD equation of state was applied to the data analysis. The DFT-MD equation of state suggests a slightly higher compressibility of deuterium in the studied regime than previously used chemical EOS models. An estimate of hydrogen compressibility was also obtained from the scattering measurement on hydrogen DAC, which was in good agreement with previous experimental data. This work has made a significant step towards improved

understanding of the microscopic structure and equation of state of the extreme states of hydrogen isotopes and understanding the internal structure of the Jovian planets.

The experimental set up used in the deuterium shock-compression experiment at the Omega laser facility described in Chapter 3 has proven to provide reliable EOS measurements. The deuterium was kept inside a Cu cryogenic cell and cooled down to $\sim 18-20$ K undergoing a phase transition to a liquid state. In particular the target design underwent a number of changes during the course of the three-year experimental campaign, which resulted in a steady improvement of the scattering data quality, in particular towards to end of the campaign, where the signal-to-noise ratio was reduced significantly after the introduction of a new x-ray backlighter material (a 5 μm thick Parylene D foil) replacing the previously used thicker (12 μm) Saran foil. The narrow-band ($\sim$ 9 eV) Cl Ly-α x-ray probe at 2.96 keV was emitted by highly ionized hydrogen-like atoms in the ablation plasma heated by the inverse bremsstrahlung process [19]. These conditions were created by sixteen tightly focused 1 ns beams at 10^{16} W/cm^2 with 500 J in each beam and a 200 μm focal spot incident onto a chlorinated plastic backlighter foil. The radiation was then collimated by a Ta pinhole (200 μm diameter), which created a strong x-ray pulse with the effective number of photons of the order of $\sim 10^{13}$ photons. Time-resolved measurements of the x-ray probe showed a good agreement with the duration of the laser pulse. The WDM conditions were created within the shock ablatively driven by the 3ω UV Omega laser drive ($\lambda = 351$ nm) consisting of 6 pairs of 1 ns laser pulses with a flat intensity profile created by phase plates and polarization smoothing [188]. These square pulses were then staggered in time forming a 6 ns constant drive with intensities of 10^{14} W/cm^2, optimal energy output $400 - 500$ J/beam, and 10^{13} W/cm^2 for FCC detuned beams.

The backlighter x-rays were scattered by warm dense deuterium scattered at 90° to a gated Thomson spectrometer (GTS) composed of a HOPG mosaic crystal (ZYB, mosaicity: $\gamma \sim 0.8° \pm 0.2°$) [195] coupled with an x-ray framing camera (XRFC), with a micro-channel-plate (MCP) combined with a CCD detector. The crystal was placed at the optimal Bragg angle of $\theta_B = 38.6°$. The MCP camera has four individually powered strips charged in a sequence during the 1 ns backlighter providing an improved temporal resolution of the scattering measurement. The integration time of each strip was 250 ps. A Be blast shield was used to block any visible radiation and stop any debris from damaging the specrometer. The target was also equipped with gold shields designed to block any direct x-ray emission from any other part of the target than the scattering channel. In addition to XRTS, for the lower intensity drive two-arm line-VISAR system, operating at 532 nm, was used to measure the shock

velocity in the deuterium sample [70]. This system produced a continuous record of the shock velocity history as well as a 1-D image of the spatial profile of the shock. The shock diameter was measured by VISAR and was found to grow from 530 ± 50 μm to 830 ± 30 μm, which is consistent with best-focus spot size expected for the laser beams when phase plates have been used ($600 - 800$ μm). The density and pressure of the shocked material can be derived from the shock velocity measurement by applying the single shock Hugoniot equations with a comparison to a known EOS table. An independent temperature measurement was obtained using the SOP diagnostic, which recorded self-emission from the shock front in a narrow wavelength band around $\lambda_c = 684$ nm [71].

The VISAR and SOP measurements for the 10^{13} W/cm^2 drive provided an initial shock velocity of 16.9 ± 0.9 km/s and radiation temperature $T_{sop} = 0.57 \pm 0.05$ eV [2]. The velocity measurement was obtained by matching the phase shift measured by the two VISAR interferometer arms with different optical delay [70]. The SOP data was used to measure the shock surface temperature by comparing the measured emission intensity with a grey body radiation distribution [2]. These results were compared with 1-D *HELIOS* and 2-D *DRACO* hydrodynamic simulations. A good agreement with the measured data was found for the *HELIOS* simulation at 3 TW/cm^2 ($\sim 70\%$ reduction of drive intensity), which produced shock velocities of $\sim 16 - 19$ km/s. The simulated shock surface temperature was found to be around 1 eV. The shock velocity predicted by the 2-D *DRACO* simulations was close to 20 km/s, but was subject to fast fluctuations as a result of a large value chosen for the flux limiter during the simulation, which decreased the effect of heat conduction. The density, pressure and expected temperature of the shocked material was then extracted from the velocity measurement by VISAR by applying the Hugoniot equations to known initial conditions as described in Chapter 4. The three different theoretical EOS models were used to carry out those calculations. These included the SESAME table [17], widely used for ICF applications; the model by Saumon and Chabrier (S&C) [122, 123], often used for astrophysical purposes, and the density-functional molecular dynamics (DFT-MD) simulations of fluid hydrogen [37, 38]. Each of these models then provided a different set of thermodynamic conditions. The results are summarized in section 4.6. A significant difference in compressibility was observed between the pure *chemical models* (SESAME and S&C) and the *physical* DFT-MD EOS, which provided a significantly greater compressibility of deuterium under the studied conditions. The self-consistency of the results based on the different EOS models was checked by a direct comparison of their temperature prediction to the

SOP temperature measurement. Only the DFT-MD calculations were consistent with the SOP temperature measurement providing the shock pressure of $P_s = 37.5 \pm 3.9$ GPa and mass density $\rho_s = 0.72 \pm 0.01$ g/cm^3 and $T_s = 0.66 \pm 0.09$ eV. The DFT-MD predicts a very high ionization state $70 - 100$ % at the given temperatures. This is in agreement with the experimental results of Celliers *et al.* [43], which show that, at shock velocities of interest, there was saturation of the reflectivity, which indicates a fully ionized state of the compressed deuterium. The chemical models on the other hand tend to underestimate the ionization of the system in this regime.

The scattering parameter was given by the geometry of the scattering process and the plasma conditions within the sample and was found to be $\alpha \approx 0.6 - 1$ for the various XRTS shots, falling into the intermediate region close to the non-collective regime, where the scattering spectrum is sensitive to both electron temperature and density. A number of different techniques were employed to obtain fits to the scattering spectra, which could be used to extract information on the thermodynamic conditions from the spectral shapes. In the case of the lower intensity drive at 10^{13} W/cm^2 the scattering data was contaminated by signal from the bulk of the cold molecular deuterium, which remained within the field of view of the GTS spectrometer adding an unwanted contribution of the bound-free transitions, and thus complicated the analysis of the total scattering spectrum. An alternative technique where a result of the 1-D *HELIOS* simulations was used to aid the data analysis of the scattering spectrum. The output of the simulations provided an estimate of plasma conditions expected for all regions contributing to the scattering signal including the dense shocked material, hot expanding corona of low density behind the shock, and the cold unshocked material before the shock-wave. This was then used to calculate a synthetic scattering profile expected for each region. Each profile was computed using the XRS code which computed a full scattering profile including the downshifted Compton feature, calculated using the finite temperature RPA, and the elastic Rayleigh peak, where the bound electron response is obtained from the SOCPN model [139, 29]. These calculated profiles were then each weighted by their mass density and relative volume to scale the relative contributions to the total signal finding an excellent agreement of the resultant fit to the scattering spectrum from the experiment. The contribution from the shocked region (warm dense deuterium) then corresponded to the plasma conditions: $n_e = 1.0 - 2.0 \times 10^{23}$ cm^{-3}, $T_e \sim 1$ eV and $Z = 0.6 - 1$; which are in a good agreement with previous VISAR and SOP measurements and the DFT-MD simulations.

Similar treatment was not necessary with the higher intensity drive at 10^{14} W/cm^2 where much a wider shock travelling at greater velocity was created leaving virtually no cold material within the field of view of the scattering measurement, while the contribution from the hot corona was found to have a negligible effect on the final spectral shape of the scattering signal. At these conditions a single scattering profile calculated using the XRS code could successfully be fitted to the scattering data obtaining: $n_e = 0.8 \pm 0.2 \times 10^{23}$ cm^{-3}, $T_e = 15 \pm 2$ eV and $Z = 0.6 - 0.85$. An improved data with much lower noise ratio was obtained after improvement in target alignment and cooling were made and Parylene D backlighter foil was used instead of Saran. The best fit to this data set was calculated using a more advanced version of the XRS code, where the free electron contribution was computed using the RPA, but a more sophisticated approach was applied to the calculation of the Rayleigh peak. Here the value of the ion-ion structure factor was fixed $S_{ii}(k) = 1$, which was obtained from DFT-MD simulations, and the ionization state of the plasma was then obtained from this using the total intensity of the ionic peak as a fitting parameter. The resultant conditions obtained from these fits were $n_e = 0.4 \pm 0.2 \times 10^{23}$ cm^{-3}, $T_e = 3 \pm 2$ eV and $Z = 0.35 \pm 0.15$, which are in an excellent agreement with average plasma conditions obtained from 2-D *DRACO* simulations: $n_e \approx 0.5 \times 10^{23}$ cm^{-3}, $T_e \approx 3$ eV and $Z \approx 0.3$ respectively.

The conditions inferred by combining VISAR, SOP, XRTS and EOS models yielded a range of values for the degeneracy parameter (ratio of thermal and Fermi energies) of $\Theta = T_e/T_F \sim 0.1 - 2.5$, Wigner-Seitz parameter $r_s = d/a_B \sim 2 - 3$ and an ionic coupling parameter $\Gamma_{ii} = e^2/4\pi\epsilon_0 dk_B T_s \sim 0.6 - 21$. The analysis thus confirms that the state of matter created falls into the WDM regime of moderately-to-strongly coupled, partially or fully degenerate plasma at conditions equivalent to the interiors of giant planets. In this regime, the applicability of the chemical models is questionable [37] but DFT-MD simulations provide a reliable description of such states [2, 105]. Introducing SOP as a tool for temperature measurements together with VISAR diagnostics has made it possible to identify the EOS consistent with both shock velocity and temperature measurements without relying on pressure standards [112].

A proof-of-principle experiment was conducted on the I15 (Extreme Conditions) beamline at the Diamond Light Source. The hydrogen gas loaded inside a 0.1 mm thick steel gasket with diameter of 250 μm was compressed using a diamond anvil cell and probed by monochromatic ~ 20 eV x-rays from the synchrotron. The inelastic x-ray scattering spectra from hydrogen DACs at $P_1 = 2.8$ GPa (liquid phase) and

P_2 = 6.4 GPa (solid phase) were observed in Von Hamos geometry using a curved HAPG crystal [195] coupled to a photon-counting detector (PILATUS 100k) with scattering angle of 32.2±1.1° with the scattering parameter $\alpha = 0.3$ corresponding to the non-collective scattering regime. The DAC was positioned with 20 μm accuracy, corresponding to an uncertainty of 10 μm ($\sim$ 1 eV) at the detector plane. The pressure within the anvil cell was measured through the well known relationship for fluorescence of ruby under pressure [92] (a small ruby probe was buried inside the anvil cell together with the hydrogen sample and the fluorescence was measured using an optical laser and a calibrated spectrometer). Since the pressure and temperature of the hydrogen in the anvil cell are known (room temperature, T = 300 K) the electron density could be determined from the equation of state (EOS) data for compressed hydrogen experimentally determined by Ref. [21] and was found to be 6.0×10^{22} cm^{-3} for P_1 and 7.9×10^{22} cm^{-3} at P_2 at which hydrogen is fully degenerate.

The scattering signal from the hydrogen sample is weak compared to the diamond as a result of the small sample volume needed to achieve high compression of the hydrogen gas within the larger anvils and the fact that each carbon atom has more electrons to scatter from than the hydrogen atoms. In order to compensate for the dominant Compton scattering from the diamond anvils, we retrieved the hydrogen scattering data in the form of a ratio of spectra from hydrogen at P_1 and P_2 through a careful reduction analysis procedure using the measured signal referenced to the empty cell described in section 6.3.2. The single scattering spectrum for liquid deuterium at P_1 = 2.8 GPa was obtained from this experimental ratio by multiplication by a synthetic inelastic spectrum calculated for the solid hydrogen at P_2. This pressure was chosen, because at the higher pressure we have polycrystalline solid hydrogen [241]. Thus the electrons are effectively free as they satisfy the Bloch functions for electronic motion inside the periodic potentials within the crystalline lattice of localized ions. This phase is also more degenerate (lower degeneracy factor $\Theta = k_B T/E_F$) resulting from higher Fermi energy making the effects of finite temperature less important. Therefore the calculation of the free electron response in the scattering spectrum for P_2 can be justifiably carried out using the RPA at $T = 0$ K, which provides the Lindhard dielectric function and the structure factor is then obtained through the fluctuation-dissipation theorem [163]. In this experiment, k lies outside the Brillouin zone boundary, the lattice does not influence scattering from the electrons.

The resultant spectrum obtained from the experimental ratio was then compared to another profile, which was calculated using the RPA with the static local field

correction estimated using the Utsumi-Ichimaru equations (assuming a nearly free electron gas for the solid H) to be $G(k,\omega) \approx G(k) = 0.907$ to simulate the electron coupling in the liquid hydrogen at $P_1 = 2.8$ GPa ($r_s = 2.99$, $k/k_F \approx 4.6$), the full calculation is shown in section 6.4. There was a noticeable shift of $\sim 17 \pm 1$ eV between the peaks of the experimental and calculated spectra, which is a result of our assumptions breaking down in the case of liquid hydrogen, where the electrons are no longer free and short range correlations can become important. The calculated response overlaps with the experimental data for $G(k = 5.59 \pm 0.19$ x 10^{10} m^{-1}, $\omega \sim 130$ eV$) = -9 \pm 1.5$. However, since $\omega \sim 130$ eV is significantly larger than the plasma frequency ω_p, static approximations, such as the one of Utsumi-Ichimaru, may not be applicable here. Our results are the first experimental measurement of local field effects across the liquid to solid phase transition in hydrogen. They indicate a much stronger effect of correlations than suggested by fluid theories. This is important since the local field correction can be linked to the dynamic properties of the compressed material, namely the isothermal compressibility and conductivity [26]. An approximate value of compressibility of hydrogen at 2.8 GPa was obtained: $\kappa = 1.94 \times 10^{-10}$ Pa^{-1} giving the compressibility ratio $Z = \kappa/\kappa_0 \sim 0.54$. This result is similar to previous experimental measurements by Stewart [243], who used the piston displacement method to reach pressures in hydrogen samples of up to 2 GPa at low temperatures (4 K) to obtain the compression ratio of 0.445.

In conclusion, different conditions relevant to the interiors of Jovian planets have been probed in this work. In the laser experiments the VISAR, SOP and XRTS diagnostics measured the thermodynamic conditions of warm dense deuterium at pressures and temperatures directly relevant to the interior of Jupiter and similar planets. Under these conditions the electron degeneracy (quantum effects) and ion coupling play a very important role influencing the EOS, while the electron coupling is negligible. Thus, the ideal gas description of this state of matter (WDM) is insufficient. The experimental findings in this thesis have confirmed that the DFT-MD simulations provide the most accurate description of this regime. The combined VISAR and SOP measurement was used to reconstruct the Hugoniot curve of a shocked liquid deuterium, which suggested a higher compressibility at the region of interest than previously used EOS tables (SESAME, S&C EOS). The higher compressibility of warm dense hydrogen as indicated by the DFT-MD EOS has serious implications for Jupiter's structure, in particular on the size of its core, the required concentration of heavier elements, and the location of the molecular to metallic transition [14, 12]. Various simulations based on the DFT suggest the existence of a large central core

of heavier elements inside Jupiter, which supports the theory of core accretion as the standard model for the formation of hydrogen rich planets [12]. Moreover, the DFT-MD models predict a shift of the metallization transition layer closer to the planetary core from previous chemical models resulting in decreased metallicity of the mantle, low concentration of heavier elements in the mantle, and differential rotation of the planet's interior [12, 13]. DFT-MD simulations predict a continuous transition from the molecular to a dissociated/metallic regime in fluid hydrogen as a function of pressure, while the S&C model predicted this transition to be of first order [37, 38, 12]. The higher compressibility of warm dense deuterium could also have significant implications on the dynamics of ICF implosions [16]. A different set of conditions were probed in the Diamond experiment described in Chapter 6, where a hydrogen sample was statically compressed using DAC at room temperature. At these significantly lower temperatures, the electron fluid is not only degenerate, but it also exhibits effects of strong electron coupling. A direct measurement of the local field correction suggested that this effect is more important than previously suggested by fluid theories [26]. This has a serious impact on the EOS of hydrogen at these conditions as well as measurable quantities such as compressibility and conductivity. These findings are relevant to the structure of colder gas giants such as Neptune and high pressure research.

The experiments described in Chapters 3, 4 and 5 (Omega campaign) provide a platform for the detailed study of compressed deuterium, and together they make an important first step towards a simultaneous measurement of all thermodynamic variables needed for EOS research including pressure (P), mass density (ρ), electron density (n_e), electron temperature (T_e), and ionization (Z) by combining inelastic x-ray scattering observations with shock velocity and optical pyrometry measurements [19, 1, 244, 20, 2]. In the next stage of this experimental campaign at the Omega laser the cryogenic target should be redesigned to allow for simultaneous XRTS and VISAR/SOP measurements. Since the VISAR diagnostic is fixed to the H14 (TIM 5) port the drive and backlighter beam configuration as well as the target itself will have to be redesigned. After the improvement of the brightness of the x-ray backlighter when Parylene D foil was used, a door opens for a collective scattering measurement. A simultaneous collective and non-colllective scattering measurement would utilize the full potential of the XRTS technique. Additional collective scattering measurement would provide increased confidence in the measurements of n_e, through the position of the plasmon feature, and T_e, from the detailed balance, on top of the non-collective measurement of these quantities as shown in Chapter 5. Such expansion

of the XRTS technique is challenging as it requires two spectrometers positioned at correct angles (ideally 90° for non-collective and $\sim 40°$ for collective XRTS), which is not trivial at facilities such as Omega. Combined and simultaneous measurements of collective and non-collective XRTS with VISAR and SOP diagnostics would provide an entirely new platform for EOS measurements for not only for laboratory astrophysics, but also for ICF, material science, geology and many other fields interested in the study of properties of materials under extreme pressures and temperatures.

Building upon the results presented in Chapter 6, I would propose to expand and improve the XRTS on diamond anvil cells method at free-electron x-ray laser facilities (FEL), where laser-driven DACs can be both heated and further compressed to the warm dense matter regime relevant to the planetary interior regime, and studied with a high-power coherent x-ray source [95]. Such FEL x-ray sources are superior to the older synchrotron technology in the intensity (photon number) of the beam and are also capable of time-resolved measurement as their pulse lengths reach $60 - 80$ fs FWHM and fast rep-rate. In particular the Matter under Extreme Conditions (MEC) endstation at LCLS would be well suited for such experiment as it comprises both high power lasers that could be used for shocking and heating pre-compressed samples, while the FEL beam from LCLS can be used as a coherent narrow-band x-ray probe. The current specs of the machine only allow the beam energy to go up to 10 keV, however with planned advances in the FEL technology, such facilities could potentially become a platform for the next generation of XRTS experiments on statically compressed samples. Under these controlled conditions the scattering wavevector could be varied allowing for the study of k-dependance of the LFC. With a careful technique development in particular of the DAC set up and backlighter source this experimental method could also be redeveloped for high power laser facilities such as Omega, NIF, or ELI, where more extreme conditions (in particular higher temperatures) could be achieved [95]. The main challenges here would be the development of thin flat anvil cells which could be ablatively driven by lasers. Also materials other than diamond, e.g. sapphire, might have to be explored allowing for study at lower x-ray probe energies. In the case of high power laser experiments new x-rays backlighter techniques capable of producing bright line emission in the region of ~ 20 keV, eg. Ag K-α at 22 keV, would have to be developed.

Appendix A

Acronyms, constants and standard variables

List of acronyms

ASBO	Active Shock BreakOut system
BL	Backlighter Laser beam
BS	Beam Splitter
CCD	Charge-Coupled Device
CID	Charge-Injection Device
CTHS	Cryogenic Target Handling System
DAC	Diamond Anvil Cell
DESY	Deutsches Elektronen-Synchrotron
DFT-MD	Density-Functional Molecular Dynamics simulations
DLFC	Dynamic Local Field Correction
DLS	Diamond Light Source synchrotron
DPP	Distributed Phase Plates
DPR	Distributed Polarization Rotators
DRACO	2-D radiation hydrodynamics code (name)
DSF	Dynamic Structure Factor
ELI	Extreme Light Infrastructure project
EOS	Equation of State
FCC	Frequency Conversion Crystals
FEL	Free Electron Laser
FWHM	Full-Width-Half-Maximum
GFMC	Green's-function Monte Carlo simulations
GTS	Gated Thomson Spectrometer
HAPG	Highly Annealed Pyrolytic Graphite mosaic crystal
HED	Harmonic Energy Diagnostic

List of acronyms

HEDP	High Energy Density Physics
HELIOS	1-D radiation-magnetohydrodynamics code (name)
HFM	Horizontal Focussing Mirror
HNC	Hypernetted Chain Scheme
HOPG	Highly Oriented Pyrolytic Graphite mosaic crystal
IB	Inverse Bremsstrahlung
ICF	Inertial Confinement Fusion
IP	Image Plate
IR	Infra-Red radiation
KDP	Potassium Dihydrogen Phosphate crystal
LANL	Los Alamos National Laboratory
LCLS	Linac Coherent Light Source, Stanford University
LFC	Local Field Correction
LILAC	1-D hydrodynamics code (name)
LLE	Laboratory of Laser Energetics
LLNL	Lawrence Livermore National Laboratory
MCP	Micro-Channel-Plate
MEC	Matter in Extreme Conditions endstation at LCLS
ND	Neutral Density filter
NIF	National Ignition Facility
OCP	One-Component Plasma
OTIS	Omega Transport Instrumentation System
PAW	Projector Augmented Wave
PET	PolyEthylene Terephthalate crystal
PILATUS	pixel apparatus for the SLS, x-ray detector (name)
PIMC	Path Integral Monte Carlo simulations
PPT	Plasma Phase Transition
PROPACEOS	PRism OPACity and Equation Of State
PSI	Paul Scherrer Institut
RAL	Rutherford Appleton Laboratory
RPA	Random Phase Approximation
S&C	Saumon and Chabrier equation of state
SESAME	The Los Alamos National Laboratory Equation of State Database
SLFC	Static Local Field Correction
SLS	Swiss Light Source
SOCP	Screened One Component Plasma model
SOCPN	Screened One Component Plasma Negative model

List of acronyms

SOP	Streaked Optical Pyrometry
SRF	Shot Request Form
SSCA	SIM Streak Camera A, x-ray streak camera
TCC	Target Chamber Centre
TF	Thomas-Fermi model
TFM	Fourier Transform Method
TIM	Ten-Inch Manipulator
TPS	Target Positioning System
TVS	Target Viewing System
UV	Ultra-Violet Radiation
VASP	Vienna Ab-initio Simulation Package
VFM	Vertical Focussing Mirror
VISAR	Velocity Interferometer System for Any Reflector
VPF	Velocity Per Fringe
WDM	Warm Dense Matter
XRFC	X-Ray Framing Camera
XRPHC	X-Ray Pinhole Camera
XRS	X-Ray Scattering code
XRTS	X-Ray Thomson Scattering
XVIS	VISAR analysis code (name)
ZYA, ZYB, ZYD, ZYH	HOPG crystals with various degrees of mosaicity

Table of constants

Constant	Symbol	Value		Units
Speed of light in vacuum	c	2.99792	$\times 10^{8}$	m/s
Permittivity of free space	ε_0	8.85419	$\times 10^{-12}$	$C^2/(J \cdot m)$
Electronic charge $(-)$	e	1.60218	$\times 10^{-19}$	C
Mass of an electron	m_e	9.10938	$\times 10^{-31}$	kg
Planck's constant	h	6.62607	$\times 10^{-34}$	$m^2 kg/s$
	$\hbar = h/2\pi$	1.05457	$\times 10^{-34}$	$m^2 kg/s$
Bohr radius	a_B	5.29178	$\times 10^{-11}$	m
Boltzmann's constant	k_B	1.38066	$\times 10^{-23}$	J/K
Pi	π	3.14159		

List of common variables

Symbol	Variable
$k = \frac{4\pi}{\lambda_0}\sin(\theta/2)$	Scattering wave vector
$\alpha = 1/k\lambda_s$	Scattering parameter
S^0_{ee}, S_{ii}	Free electron-electron, ion-ion structure factor
$\Gamma_{ii} = e^2/4\pi\epsilon_0 d k_B T_i$	Ion-ion coupling parameter
$\Theta = k_B T_e/E_F$	Degeneracy parameter
$r_s = d/a_B$	Wigner-Seitz parameter
$\omega_p = \sqrt{n_e e^2/\varepsilon_0 m_e}$	Electron plasma frequency
λ_s	Plasma screening length
$\lambda_{De} = \sqrt{\varepsilon_0 k_B T_e/e^2 n_e}$	Electron Debye screening length
$\lambda_{TF} = \sqrt{2\varepsilon_0 E_F/3n_e e^2}$	Thomas-Fermi screening length
$v_{th} = \sqrt{k_B T_e/m_e}$	Thermal velocity of electrons
$E_F = (\pi^2\hbar^2/2m_e)\,(3n_e/\pi)^{2/3}$	Fermi energy
$T_F = E_F/k_B$	Fermi temperature
$k_F = (3\pi^2 n_e)^{1/3}$	Fermi wavenumber
$d = (3/(4\pi n_e))^{1/3}$	Inter-particle spacing
n_e, n_i	Electron, ion density
ρ	Mass density
T_e, T_i	Electron, ion temperature
Z	Ionization degree
U_s, U_p	Shock, particle velocity

Appendix B

The Lindhard dielectric function (RPA)

The dielectric function can be obtained from the random phase approximation (RPA). A detailed derivation of the dielectric function can be found in a paper by Arista and Brandt [163], who calculated it for all degrees of degeneracy. Many textbooks also provide a good background on the RPA as well as the explicit expressions for the Lindhard dielectric function at $T = 0$ corresponding to a fully degenerate free electron gas used in Chapter 6 [146, 159].

Since the dielctric function can be linked to the dynamic structure factor, it is used to calculate synthetic scattering spectra. The explicit expressions used to calculate the free electron part of the dynamic structure factor $S(k, \omega)$ used to calculate the inelastic spectrum for the degenerate hydrogen in section 6.4. is provided in this appendix. The dielectric response function can be separated into its real and imaginary parts as [146]:

$$\varepsilon_{RPA}(k, \omega) = \varepsilon_1(k, \omega) + i\varepsilon_2(k, \omega), \tag{B.1}$$

while the energy-loss function, which describes the spectrum of excitations in the plasma through momentum and energy transfer, is defined through the fluctuation-dissipation theorem as [130]:

$$S(k, \omega) = \frac{\varepsilon_0 \hbar k^2}{\pi e^2 n_e} \cdot \mathrm{Im}\left[\frac{-1}{\varepsilon(k, \omega)}\right] = \frac{\varepsilon_0 \hbar k^2}{\pi e^2 n_e} \cdot \frac{\varepsilon_2(k, \omega)}{|\varepsilon(k, \omega)|^2} \tag{B.2}$$

$$= \frac{\varepsilon_0 \hbar k^2}{\pi e^2 n_e} \cdot \frac{\varepsilon_2(k, \omega)}{\varepsilon_1^2(k, \omega) + \varepsilon_2^2(k, \omega)}. \tag{B.3}$$

The explicit expressions for $\varepsilon_1(k,\omega)$ and $\varepsilon_2(k,\omega)$ for a fully degenerate electron gas are found from equations 2.23 and 2.24 by summing over the momentum space; the calculation was first done by Lindhard (1954) [160]:

$$\begin{aligned}\varepsilon_1(k,\omega) &= 1+\frac{k_{TF}^2}{k^2}\left\{\frac{1}{2}+\frac{k_F}{4k}\left[\left(\frac{(\omega+\hbar k^2/2m)^2}{(kv_F)^2}-1\right)\ln\left|\frac{\omega-kv_F+\hbar k^2/2m_e}{\omega+kv_F+\hbar k^2/2m_e}\right|\right.\right.\\ &\left.\left.-\left(\frac{(\omega-\hbar k^2/2m_e)^2}{(kv_F)^2}-1\right)\ln\left|\frac{\omega-kv_F-\hbar k^2/2m_e}{\omega+kv_F-\hbar k^2/2m_e}\right|\right]\right\}, \qquad \text{(B.4)}\end{aligned}$$

with

$$\begin{aligned}\varepsilon_2(k,\omega) &= \frac{\pi}{2}\frac{k_{TF}^2}{k^2}\frac{\omega}{kv_F}, \text{ for } 0\le\omega\le kv_F-\frac{\hbar k^2}{2m_e}\\ &= \frac{\pi}{4}\frac{k_{TF}^2}{k^2}\frac{k_F}{k}\left[1-\frac{\left(\omega-\frac{\hbar k^2}{2m_e}\right)^2}{(kv_F)^2}\right], \text{ for } kv_F-\frac{\hbar k^2}{2m_e}\le\omega\le kv_F+\frac{\hbar k^2}{2m_e}\\ &= 0, \text{ for } \omega\ge kv_F+\frac{\hbar k^2}{2m_e}, \qquad \text{(B.5)}\end{aligned}$$

for $k<2k_F$ and

$$\varepsilon_2(k,\omega)=\frac{\pi}{4}\frac{k_{TF}^2}{k^2}\frac{k_F}{k}\left[1-\frac{\left(\omega-\frac{\hbar k^2}{2m_e}\right)^2}{(kv_F)^2}\right], \frac{\hbar k^2}{2m_e}-kv_F\le\omega\le\frac{\hbar k^2}{2m_e}+kv_F \qquad \text{(B.6)}$$

for $k>2k_F$. Here k is the scattering vector (equation 2.33), $k_{TF}=2\pi/\lambda_{TF}$ is the Thomas-Fermi screening wavenumber of the electrons (equation 2.26) and $v_F=\hbar k_F/m_e$ is the Fermi velocity with the Fermi wavenumber $k_F=(3\pi^2 n_e)^{1/3}$. These expressions correctly reproduce many features in the scattering spectrum including the effect of screening and plasmon oscillations at ω_p in the plasma. In the case of calculated spectra in section 6.4.1 $k>2k_F$, thus equation B.6 was used to obtain $\varepsilon_2(k,\omega)$.

Appendix C

Publications

Peer-reviewed publications:

1. K. Falk, A. P. Jephcoat, B. J. B. Crowley, R. R. Fäustlin, C. Fortmann, F. Y. Khattak, A. K. Kleppe, D. Riley, S. Toleikis, J. Wark, H. Wilhelm and G. Gregori, *Measurement of the dynamic response of compressed hydrogen by inelastic X-ray scattering*, J. Phys.: Conf. Ser., **244**, 042014 (2010).

2. K. Falk, S. P. Regan, J. Vorberger, M. A. Barrios, T. R. Boehly, D. E. Fratanduono, S. H. Glenzer, D. G. Hicks, S. X. Hu, C. D. Murphy, P. B. Radha, S. Rothman, A. P. Jephcoat, J. S. Wark, D. O. Gericke, and G. Gregori, *Self-Consistent Measurement of the Equation of State of Liquid Deuterium*, High Energy Density Physics, **8** (1), 76-80 (2012).

3. K. Falk, S. P. Regan, J. Vorberger, B. Crowley, S. H. Glenzer, S. X. Hu, C. D. Murphy, P. B. Radha, A. P. Jephcoat, J. S. Wark, D. O. Gericke, and G. Gregori, *Comparison Between X-Ray Scattering and VISAR Measurements from Shocked Liquid Deuterium at Omega* (complete, to be submitted 2012).

4. S. P. Regan, P. B. Radha, T. R. Boehly, T. Doeppner, K. Falk, S. H. Glenzer, V. N. Goncharov, G. Gregori, O. L. Landen, R. L. McCrory, D. D. Meyerhofer, P. Neumayer, T. C. Sangster and V. A. Smalyuk, *Inferring the electron temperature and density of shocked liquid deuterium using inelastic X-ray scattering*, J. Phys.: Conf. Ser., **244**, 042017 (2010).

5. S. P. Regan, K. Falk, G. Gregori, P. B. Radha, S. X. Hu, T. R. Boehly, B. Crowley, S. H. Glenzer, O. L. Landen, D. O. Gericke, T. Doeppner, C. D. Murphy, T. C. Sangster, J. Vorberger and D. D. Meyerhofer, *Inelastic X-ray Scattering from Shocked Liquid Deuterium*, Phys. Rev. Lett. (submitted 2011).

6. C. Zulick, F. J. Dollar, H. Chen, K. Falk, A. Hazi, C. Murphy, J. Park, J. Seely, C. I. Szabo, R. Tommasini, R. Shepherd, and K. Krushelnick, *K-Shell Spectroscopy of Au Plasma Generated with a Short Pulse Laser*, Canadian Journal of Physics, **89** (5), 647-651 (2011).

7. H. Chen, D. D. Meyerhofer, S. C. Wilks, R. Cauble, F. Dollar, K. Falk, W. Goldstein, G. Gregori, A. Hazi, E. I. Moses, C. D. Murphy, J. Myatt, J. Park, B. Remington, J. Seely, R. Shepherd, A. Spitkovsky, C. Stoeckl, C. I. Szabo, R. Tommasini, K. Zulick, P. Beiersdorfer, *Towards laboratory produced relativistic electron-positron pair plasmas*, High Energy Density Physics, **7** (4), 225-229 (2011).

8. N. Ozaki, T. Jitsui, G. Gregori, H. Uranishi, Y. Inubushi, A. Benuzzi-Mounaix, D. Riley, T. Kimura, K. Miyanishi, K. Falk, M. Koenig, M. Makita, S. Mazeve, C. D. Murphy, T. Sano, Y. Sakawa, and R. Kodama, *Strongly coupled ion behavior observed in ultrahigh shock compressed diamond* (to be submitted 2012).

Talks and poster presentations:

- Inertial Fusion Sciences and Applications (IFSA), Sep 6-11, 2009 in San Francisco, CA
  Poster title: *Measurement of The Dynamic Response Function of Compressed Hydrogen by X-Ray Thomson Scattering*

- 52nd Annual Meeting of the APS Division of Plasma Physics, Nov 8-12, 2010 in Chicago, IL
  Session JO6: EOS and Material Dynamics
  Talk title: *Inferring the equation of state of shocked liquid deuterium*

- Christmas meeting of the High Power Laser science community, Dec 15-17, 2010 in Abingdon, UK
  Talk title: *Inferring the equation of state of shocked liquid deuterium on Omega*

- Christmas meeting of the High Power Laser science community, Dec 14-16, 2011 in Abingdon, UK
  Poster title: *Deuterium under Extreme Conditions of Planetary Interiors*

- SET for BRITAIN 2011: Poster presentation by early-career research scientists, engineers and technologists, Mar 14, 2011, Houses of Parliament, London (Parliamentary and Scientific Committee, Institute of Physics)

Poster title: *Inferring the equation of state of shocked liquid deuterium*
– Bronze Award in Physical Sciences (Physics)

- International Workshop on Warm Dense Matter – 2011, Jun 5-8, 2011 in Pacific Grove, CA
  Talk title: *Inferring the equation of state of WDM deuterium at Omega*
  (http://www.lbl.gov/conferences/wdm/assets/docs/talks-2011/Katerina_Falk.pdf)

- International Conference on Quantum, Atomic, Molecular and Plasma Physics (QuAMP), Sep 18-22, 2011 in Oxford, UK
  Poster title: *Equation of State of Deuterium under Extreme Conditions of Planetary Interiors*

- Seminars given at LLNL, LANL, SLAC (Stanford University) and Oxford
  Talk title: *Inferring the equation of state of hydrogen and deuterium*

Bibliography

[1] S. P. Regan, P. B. Radha, T. R. Boehly, T. Doeppner, K. Falk *et al.*, *Inferring the electron temperature and density of shocked liquid deuterium using inelastic X-ray scattering*, J. Phys.: Conf. Ser., **244**, 042017 (2010).

[2] K. Falk, S. P. Regan, J. Vorberger, M. A. Barrios, T. R. Boehly *et al.*, *Self-Consistent Measurement of the Equation of State of Liquid Deuterium*, HEDP, **8** (1), 76–80 (2012).

[3] K. Falk, A. P. Jephcoat, B. J. B. Crowley, R. R. Fäustlin, C. Fortmann *et al.*, *Measurement of the dynamic response of compressed hydrogen by inelastic X-ray scattering*, J. Phys.: Conf. Ser., **244**, 042014 (2010).

[4] J. Nuckolls, L. Wood, A. Thiessen and G. Zimmerman, *Laser Compression of Matter to Super-High Densities: Thermonuclear (CTR) Applications*, Nature, **239**, 139 (1972).

[5] J. Lindl, *Development of the indirectdrive approach to inertial confinement fusion and the target physics basis for ignition and gain*, Phys. Plasmas, **2** (11), 3933–4024 (1995).

[6] J. D. Lawson, *Some criteria for a power producing thermonuclear reactor*, Proc. Phys. Soc. B, **70**, 6 (1957).

[7] R. McCrory, S. P. Regan, S. J. Loucks, D. D. Meyerhofer, S. Skupsky *et al.*, *Direct-drive inertial confinement fusion research at the Laboratory for Laser Energetics: charting the path to thermonuclear ignition*, Nucl. Fusion, **45**, S283 (2005).

[8] J. P. Chittenden, *The Z-pinch approach to fusion*, Physics World (May 2000).

[9] S. X. Hu, B. Militzer, V. N. Goncharov and S. Skupsky, *Strong Coupling and Degeneracy Effects in Inertial Confinement Fusion Implosions*, Phys. Rev. Lett., **104** (23), 235003 (2010).

[10] W. Hubbard, *Interiors of the giant planets*, Science, **214** (4517), 145–149 (1981).

[11] T. Guillot, *A comparison of the interiors of Jupiter and Saturn*, Planetary Space Sci., **47**, 1183–1200 (1999).

[12] B. Militzer, W. B. Hubbard, J. Vorberger, I. Tamblyn and S. A. Bonev, *A massive core in jupiter predicted from first-principles simulations*, Astrophys. J., **668**, L45–L48 (2008).

[13] N. Nettelmann, B. Holst, A. Kietzmann, M. French, R. Redmer *et al.*, *Ab Initio Equation of State Data for Hydrogen, Helium, and Water and the Internal Structure of Jupiter*, Astrophys. J., **683** (2), 1217–1228 (2008).

[14] T. Guillot, *The Interiors of Giant Planets: Models and Outstanding Questions*, Annu. Rev. Earth Planet. Sci., **33**, 493–530 (2005).

[15] B. A. Remington, R. P. Drake and D. D. Ryutov, *Experimental astrophysics with high power lasers and Z pinches*, Rev. Mod. Phys., **78** (3), 755–807 (2006).

[16] National Research Council, *Frontiers in High Energy Density Physics: The X-Games of Contemporary Science*, National Academies Press (2003).

[17] G. I. Kerley, *Equation of state and phase diagram of dense hydrogen*, Phys. Earth Planet. Interiors, **6**, 78–82 (1972).

[18] G. I. Kerley, *Equations of State for Hydrogen and Deuterium*, SANDIA REPORT: SAND2003-3613, pp. 1–85 (Dec 2003).

[19] S. H. Glenzer and R. Redmer, *X-ray Thomson Scattering in High Energy Density Plasmas*, Rev. Mod. Phys., **81** (4), 1625–1663 (2009).

[20] D. G. Hicks, T. R. Boehly, P. M. Celliers, J. H. Eggert, S. J. Moon *et al.*, *Laser-driven single shock compression of fluid deuterium from 45 to 220 GPa*, Phys. Rev. B, **79**, 014112 (2009).

[21] H.-K. Mao, A. P. Jephcoat, R. J. Hemley, L. W. Finger, C. S. Zha *et al.*, *Synchrotron X-ray diffraction measurements of single-crystal hydrogen to 26.5 gigapascals*, Science, **239** (4844), 1131–1134 (1988).

[22] F. F. Chen, *Introduction to Plasma Physics and Cotroled Fusion. Volume I.*, Springer, second edition (1984).

[23] A. Höll, T. Bornath, L. Cao, T. Döppner, S. Düsterer *et al.*, *Thomson scattering from near-solid density plasmas using soft x-ray free electron lasers*, HEDP, **3**, 120–130 (2007).

[24] L. Tonks and I. Langmuir, *Oscillations in ionized gases*, Phys. Rev., **33** (2), 195–210 (1929).

[25] F. Haas, G. Manfredi and M. Feix, *Multistream model for quantum plasmas*, Phys. Rev. E, **62** (2), 2763 (2000).

[26] S. Ichimaru, *Strongly coupled plasmas: high-density classical plasmas and degenerate electron liquids*, Rev. Mod. Phys., **54** (4), 1017–1059 (1982).

[27] S. Galam and J. P. Hansen, *Statistical mechanics of dense ionized matter. VI. Electron screening corrections to the thermodynamic properties of the one-component plasma*, Phys. Rev. A, **14** (2), 816 (1976).

[28] R. L. Liboff, *Criteria for physical domains in laboratory and solidstate plasmas*, J. Appl. Phys., **56** (9), 2530–2535 (1984).

[29] D. O. Gericke, J. Vorberger, K. Wünsch and G. Gregori, *Screening of ionic cores in partially ionized plasmas within linear response*, Phys. Rev. E, **81**, 065401(R) (2010).

[30] M. W. C. Dharma-wardana and F. Perrot, *Simple Classical Mapping of the Spin-Polarized Quantum Electron Gas: Distribution Functions and Local-Field Corrections*, Phys. Rev. Lett., **84** (5), 959 (2000).

[31] F. Perrot and M. W. C. Dharma-wardana, *Spin-polarized electron liquid at arbitrary temperatures: Exchange-correlation energies, electron-distribution functions, and the static response functions*, Phys. Rev. B, **62** (24), 16536 (2000).

[32] G. Gregori, S. Glenzer and O. Landen, *Generalized x-ray scattering cross section from nonequilibrium plasmas*, Phys. Rev. E, **74**, 026402 (2006).

[33] T. Guillot, *Interiors of giant planets inside and outside the solar system*, Science, **286**, 72 (1999).

[34] R. P. Drake, *High-energy-density physics: fundamentals, inertial fusion, and experimental astrophysics, Shock wave and high pressure phenomena*, Springer (2006).

[35] M. A. Morales, C. Pierleoni, E. Schwegler and D. M. Ceperley, *Evidence for a first-order liquid-liquid transition in high-pressure hydrogen from ab initio simulations*, PNAS, **107** (29), 12799 (2010).

[36] T. Guillot, W. B. Hubbard, D. J. Stevenson and D. Saumon, *Jupiter: The Planet, Satellites and Magnetosphere - The Interior of Jupiter*, Cambridge Planetary Science (Eds. F. Bagenal, T. E. Dowling and W. B. McKinnon), Cambridge University Press (2004).

[37] J. Vorberger, I. Tamblyn, B. Militzer and S. A. Bonev, *Hydrogen-helium mixtures in the interiors of giant planets*, Phys. Rev. B, **75**, 024206 (2007).

[38] J. Vorberger, I. Tamblyn, S. A. Bonev and B. Militzer, *Properties of Dense Fluid Hydrogen and Helium in Giant Gas Planets*, Contrib. Plasma Phys., **47** (4-5), 375–380 (2007).

[39] D. Saumon, G. Chabrier and H. V. Horn, *An equation of state for low-mass stars and giant planets*, Astrophys. J. Suppl. Ser., **99**, 713–741 (1995).

[40] I. Silvera, *The insulator-metal transition in hydrogen*, PNAS, **107** (29), 12743 (2010).

[41] L. B. Da Silva, P. Celliers, G. W. Collins, K. S. Budil, N. C. Holmes *et al.*, *Absolute equation of state measurements on shocked liquid deuterium up to 200 GPa (2 Mbar)*, Phys. Rev. Lett., **78** (3), 483 (1997).

[42] G. W. Collins, L. B. D. Silva, P. Celliers, D. M. Gold, M. E. Foord *et al.*, *Measurements of the equation of state of deuterium at the fluid insulator-metal transition*, Science, **281**, 1178 (1998).

[43] P. M. Celliers, G. W. Collins, L. B. da Silva, D. M. Gold, R. Cauble *et al.*, *Shock-induced transformation of liquid deuterium into a metallic fluid*, Phys. Rev. Lett., **84** (24), 5564 (2000).

[44] M. D. Knudson, D. L. Hanson, J. E. Bailey, C. A. Hall, J. R. Asay *et al.*, *Equation of state measurements in liquid deuterium to 70 GPa*, Phys. Rev. Lett., **87** (22), 225501 (2001).

[45] G. V. Boriskov, A. I. Bykov, R. I. Il'Kaev, V. D. Selemir, G. V. Simakov *et al.*, *Shock compression of liquid deuterium up to 109 GPa*, Phys. Rev. B, **71**, 092104 (2005).

[46] V. Fortov, R. Ilkaev, V. Arinin, V. Burtzev, V. Golubev *et al.*, *Phase transition in a strongly nonideal deuterium plasma generated by quasi-isentropical compression at megabar pressures*, Phys. Rev. Lett., **99** (18), 185001 (2007).

[47] M. I. Eremets and I. A. Troyan, *Conductive dense hydrogen*, Nature Materials, **10** (12), 927–931 (2012).

[48] D. J. Stevenson and E. E. Salpeter, *The phase diagram and transport properties for hydrogen-helium fluid planets*, Astrophys. J. Suppl. Ser., **35**, 221–137 (1977).

[49] E. E. Salpeter, *On convection and gravitational layering in Jupiter and in stars of low mass*, Astrophys. J., **181**, 83–86 (1973).

[50] O. Pfaffenzeller, D. Hohl and P. Ballone, *Miscibility of hydrogen and helium under astrophysical conditions*, Phys. Rev. Lett., **74** (13), 2599 (1995).

[51] J. E. Klepeis, K. J. Schafer, T. W. Barbee and M. Ross, *Hydrogen-helium mixtures at megabar pressures: Implications for Jupiter and Saturn*, Science, **254** (5034), 986–989 (1991).

[52] D. J. Stevenson, *Interiors of the giant planets*, Ann. Rev. Earth Planet. Sci., **10**, 257–95 (1982).

[53] J. J. Lissauer, *Planet formation*, Ahnu. Rev. Astron. Astrophys., **31**, 129–74 (1993).

[54] A. P. Boss, *Evolution of the solar nebula. IV. Giant gaseous protoplanet formation*, Astrophys. J., **503**, 923 (1998).

[55] D. J. Ampleford, *Astrophysical Jets with Conical Wire Arrays: Radiative Cooling, Rotation & Deflection*, Dense Z-Pinches: 7^{th} International Conference, pp. 1–6 (Jan 2009).

[56] S. Eliezer, *The interaction of high-power lasers with plasmas*, Series in plasma physics, CRC Press (2002).

[57] W. L. Kruer, *The Physics of Laser Plasma Interactions*, Volume 73 of Frontiers in Physics, Westview Press (2003).

[58] M. E. García Saiz, *X-ray scattering from warm dense matter*, Ph.D. thesis, Queens University Belfast (Jun 2008).

[59] T. P. Hughes and M. B. Nicholson-Florence, *Intensity dependence of the inverse bremsstrahlung absorption coefficient in hot plasmas*, J. Phys. A: Gen. Phys., **1** (2), 588 (1968).

[60] M. H. Key and I. J. Spalding, *Interactions of Intense Laser Radiation with Plasma [and Discussion]*, Phil. Trans. R. Soc. Lond. A, **300**, 599–612 (1981).

[61] P. Gibbon and E. Förster, *Short-pulse laser-plasma interactions*, Plasma Phys. Control. Fusion, **38**, 769–793 (1996).

[62] P. D. Gupta, Y. Y. Tsui, R. Popil, R. Fedosejevs and A. A. Offenberger, *Experimental study of KrF-laser-high-Z-plasma interaction dominated by radiation transport*, Phys. Rev. A, **34** (5), 4103 (1986).

[63] B. H. Ripin, R. R. Whitlock, F. C. Y. S. P. Obenschain, E. A. McLean and R. Decoste, *Long-Pulse Laser-Plasma Interactions at* $10^{12} - 10^{15}$ W/cm^2, Phys. Rev. Lett., **43** (5), 350 (1979).

[64] P. Mora, *Theoretical model of absorption of laser light by a plasma*, Phys. Fluids, **25** (6), 1051 (1982).

[65] M. H. Key, W. T. Toner, T. J. Goldsack, J. D. Kilkenny, S. A. Veats *et al.*, *A study of ablation by laser irradiation of plane targets at wavelengths 1.05, 0.53, and 0.35 μm*, Phys. Fluids, **26** (7), 2011 (1983).

[66] B. Meyer and G. Thiell, *Experimental scaling laws for ablation parameters in plane target-laser interaction with 1.06 μm and 0.35 μm laser wavelengths*, Phys. Fluids, **27** (1), 302 (1984).

[67] A. Ng, D. Pasini, P. Celliers, D. Parfeniuk, L. D. Silva *et al.*, *Ablation scaling in steadystate ablation dominated by inversebremsstrahlung absorption*, Appl. Phys. Lett., **45** (10), 1046–1048 (1984).

[68] R. Fabbro, B. Faral, J. Virmont, F. Cottet, J. P. Romain *et al.*, *Experimental study of ablation pressures and target velocities obtained in 0.26 m wavelength laser experiments in planar geometry*, Phys. Fluids, **28** (22), 3414 (1985).

[69] A. C. Forsman and G. A. Kyrala, *Non-Doppler shift related experimental shock wave measurements using velocity interferometer systems for any reflector*, Phys. Rev. E, **63**, 056402 (2001).

[70] P. M. Celliers, D. K. Bradley, G. W. Collins, D. G. Hicks, T. R. Boehly *et al.*, *Line-imaging velocimeter for shock diagnostics at the OMEGA laser facility*, Rev. Sci. Instrum., **75** (11), 4916 (2004).

[71] J. E. Miller, T. R. Boehly, A. Melchior, D. D. Meyerhofer, P. M. Celliers *et al.*, *Streaked optical pyrometer system for laser-driven shock-wave experiments on OMEGA*, Rev. Sci. Instrum., **78**, 034903 (2007).

[72] B. Nagler, U. Zastrau, R. R. Fäustlin, S. M. Vinko, T. Whitcher *et al.*, *Turning solid aluminium transparent by intense soft X-ray photoionization*, Nature Physics, **5**, 693–696 (2009).

[73] M. Harb, R. Ernstorfer, C. T. Hebeisen, G. Sciaini, W. Peng *et al.*, *Electronically Driven Structure Changes of Si Captured by Femtosecond Electron Diffraction*, Phys. Rev. Lett., **100**, 155504 (2008).

[74] A. Benuzzi-Mounaix, M. K. A. Ravasio, T. Vinci, N. Ozaki, M. R. le Gloahec *et al.*, *Laser-driven shock waves for the study of extreme matter states*, Plasma Phys. Control. Fusion, **48**, B347–B358 (2006).

[75] J. R. Rygg, F. H. Séguin, C. K. Li, J. A. Frenje, M. J.-E. Manuel *et al.*, *Proton radiography of inertial fusion implosions*, Science, **319**, 1223 (2008).

[76] L. Spitzer, *Physics of Fully Ionized Gases*, Interscience, New York (1962).

[77] M. W. C. Dharma-wardana and F. Perrot, *Energy relaxation and the quasiequation of state of a dense two-temperature nonequilibrium plasma*, Phys. Rev. E, **58** (3), 3705–18 (1998).

[78] T. Ao, L. Vollrath and A. Ng, *Optical Probing of the Electron Temperature Gradient*, CP620, Shock Compression of Condensed Matter - 2001, **620**, 1243–1246 (2002).

[79] J. Delettrez, *Thermal electron transport in direct-drive laser fusion*, Canadian Journal of Physics, **64** (8), 932–943 (1986).

[80] J. Delettrez, R. Epstein, M. C. Richardson, P. A. Jaanimagi and B. L. Henke, *Effect of laser illumination nonuniformity on the analysis of time-resolved x-ray measurements in uv spherical transport experiments*, Phys. Rev. A, **36** (8), 3926–34 (1987).

[81] S. H. Glenzer, G. Gregori, R. W. Lee, F. J. Rogers, S. W. Pollaine *et al.*, *Demonstration of spectrally resolved X-ray scattering in dense plasmas*, Phys. Rev. Lett., **90** (17), 175002 (2003).

[82] G. Gregori, S. H. Glenzer, K. B. Fournier, K. M. Campbell, E. L. Dewald *et al.*, *X-Ray Scattering Measurements of Radiative Heating and Cooling Dynamics*, Phys. Rev. Lett., **101**, 045003 (2008).

[83] A. L. Kritcher, P. Neumayer, J. Castor, T. Döppner, R. W. Falcone *et al.*, *Ultrafast X-ray Thomson Scattering of Shock-Compressed Matter*, Science, **322**, 69 (2008).

[84] R. R. Fäustlin, T. Bornath, T. Döppner, S. Düsterer, E. Förster *et al.*, *Observation of ultrafast nonequilibrium collective dynamics in warm dense hydrogen*, Phys. Rev. Lett., **104**, 125002 (2010).

[85] C. E. Weir, E. R. Lippincott, A. V. Valkenburg and E. N. Bunting, *Infrared studies in 1-micron to 15-micron region to 30,000 athmospheres*, J. Res. Nat. Bur. Stand. Sec. A, **63** (1), 55 (1959).

[86] W. A. Bassett, *Diamond anvil cell, 50th birthday*, High Pres. Res., **29** (2), 163 (2009).

[87] H.-K. Mao and R. J. Hemley, *New windows on the Earth's deep interior*, Reviews in Mineralogy and Geochemistry, **37**, 1 (1998).

[88] S. Sinogeikin, *Practical Aspects of High Practical Aspects of High Pressure Experiments*, Short Course: Synchrotron X-Ray Methods in High Pressure Research, Advanced Photon Source, Argonne National Laboratory, Argonne IL (September 15-18, 2010).

[89] Z. Konopkova, *Thermal Conductivity of Materials under Conditions of Planetary Interiors*, Ph.D. thesis, Uppsala University (2011).

[90] S. N. K. Sundberg, *Optical and Raman Spectroscopic Studies on H_2O at High Pressure*, Ph.D. thesis, Uppsala University (2005).

[91] J. D. Barnett, S. Block and G. J. Piermarini, *An optical fluorescence system for quantitative pressure measurement in the diamond-anvil cell*, Rev. Sci. Instrum., **44**, 1 (1973).

[92] K. Syassen, *Ruby under pressure*, High Pressure Research, **28** (2), 75–126 (2008).

[93] I. F. Silvera, S. J. Jeon and H. E. Lorenzana, *Pressure dependence of the vibron modes in solid hydrogen and deuterium*, Phys. Rev. B, **46** (9), 5791 (1992).

[94] P. Loubeyre, P. M. Celliers, D. G. Hicks, A. Dewaele, J. Pasley *et al.*, *Coupling static and dynamic compressions: First measurements in dense hydrogen*, High Pres. Res., **24** (1), 25 (2004).

[95] J. Eggert, S. Brygoo, P. Loubeyre, R. S. McWilliams, P. M. Celliers *et al.*, *Hugoniot Data for Helium in the Ionization Regime*, Phys. Rev. Lett., **100**, 124503 (2008).

[96] E. Nardi, *Scattering of x rays by the bound and free electrons in dense plasma*, Phys. Rev. A, **43** (4), 1977 (1991).

[97] E. Nardi, Z. Zinamon, D. Riley and N. C. Woolsey, *X-ray scattering as a dense plasma diagnostic*, Phys. Rev. E, **57** (4), 4693 (1998).

[98] N. C. Woolsey, D. Riley and E. Nardi, *Kilovolt x-ray scattering from a plasma*, Rev. Sci. Instrum., **69** (2), 418 (1998).

[99] D. Riley, N. C. Woolsey, D. McSherry, I. Weaver, A. Djaoui *et al.*, *X-ray diffraction from a dense plasma*, Phys. Rev. Lett., **84** (8), 1704 (2000).

[100] O. L. Landen, S. H. Glenzer, M. J. Edwards, R. W. Lee, G. W. Collins *et al.*, *Dense matter characterization by X-ray Thomson scattering*, J. Quant. Spectrosc. Radiat. Transf., **71**, 465–478 (2001).

[101] S. H. Glenzer, G. Gregori, F. J. Rogers, D. H. Froula, S. W. Pollaine *et al.*, *X-ray scattering from solid density plasmas*, Phys. Plasmas, **10** (6), 2433 (2003).

[102] S. H. Glenzer, O. L. Landen, P. Neumayer, R. W. Lee, K. Widmann *et al.*, *Observations of Plasmons in Warm Dense Matter*, Phys. Rev. Lett., **98**, 065002 (2007).

[103] M. K. Urry, G. Gregori, O. L. Landen, A. Pak and S. H. Glenzer, *X-ray probe development for collective scattering measurements in dense plasmas*, J. Quant. Spectrosc. Radiat. Transf., **99**, 636–648 (2006).

[104] H. Sawada, S. P. Regan, D. D. Meyerhofer, I. V. Igumenshchev, V. N. Goncharov *et al.*, *Diagnosing direct-drive, shock-heated, and compressed plastic planar foils with noncollective spactrally resolved x-ray scattering*, Phys. Plasmas, **14**, 122703 (2007).

[105] M. E. García Saiz, G. Gregori, D. O. Gericke, J. Vorberger, B. Barbrel *et al.*, *Probing warm dense lithium by inelastic X-ray scattering*, Nature Physics, **4**, 940–944 (2008).

[106] R. Cauble, P. M. Celliers, G. W. Collins, L. B. da Silva, D. M. Gold *et al.*, *Equation of State and Material Property Measurements of Hydrogen Isotopes at the High-Pressure, High-Temperature, Insulator-Metal Transition*, Astrophys. J. Suppl. Ser., **127** (2), 267–273 (2000).

[107] T. R. Boehly, D. G. Hicks, P. M. Celliers, T. J. B. Collins, R. Earley *et al.*, *Properties of fluid deuterium under double-shock compression to several Mbar*, Phys. Plasmas, **11** (9), L49–L52 (2004).

[108] D. G. Hicks, T. R. Boehly, P. M. Celliers, J. H. Eggert, E. Vianello *et al.*, *Shock compression of quartz in the high-pressure fluid regime*, Phys. Plasmas, **12**, 082702 (2005).

[109] M. D. Knudson, D. L. Hanson, J. E. Bailey, R. W. Lemke, C. A. Hall *et al.*, *Equation of state measurements in liquid deuterium to 100 GPa*, J. Phys. A: Math. Gen., **36**, 6149–58 (2003).

[110] M. D. Knudson, D. L. Hanson, J. E. Bailey, C. A. Hall, J. R. Asay *et al.*, *Principal Hugoniot, reverberating wave, and mechanical reshock measurements of liquid deuterium to 400 GPa using plate impact techniques*, Phys. Rev. B, **69**, 144209 (2004).

[111] S. I. Belov, G. V. Boriskov, A. I. Bykov, R. I. Il'Kaev, N. B. Luk'yanov *et al.*, *Shock compression of solid deuterium*, JETP Letters, **76** (7), 433–435 (2002).

[112] M. D. Knudson and M. P. Desjarlais, *Shock compression of Quartz to 1.6 tPa: redefining a Pressure standard*, Phys. Rev. Lett., **103**, 225501 (2009).

[113] G. W. Collins, P. M. Celliers, L. B. da Silva, R. Cauble, D. M. Gold *et al.*, *Temperature measurements of shock compressed liquid deuterium up to 230 GPa*, Phys. Rev. Lett., **87** (16), 165504 (2001).

[114] J. E. Bailey, M. D. Knudson, A. L. Carlson, G. S. Dunham, M. P. Desjarlais *et al.*, *Time-resolved optical spectroscopy measurements of shocked liquid deuterium*, Phys. Rev. B, **78**, 144107 (2008).

[115] S. T. Weir, A. C. Mitchell and W. J. Nellis, *Metallization of fluid molecular hydrogen at 140 GPa (1.4 Mbar)*, Physical review letters, **76** (11), 1860 (1996).

[116] W. J. Nellis, A. A. Louis and N. W. Ashcroft, *Metallization of Fluid Hydrogen*, Phil. Trans. R. Soc. A, **356**, 119–135 (1998).

[117] W. J. Nellis, *Dynamic compression of materials: metallization of fluid hydrogen at high pressures*, Rep. Prog. Phys. IOP, **69**, 1479–1580 (2006).

[118] R. J. Hemley, H.-K. Mao, L. W. Finger, A. P. Jephcoat, R. M. Hazen *et al.*, *Equation of state of solid hydrogen and deuterium from single-crystal x-ray diffraction to 26.5 GPa*, Phys. Rev. B, **42** (10), 6458 (1990).

[119] P. Loubeyre, R. Letoullec, D. Hausermann, M. Hanfland, R. J. Hemley *et al.*, *X-ray diffraction and equation of state of hydrogen at megabar pressures*, Nature, **383**, 702–704 (1996).

[120] P. Loubeyre, F. Occelli and R. LeToullec, *Optical studies of solid hydrogen to 320 GPa and evidence for black hydrogen*, Nature, **416**, 613–617 (2002).

[121] H.-K. Mao and R. J. Hemley, *Ultrahigh-pressure transitions in solid hydrogen*, Rev. Mod. Phys., **66** (2), 671–692 (1994).

[122] D. Saumon and G. Chabrier, *Fluid Hydrogen at High Density: The Plasma Phase Transition*, Phys. Rev. Lett., **62** (20), 2397 (1989).

[123] D. Saumon and G. Chabrier, *Fluid hydrogen at high density: Pressure Ionization*, Phys. Rev. A, **46** (4), 2084 (1992).

[124] B. Holst, R. Redmer and M. P. Desjarlais, *Thermophysical properties of warm dense hydrogen using quantum molecular dynamics simulations*, Phys. Rev. B, **77**, 184201 (2008).

[125] B. Militzer and D. M. Ceperley, *Path Integral Monte Carlo Calculation of the Deuterium Hugoniot*, Phys. Rev. Lett., **85** (9), 1890 (2000).

[126] G. Gregori, *Graduate Class in Plasma Physics: Statistical Theory and Strongly Coupled Plasmas*, University of Oxford (2009).

[127] S. Ichimaru, *Basic principles of plasma physics: a statistical approach*, Issue 41 of Frontiers in physics, W. A. Benjamin (1973).

[128] J.-P. Hansen and I. R. McDonald, *Theory of simple liquids*, Academic Press (2006).

[129] L. D. Landau and E. M. Lifshitz, *Physical kinetics: Volume 10 of Course of theoretical physics*, Butterworth-Heinemann (1981).

[130] G. Gregori, S. H. Glenzer, W. Rozmus, R. W. Lee and O. L. Landen, *Theoretical model of x-ray scattering as a dense matter probe*, Phys. Rev. E, **67**, 026412 (2003).

[131] J. Chihara, *Difference in x-ray scattering between metallic and non-metallic liquids due to conduction electrons*, J. Phys. F: Met. Phys., **17**, 295–304 (1987).

[132] J. Chihara, *Interaction of photons with plasmas and liquid metals-photoabsorption and scattering*, J. Phys.: Condens. Matter, **12**, 231–247 (2000).

[133] D. Froula, J. Sheffield, S. H. Glenzer and N. C. Luhmann, *Plasma Scattering of Electromagnetic Radiation: Theory and Measurement Techniques*, Academic Press, second edition (2010).

[134] J. Chihara, *Effective interionic interaction in liquid metals: liquid metallic hydrogen*, J. Phys. C: Solid State Phys., **19**, 1665 (1986).

[135] R. W. James, *The Optical Properties of Diffraction of X-Rays*, Ox Bow Press, Woodbridge, CT (1962).

[136] L. Pauling and J. Sherman, *Screening constants for many-electron atoms - The calculation and interpretation of X-ray term values, and the calculation of atomic scattering factors*, Zeitschrift Für Kristallographie, **81** (1/2), 1–29 (1932).

[137] J. P. Hansen, *Statistical mechanics of dense ionized matter. I. Equilibrium properties of the classical one-component plasma*, Phys. Rev. A, **8** (6), 3096 (1973).

[138] J. P. Hansen, I. R. McDonald and E. L. Pollock, *Statistical mechanics of dense ionized matter. III. Dynamical properties of the classical one-component plasma*, Phys. Rev. A, **11** (3), 1025 (1975).

[139] G. Gregori, A. Ravasio, A. Höll, S. H. Glenzer and S. J. Rose, *Derivation of the static structure factor in strongly coupled non-equilibrium plasmas for X-ray scattering studies*, HEDP, **3**, 99–108 (2007).

[140] K. Wünsch, J. Vorberger, M. Schlanges and D. O. Gericke, *Ion structure for x-ray Thomson scattering in dense fusion plasmas*, J. Phys.: Conf. Ser., **112**, 032077 (2008).

[141] K. Wünsch, P. Hilse, M. Schlanges and D. O. Gericke, *Structure of strongly coupled multicomponent plasmas*, Phys. Rev. E, **77**, 056404 (2008).

[142] V. Schwarz, B. Holst, T. Bornath, C. Fortmann, W. D. Kraeft *et al.*, *Static ion structure factor for dense plasmas: Semi-classical and ab initio calculations*, HEDP, **6**, 305–310 (2010).

[143] R. Kubo, *Statistical-Mechanical Theory of Irreversible Processes.II. : Response to Thermal Disturbance*, J. Phys. Soc. Jpn., **12** (11), 570 (1957).

[144] E. E. Salpeter, *Electron Density Fluctuations in a Plasma*, Phys. Rev., **120**, 1528 (1960).

[145] D. Pines and D. Bohm, *A Collective Description of Electron Interactions: II. Collective vs Individual Particle Aspects of the Interactions*, Phys. Rev., **82** (2), 338–353 (1952).

[146] D. Pines, *Elementary excitations in solids: lectures on protons, electrons, and plasmons*, Advanced Book Program Series, Perseus Books (1999).

[147] J. W. DuMond and H. A. Kirkpatrick, *Experimental evidence for electron velocities as the cause of Compton line breadth with the multicrystal spectrograph*, Physical Review, **37**, 136 (1931).

[148] D. Salzmann, *Atomic physics in hot plasmas*, Volume 97 of International series of monographs on physics, Oxford University Press (1998).

[149] J. C. Kimball, *Short-Range Correlations and Electron-Gas Response Functions*, Phys. Rev. A, **7** (5), 1648 (1973).

[150] J. C. Kimball, *High-density expansion of the electron-gas correlation function*, Phys. Rev. B, **14** (6), 2371 (1976).

[151] D. K. Bradley, J. Kilkenny, S. J. Rose and J. D. Hares, *Time-resolved continuum-edge-shift measurements in laser-shocked solids*, Phys. Rev. Lett., **59** (26), 2995 (1987).

[152] D. Riley, O. Willi, S. J. Rose and T. Afshar-Rad, *Blue shift of the K absorption edge in laser-shocked solids*, Europhys. Lett., **10** (2), 135–140 (1989).

[153] J. C. Stewart and K. D. Pyatt, *Lowering of ionization potentials in plasmas*, Astrophys. J., **144**, 1203 (1966).

[154] R. Zimmermann, K. Kilimann, W. D. Kraeft, D. Kremp and G. Röpke, *Dynamical Screening and Self-Energy of Excitons in the Electron-Hole Plasma*, Physica Status Solidi B - Basic Solid State Physics, **90** (1), 175 (1978).

[155] F. J. Rogers, H. C. Graboske and D. J. Harwood, *Bound eigenstates of the static screened Coulomb potential*, Phys. Rev. A, **1** (6), 1577 (1970).

[156] P. Eisenberger and P. M. Platzman, *Compton Scattering of X Rays from Bound Electrons*, Phys. Rev. A, **2** (2), 415 (1970).

[157] A. Issolah, Y. Garreau, B. Lévy and G. Loupias, *Experimental check of core Compton profiles, calculated using a quasi-self-consistent-field method*, Phys. Rev. B, **44** (20), 11029 (1991).

[158] H. Smith, *The Lindhard Function and Teaching of Solid State Physics*, Physica Scripta, **28**, 287–293 (1983).

[159] G. D. Mahan, *Many-Particle Physics*, Springer (1990).

[160] J. Lindhard, *On the properties of a gas of charged particles*, Kgl. Danske Videnskab. Selskab Mat.-fys. Medd., **28** (8), 1–57 (1954).

[161] N. W. Ashcroft and N. D. Mermin, *Solid State Physics*, Holt-Saunders International Editions: Science : Physics, Holt, Rinehart and Winston (1976).

[162] M. Gell-Mann and K. A. Brueckner, *Correlation energy of an electron gas at high density*, Phys. Rev., **106** (2), 364 (1957).

[163] N. R. Arista and W. Brandt, *Dielectric response of quantum plasmas in thermal equilibrium*, Phys. Rev. A, **29** (3), 1471 (1984).

[164] S. Eliezer, A. K. Ghatak and H. Hora, *Fundamentals of equations of state*, World Scientific (2002).

[165] G. Gregori, U. Kortshagen, J. Heberlein and E. Pfender, *Analysis of Thomson scattered light from an arc plasma jet*, Phys. Rev. E, **65** (4), 046411 (2002).

[166] G. Gregori and D. O. Gericke, *Low frequency structural dynamics of warm dense matter*, Phys. Plasmas, **16**, 056306 (2009).

[167] S. G. Brush, H. L. Sahlin and E. Teller, *Monte Carlo Study of a One-Component Plasma. I*, J. Chem. Phys., **45** (6), 2102 (1966).

[168] E. J. Linnebur and J. J. Duderstadt, *Theory of light scattering from dense plasmas*, Phys. Fluids, **16** (5), 665 (1973).

[169] D. B. Boercker and R. M. More, *Statistical mechanics of a two-temperature, classical plasma*, Phys. Rev. A, **33** (3), 1859 (1986).

[170] J. P. Mithen, J. Daligault and G. Gregori, *Extent of validity of the hydrodynamic description of ions in dense plasmas*, Phys. Rev. E, **83**, 015401(R) (2011).

[171] A. Grinenko, D. O. Gericke, S. H. Glenzer and J. Vorberger, *Probing the Hydrogen Melting Line at High Pressures by Dynamic Compression*, Phys. Rev. Lett., **101**, 194801 (2008).

[172] G. I. Kerley, *SANDIA REPORT (SAND2003-3613): Equations of State for Hydrogen and Deuterium*, Technical report, Sandia National Laboratories (2003).

[173] M. D. Knudson, D. L. Hanson, J. E. Bailey, C. A. Hall and J. R. Asay, *Use of a wave reverberation technique to infer the density compression of shocked liquid deuterium to 75 GPa*, Phys. Rev. Lett., **90** (3), 035505 (2003).

[174] Bonshov, *et al.*, Doklady, **48**, 553 (2003).

[175] T. J. Lenosky, J. D. Kress and L. A. Collins, *Molecular-dynamics modeling of the Hugoniot of shocked liquid deuterium*, Phys. Rev. B, **56** (9), 5164 (1997).

[176] T. J. Lenosky, S. R. Bickham, J. D. Kress and L. A. Collins, *Density-functional calculation of the Hugoniot of shocked liquid deuterium*, Phys. Rev. B, **61** (1), 1–4 (2000).

[177] G. Kresse and J. Furthmüller, *Efficient iterative schemes for ab initio total-energy calculations using a plane-wave basis set*, Phys. Rev. B, **54** (16), 11169 (1996).

[178] G. Kresse and D. Jouber, *From ultrasoft pseudopotentials to the projector augmented-wave method*, Phys. Rev. B, **59** (3), 1758 (1999).

[179] J. J. MacFarlane, I. E. Golovkin and P. R. Woodruff, *HELIOS-CR-A 1-D radiation-magnetohydrodynamics code with inline atomic kinetics modeling*, J. Quant. Spectrosc. Radiat. Transf., **99**, 381–397 (2006).

[180] P. B. Radha, T. J. B. Collins, J. A. Delettrez, Y. Elbaz, R. Epstein *et al.*, *Multidimensional analysis of direct-drive, plastic-shell implosions on OMEGA*, Phys. Plasmas, **12**, 056307 (2005).

[181] *LLE Review: Quarterly Report Volume 123*, Laboratory for Laser Energetics, University of Rochester (April - June 2010).

[182] W. F. Huebner, A. L. Merts, N. H. Magee and M. F. Argo, *Report LA-6760-M*, Los Alamos National Laboratory (1977).

[183] R. C. Malone, R. L. McCrory and R. I. Morse, *Indications of strongly flux-limited electron thermal conduction in laser-target experiments*, Phys. Rev. Lett., **34**, 721 (1975).

[184] L. Spitzer and R. Härm, *Transport phenomena in a completely ionized gas*, Phys. Rev., **89**, 977 (1953).

[185] D. Keller, T. J. B. Collins, J. A. Delettrez, P. W. McKenty, P. B. Radha *et al.*, Bull. Am. Phys. Soc., **44** (37) (1999).

[186] J. Marozas, F. J. Marshall, R. S. Craxton, I. V. Igumenshchev, S. Skupsky *et al.*, *Polar-direct-drive simulations and experiments*, Phys. Plasmas, **13**, 056311 (2006).

[187] T. R. Boehly, D. L. Brown, R. S. Craxton, R. L. Keck, J. P. Knauer *et al.*, *Initial performance results of the OMEGA laser system*, Optics Communications, **133**, 495–506 (1997).

[188] S. P. Regan, J. A. Marozas, R. S. Craxton, J. H. Kelly, W. R. Donaldson *et al.*, *Performance of 1-THz-bandwidth, two-dimensional smoothing by spectral dispersion and polarization smoothing of high-power, solid-state laser beams*, JOSA B, **22** (5), 998–1002 (2005).

[189] S-AA-M-12, *OMEGA System Operations Manual - Volume I - System Description, Chapter 5: Optomechanical System*, Laboratory for Laser Energetics, University of Rochester (May 2003).

[190] T. J. Kessler, Y. Lin, J. J. Armstrong and B. Velazquez, *Phase conversion of lasers with low-loss distributed phase plates*, Proc. SPIE, **95**, 1870 (1993).

[191] Y. Lin, T. J. Kessler and G. N. Lawrence, *Distributed phase plates for super-Gaussian focal-plane irradiance profiles*, Opt. Lett., **20** (7), 764–766 (1995).

[192] R. S. Craxton, *LLE Review: Quarterly Report Volume 63*, Laboratory for Laser Energetics, University of Rochester (April-June 1995).

[193] R. S. Craxton, *High efficiency frequency tripling schemes for high-power Nd: glass lasers*, IEEE J. Quantum Electron., **QE-17**, 1771–1782 (1981).

[194] NLUF, *National Laser Users' Facility: Users' Guide*, Laboratory for Laser Energetics, University of Rochester (May 2007).

[195] H. Legall, H. Stiel, M. Schnürer, M. Pagels, B. Kanngießer *et al.*, *An efficient X-ray spectrometer based on thin mosaic crystal films and its application in various fields of X-ray spectroscopy*, J. App. Cryst., **42**, 572–9 (2009).

[196] G. E. Ice and C. J. Sparks, *Mosaic crystal x-ray spectrometer to resolve inelastic background from anomalous scattering experiments*, Nucl. Instrum. Methods Phys. Res. A, **291**, 110–116 (1990).

[197] M. Sánches del Río, M. Gambaccini, G. Pareschi, A. Taibi, A. Tuffenelli *et al.*, *Focusing properties of mosaic crystals*, Proc. SPIE, **3448**, 246–255 (1998).

[198] A. Tuffanelli, M. Gambaccini, A. Fantini, M. Sánches del Río, G. Pareschi *et al.*, *Comparative characterization of highly oriented pyrolytic graphite by means of diffraction topography*, Proc. SPIE, **3773**, 192–198 (1999).

[199] A. Pak, G. Gregori, J. Knight, K. Campbell, . Price *et al.*, *X-ray line measurements with high efficiency Bragg crystals*, Rev. Sci. Instrum., **75** (10), 3747 (2004).

[200] J. D. Kilkenny, *High Speed Proximity Focused X-Ray Cameras*, Laser Part. Beams, **9** (49) (1991).

[201] D. K. Bradley, P. M. Bell, O. L. Landen, J. D. Kilkenny and J. Oertel, *Development and Characterization of a Pair of 30-40 ps X-Ray Framing Cameras*, Rev. Sci. Instrum., **66** (1), 716 (1995).

[202] J. D. Kilkenny, P. Bell, R. Hanks, G. Power, R. E. Turner *et al.*, *High-Speed Gated X-Ray Imagers*, Rev. Sci. Instrum., **59** (8), 1793 (1988).

[203] P. M. Bell, J. D. Kilkenny, G. Power, R. Bonner and D. K. Bradley, *Ultrahigh Speed and High Speed Photography, Photonics, and Videography VII*, volume 1155, chapter Multiframe x-ray images from a single meander stripline coated on a microchannel plate, p. 430, SPIE, Bellingham, WA (1989).

[204] R. E. Turner, O. L. Landen, D. K. Bradley, S. S. Alvarez, P. M. Bell *et al.*, *Comparison of charge coupled device vs film readouts for gated micro-channel plate cameras*, Rev. Sci. Instrum., **72** (1), 706 (2001).

[205] F. J. Marshall, T. Ohki, D. McInnis, Z. Ninkov and J. Carbone, *Imaging of laser-plasma x-ray emission with charge-injection devices*, Rev. Sci. Instrum., **72** (1), 713 (2001).

[206] D. H. Kalantar, P. M. Bell, R. L. Costa, B. A. Hammel, O. L. Landen *et al.*, *Characterization of X-ray streak cameras for use on Nova*, Proc. SPIE, **2869**, 680 (1997).

[207] L. M. Barker and R. E. Hollenbach, *Laser interferometer for measuring high velocities of any reflecting surface*, J. Appl. Phys., **43** (11), 4669–4675 (1972).

[208] M. Takeda, H. Ina and S. Kobayashi, *Fourier-transform method of fringe-pattern analysis for computer-based topography and interferometry*, J. Opt. Soc. Am., **72** (1), 156 (1982).

[209] L. M. Barker and K. W. Schuler, *Correction to the velocity-per-fringe relationship for the VISAR interferometer*, J. Appl. Phys., **45** (8), 3692–3693 (1974).

[210] Y. B. Zel'dovich and Y. P. Raizer, *Physics of Shock Waves and High Temperature Hydrodynamic Phenomena*, Dover, Mineola, NY (2002).

[211] D. W. Phillion and C. J. Hailey, *Brightness and duration of x-ray line sources irradiated with intense 0.53-m laser light at 60 and 120 ps pulse width*, Phys. Rev. A, **34** (6), 4886 (1986).

[212] J. E. Bateman, *The detection of hard X-rays (10-140 keV) by channel plate electron multipliers*, Nucl. Instrum. Methods, **144** (3), 537–545 (1977).

[213] G. Gregori, S. Glenzer, F. Rogers, S. Pollaine, O. L. Landen *et al.*, *Electronic structure measurements of dense plasmas*, Phys. Plasmas, **11** (5), 2754 (2004).

[214] G. Gregori, S. H. Glenzer, H. K. Chung, D. H. Froula, R. W. Lee *et al.*, *Measurement of carbon ionization balance in high-temperature plasma mixtures by temporally resolved X-ray scattering*, J. Quant. Spectrosc. Radiat. Transf., **99**, 225–237 (2006).

[215] S-AD-M-011, *OMEGA System Operations Manual - Volume VII - System Description, Chapter 7: Experimental System*, Laboratory for Laser Energetics, University of Rochester (July 2007).

[216] D. G. Hicks, *XVIS program for VISAR analysis*, Lawrence Livermore National Laboratory, 7000 East Avenue, Livermore, CA 94550, USA.

[217] J. M. Walsh, M. H. Rice, R. G. McQueen and F. L. Yarger, *Shock-wave compressions of twenty-seven metals. Equations of state of metals*, Phys. Rev., **108** (2), 196 (1957).

[218] M. P. Desjarlais, *Density-functional calculations of the liquid deuterium Hugoniot, reshock, and reverberation timing*, Phys. Rev. B, **68** (6), 064204 (2003).

[219] S. Atzeni and J. Meyer-ter-Vehn, *The physics of inertial fusion: beam plasma interaction, hydrodynamics, hot dense matter*, Issue 125 of International series of monographs on physics, Oxford University Press (2004).

[220] G. B. Rybicki and A. P. Lightman, *Radiative processes in astrophysics*, Wiley-VCH (1979).

[221] D. A. Greenwood, *The Boltzmann equation in the theory of electrical conduction in metals*, Proc. Phys. Soc. Lond. A, **71**, 585 (1958).

[222] H. Reinholz, R. Redmer, G. Röpke and A. Wierling, *Long-wavelength limit of the dynamical local-field factor and dynamical conductivity of a two-component plasma*, Phys. Rev. E, **62** (4), 5648 (2000).

[223] B. Barbrel, M. Koenig, A. Benuzzi-Mounaix, E. Brambrink, C. R. D. Brown *et al.*, *Measurement of Short-Range Correlations in Shock-Compressed Plastic by Short-Pulse X-Ray Scattering*, Phys. Rev. Lett., **102**, 165004 (2009).

[224] G. Wheatley, *Applied Numerical Analysis*, Pearson Education, seveth edition (2004).

[225] L. von Hamos, Naturwissenschaften, pp. 705–706 (1932).

[226] H. Legall, H. Stiel, A. Antonov, I. Grigorieva, V. Arkadiev *et al.*, *A new generation of X-ray optics based on pyrolytic graphite*, Proc. FEL, BESSY, Berlin, FRAAU04, pp. 798–801 (2006).

[227] PSI, *PILATUS Project (http://pilatus.web.psi.ch/pilatus.htm).*

[228] X. Lu, S. Venugopalan, H. J. Kim, M. Grimsditch, S. Rodriguez *et al.*, *Doubly resonant Raman electron paramagnetic transitions of Cr^{3+} in ruby (Al_2O_3: Cr^{3+})*, Phys. Rev. B, **79** (23), 235204 (2009).

[229] J. H. Eggert, K. A. Goettel and I. F. Silvera, *Ruby at high pressure. I. Optical line shifts to 156 GPa*, Phys. Rev. B, **40** (8), 5724 (1989).

[230] J. H. Eggert, K. A. Goettel and I. F. Silvera, *Ruby at high pressure. II. Fluorescence lifetime of the R line to 130 GPa*, Phys. Rev. B, **40** (8), 5733 (1989).

[231] J. H. Eggert, F. Moshary, W. J. Evans, K. A. Goettel and I. F. Silvera, *Ruby at high pressure. III. A pumping scheme for the R lines up to 230 GPa*, Phys. Rev. B, **44** (14), 7202 (1991).

[232] G. J. Piermarini, S. Block, J. D. Barnett and R. A. Forman, *Calibration of the R1 ruby florescence line to 195 kbar*, J. Appl. Phys., **46**, 2774–80 (1975).

[233] H.-K. Mao, J. Xu and P. M. Bell, *Calibration of the ruby pressure gauge to 800 kbar under quasi-hydrostatic conditions*, J. Geophys. Res., **91**, 4673–4676 (1986).

[234] W. B. Holzapfel, *Progress in the realization of a practical pressure scale for the range 1–300 GPa*, High Pres. Res., **25**, 87 (2005).

[235] A. Chijioke, W. J. Nellis, A. Soldatov and I. F. Silvera, *The ruby pressure standard to 150 GPa*, J. Appl. Phys. 98, **98**, 114905 (2005).

[236] P. I. Dorogokupets and A. R. Oganov, *Ruby pressure scale: revision and alternatives*, Proc. Joint 20th AIRAPT and 43th EHPRG International Conference on High Pressure Science and Technology, Karlsruhe/Germany (2005).

[237] M. S. Anderson and C. A. Swenson, *Experimental compressions for normal hydrogen and normal deuterium to 25 kbar at 4. 2 K*, Phys. Rev. B, **10** (12), 5184–5191 (1974).

[238] A. Savitzky and M. E. Golay, *Smoothing and differentiation of data by simplified least squares procedures.*, Analytical Chemistry, **36** (8), 1627 (1964).

[239] W. H. Press, S. A. Teukolsky, W. T. Vetterling and B. P. Flannery, *Numerical Recipes in C*, Cambridge University Press, second edition (1992).

[240] G. Gregori, S. H. Glenzer and O. L. Landen, *Strong coupling corrections in the analysis of x-ray Thomson scattering measurements*, J.Phys. A: Math. Gen., **36**, 5971–5980 (2003).

[241] E. Gregoryanz, *Raman Spectroscopy of Hot Dense Hydrogen*, Phys. Rev. Lett., **90** (17), 4 (2003).

[242] K. Utsumi and S. Ichimaru, *Dielectric formulation of strongly coupled electron liquids at metallic densities. VI. Analytic expression for the local-field correction*, Phys. Rev. A, **26** (1), 603 (1982).

[243] J. W. Stewart, *Compression of Solidified Gases to 20,000 kg/cm^2 at Low Temperature*, J. Phys. Chem. Solids, **1**, 146–158 (1956).

[244] S. P. Regan, K. Falk, G. Gregori, P. B. Radha, S. X. Hu *et al.*, *Inelastic X-ray Scattering from Shocked Liquid Deuterium*, submitted to Phys. Rev. Lett. (2012).